PROBABILISTIC TRANSIENT ANALYSIS OF FUEL CHOICES FOR SODIUM FAST REACTORS

By

Matthew R. Denman

B.S. Nuclear Engineering
University of Florida, 2007

SUBMITTED TO THE DEPARTMENT OF NUCLEAR SCIENCE AND ENGINEERING IN PARTIAL FULFILLMENT OF THE REQUIREMENTS FOR THE DEGREE OF

DOCTOR OF PHILOSOPHY IN NUCLEAR SCIENCE AND ENGINEERING
AT THE
MASSACHUSETTS INSTITUTE OF TECHNOLOGY

JUNE, 2011

Signature of Author: ______________________________
Department of Nuclear Science and Engineering
February 10, 2011

Certified by: ______________________________
Dr. Neil E. Todreas, Thesis Supervisor
Professor Emeritus of Nuclear Science and Engineering

Certified by: ______________________________
Dr. Michael J. Driscoll, Thesis Reader
Professor Emeritus of Nuclear Science and Engineering

Accepted by: ______________________________
Dr. Mujid S. Kazimi
Chair, Department Committee on Graduate Students

Probabilistic Transient Analysis of Fuel Choices for Sodium Fast Reactors

By

Matthew R. Denman

B.S. Nuclear Engineering
University of Florida, 2007

SUBMITTED TO THE DEPARTMENT OF NUCLEAR SCIENCE AND ENGINEERING IN PARTIAL FULFILLMENT OF THE REQUIREMENTS FOR THE DEGREE OF

DOCTOR OF PHILOSOPHY IN NUCLEAR SCIENCE AND ENGINEERING
AT THE
MASSACHUSETTS INSTITUTE OF TECHNOLOGY

JUNE, 2011

Abstract

This thesis presents the implications of using a risk-informed licensing framework to inform the design of Sodium Fast Reactors. NUREG-1860, more commonly known as the Technology Neutral Framework (TNF), is a risk-informed licensing process drafted by the Nuclear Regulatory Commission's (NRC) Office of Nuclear Regulatory Research. The TNF determines the acceptability of accident sequences by examining the 95th percentile estimate of both the frequency and quantity of radioactive material release and compares this value to predetermined limits on a Frequency-Consequence Curve. In order to apply this framework, two generic pool type sodium reactors, one using metal fuel and one using oxide fuel, were modeled in RELAP5-3D in order to determine the transient response of reactors to unprotected transient overpower and unprotected loss of flow events. Important transient characteristics, such as the reactivity coefficients, were treated as random variables which determine the success or failure of surviving the transient. In this context, success is defined as the cladding remaining intact and the avoidance of sodium boiling. In order to avoid running an excessive amount of simulations, the epistemic uncertainties around the random variables are sampled using importance sampling.

For metallic fuel, the rate of fuel/cladding eutectic formation has typically been modeled as an Arrhenius process which depends only on the temperature of the fuel/cladding interface. Between the 1960s and the 1990s, numerous experiments have been conducted which indicate that the rate of fuel/cladding eutectic formation is more complex, depending upon fuel/cladding interfacial temperature, fuel constituents (uranium metal or uranium zirconium), cladding type (stainless steel 316, D9 or HT9), linear power, plutonium enrichment and burnup. This thesis improves the modeling accuracy of eutectic formation through the application of multivariable regression using a database of fuel/cladding eutectic experiments and determines that the remaining uncertainty governing the rate of eutectic formation should not significantly affect the frequency of cladding failure for tested cladding options.

The general conclusion from this thesis is that when using NUREG-1860 to license metal or oxide fueled SFRs, it is steady state, not transient, cladding considerations which control optimal operating temperature, currently corresponding to an approximate core outlet temperature of 550°C. Metallic cores traditionally have been designed with core outlet temperatures of 510°C and increasing this temperature to 550°C may decrease the busbar cost by 19% when combined with the adoption of a Supercritical-CO_2 power conversion cycle, reduced containment requirements, and Printed Circuit Heat Exchangers. While both fuel types will be shown to meet the NUREG-1860 requirements, the frequency of radiation release for unprotected loss of flow and unprotected transient overpower events for metallic fuel has been shown to be orders of magnitude lower than for oxide fuel.

Thesis Supervisor: Neil E. Todreas
Professor Emeritus
MIT Department of Nuclear Science and Engineering

Thesis Reader: Michael J. Driscoll
Professor Emeritus
MIT Department of Nuclear Science and Engineering

Acknowledgments

First of all, I would like to thank my advisors, Professor Neil Todreas and Professor Mike Driscoll, for their guidance and encouragement throughout the duration of this project, not to mention their countless suggested revisions to this thesis. I am grateful to all of the NERI project contributors who have supported this work. Specifically, I would like to thank Professors Apostolakis, Denning, Zuchetti and Golay, who guided the NERI project over the course of my thesis.

I would like to thank Matt Memmott and Koroush Shirvan for assisting me with numerous issues concerning the ABR1000 RELAP5-3D model.

Finally, I would like to thank all of the friends and family members who have supported me over the past couple of years. While there are too many to list, I am especially grateful for the support and encouragement that I received from my parents. I would also like to thank my fiancée Rachel E. Sharples for proof-reading some of my writing when I was too tired and helping conceive the BEAGLE acronym.

This work is a product of the project "Risk-Informed Balancing of Safety, Non-Proliferation, and Economics for the Sodium-Cooled Fast Reactor (SFR)" supported by the US Department of Energy under a NERI contract (DE-FG07-07ID14888). The views presented here are those of the authors and do not necessarily represent the views of the US Department of Energy.

Table of Contents

List of Figures

List of Tables

List of Acronyms

ABR-1000	Advanced Burner Reactor- 1000MW$_{th}$
ALMR	Advanced Liquid Metal Reactor
CDA	Core Disruptive Accident
CDF	Cumulative Distribution Function
CRBR	Clinch River Breeder Reactor
DC	Direct Couple
DRAC	Direct Reactor Auxiliary Cooling
EBR-II	Experimental Breeder Reactor-II
EC	Event Category
EFR	European Fast Reactor
ES	Energetic Scenario
FC	Frequency-Consequence
FCD	Fractional Cumulative Damage
FFTF	Fast Flux Test Facility
GE	General Electric
GFR	Gas Fast Reactor
HCF	Hot Channel Factor
IFR	Intergal Fast Reactor
IS	Importance Sampling
JAEA	Japan Atomic Energy Agency
JSFR	Japanese SFR
LBE	Licensing Basis Events
LOF	Loss Of Flow
LOHS	Loss Of Heat Sink
LWR	Light Water Reactor
MC	Monte Carlo
MCMC	Markov Chain Monte Carlo
NERI	Nuclear Energy Research Imitative
O&M	Operation and Maintenance
PCHE	Printed Circuit Heat Exchanger
PDF	Probability Distribution Function

PRA	Probabilistic Risk Assessment
PRAC	Primary Reactor Auxiliary Cooling
PRISM	Power Reactor Innovative Safe Modular
PSER	Preliminary Safety Evaluation Report
PSID	Preliminary Safety Information Document
RPS	Reactor Protection System
RVACS	Reactor Vessel Auxiliary Cooling System
S-CO_2	Supercritical Carbon Dioxide
SFR	Sodium Fast Reactor
S-PRISM	Super-PRISM
TNF	Technology Neutral Framework
TOP	Transient OverPower
ULOF	Unprotected Loss of Flow
ULOHS	Unprotected Loss of Heat Sink
UTOP	Unprotected Transient Overpower

I INTRODUCTION

This thesis is a product of work conducted for the project "Risk-Informed Balancing of Safety, Non-Proliferation, and Economics for the Sodium-Cooled Fast Reactor (SFR)" supported by the US Department of Energy under a NERI contract (DE-FG07-07ID14888). The premise of this project is that, while Sodium Fast Reactors have many promising characteristics when compared to Light Water Reactors (LWRs), SFRs are typically deemed more expensive, and thus cost prohibitive. It was believed that risk-information may be able to reduce unnecessary conservatism incorporated into existing SFR designs, most likely due to lack of knowledge about, or a deterministic approach to, reactor safety. Over the course of this project, NUREG-1860 (1), a theoretical risk-informed licensing structure produced by the Office of Regulatory Research in the Nuclear Regulatory Commission, was adopted to provide guidance in determining what design alternatives would, or would not, be acceptable from a regulatory perspective.

This thesis focuses on three aspects of risk-informing the SFR: what, if any, may be the design implications of choosing either a metal or oxide fuel form, how much can the busbar electricity cost be reduced by maximizing thermodynamic efficiency and how should modeling of the rate of metallic fuel/cladding eutectic formation be improved to take into account the approximately 30 years of experimental work in this area.

I.1 Sodium Fast Reactors Overview

Sodium reactors have many design alternatives which should be considered during cost reduction analysis. These design alternatives can be changes to the plant layout which significantly affect capital cost, such as whether to adopt a loop or a pool design, changes which affect core design, such as using oxide or metal fuel forms or the inclusion of Self Actuated Shutdown Systems (SASS). (2). In fact, many proposed SFR have multiple core designs to allow flexibility in fuel design or primary mission, such as producing electricity or burning long-lived actinides (3) (4).

The primary difference between loop and pool reactors is that loop reactors place the primary system pump and intermediate heat exchanger outside of the reactor vessel which requires more piping, thus increasing the potential for sodium leaks, but allow for a smaller vessel diameter (5). The smaller vessel diameter results in lower primary sodium inventory that can be used for emergency cooling but saves in capital cost.

Sodium reactor designs often rely on passive safety to provide an extra layer of protection against severe accidents. While passive systems do not have to be externally activated like active systems, the uncertainties surrounding passive response require large safety margins to safely mitigate an accident. Provisions of these large margins may constrain the economic viability of reactors that rely fully on passive systems, especially if inherent shutdown from reactivity feedbacks is required in anticipated transients without scram.

The US efforts to create a commercial sodium reactor have evolved in approach and design between the 1970s and present day. The first major commercial reactor licensing project undertaken was Clinch River Breeder Reactor (CRBR), which was a loop-type SFR with oxide fuel. This design attempted to mirror LWR designs which were constructed during CRBR's design phase. Substantial regulatory effort was expended responding to intervenor's insistence that Hypothetical Core Destructive Accidents (HCDAs) be considered as part of the design basis of CRBR. The NRC Atomic Safety and Licensing Board (ASLB) eventually excluded HCDAs from the licensing basis, with the NRC staff stating:

> *It is our current position that the probability of core melt and disruptive accidents can and must be reduced to a sufficiently low level to justify their exclusion from the design basis accident spectrum.*

After CRBR was canceled after cost overruns and licensing delays in 1983, the DOE embarked on the Integral Fast Reactor (IFR) program in 1984. This program emphasized a pool type reactor concept that would avoid some of the regulatory hurdles which impeded CRBR. After an initial design competition between the PRISM (GE) and SAFR (Rockwell) reactor concepts, with both designs submitting Preliminary Safety Evaluation

Reports (PSER) to the NRC in 1986, the GE-led PRISM reactor became the focus of the IFR program in 1988. After becoming the focus of the IFR, PRISM plant design was renamed the Advanced Liquid Metal Reactor (ALMR), while the core maintained the PRISM designation (6). After the ALMR program ended, GE changed the plant design name back to PRISM. When GE decided to uprate the thermal power level to 1000MWth (circa 1999), they renamed the plant design S-PRISM. After stopping work on S-PRISM in 2003, in 2005 GE resumed work but changed the name of the plant back to PRISM (7).

Many individual SFR designs were considered as reference designs for detailed analysis. The primary SFR designs examined were Argonne's 1000MW$_{th}$ Advanced Burner Reactor (ABR-1000), GE's Super Power Reactor Inherently Safe Module (S-PRISM), the Japan Atomic Energy Agency's (JAEA) Sodium-cooled Fast Reactor (JSFR), and the Russian BN1800. Table 1 summarizes key parameters of the different designs. Of the full scale power reactors, the S-PRISM reactor is unique due to its emphasis on modularity. The S-PRISM chose a relatively small power/modular design to reduce the construction time. By building reactors in two-unit power blocks, the cost of the plant can be distributed over a longer period of time while some revenue from the plant can be generated before the entire power block is built (5) (2).

The JSFR is much larger than the S-PRISM reactor and uses its loop design to emphasize passive cooling of the high power core. All of the JSFR's decay heat removal systems are approximately 38 meters above the core to ensure natural circulation and the pressure drop across the core was kept to 0.2MPa (3). The JSFR also has many designs depending on desired fuel type, fuel inventory, and desired outlet temperature. Unfortunately, the lack of a PRA or detailed design data on the JSFR limited the transient analysis in this thesis to pool type reactors, such as the ABR-1000 and S-PRISM.

Table 1- Current Sodium Reactor Parameters (2) (8) (9) (10)

Parameter	*ABR-1000*	*S-PRISM*	*JSFR*	*BN1800*
Power Level	1000MWt/ 95MWe	1000MWt/ 380MWe	3570MWth/ 1500MWe	4000MWth/ 1800MWe
Inlet/Outlet Temp	355C/510°C	371°C/510°C	395°C/550°C	410°C/575°C
Fuel	U-TRU-ZR	Metal or Oxide	Oxide or Metal	Nitride
Cladding	HT-9	HT9M	ODS	N/A
Pool/Loop	Loop	Pool	Loop	Pool

A reference design was established based on a small, pool-type design with metallic fuel, a reinforced concrete containment, and seismic isolation (horizontal accelerations). This design is similar to the ANL ABR-1000 design (8) (11). Key to the evaluation of Licensing Basis Events (LBEs) in NUREG-1860, a.k.a. the Technology Neutral Framework (TNF), is a level 3 Probabilistic Risk Assessment (PRA), but PRAs for commercial power reactors were only available for PRISM (Level 3) and ALMR (Level 1).[1] The ALMR PRA is an evolution of the PRISM PRA, both describing medium sized pool type reactors with Reactor Vessel Auxiliary Cooling System (RVACS) as the primary decay heat removal system. In order to evaluate design alternatives, a computational model of the reactor was required. This model needed detailed design information (e.g., core inlet flow distributions, orificing schemes, reactivity coefficients, etc.) which is not available in the open literature for the PRISM or ALMR designs. As a result, a generic pool type SFR was modeled in RELAP5-3D and SAS4a but with the general features of the ANL 1000MW$_{th}$ Advanced Burner Reactor, ABR-1000. This design has a PWR-type containment, both Direct Reactor Auxiliary Cooling (DRAC) and Primary Reactor Auxiliary Cooling (PRAC) emergency decay heat removal system, does not incorporate the Gas Expansion Modules (GEMS) system, and does not include other advanced Self Actuated Shutdown Systems (SASS). Insights were obtained from the

---

[1] A level 1 PRA stops at core damage. A level 3 PRA extends to offsite consequences.

PRAs but without greater design detail it was not possible to assign specific frequency estimates to specific accident scenarios for the reference design. The ability of a design variation to satisfy the TNF criteria was evaluated in a semi-quantitative manner.

I.2 Historical SFR Licensing

The current US SFR licensing knowledge has come about from the Clinch River Breeder Reactor (CRBR) and the Advanced Liquid Metal Reactor (ALMR) program interactions with the NRC. In the 1970s and early 1980s, the Department of Energy attempted to license CRBR but Congress cut funding before a construction permit was issued by the NRC. While core disruptive accidents (CDAs) were not considered as part of the design basis for CRBR, accidents which could lead to CDAs, including unprotected accidents and large break loss of coolant accidents, took a large amount of regulatory attention which prolonged the licensing process. No construction permit was issued for CRBR, but the CRBR licensing process did result in a NRC Safety Evaluation Report in 1983, NUREG-0968. (Ivans, 2006) In order to avoid CRBR's experience with CDAs, the ALMR design incorporated more passive safety measures into the PRISM core design. Under the ALMR program, the DOE submitted a Preliminary Safety Information Document (PSID) to the NRC in 1986 and the NRC in turn issued a Preliminary Safety Evaluation Report (PSER) in 1994. While the incorporation of passive safety features succeeded in reducing some of the regulatory concern with CDAs, to satisfy defense-in-depth the NRC still forced changes to the ALMR including the addition of an ultimate shutdown system and containment dome (6).

The NRC staff used a risk-informed approach for accident selection for the ALMR. They divided accident sequences into four Event Categories (EC I through EC IV) based on the initiating frequency of each sequence. Each EC's requirements were then generally related to requirements assigned to LWR accident classifications. For example, sequences in EC I had initiating frequencies greater than 10^{-2}/yr and their requirements corresponded to Anticipated Operational Occurrences in LWRs. Accidents categorized in EC II have initiating frequencies ranging from 10^{-2}/yr to 10^{-4}/yr and defined the design basis accidents for the reactor. These accidents were analyzed with conservative assumptions, (e.g., all parameters at their 2-sigma values) and any components used in the analysis were held to safety grade standards. The primary performance requirement for EC II accidents was to avoid any core damage, typically by setting conservative limits for failure metrics (e.g., cladding damage fractions must remain less than 0.2, coolant temperatures must remain below their boiling point). Accidents in EC III extended over the next two orders of magnitude, 10^{-4}/yr to 10^{-6}/yr, and constituted the Beyond Design Basis Accidents. Core damage was allowed for EC III sequences but radioactive materials had to be contained in the primary system. EC IV sequences constituted all accidents having a frequency of less than 10^{-6}/yr and had no direct parallel with LWR accident groupings, but were used to define containment requirements. For example, an Energetic Core Disruptive Accident induced a break in the reactor vessel head was used to determine the ALMR, and later S-PRISM, containment pressure requirements. (8) (6)

While the NRC attempted to align accidents with their ECs using initiating frequencies, there was also a deterministic classification scheme that occasionally conflicted with the frequency classification. For example, unprotected accidents, or accidents where the Reactor Protection System (RPS) fails, were classified as EC III, because the deterministic definition for EC III is the failure of two major safety systems (8). This classification was in conflict with the frequency definition for EC III, between 10^{-4}/yr to 10^{-6}/yr, because the RPS has a point estimate unreliability of 10^{-7}/demand. Major safety systems should have an unreliability of less than 10^{-2}/yr, theoretically pushing all unprotected accidents into EC IV. These discrepancies were not resolved before funding was cut to the ALMR program in 1994. (6)

I.3 Metal and Oxide Fuel Overview

Most current reactor designs have core layouts for both metal and oxide fuels. Metal fuels have higher thermal conductivity and allow for higher heavy metal loading than oxide fuels. Unfortunately, metallic fuels also have relatively low melting point and uranium, plutonium, and rare earth fission products from metallic fuel form an eutectic with the iron in the stainless steel cladding leading to cladding thinning, which limits cladding temperatures to lower values than oxide fuels. Limited operational experience exists for metallic fuels when compared to oxide fuel. Thus most reactor designs have an oxide core option until metallic fuels are fully qualified for power generation (8).

For the purpose of this thesis, two generic pool type sodium reactors, one using metal fuel and one using oxide fuel, were modeled in RELAP5-3D in order to determine the comparative transient response of reactors with these two fuels to various licensing basis events. In order to compare the probabilities of failure between these fuels, important transient characteristics, such as the reactivity coefficients, were treated as random variables which determine the success or failure of the survival of the transient. In this context, success is defined as the simulation maintains cladding integrity and avoids sodium boiling.

I.4 Thermodynamic Efficiency Overview

Increasing plant thermal efficiency is the most effective way to reduce the per megawatt cost of the SFR. Every component of the busbar cost of a nuclear reactor (capital, fuel, and operation and maintenance) is inversely proportional to the plant thermal efficiency. Eq. I.1, from the Gas Fast Reactor (GFR) report (12), approximates the busbar electricity costs of generic nuclear plant as:

$$e_{capital} = \frac{\phi I}{8766 Q \eta L}, e_{Fuel} = \frac{100F}{24B\eta L}, e_{O\&M} = \frac{100\theta}{8766 Q \eta L} \qquad \text{I.1}$$

where ϕ is the fixed charge rate in %/yr, I is the capital cost in \$, η is the cycle efficiency in percent, L is the average capacity factor, Q is the plant power rating in kWth, B is the burnup in MWD/kgHM, and F is the lifetime levelized fuel cost in \$/kg. From the relations above, Eq. I.2 can be derived, which shows that:

$$\frac{\delta e_{capital}}{e_{capital}} = \frac{-\delta\eta}{\eta}, \frac{\delta e_{fuel}}{e_{fuel}} = \frac{-\delta\eta}{\eta}, \frac{\delta e_{O\&M}}{e_{O\&M}} = \frac{-\delta\eta}{\eta} \qquad \text{I.2}$$

Assuming a starting efficiency of 40%, which is typical for SFRs, a 1% efficiency increase will result in a fractional efficiency increase of 2.5% (0.01/0.4). Capital, fuel, and O&M costs all decrease proportionally with efficiency increases as can be seen in Eq. 2, resulting in a busbar decrease of 2.5%. No other factor in Eq. I.1 affects all of the components of busbar cost in this manner.

I.5 Fuel/Clad Eutectic Overview

Many U.S. SFR designs utilize binary or ternary metallic fuel with stainless steel cladding (13). At high temperatures, iron from the cladding will diffuse into the fuel, and uranium, plutonium and rare earth fission products from the fuel will diffuse into the cladding to form a low melting point fuel/cladding eutectic. The erosion of the cladding due to this eutectic formation may accelerate creep rupture, thus allowing the radioactive fission products to escape into the sodium coolant. Accurate modeling of this phenomenon may be important to making the SFR more economically competitive, but currently the eutectic formation rate is predicted using only the temperature of the fuel/cladding interface. This thesis improves the modeling accuracy of eutectic formation through the application of a multivariable linear regression with model uncertainty distributions.

I.6 Structure of the Thesis

This thesis is primarily designed to support the Case Studies of the final NERI report, specifically Sections V.2 and V.3. Chapter II of this thesis overviews the methodologies employed in support of the:

- Metal and oxide fuel comparison in Chapter III (Section V.2 in the NERI report),
    - Transient response characteristics of TRansUranic (TRU)-bearing metal and oxide driver fuels in beyond-design-basis scenarios
    - Liquidus steady state limit for U-19Pu-10Zr
- Thermodynamic efficiency evaluations in Chapter IV (Section V.3 in the NERI report),
    - Elevating core outlet temperatures,
    - Removing the intermediate loop,
    - Changing to a compact heat exchanger design,

  - Changing from a Rankine cycle to a Supercritical-CO_2 power conversion cycle.

- Rate of fuel/cladding eutectic formation modeling in Chapter V (no corresponding Section in the NERI report).
  - Consolidation of fuel/cladding eutectic experiments,
  - Improving model accuracy using multivariable regression,
  - Quantitatively evaluating the residual uncertainty in both existing and new predictive relationships.

In the methodology section, the titles of the subsections which describe methodologies used in the creation of the final NERI report will have the corresponding report section number in the section title. Thus II.1 Evaluating Design Alternatives (NERI Report Sections V.2, V.3) indicates that section II.1 was used in the analysis of case studies V.2 and V.3 of the NERI report.

II METHODOLOGY

The following section describes the methodologies used to create probabilistic models and risk-inform design alternatives for the sodium fast reactors. These methods include:

1. Evaluating Design Alternatives – A process evaluating of the acceptability of design alternatives, including how the Technology Neutral Framework can be utilized to determine safety criteria,
2. Semi-Statistical Method for Determining Steady State Peak Cladding Temperature – A process for incorporating overlapping deterministic with statistical hot channel factors in order to set an upper bound on the likely peak or mid-wall cladding temperature.
3. RELAP5 SFR Model Overview – The primary system of the medium sized (1000MWth) pool type SFR RELAP5-3D model used in transient analysis is briefly overviewed, with a more complete description of the model found in Appendix B,
4. Uncertainty Propagation via RELAP – The code package BEAGLE, which produces, runs and post-processes a predetermined number of stochastic RELAP simulations,
5. Evaluating Failure Probabilities with Non-Integer Evidence – A method for evaluating the 95th percentile of importance sampled simulations such as those produce by BEAGLE,
6. Multivariable Linear Regression – A technique use to improve the modeling accuracy of the predicate relationship multiple dependant variables,
7. Model Uncertainty – A technique in which verification data is used to create a probabilistic distribution around a model output through the code MUTT.

II.1 Evaluating Design Alternatives (NERI Report Sections V.2, V.3)

In order to determine the optimal design alternatives, a consistent approach was needed to screen and compare potential design options. First, a method for using the Technology Neutral Framework to screen the safety acceptability of a design will be discussed. Next, the Elliot decision diagram will be discussed, which screens each design alternative for required safety and proliferation resistance standards before ranking them based on their economic merit.

II.1.A Technology Neutral Framework

The TNF is a theoretical regulatory structure drafted by the Nuclear Regulatory Commission's Office of Research (1). It is designed to provide more flexibility in the licensing process since current regulations focus almost exclusively on Light Water Reactor designs. By moving the licensing process into frequency-consequence space, regulations can be formed around limiting the public's risk to radiation exposure, as opposed to prescriptive regulations on one type of reactor's parameters. One of the TNF's unique features is that sequences with either a release frequencies less than a mean threshold frequency of 10^{-8}/yr, or a 95th percentile below less than 10^{-7}/yr, can be screened from the design basis.

The TNF functions by grouping accidents of similar phenomenology together. Within each group, the 95th percentile of the highest frequency of radiological release is combined with the 95th percentile of the highest dose to form the Licensing Basis Event (LBE). This LBE is then plotted on the Frequency-Consequence Curve (FCC), as illustrated in Figure 1. If the LBE falls within the acceptable region, the group response to the sequence is considered acceptable. Figure 2 shows the justifications for the dose limit on the FCC given in NUREG-1860.

During the analysis of LBEs, any system or component that is credited in the analysis is considered a safety grade component. Since most systems on the power conversion side of the plant are not safety grade, they are considered failed once the LBE is initiated, thus turning all LBEs into loss of heat sink accidents. Two internal LBEs are considered in this thesis: Transient OverPower (TOP) and Loss Of Flow (LOF).

External LBEs, such as earthquakes, are not considered here but may prove to be the most limiting constraint in the TNF. Very little evidence exists for earthquakes with a return period of 10^{-5}/yr-10^{-7}/yr causing large uncertainties in the predicted magnitudes. It is conceivable that designing any structure to handle the 95th percentile earthquake in this frequency range would be cost prohibitive (14).

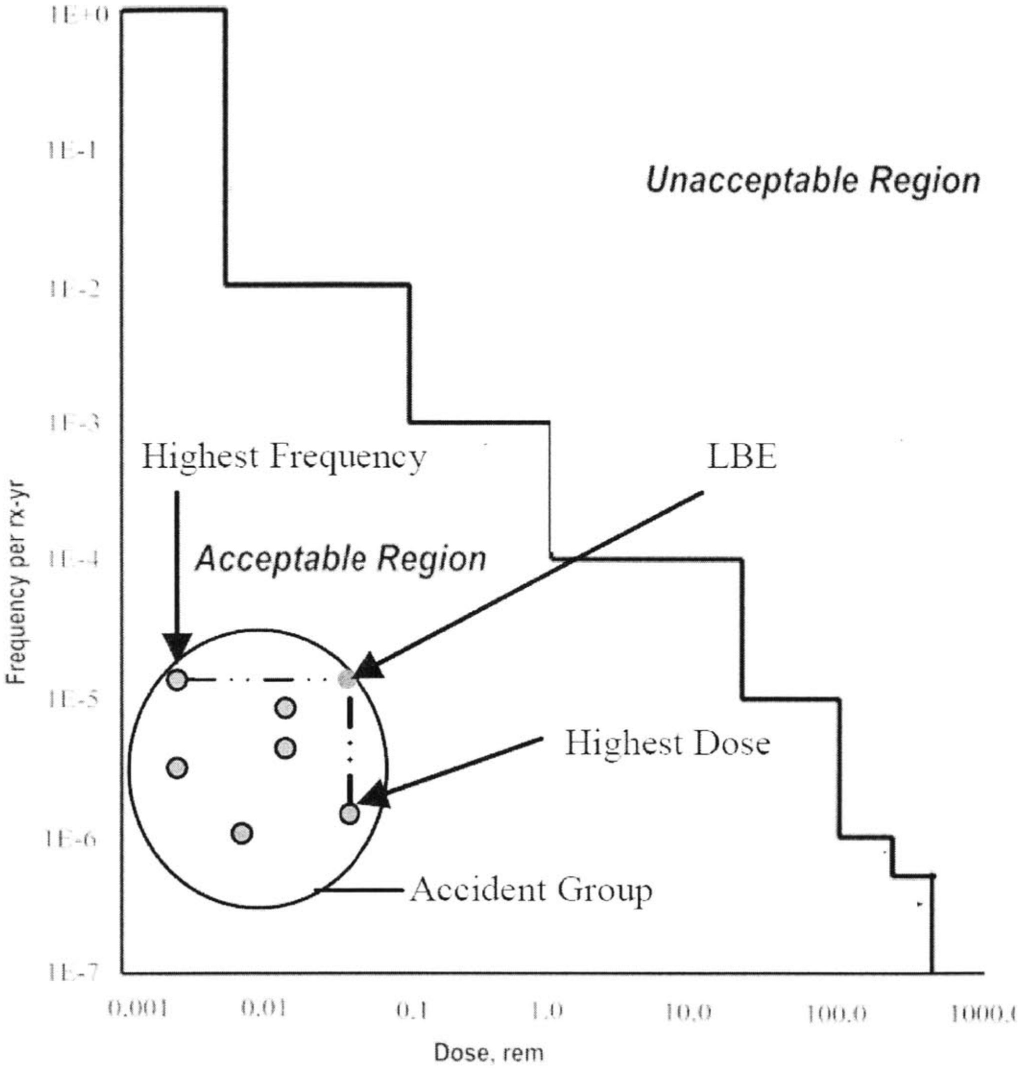

Figure 1 - Frequency-Consequence Curve (1).

Finally, it should be noted that while the TNF incorporates many risk-based concepts, pillars of traditional regulatory structure, such as defense in depth, are still required. For example, while a reactor design may not require containment under the FCC, some form of containment is still required to satisfy defense in depth, although it may not need to be as large or robust as LWR containments.

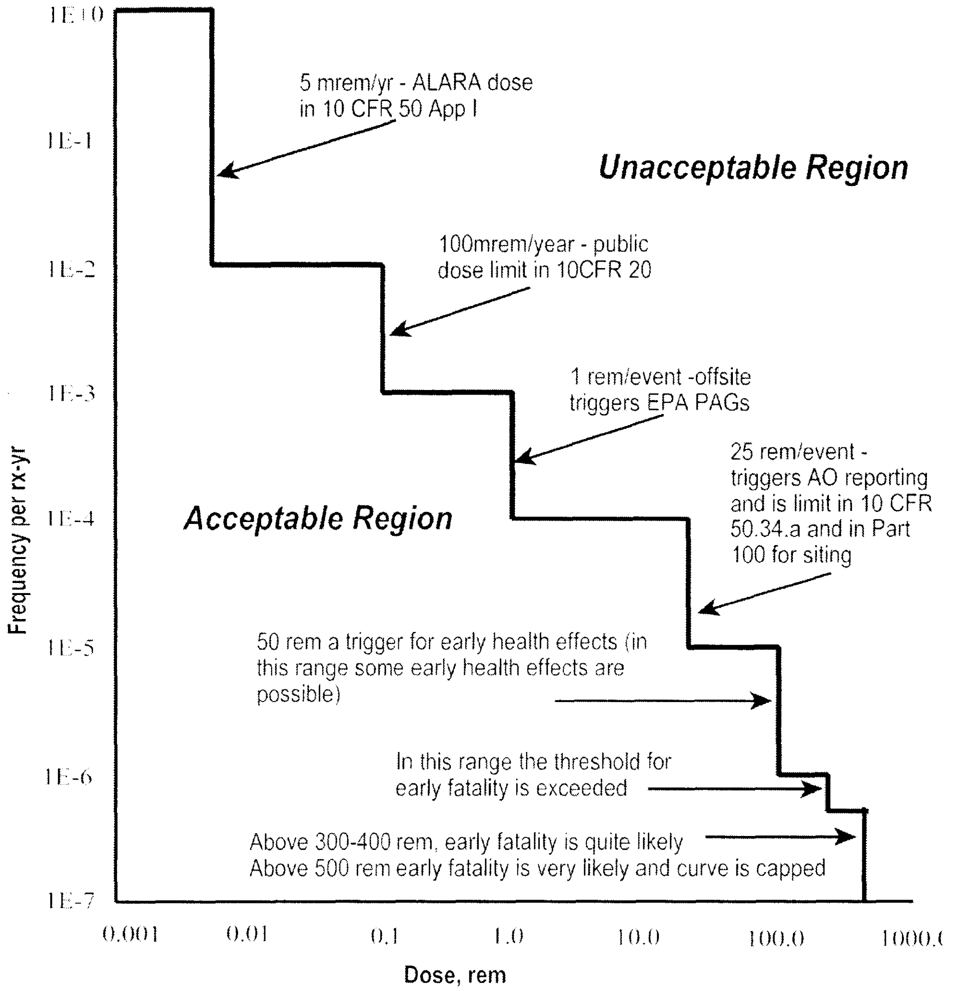

Figure 2– Frequency-Consequence Curve with Dose Justifications (1)

II.1.B Elliot Design Alternative Evaluation Decision Process

In order to ensure that any design modifications, such as increasing the core outlet temperature, satisfy non-proliferation and safety goals, it is proposed that all design modifications go through the decision process shown on the map in Figure 3. First, the original design must pass through the decision map to ensure that all licensing basis events meet the TNF safety requirements, and that the design meets the proliferation resistance goals. If the original design fails either of these checks, then alternatives must be examined which will allow the design to satisfy the screening boxes in Figure 3. Once the base design satisfies these criteria, then the design alternatives can be evaluated to reduce the cost of the reactor. Currently, several cost saving design alternatives are being studied, including:

- Metal or Oxide driver fuel,
- Increasing the core outlet temperature,
- Moving to a S-CO2 power conversion cycle,
- Removing the Intermediate-Loop,
- Reducing containment requirements.

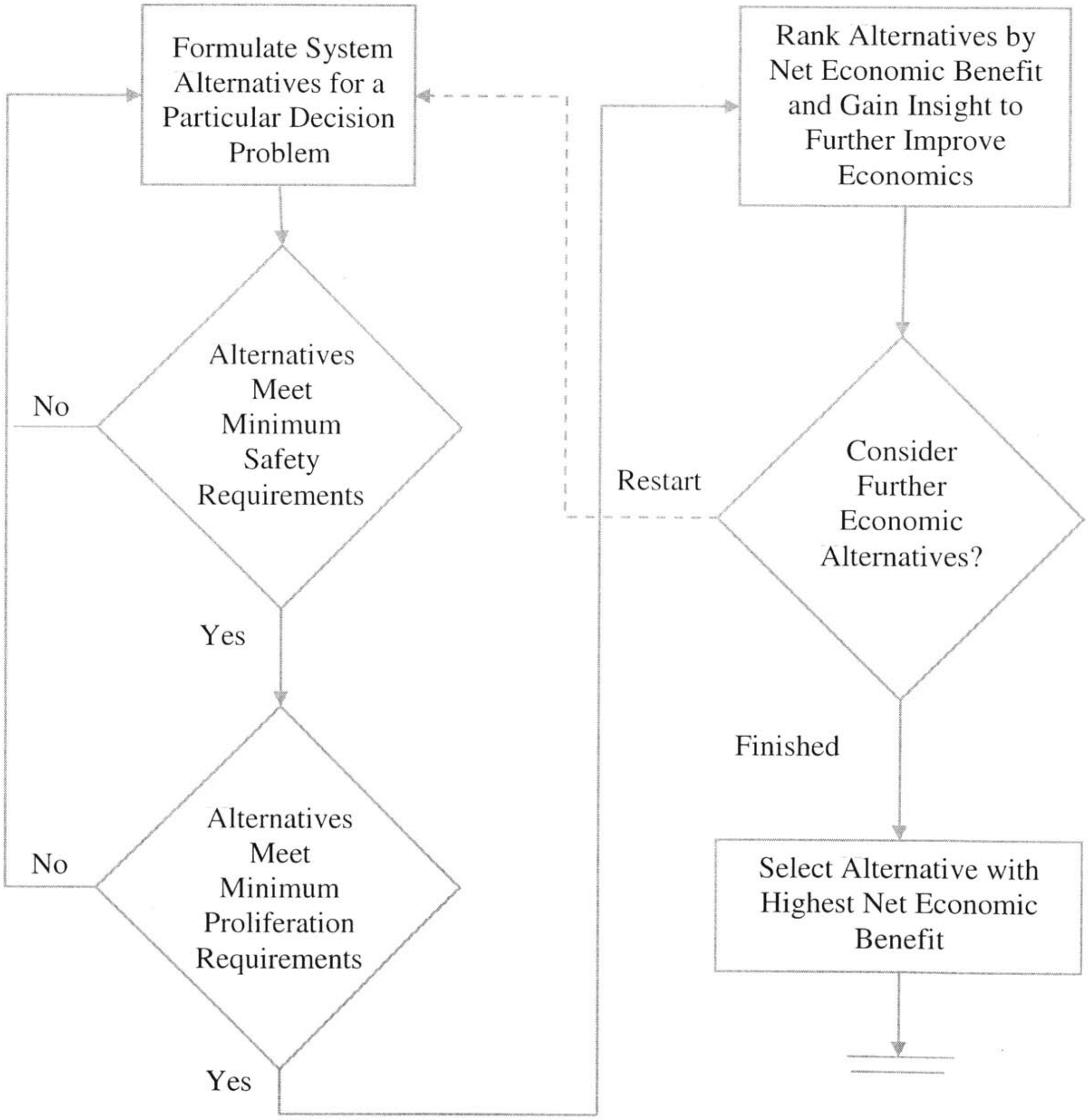

Figure 3– Elliot Design Alternative Decision Process

In order to satisfy the FCC, both the 95th percentile of the frequency and magnitude of radioactive material release are required. Calculation of radioactivity release can be difficult, but for low probability accidents where the frequency of core damage is below the FCC frequency threshold there is no release limit. Radiation releases corresponding to levels which would fall within the unacceptable region, (e.g., releases exceeding approximately 100 rem) at low probabilities typically would only arise after severe core damage. Thus, if the core damage frequency can be established to be below the threshold frequency, the system response is considered acceptable without dose calculations. If this requirement is too stringent or would cause the designer to add systems, thus increasing costs, then dose estimates will be required for the associated end states of those sequences. The optimal configuration of design parameters can be selected through the following procedure:

1. Determine the 95th percentile of the frequency of radiation release for the most limiting LBE.
2. Adjust the core outlet temperature and add or remove redundant safety features until the radiation release frequency and magnitude is within the acceptable region of the FCC.
3. Check to ensure that the changes to the reactor configuration did not inadvertently place LBEs, which originally had lower failure probabilities, above the FCC curve. If so, repeat Part 2 with the new limiting accident group.

II.2 Semi-Statistical Method for Determining Steady State Peak Cladding Temperature (V.2, V.3)

As the first barrier to radioactive material release, fuel cladding must be operated at temperatures which will allow for highly reliable performance, especially against creep and eutectic deformations. Due to approximations used in analysis or natural fluctuations in the state of the reactor, the cladding temperature calculated through a best estimate analysis is not conservative. Thus, operation of the cladding at the recommended temperature limit without incorporating safety factors may lead to unreliable cladding performance (15) (16). Figure 4 shows the semi-statistical hot channel factor method which will be used to calculate steady state peak cladding temperature in this thesis.

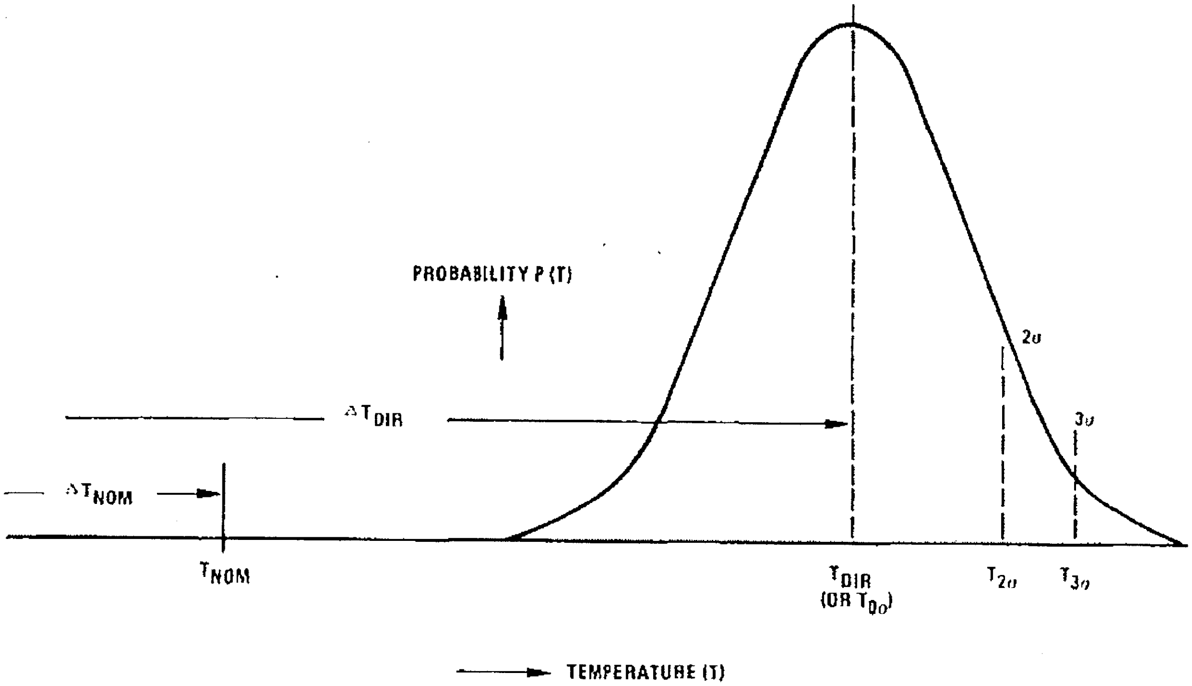

Figure 4 – Graphical Representation of the Semi-Statistical Hot Channel Factor Methodology (16)

Table 2 and Table 3 show the direct and statistical uncertainties that will determine the cladding temperature for a given outlet temperature. These uncertainties are the same for metal and oxide fuel, with the exception that metal fuel does not have pellet-clad eccentricity after 1 to 2 atom % burnup due to gap closure as a result of fuel swelling (Vilim, 1985). The direct uncertainties are applied to the nominal temperature rise in the j^{th} component in the hot channel, where j represents either the coolant, film, or clad, by multiplying the hot channel factor from the i^{th} source, $f_{i,j}$, to the temperature rise in the j^{th} component, as in Eq.II.1.

$$\Delta T_{dir}{}^{j} = \Delta T_{nom}{}^{j} \prod_{i=1}^{k} f_{i,j} \qquad \text{II.1}$$

Table 2 – Metal and Oxide Fuel Direct Uncertainties ($f_{i,j}$) for a 1000MW$_{th}$ Liquid Metal Reactor Core (15).

Source of Uncertainty	Coolant Temperature Rise	Film Temperature Rise	Clad MW Temperature Rise
Measurement	1	1	1
Reactor physics models	1.06	1.06	1.06
Control rod banking	1.02	1.02	1.02
Interassembly flow distribution	1.02	-	-
Intraassembly flow distribution	1.03	1.006	-
Pellet cladding eccentricity	-	1.14	1.14
Cladding circumferential temperatures distribution	-	1.8	0.8
Cladding conductivity and thickness	-	-	1.05
Total	**1.14**	**2.23**	**1.04**

Table 3– Metal and Oxide Fuel Statistical Uncertainties ($f_{i,j}{}^{3\sigma}$) for a 1000MW$_{th}$ Liquid Metal Reactor Core (15).

Source of Uncertainty	Coolant Temperature Rise	Film Temperature Rise	Clad MW Temperature Rise
Fissile fuel distribution	1.052	1.052	1.052
Nuclear data	1.02	1.02	1.02
Balance of plant	1.14	-	-
Loop temperature imbalance	1	-	-
Interassembly flow distribution	1.05	-	-
Intraassembly flow distribution	1.058	1.005	-
Subchannel flow area	1.01	-	-
Wire wrap orientation	1	-	-
Coolant properties	1.013	-	-
Film heat transfer coefficient	-	1.12	-
Pellet cladding eccentricity	-	1.174	1.174

Statistical uncertainties are treated differently than direct uncertainties. The temperature rise due to statistical uncertainty is calculated for each component of the hot channel, with direct uncertainties included, and each horizontal row is added until reaching the component of interest, in this case to the cladding mid-wall (MW in Table 2 and Table 3). The mid-wall temperature controls thermal creep in the cladding and thus is of interest in this analysis. Because the cladding temperature is the limiting parameter governing core outlet temperature for oxide and metal fuel within the core, all components up to the cladding mid-wall, spanning the coolant, film and cladding temperature rises for a given source of uncertainty, are added horizontally. This horizontal addition ensures that a random fluctuation in the expected fissile fuel distribution, for example, will lead to a corresponding fluctuation in the coolant, film, and cladding. If these values were added in a root-mean-square manner, then a fluctuation in a given value will affect each component differently, which is not a physical result. Next, the horizontal sum for each source of uncertainty is added in a root-mean-square manner to calculate the overall statistical uncertainty. This method is shown by Eq.II.2 and Eq.II.3 (16). It should again be noted that the pellet cladding eccentricity was removed from the metallic hot channel factor because the metal fuel quickly expands until it touches the clad, removing this eccentricity that is found in a ceramic fuel design (15).

$$\Delta T_{3\sigma}{}^{i} = \sum_{j=1}^{3} \Delta T_{dir}{}^{j} f_{i,j}{}^{3\sigma} \qquad \text{II.2}$$

$$\Delta T_{3\sigma}{}^{Tot.\ Clad\ MW} = \sqrt{\sum_{i=1}^{k} (\Delta T_{3\sigma}{}^{i})^2} \qquad \text{II.3}$$

The statistical cladding temperature rise is then added to the direct cladding temperature to determine the total peak cladding temperature. Because the horizontal procedure only uses the temperature rise within components and not the temperature of the component, the inlet temperature can be moved independently of the modeled uncertainties to increase outlet temperature without changing the total hot channel factor. Eventually, pushing the operating temperature too hot will increase these uncertainties, but, due to limited information, this analysis assumes any changes in the hot channel factors are minimal at the core outlet temperatures of interest.

II.3 RELAP5 SFR Model Overview (V.2, V.3)

For transient analysis in this thesis, a RELAP5-3D (17) model is used to predict a typical SFR's behavior during postulated LBEs. A model metal fuel was developed as a subchannel analysis code by Matthew Memmott and was modified to predict SFR transient response based on a 0.7 Conversion Ratio 1000 MW_{th} metal fueled pool type reactor modeled after the ABR-1000 (18) (8). This model does not include any advanced safety features such as Gas Expansion Modules or Curie Point Latches and is designed to determine generic SFR responses to potential LBEs, up to sodium boiling. To ensure a conservative analysis, all reactor parameters, such as reactivity coefficients and plenum pressures, are modeled at their end of cycle conditions. One of the design alternatives analyzed was the adoption of oxide fuel instead of metal fuel, thus an oxide fuel RELAP model was required. For the oxide core, the metal fuel in the RELAP5-3D model was replaced by oxide fuel as defined by the oxide fuel ABR-1000 design (8). The only change made to the RELAP5-3D model outside the core when converting the metal fuel model to an oxide fuel model was that the pump coast-down halving time was increased from 4 seconds in the metal reactor to 20 seconds in the oxide reactor.

In order to analyze the effects of increasing the core outlet temperature on transient response, the base case RELAP5-3D results are calculated for an average core outlet temperature of 510°C. The core is assumed to have a radial core peaking factor of 1.22 for hot channel calculations. This core peaking factor equates to peak channel outlet temperatures of 530°C after appropriate core orificing schemes are implemented.

RELAP5-3D does not have an internal cladding failure model. In order to predict cladding deformation and failure due to a combination of thermal creep and fuel/cladding eutectic effects, a simplified 1-D cladding damage model was created. This model uses the cladding temperature profiles from RELAP5 with the empirical creep and eutectic equations from SAS4A's DEFORM5 module to predict the cladding damage fraction for each simulation (19). Simulations in which the cladding damage fractions are calculated to be above 1.0 are assumed to experience cladding failure. This failure module is run after the RELAP5 simulations are complete, and as a result, negative feedbacks such as in-pin fuel motion and fuel sweep-out after cladding failure are not included in this analysis. A detailed description of this failure model can be found in Appendix A.

RELAP5-3D has many limitations when compared to traditional sodium safety analysis codes such as SAS4A. In addition to the lack of a cladding deformation model, RELAP5-3D does not handle in-pin fuel motion or sodium boiling. The lack of in-pin fuel motion should tend to make the results more conservative, i.e. higher system temperatures, because movement of the fuel up the pin will add negative reactive to the core. For molten fuel, if the cladding ruptures the fuel will flow to the rupture point causing reactivity swings which are not accounted for in the current RELAP5-3D model. Conversely, the lack of sodium boiling will cause the RELAP5-3D results to be non-conservative because of the high sodium void worth in sodium reactors. Currently, the onset of sodium boiling is assumed to occur at the instant that the sodium temperature rises above the boiling point. While this initial approximation is conservative, future events become highly uncertain. The unaccounted positive reactivity from local sodium boiling may cause bulk boiling that is not predicted in the RELAP5-3D calculation.

Additionally, many of the passive safety features of a sodium core, including core radial expansion and control rod drive line expansion, are modeled as first order approximations as a function of the core outlet and control assembly outlet temperatures, respectively. The expansions of these components are more complicated and are dependent on the temperature at multiple points in the reactor.

It should be noted that due to these approximations, the RELAP5-3D ABR-1000 model experiences some discrepancy when compared with SAS4a results (19). One key discrepancy is that the ABR-1000 cold pool heats up much slower in SAS4a than in RELAP5-3D simulations. The most likely cause for this discrepancy is that the ABR1000 report does not provide the intermediate loop sodium inventory and thus an engineering judgment was made by the model's creator that satisfied his requirements. This inventory was assumed to be 533 MT, almost 2 times smaller than was modeled with SAS4a. This missing sodium reduces the thermal sink in the RELAP5-3D simulations, accelerating the heatup of the primary pool.

Figure 5 shows the primary system layout of the reference SFR RELAP5-3D design. A more detailed examination of the reactor design can be found in Appendix B.

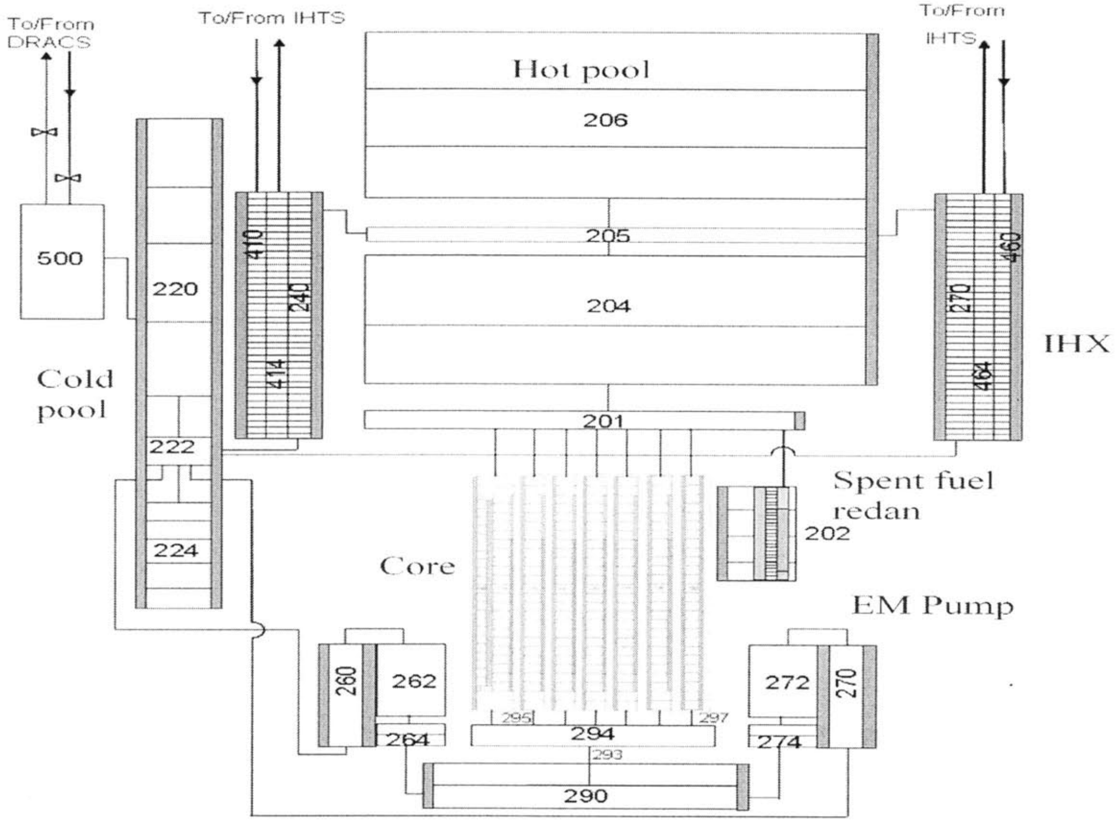

Figure 5- SFR RELAP5-3D Primary System Model (18)

The reactivity coefficients for the ABR-1000 model are taken from the End Of Life (EOL) TransUranic (TRU) metal and oxide core designs. These reactivity coefficients can be found in Table 4 (8). It should be noted that while the oxide core does have a slightly more negative Doppler coefficient, both TRU designs have the same sodium density coefficients, which is not typical for metal and oxide core designs (20) (3). Due to the harder neutron spectrum, most metallic cores have a more positive sodium density coefficient.

Table 4 – Reactivity Coefficients for Metal and Oxide Fuel ABR-1000 Designs

Reactivity Coefficient	Metal		Oxide	
	BOC	EOC	BOC	EOC
Sodium Density (¢/°C)	0.1	0.12	0.1	0.12
Doppler(¢/°C)	-0.1	-0.1	-0.12	-0.12
Axial Expansion(¢/°C)	-0.06	-0.06	-0.05	-0.05
Core Radial Expansion(¢/°C)	-0.38	-0.38	-0.31	-0.3
Control Rod Drive Line Expansion (¢/cm)	-49	-51	-26	-28

II.4 Uncertainty Propagation via RELAP (V.2, V.3)

In nuclear power, special attention is given to designing for low-probability high-consequence accidents which have the potential for large radioactivity release to the public. Thus, the nuclear industry has increased modeling complexity to analyze these accidents and improved their designs to increase system reliability through additional redundancy and incorporation of passive safety systems. Both of these trends make it difficult for a risk analyst to determine the failure probability: more complicated modeling takes longer to complete and higher system reliability means more Monte-Carlo simulations need to be conducted to approximate the failure probability (21).

Numerous approaches have been made to simplify these problems. Meta-models such as response surfaces and Gaussian-process programs are created to approximate the response of the complex systems without the drawback of long run times. Advanced numerical techniques such as Importance Sampling (IS) and Latin Hypercube Sampling (LHS) allow for low failure probabilities to be resolved with orders of magnitude fewer simulations than by traditional Monte Carlo Sampling (MCS). Each of these approaches has its drawbacks. Meta-model may not capture the finer points of the underlying codes or may be extremely mathematically complicated. Advanced sampling techniques, such a IS or LHS, have the potential for either increasing or decreasing the variance. Even with these drawbacks, both techniques are helping risk analyst better understand the reliability of the system.

Unfortunately for risk analysis, many regulators want not only the mean but the 95th percentile, or some other conservative estimate, of failure. For sequences where only a few predicted failures are expected after the simulations are conducted, this request leads to a few interesting questions such as:

- What assumed distribution should the data take?
- How does the data relate to the underlying system if an advanced sampling scheme is used?

Small pool type sodium reactors are designed to survive most unprotected transients without cladding rupture. To avoid running a prohibitive number of RELAP5 simulations, the sampling distributions should be biased in such a way as to force sampling of larger, and thus more limiting, reactivity coefficients while providing an unbiased estimate of the failure probabilities. By biasing the sampling procedure through importance sampling, each simulation is no longer assigned the same weight when calculating failure probabilities and small failure probabilities can be calculated with fewer simulations.

II.4.A Sampling Random Variables

Let us examine importance sampling by assuming that the conditional cumulative failure distribution, $F(t|\lambda)$, has a parameter uncertainty distribution $\pi(\lambda)$ about λ. Generically, the true value of λ is not known and thus is allowed to take a range of values defined by the probability distribution function $\pi(\lambda)d\lambda$ (e.g., normal, log-normal, uniform, etc.). The value of λ will determine when or if the simulation will result in cladding failure, represented by $F(t|\lambda)$. If the value of λ causes the simulation to result in cladding failure, $F(t|\lambda)$ will change from 0 to 1 at the failure time t=T. If the value of λ does not cause the simulation to result in failure, as defined by the analysist, $F(t|\lambda)$ will remain zero. Using these definitions, the time dependent failure probability is defined in Eq. II.4.

$$F(t) = \int F(t|\lambda)\, \pi(\lambda)\, d\lambda \qquad \text{II.4}$$

Using Monte Carlo simulation, this integral is approximated by a summation of evaluations of F(t| λ) for values of λ sampled from $\pi(\lambda)$. This technique is expressed mathematically in Eq. II.5 The difference between F(t| λ) and F(t) can be seen in Figure 6.

$$F(t) \cong \frac{1}{N}\sum_{i=1}^{N} F(t|\lambda_i) \tag{II.5}$$

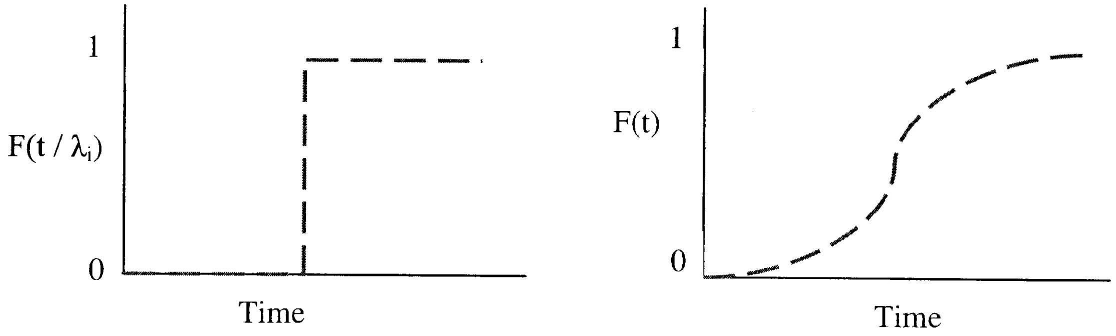

Figure 6 – Schematic Representation of F(t/ λ_i) and F(t).
F(t/ λ_i) is a binomial function which moves from 0 (success) to 1 (failure) at the time t when the cladding damage fraction (CDF) = 1.0. F(t) is the integral of F(t/ λ_i) where every set of λ_i yields a new failure time.

Unfortunately, if $F(t)$ is small then failures may only occur in the tail of $\pi(\lambda)$ which have a low probability of being sampled. Thus, for the desired values of λ to be significantly sampled, the sampling distribution is to be transformed into a more desirable distribution function, $I(\lambda)$. This function is known as the importance function. By multiplying Eq. II.4 by the unity function $\int \frac{I(\lambda)}{I(\lambda)} d\lambda$ and rearranging terms, Eq. II.6 is produced (22) (23).

$$F(t) = \int F(t|\lambda)\frac{\pi(\lambda)}{I(\lambda)} I(\lambda)\, d\lambda \tag{II.6}$$

Because $I(\lambda)$ is the desired sampling distribution for the Monte Carlo approximation of F(t), every draw of $I(\lambda)$ is weighted by the ratio of the original and the desired sampling distribution. This transformation is seen in Eq. II.7 and Eq. II.8.

$$w(\lambda) = \frac{\pi(\lambda)}{I(\lambda)} \qquad \text{II.7}$$

$$F(t) = \int F(t|\lambda)\, I(\lambda)\, w(\lambda)\, d\lambda \qquad \text{II.8}$$

Using Monte Carlo, this integral is approximated by a summation of evaluations of F(t| λ) for values of λ sampled from $I(\lambda)$ and weighted by $w(\lambda)$, which itself is a function of λ. This technique is expressed mathematically in Eq. II.9. Note that the weight of a given sample of λ is now a function of λ (Anderson, 1999).

$$F(t) \cong \frac{1}{\sum_{i=1}^{N} w(\lambda_i)} \sum_{i=1}^{N} w(\lambda_i)\, F(t|\lambda_i) \qquad \text{II.9}$$

Eq. II.4 can be re-written for a RELAP5-3D model by replacing the dominate variables in the RELAP5-3D model with probability distributions and adding a $\pi(.)d(.)$ to Eq. II.4 for every uncertain parameter. For an unprotected transient overpower, Eq. II.4 is then re-written as Eq. II.10,

$$\begin{aligned} F(t) = {} & \\ & \int_{\rho'}^{\rho''} \int_{-\infty}^{\infty} \int_{-\infty}^{\infty} \int_{-\infty}^{\infty} \int_{-\infty}^{\infty} \int_{-\infty}^{\infty} F(t|\{\rho, \alpha_{Dop}, \alpha_{Na}, \alpha_{CRDL}, \alpha_{CRE}, \alpha_{AE}\}) \\ & \quad \pi(\alpha_{Dop}) d\alpha_{Dop} \pi(\alpha_{Na})\, d\alpha_{Na}\, \pi(\alpha_{CRDL}) d\alpha_{CRDL} \\ & \quad \pi(\alpha_{CRE}) d\alpha_{CRL}\, \pi(\alpha_{AE}) d\alpha_{AE}\, \pi(\rho) d\rho \end{aligned} \qquad \text{II.10}$$

where the amount of reactivity inserted is ρ, $\pi(\rho)d\rho$ is a linear distribution between ρ' and ρ'', and $\pi(\alpha_i)d\alpha_i$ is a normal distribution for given distributed reactivity coefficients; the same weighting scheme is used to bias sampling for all variables. If this were a loss of flow event, the uncertain variable ρ will be replaced by the pump dependent flow halving time τ. Both transient types will be discussed in more detail in Section III.3.A.

The limitation of importance sampling is that the optimal sampling scheme cannot be known a priori, but as larger values for all distributed values will lead to shorter failure times the following sampling scheme is selected:

- 50% of the draws are selected between the 95th and 100th percentile of the distribution
- 45% of the draws are selected between the 50th and 95th percentiles of the distribution
- 5% of the draws are selected between the 0th and 50th percentiles of the distribution

The importance functions used for linear and normal distributions using the sampling scheme above can be found in Eq. II.11 and Eq.II.12 respectively and graphed in Figure 7.

$$I(\rho) = \left\{ \begin{array}{l} \frac{1}{(\rho'' - \rho')}\frac{0.2}{0.5}, \\ \quad \rho' < \rho < \rho' + (\rho'' - \rho') * .5 \\ \\ \frac{1}{(\rho'' - \rho')}\frac{0.3}{0.45}, \\ \rho' + (\rho'' - \rho') * .5 < \rho < \rho' + (\rho'' - \rho') * .95 \\ \\ \frac{1}{(\rho'' - \rho')}\frac{0.5}{0.05}, \\ \quad \rho' + (\rho'' - \rho') * .95 < \rho < \rho'' \end{array} \right\} \qquad \text{II.11}$$

$$I(\alpha) = \left\{ \begin{array}{ll} N(\mu,\sigma)\frac{0.2}{0.5}, & -\infty < \frac{\alpha - \mu}{\sigma} < 0 \\ N(\mu,\sigma)\frac{0.3}{0.45}, & 0 < \frac{\alpha - \mu}{\sigma} < 1.65 \\ N(\mu,\sigma)\frac{0.5}{0.05}, & 1.65 < \frac{\alpha - \mu}{\sigma} < \infty \end{array} \right\} \qquad \text{II.12}$$

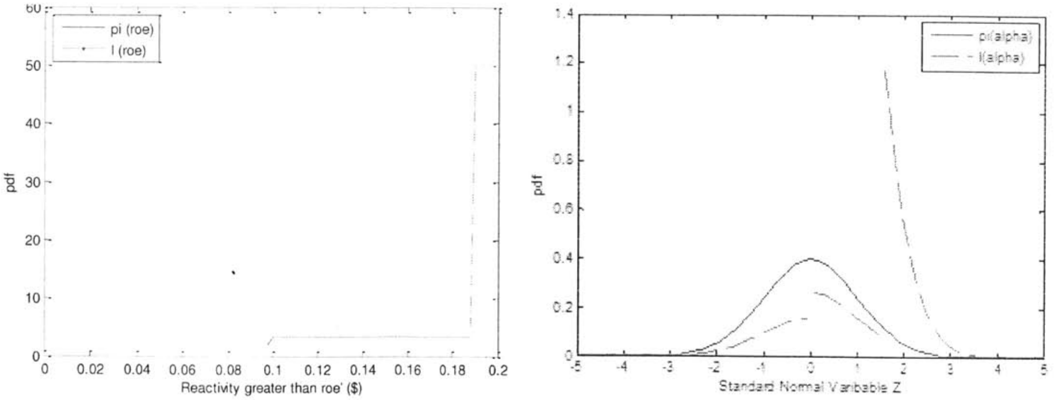

Figure 7– Comparing $\pi(\rho)$ to $I(\rho)$ *and* $\pi(\alpha)$ to $I(\alpha)$

Thus the weighting functions $w(\rho)$ and $w(\alpha)$ can be calculated as in Eq. II.13 and Eq.II.14:

$$w(\rho) = \frac{\pi(\rho)}{I(\rho)}$$

$$= \left\{ \begin{array}{c} \dfrac{\dfrac{1}{(\rho'' - \rho')}}{\dfrac{1}{(\rho'' - \rho')}\dfrac{0.2}{0.5}} = 2.5, \\ \rho' < \rho < \rho' + (\rho'' - \rho') * .5 \\ \\ \dfrac{\dfrac{1}{(\rho'' - \rho')}}{\dfrac{1}{(\rho'' - \rho')}\dfrac{0.3}{0.45}} = 1.5, \\ \rho' + (\rho'' - \rho') * .5 < \rho < \rho' + (\rho'' - \rho') * .95 \\ \\ \dfrac{\dfrac{1}{(\rho'' - \rho')}}{\dfrac{1}{(\rho'' - \rho')}\dfrac{0.5}{0.05}} = 0.1, \\ \rho' + (\rho'' - \rho') * .95 < \rho < \rho'' \end{array} \right\} \qquad \text{II.13}$$

$$w(\alpha) = \frac{\pi(\alpha)}{I(\alpha)} = \left\{ \begin{array}{ll} \dfrac{N(\mu,\sigma)}{N(\mu,\sigma)\dfrac{0.2}{0.5}} = 2.5, & -\infty < \dfrac{\alpha - \mu}{\sigma} < 0 \\ \dfrac{N(\mu,\sigma)}{N(\mu,\sigma)\dfrac{0.3}{0.45}} = 1.5, & 0 < \dfrac{\alpha - \mu}{\sigma} < 1.65 \\ \dfrac{N(\mu,\sigma)}{N(\mu,\sigma)\dfrac{0.5}{0.05}} = 0.1, & 1.65 < \dfrac{\alpha - \mu}{\sigma} < \infty \end{array} \right\} \qquad \text{II.14}$$

It should be noted that by design $w(\rho)= w(\alpha)$ and are independent of ρ and α within the weight bins. By performing the transformation in Eq. II.6, Eq. II.10 can now be re-written as Eq. I.15.

$$F(t) = \qquad \text{II.15}$$

$$\begin{aligned}
&\int_{\rho'}^{\rho''}\int_{-\infty}^{\infty}\int_{-\infty}^{\infty}\int_{-\infty}^{\infty}\int_{-\infty}^{\infty}\int_{-\infty}^{\infty} F(t|\{\rho,\alpha_{Dop},\alpha_{Na},\alpha_{CRDL},\alpha_{CRE},\alpha_{AE}\})\\
&\big(I(\alpha_{Dop})I(\alpha_{Na}) * I(\alpha_{CRDL})I(\alpha_{CRE})\, I(\alpha_{AE})I(\rho)\big)\\
&\big(w(\alpha_{Dop})w(\alpha_{Na})\, w(\alpha_{CRDL})w(\alpha_{CRE})\, w(\alpha_{AE})w(\rho)\big)\\
&d\alpha_{Dop}\, d\alpha_{Na}\, d\alpha_{CRDL}\, d\alpha_{CRL}\, d\alpha_{AE}\, d\rho
\end{aligned}$$

Similar to Eq. II.6, this integral can be evaluated through a Monte Carlo process as in Eq. II.16, while Eq. II.17 calculates the variance (22) (23).

$$\begin{aligned}
&\overline{F(t)} \cong\\
&\frac{1}{\sum_{i=1}^{N} w_i(\alpha_{Dop})w_i(\alpha_{Na})\, w_i(\alpha_{CRDL})\, w_i(\alpha_{CRE})\, w_i(\alpha_{AE})w_i(\rho)}\\
&\Bigg[\sum_{i=1}^{N} w_i(\alpha_{Dop})w_i(\alpha_{Na})\, w_i(\alpha_{CRDL})\, w_i(\alpha_{CRE})\, w_i(\alpha_{AE})w_i(\rho)\\
&F\left(t\middle|\left\{\rho_i,\alpha_{Dop_i},\alpha_{Na_i},\alpha_{CRDL_i},\alpha_{CRE_i},\alpha_{AE_i}\right\}\right)\Bigg]
\end{aligned}\tag{II.16}$$

$$\begin{aligned}
&Var(F(t)) \cong\\
&\frac{1}{\sum_{i=1}^{N} w_i(\alpha_{Dop})w_i(\alpha_{Na})\, w_i(\alpha_{CRDL})\, w_i(\alpha_{CRE})\, w_i(\alpha_{AE})w_i(\rho)}\\
&\Bigg[\frac{1}{\sum_{i=1}^{N} w_i(\alpha_{Dop})w_i(\alpha_{Na})w_i(\alpha_{CRDL})w_i(\alpha_{CRE})\, w_i(\alpha_{AE})w_i(\rho)}\\
&\sum_{i=1}^{N}\left(w_i(\alpha_{Dop})w_i(\alpha_{Na})\, w_i(\alpha_{CRDL})\, w_i(\alpha_{CRE})\, w_i(\alpha_{AE})w_i(\rho)\right)^2\\
&F\left(t\middle|\left\{\rho_i,\alpha_{Dop_i},\alpha_{Na_i},\alpha_{CRDL_i},\alpha_{CRE_i},\alpha_{AE_i}\right\}\right)^2 - \overline{F(t)}^2\Bigg]
\end{aligned}\tag{II.17}$$

II.4.B Description of BEAGLE Hierarchy

The Bayesian Experimental Automated Graphical Labor-saving Estimate (BEAGLE) scripts were written to conduct and post-process Monte Carlo simulations via RELAP5-3D. BEAGLE has three main stages:

1. RELAP Input Generator – Writes a user defined number of RELAP inputs and defines basic parameters and distributions from which to sample. This stage also allows for the option to conduct biased importance sampling.
2. RELAP Automation – Automates the process of running every RELAP file generated by the input generator.
3. RELAP Output Extraction – Reads every RELAP output and transforms minor edit variables into MATLAB objects.
4. Cladding Failure Calculation – Calculates transient induced cladding damage fractions and computes the statistical weight of the simulation resulting in failed cladding.

BEAGLE is structured as a series of MATLAB scripts (24), RELAP executables, text files and batch files. This structure allows for great flexibility by the user, but results in complex process maps. The file extension of each script or document is given within the boxes of each process map and Table 5 indicates what type of script or document corresponds with a given extension.

Table 5 – BEAGLE File Extension Key

File Extension	Description
*.m	MATLAB script file: used for calculations and data extraction
*.mat	MATLAB data saved as an external files
*.i	RELAP input file
*.o	RELAP output file
*.r	RELAP restart file
*.bat	Windows script file: used to loop RELAP runs or index folder locations

(i) RELAP Input Generator

The structure of the Input Generator module is shown in Figure 8. This module has 3 MATLAB scripts which create a user defined number of input files distributed into a user defined number of folders. Multiple folders are utilized in order to run multiple RELAP5-3D simulations on a single computer. This is only recommend for multi-core processors, because running multiple RELAP5-3D simulations on a single processor will severely hinder runtime.

Importance.m is a MATLAB script which determines the weight function that is combined with the probability distributions for importance sampling. If importance sampling is not desired, the function in this script should be set to a constant value.

Reactivity Generator.m is the main input/output script for the input generator model. In this script, the user specifies the number of RELAP files per fold, the number of parallel RELAP runs desired, the uncertainty distributions for the random variables, the portion of the distributions desired (mean value, 2 sigma or randomly sampled), and output options such as printing summary plots and/or input files. A summary plot from Reactivity Generator for an Unprotected Transient OverPower (UTOP) can be seen in Figure 9. In this example, the magnitude of reactivity insertion originally uniformly distributed from $0.3 to $0.9 but the sampling distribution has been biased, as described in Section II.4.A. The remaining reactivity coefficients are normally distributed without biasing. All parameters, except the Doppler coefficient, are represented by histograms. The Doppler values are plotted because RELAP5-3D reads Doppler coefficients as a temperature-dependent tabular value, not a point estimate. Once complete, Reactivity Generator saves the importance sampling weights and the values of the sampled parameters in the file Par_sum.mat. This file will be used again in the cladding failure module.

The last script in the Input Generator module is Auto.m. This file contains the RELAP5-3D transient file formatted in MATLAB's fprintf statements. Random parameters are replaced with the variables sampled in Reactivity Generator.m. Auto.m is called multiple times until every input is written.

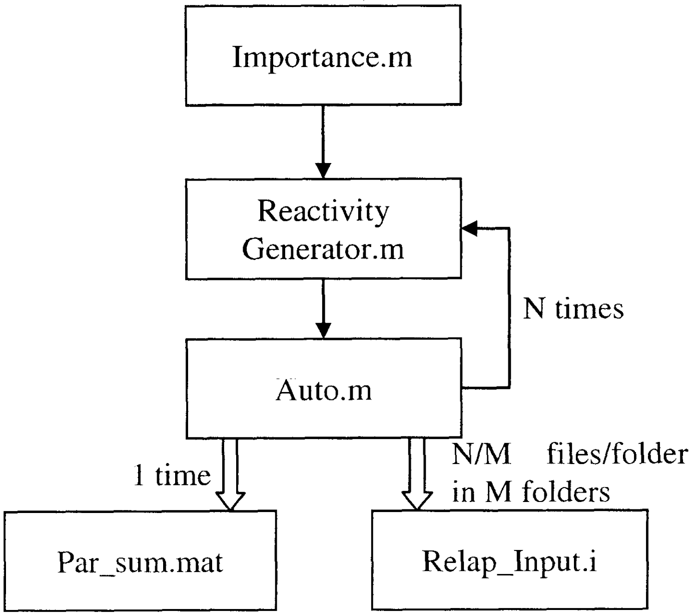

Figure 8 - RELAP Input Generator Module Flow Map

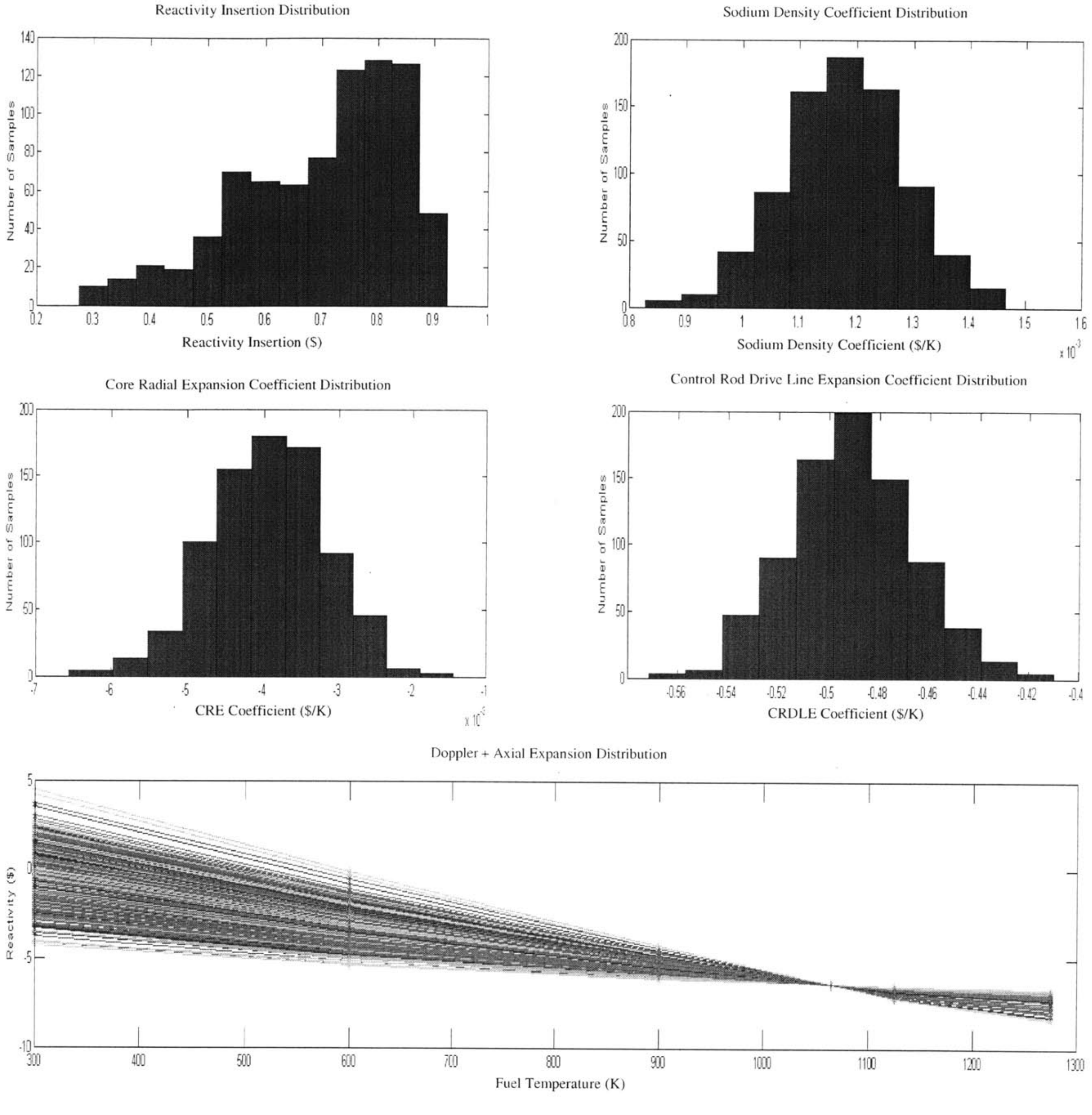

Figure 9 – 800 Random Samples for RELAP Simulations

(ii)RELAP Automation

The structure of the Automation module is shown in Figure 10. The RELAP automation module is comprised almost exclusively of *.bat files, which is windows intrinsic scripting language. All transient simulations should start from the same Steady_State.r file which provides the initial conditions for the transient, including temperature and fluid flow distributions throughout the core. The Multi_RELAP.bat script contains the location of the input folder, RELAP5-3D executable, and Steady_State.r file. Activating Multi_RELAP.bat will cause the script to run every input file in the designated folder in a serial fashion using the Run.bat file. The Run.bat is required because the *.bat scripting language does not allow for arrays. This module is the most time consuming portion of BEAGLE and running in multiple folders on multiple processors is highly recommended.

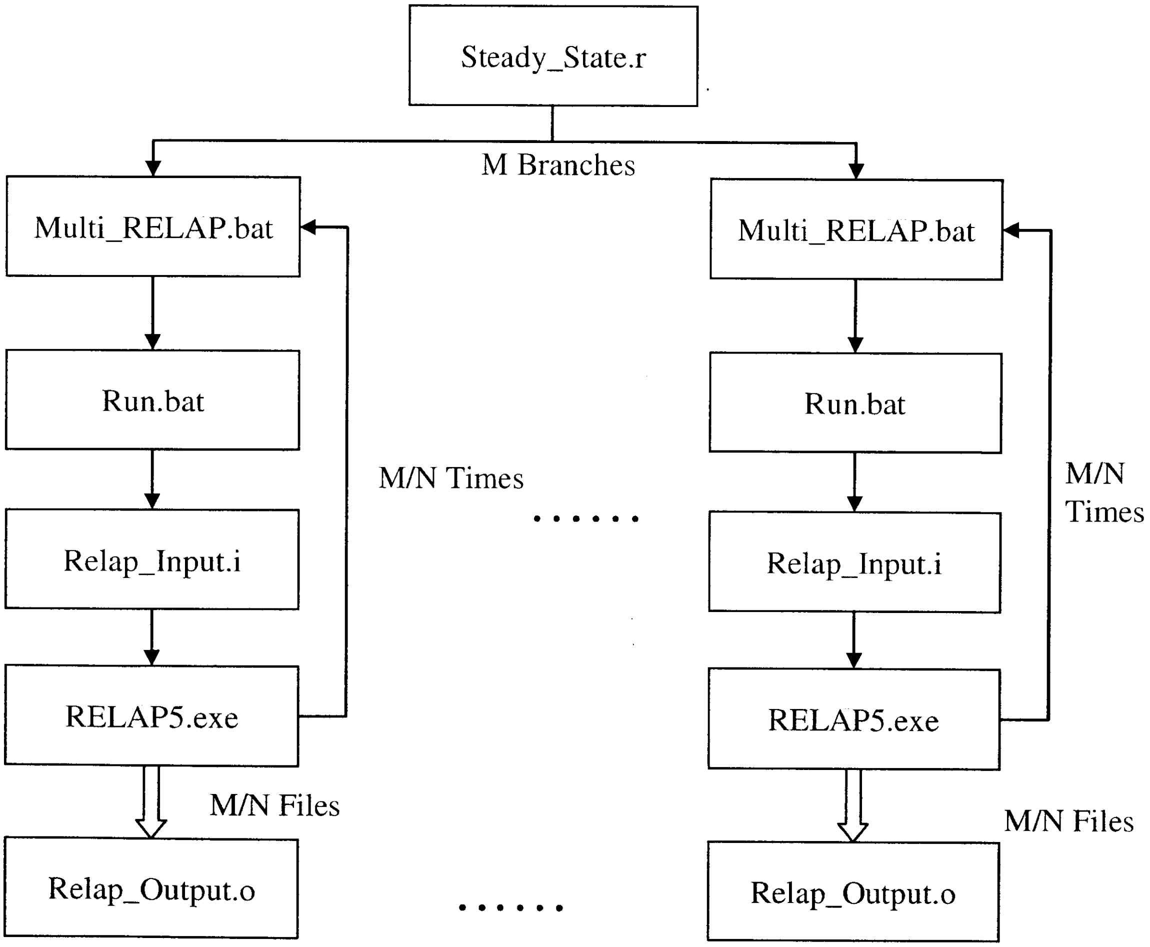

Figure 10 - RELAP Automation Module Flow Map

(iii) RELAP Output Extraction

The structure of the Output Extraction module is shown in Figure 11. Once all of the RELAP5-3D simulations for a given transient have finished, the Output Extraction module can reformat the RELAP5-3D outputs into MATLAB arrays for further post-processing. The first stage of the Output Extraction module is to comprise a list of RELAP5-3D outputs. This is accomplished through Multi.bat, which looks through the operation directory and complies a list of all output folders. Folder.bat then enters each folder and copies the full directory location of all files ending in *.o into the file List.l. Multi.bat and Folder.bat interact in a similar manner to Multi_RELAP.bat and Run.bat, due to the same array challenges, as mentioned previously.

Once the list of output file locations is compiled, Output_Process.m can begin the process of moving the data from the output text files into MATLAB objects and arrays. Output_Process.m extracts the data from List.l and creates a MATLAB array of file directories which it sends to Sortdata.m. Sortdata.m then loops through the array of file locations, sending each location through Reader.m. The number of minor edit variables tracked in the RELAP5-3D output files needs to be hard-coded into Reader.m. Unfortunately, RELAP5-3D output files only print minor edit variables in 20 time step blocks, each separated by hundreds of lines of debugging data. Reader.m was coded to search the entire input file and properly join each set of data, but the process is only as robust as was needed to extract the data for this thesis.

Once Sortdata.m processes all of the RELAP5-3D output files, Output_Process.m saves the output files into a *.mat file for future reference. The option to plot desired transient data using Plotter.m appears at the end of Output_Process.m, but Plotter.m can be called independently if desired.

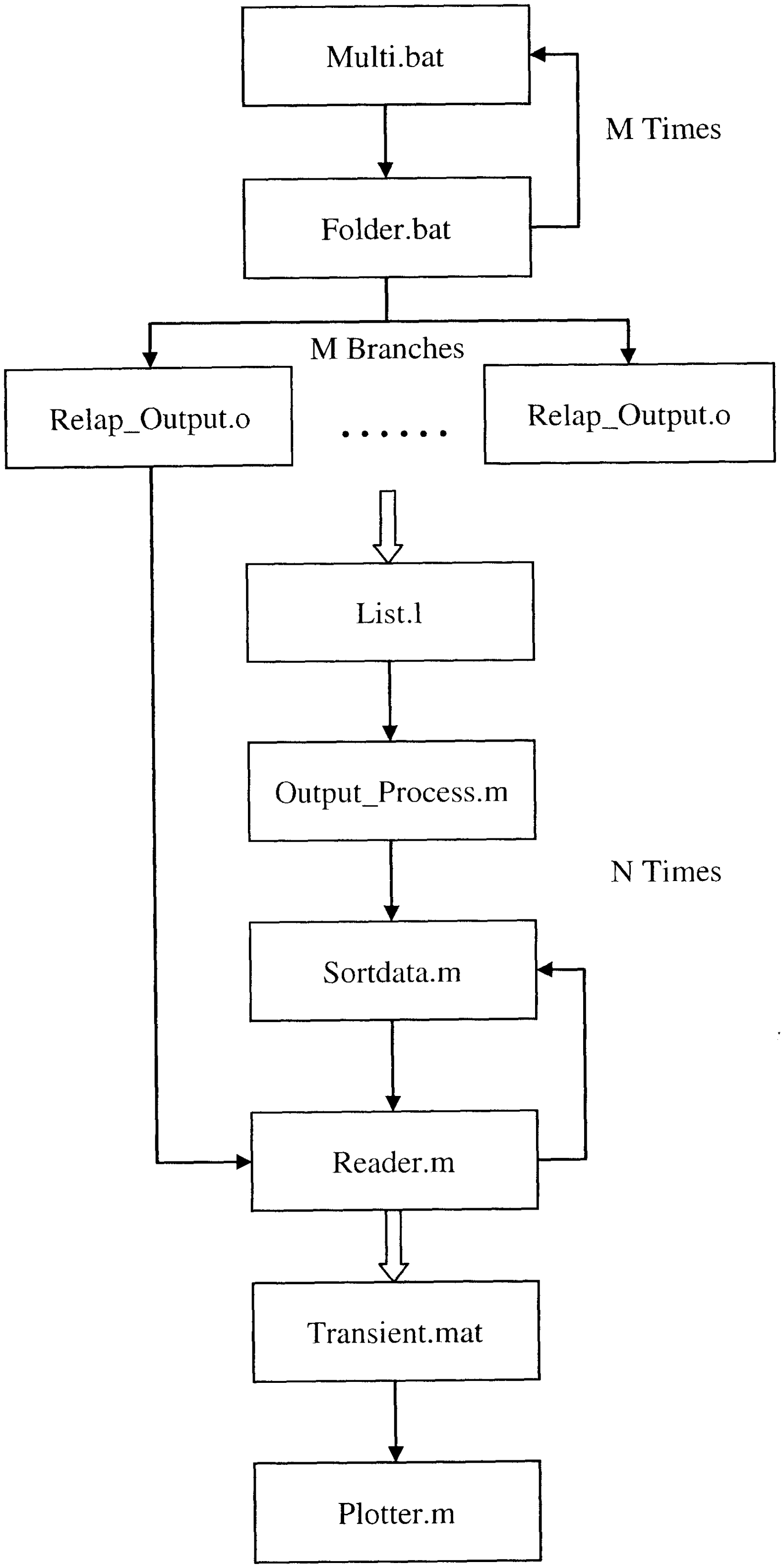

Figure 11 - RELAP Output Extraction Module Flow Map

(iv)RELAP Cladding Failure Calculation

The structure of the Cladding Failure Calculation module is shown in Figure 12. Object_Builder.m is the primary file in this module. Creep_Failure.m calculates the cladding damage fraction due to thermal creep and fuel/cladding eutectic wastage for every RELAP5-3D transient simulation. Creep_Failure.m outputs the Cladding Damage Fraction, Radius, and Thickness as a function of time, which Object_Builder stores in the transient object. Once every simulation has been analyzed, the results are sent to Damage_Plotter.m to be graphed. Damage_Plotter.m also determines if cladding failure, local sodium boiling, or bulk sodium boiling occurred during the transient. Using the statistical weight of each simulation from Par_sum.mat, Damage_Plotter.m calls Non-Integer.m to conduct the Bayesian inference on the Damage_Plotter.m results. Non-Integer.m produces probability density functions, cumulative distribution functions, mean and 95th percentiles of cladding failure, hot channel sodium boiling and core wide sodium boiling.

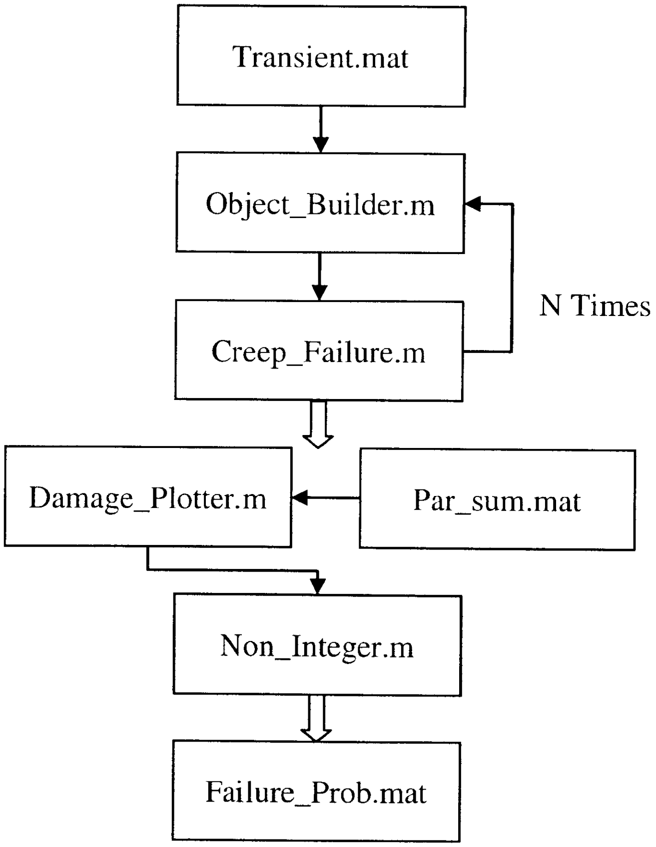

Figure 12 - RELAP Cladding Failure Module Flow Map

II.5 Evaluating Failure Probabilities with Non-Integer Evidence (V.2, V.3)

The TNF determines the acceptability of accident sequences by examining the 95th percentile estimate of both the frequency and quantity of radiological release (1). Estimating the 95th percentile of accidents sequences can be difficult as many advanced reactors are designed to have high reliability when confronted with licensing basis transients. While statistical techniques such as importance sampling exist to estimate the mean and variance of an estimate, classical statistics does not provide insight to the shape of the distribution around that estimate. This section proposes a method in which the evidence derived from importance sampling may be used in Bayesian updating to provide a posterior distribution with which a 95th percentile frequency or dose can be estimated.

II.5.A Background

The following method is developed to estimate the 95th percentile of thermal creep-induced cladding failure for a generic SFR. Epistemic uncertainties for reactivity coefficients, reactivity insertions and pump coastdown rates were propagated using importance sampling through the RELAP5-3D SFR model.

Once the simulations have been analyzed to determine if failure has occurred, in this example defined as cladding rupture or sodium boiling, the mean probability of failure can be estimated by dividing the total weight of the failed simulations by number of simulations conducted. The risk analyst is then left to ponder how to transform this evidence into an uncertainty distribution around the calculated probability of failure. Bayes Theorem may be used to combine the evidence observed from the computer simulations with a prior distribution, which describes the analyst's beliefs before the simulations were conducted, to form a posterior uncertainty distribution. This posterior distribution describes the analyst's new beliefs and can be updated with additional evidence or propagated through a PRA. Eq.II.18 calculates the mean probability of failure, $\hat{p}$,

$$\hat{p} = \frac{1}{N}\sum_{i=1}^{N} w_i I_i \qquad \text{II.18}$$

where I_i is the indicator variable for the i^{th}, 1 indicating failure and 0 indicating no failure, w_i is the weight of the i^{th} simulation resulting from the importance sampling scheme, all over N total simulations. The uncertainty around this estimate, $\pi'(p)$, is determined using Bayes Theorem shown in Eq. II.19,

$$\pi'(p) = \frac{\pi(p)\, L(E|p)}{\int_0^1 \pi(p)\, L(E|p) dp} \qquad \text{II.19}$$

where $\pi(p)$ is the uncertainty distribution around the probability of failure p and $L(E|p)$ is the likelihood of seeing evidence E given the failure probability is p (22).

II.5.B Method

The first step in Bayesian updating is identifying the form of the likelihood function. A likelihood function takes evidence, *E,* and determines what the probability of seeing that evidence, or put another way the likelihood of the evidence, is given the underlying probability of the event. It is proposed that the likelihood function should take the form of a Binomial function, which evaluates the probably of a given Bernoulli sequence. According to Ang and Tang, a Bernoulli sequence is defined as a sequence that has two possible outcomes. These outcomes could be occurrence or nonoccurrence of an event (e.g., the cladding may or may not rupture, the Fraction of Cladding Damage (FCD), defined in Appendix A, may or may not exceed a specified value) (22). Bernoulli sequences have the following assumptions:

1. There exist only two possible outcomes.
2. Every trial is statistically independent.
3. The probability of occurrence for every trial is constant.

The analysis conducted on the SFR obeys these assumptions. For example, only two possible outcomes exist, the simulation may or may not result in a FCD of greater than 1.0. The FCD is a representation of the eutectic accelerated thermal creep of the cladding and a value greater than 1.0 indicates breach of the cladding (19). Under unbiased Monte Carlo simulations, the values for the reactivity coefficients would be independently sampled from their corresponding epistemic uncertainty distributions (25). If importance sampling is used, the biased sampling distributions are chosen *a priori* thus still satisfying the statistical independence assumption. It should be noted that Markov Chain Monte Carlo (MCMC) cannot be used because every sample is correlated to the previous sample in MCMC. Because the underlying distributions are the same for each trial, the probability of occurrence is also the same; the epistemic values sampled just determine success or failure of the trial. Thus, the third assumption is satisfied.

Each RELAP5 simulation produces a range of outputs including time dependent temperature, pressure, flow rates, and FCDs for various components. Each of these parameters will have a distribution due to the epistemic uncertainties, but for now only the FCD will be examined. In fact, because cladding failure is modeled as a Bernoulli sequence, the only information, or evidence, extracted from each simulation is whether or not the FCD exceeds 1.0. It is probable that some of the ignored information could be used to provide a more accurate estimate of the failure probability, but incorporating this evidence is left as future work. Thus, the evidence provided from unbiased Monte Carlo simulations is shown in Eq. I.20,

$$x = \sum_{i=1}^{N} I_i \qquad \text{II.20}$$

where x is the number of cladding failures, N is the number of simulation, and I_i is an indicator variable which is 1 if the i^{th} trial results in a FCD greater than 1.0 and 0 otherwise.

If importance sampling is used to bias the sampling distributions, each simulation will receive a weight corresponding to the portion of the distribution being sampled. This is requires a relaxation in assumption 3 which states that probability of occurrence of every run is the same. In one sense, the assumption still holds as the probability of sampling a given value from the importance distribution is the same from trial to trial. The assumption is bent because a larger number of samples are taken from the tail of the epistemic distribution than justified, causing the results to be weighted to compensate for the biased statistics. To incorporate importance sampled data, the number of failures, x, can be defined using Eq.II.21.

$$x = \sum_{i=1}^{N} W_i \, I_i \qquad \text{II.21}$$

where W_i is the total weight of the i^{th} trial. The ramifications of representing the failure data in this way will be discussed later.

As the underlying evidence has been defined to satisfy a Bernoulli sequence with x failures in N trials, the likelihood function will take the form of the Binomial distribution shown in Eq. II.22. As was stated previously, the likelihood function evaluates the evidence based on a given probably of failure, p.

$$L(x|N,p) = \frac{n!}{x!\,(N-x)!} p^{x}(1-p)^{N-x} \qquad \text{II.22}$$

These definitions are straightforward if the evidence is derived from experiments or unbiased Monte Carlo simulations, but if the evidence for cladding failure is derived from importance sampling, the applicability of the binomial distribution is not straightforward. This difficulty mathematically manifests itself through the factorials in the binomial distribution, Eq.II.22, which restrict both the number of trials and failures to integer values. With importance sampling, the number of failures is the sum of the weights of the failed simulations, as seen in Eq. II.21.

Apostolakis suggested that, for thought experiments of subjective design, noninteger values are acceptable for discrete likelihood functions by replacing the factorials with gamma functions, Eq. II.23 (26). The resulting likelihood function can be evaluated for no integer evidence.

$$L(x|N,p) = \frac{\Gamma(N+1)}{\Gamma(x+1)\Gamma(N-x+1)} \, p^{x}(1-p)^{N-x} \qquad \text{II.23}$$

This modification is academic, since the likelihood function appears in both the numerator and denominator of Eq.II.23, thus canceling all constant terms (i.e., factorials and gamma functions).

The forms of the prior and posterior distributions are typically taken as the conjugate distribution of the likelihood function, if available (22). Conjugate distributions have the same functional form as the likelihood function, greatly simplifying the mathematical complexity of evaluating Eq.II.19. The conjugate distribution for the binomial function is the beta distribution, as seen in Eq. II.24. α and β are chosen based on prior knowledge of the prior distribution or calculated as a result of the updating process.

$$\pi'(p) = \frac{\Gamma(\alpha+\beta)}{\Gamma(\alpha)\Gamma(\beta)} p^{\alpha-1} (1-p)^{\beta-1} \qquad \text{II.24}$$

By using the constitutive relations between the binomial and beta distributions, the shape parameters for the posterior beta distribution, Eq.II.24, can be determined using Eq.II.25 and Eq. II.26 (22). If no prior evidence is known, the initial values for α and β are set to zero.

$$\alpha' = \alpha + x \qquad \text{II.25}$$

$$\beta' = \beta + N - x \qquad \text{II.26}$$

At this point, a posterior distribution exists that conserves the mean, but not the variance, of the importance sampled data. The third assumption for the binomial distribution assumes that all of the trials have equal weight. This assumption was relaxed when importance sampling was used to bias the underlying epistemic distributions, thus causing each simulation to be weighted differently. Most nuclear applications have low probabilities of failure (e.g., $p < 0.1$), producing a beta distribution that is heavily skewed to the right. At low values of total sampled evidence, the resulting posterior distribution can be so heavily skewed that the mean value falls above the 95th percentile estimate. This behavior disappears as enough evidence is sampled to stabilize the estimate of the cladding rupture probability.

II.5.C Validation

Figure 13 shows the mean and 95th percentile estimate of the cladding rupture probability for an Unprotected Transient OverPower (UTOP) accident scenario in a metallic fueled pool type SFR as a function of simulations. As can be seen, the 95th percentile estimate is less than the square root of the variance because the beta distribution is highly skewed to lower probabilities. This is in agreement with the sampled evidence where most failures either resulted in no failure or failure with little to no associated weight. Graphs of the mean value plus or minus the square root of the variance assume that the data is symmetrically distributed, as in a normal distribution, and are shown here more for tradition than for an indication of the confidence of the estimate.

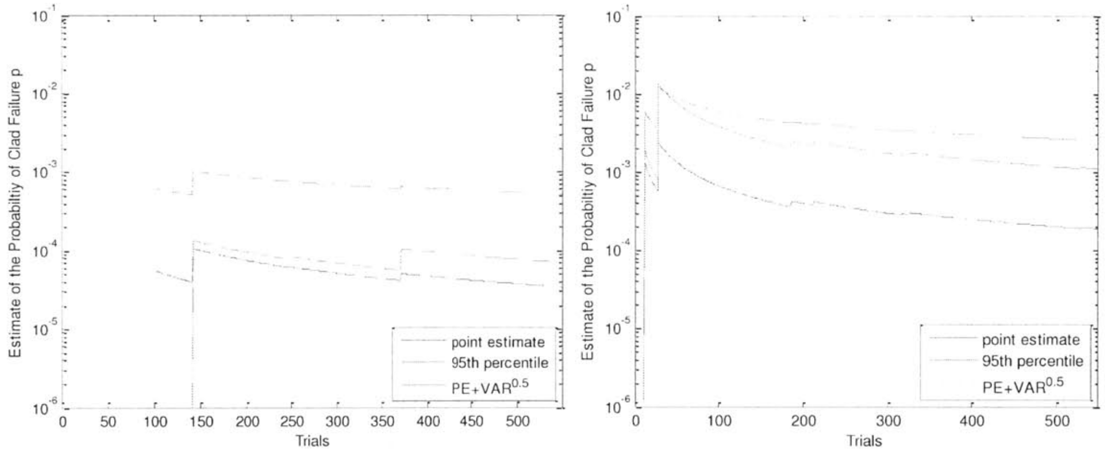

Figure 13– The Point Estimate (Mean), 95th Percentile Estimate from Bayesian Updating, and the Point Estimate plus the Square Root of the Estimate for Unprotected Transient Overpowers with a 510°C (left) and 550°C (right) Core Outlet Temperature. Because the square root of the variance is greater than the point estimate, the point estimate minus the square root of the variance is not shown.

II.5.D Summary

Risk-informed regulations, such as the TNF, set requirements on the tails of uncertainty distributions to limit their effects. This thesis proposes that Bayesian updating can be used to create uncertainty distributions from computer simulations that might otherwise be created through engineering judgment. To create uncertainty distributions without running an unfeasible number of simulations, the Binomial distribution is broadened to incorporate noninteger evidence from importance sampling. The resulting distributions can be used in a variety of PRA applications.

II.6 Multivariable Regression

The following section discusses the statistical basis for this multivariable regression. The definitions of significance levels, F statistics, t values, and regression selection methods are discussed. This methodology is used to create the new multivariable fuel/cladding eutectic formation rate predictive correlations in Section V.3.

Multivariable Regression is often employed when trends or predictive relationships are desired from a wide array of data. If there is a reason to believe that a desired variable (Y) is dependent on the state of other variables (X_1, X_2,...,X_n), then it may be reasonable to model Y as follows:

$$Y = A + \sum_{i=1}^{n} B_i X_i + \sum_{i=1,j=1}^{n,n} C_i X_i X_j + \cdots + \varepsilon \qquad \text{II.27}$$

where ε represents inherent randomness in the system and is often modeled as a normally distributed variable. A, B_i, and C_i are coefficients fitted from the data and determine how large the impact any given term has on the overall equation. Because they are statistically derived, these coefficients are only based upon data and are treated as statistical variables, often approximated as normal distributions. Eq. II.27 is often approximated by dropping higher order terms. One of the challenges of multivariable regression, due to an inherent lack of infinite resources and thus data, is that there may not be enough evidence to statistically resolve every term. If a coefficient has a high probability of being zero, it is assumed to be zero, thus omitting that term from the overall correlation (27). An example of a linear fit to data can be seen in Figure 14.

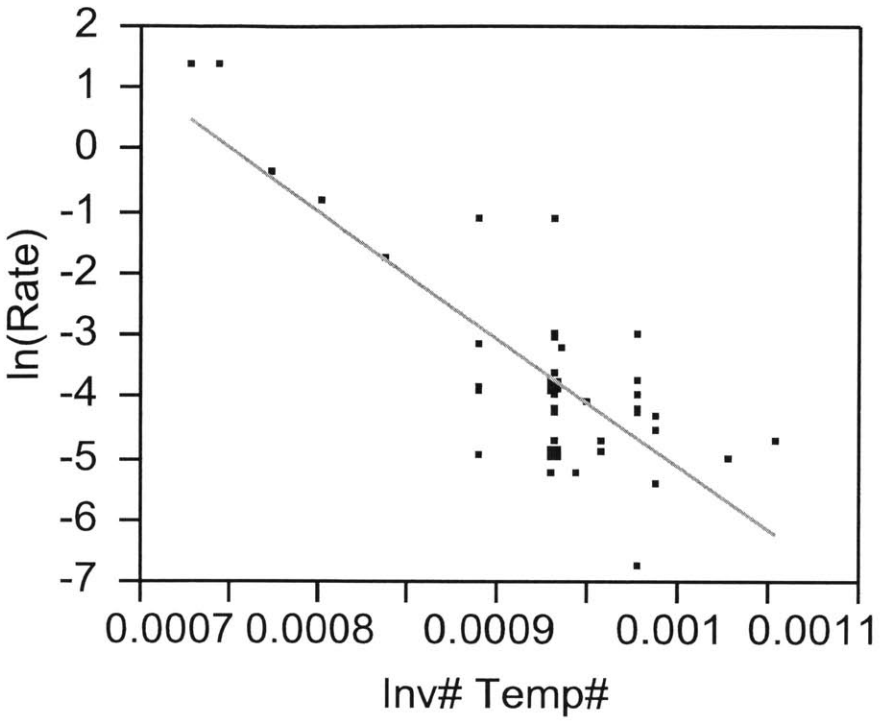

Figure 14- Linear Trend Fitted to Data

The statistical software JMP is used to conduct least-squares multivariable linear regression (28). Numerous statistical checks are formed to ensure that the overall data exhibits a linear trend, as well as that the terms making up the model are statistically significant. Statistically significant implies that there is enough evidence (data) to believe the term adds information to the model. In other words, there is a statistical reason to believe that the term exists. A 0.05 significance level is typically required to justify inclusion of a term in a linear fit, which indicates that the data only has a 5% chance of coming from a distribution where the confidence bounds of the slope of the model include zero. Figure 15 graphically illustrates a generic example of statistical significance. As noted from example coefficients 2 and 3, it is not the absolute magnitude of either point estimate or the 2.5th percentile (note: 95% Confidence Interval extends from the 2.5th percentile to the 97.5th percentile) which determines how significant a term is, but the absolute probability of the term not being zero.

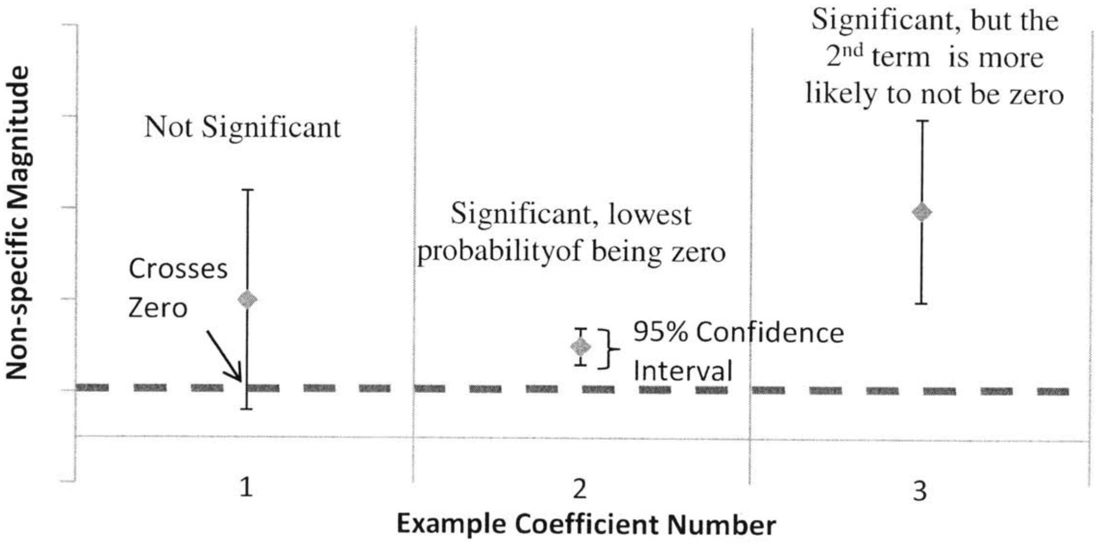

Figure 15 – Graphical Example of Statistically Significant Coefficients

Before examining the individual terms, the overall model is checked for significance. The F ratio for the model is examined to ensure that the data does indeed have a linear trend. The P>F value indicates the significance level associated with the F statistic, i.e. the probability that the data does not exhibit a linear behavior when a potential explanatory variables are included in the correlation. If this value is less than 0.05 then a linear model is significant to the 5% level, 0.01 is significant to the 1% level, and so on. In general, any model with greater than a 5% significance level should not be trusted. Once the overall model is deemed significant, then the explanatory variables are examined for significance.

The statistical significance of the explanatory variables is determined through the t statistic. The t statistic defined as the regression coefficient divided by the standard error of that coefficient. If this ratio is larger than the t value with n-k-1 degrees of freedom, where n is the total number of data points and k is the number of explanatory variables used, at the significance level of interest, then the variable is considered statistically significant. As with the f statistic, terms with a significance level of higher than 0.05 should not be included in the model, if possible.

In order to isolate the statistically significant terms, a variable selection methodology must be chosen. JMP offers three options: forward, backward, and mixed. The forward option starts with a constant term and then examines the remaining explanatory variables and selects the variable with the lowest significance level. This variable is added to the model and the significance levels of all remaining variables are re-calculated to incorporate the expanded model and the loss of a degree of freedom. JMP continues this process until none of the remaining variables have a probability less than the probably to enter threshold. JMP defaults this value to 0.25. This process is considered "greedy" because once a term is incorporated into the model; the effects of further explanatory variables on that term are not examined and included terms are not removed.

The backwards and mixed options are very similar to the forward option. The backward option begins with all the explanatory variables and removes the least significant variables until no variable exceeds the probably to enter threshold for the significance level. JMP defaults this value to 0.1. This option is also considered "greedy" in that it does not look to re-examine terms once it removes them. The last option is a mixture of the forward and backward algorithms. The mixture option conducts the forward method until no terms exist and then looks back at the adopted terms and determines if any variable should be removed using the backward method. Once the backward method can no longer remove terms, the forward method is used to add new terms. This iteration continues until no additional terms can be added or removed. Because the mixture method is the most balanced of the options, it was used to conduct all of the term selections in this analysis.

II.7 Model Uncertainty

Predictive relationships are only valuable to an analyst if the analyst has faith in the accuracy of the relationship in predicting new data. Model uncertainly is one class of methods which attempts to account for model, or in this case correlation, limitations. Model uncertainty has two primary sub-categories (29) (30):

1. Model averaging - This sub-category of model uncertainty is intended for situations where multiple independent models exist but the underlying forms are uncertain. For example, it is unknown if the underlying data is normally or log-normally distributed, in which event both models are evaluated and a weighted average of the results of each model is taken to be the final result.
2. Model error - This sub-category of model uncertainty is intended for situations where a model is accepted as an approximation of reality and the deviation of the predicted values from experimental values needs to be bounded.

Since there is no reason to believe that the actual penetration rate is a weighted average of any of these regression models, we will limit our analysis to model error quantification. One method for quantifying model error used in fire PRA is to assume that the ratio of experimental data to model prediction, henceforth referred to as the validation ratio, is an Aleatory, or inherently random, variable. Next, the analyst must determine how to model the variable, e.g. is the variable distributed via normal, lognormal, Weibull, etc., distributions. Because the fuel/clad eutectic penetration rates must be positive, a distribution that does not include negative values is required. Additionally, there exists few physical phenomenon which will determine an upper limit to rate of eutectic penetration, thus any proposed distribution should allow for extremely large values in the validation ratio.

Historically, the validation ratio has been modeled as a lognormal distribution with the shape parameters, b_m and s_m, which determine the Aleatory nature of model error. With infinite evidence, b_m and s_m would be known exactly. With finite evidence, a joint probability distribution which describes epistemic uncertainty of b_m and s_m is needed to determine the likelihoods of various combinations of b_m and s_m. If additional evidence is added which supports previous knowledge of b_m and s_m, the joint distribution will narrow until it is a delta function at the "true" value of b_m and s_m. If evidence is added which conflicts with prior evidence, which is often the case when only a small number of samples are available, then the epistemic uncertainty grows and a wider span of b_m and s_m combinations are possible.

A process for evaluating the likelihood of distributed parameters given evidence is Bayes Theorem (Eq. II.28). Notice that the general mathematical form is consistent with Eq. II.19. However, here the validation ratio, bounded between zero and infinity, is updated with information from experimental data and a model. In Eq. II.19, it is the probability which is bounded between zero and one and is updated with data derived by simulations.

$$\pi(R|R^*, M) = \frac{L(R|R^*, M)\,\pi_0(R)}{\int_0^\infty L(R|R^*, M)\,\pi_0(R)dR} = \frac{1}{k}L(R|R^*, M)\,\pi_0(R) \qquad \text{II.28}$$

where $\pi(R|R^*, M)$ is the analyst's understanding of the distribution for the validation ratio after considering the experimental data, R^*, and the model, M. $\pi_0(R)$ is the prior knowledge of the distribution for the validation ratio, and $L(R|R^*, M)$ is the likelihood of seeing the data given a particular value of the validation ratio being true. The denominator can be written as a normalization constant for simplicity. The form of the prior distribution is often the Achilles heel of Bayesian analysis because there is often no prior information to dictate $\pi_0(R)$. One common prior distribution is the uniform distribution over a range of potential values of R. Two main problems exist with the uniform distribution:

1. A range of analyzed R values must be applied. Any distribution of R must integrate to 1 over all values of R. A uniform distribution cannot extend to infinity because the area under the curve would be infinity not 1. Thus a Uniform distribution is defined by its end point, U(1E-5, 2). Any values of R which lie outside of the prior distribution will not be examined by Eq. 5 regardless of the likelihood of that R given the data.
2. Biased mean and variance. A uniform prior distribution has a mean and a variance which will bias the mean and the variance of the posterior distribution. Fortunately, with enough evidence the effects of the prior distribution will disappear.

Understanding these limitations, a uniform prior distribution, $\pi_0(R) = \mathrm{U}(10^{-6}, 35)$, is assumed to describe the analyst's prior belief of the ratio. 10^{-6} is set as the minimum value because the lognormal distribution is defined at values greater than but not equal to zero. The maximum value is set at 35 in order to examine the full effects of the tails on the mean of the lognormal distribution.

Next, the likelihood function, $L(R|R^*)$, is defined. The lognormal distribution was shown to adequately describe the validation ratio data and thus the lognormal likelihood described in Eq. II.29 is used.

$$L(R|R^*, M) = L(R|R_1R_2 \ldots R_n, b_m, s_m) = \frac{1}{\sqrt{2\pi}R\, s_m} e^{\left(-\frac{1}{2}*\frac{\ln(R)-b_m}{s_m^2}\right)} \qquad \text{II.29}$$

The R in Eq. II.29 must remain a random variable in order to evaluate the likelihood over the range of R in $\pi_0(R)$. It should be noted that the validation ratio data, R^*, is not a variable in Eq. II.29 and b_m and s_m are still unknown. Thus, Eq.II.29 should be rewritten in such a way that R^* informs the choice of b_m and s_m through another embedded Bayes Theorem. First, Eq. II.30 is generalized as an average over the joint probability distribution of b_m and s_m, $\pi(b, s_m|R^*)$, which is still undefined.

$$\begin{aligned} L(R|R^*, M) &= \iint_{b_m, s_m} L(R|b_m, s_m)\pi(b_m, s_m|R^*)db_m ds_m \\ &= \iint_{b_m, s_m} \frac{1}{\sqrt{2\pi}R\, s_m} e^{\left(-\frac{1}{2}*\frac{\ln(R)-b_m}{s_m^2}\right)} \pi(b_m, s_m|R^*)db_m ds_m \end{aligned} \qquad \text{II.30}$$

where $\pi(b, s_m|R^*)$ can be informed by the data, R^*, and prior assumptions on b_m and s_m, $\pi_0(b, s_m)$, through Eq. II.31:

$$\begin{aligned} \pi(b_m, s_m|R^*) &= \frac{L(b_m, s_m|R^*)\pi_0(b_m, s_m)}{\iint_{b_m, s_m} L(R^*|b_m, s_m)\pi_0(b, s_m)db_m ds_m} \\ &= \frac{1}{k} L(b_m, s_m|R^*)\pi_0(b_m, s_m) \end{aligned} \qquad \text{II.31}$$

where the likelihood function takes the form of Eq. II.32:

$$L(b_m, s_m|R^*) = L(b_m, s_m|R_1, R_2, \dots, R_n) = \prod_{i=1}^{n} \frac{1}{\sqrt{2\pi} R_i s_m} e^{\left(-\frac{1}{2} * \frac{\ln(R_i) - b_m}{s_m^2}\right)} \qquad \text{II.32}$$

Again, the prior distribution for b_m and s_m need to be assumed. Due to lack of information, the prior distributions for b_m and s_m are assumed to be independent uniform distributions as defined in Eq. II.33.

$$\pi_0(b_m, s_m) = \pi_0(b_m)\pi_0(s_m) = U_b(-4{,}2)U_s(10^{-6}, 2.5) \qquad \text{II.33}$$

There now exists a fully defined set of equations which can be solved to create a distribution for the model error distribution of interest, $\pi(R|R^*, M)$. While WINBUGS is an excel based program that performs Markov Chain Monte Carlo with Gibbs Sampling and has be used to solve Eq.II.28 through Eq.II.33 for fire PRA applications, the Model UncertainTy Tool (MUTT), a series of MATLAB scripts, has been created to create model uncertainty distributions for fuel/cladding eutectic validations. The MUTT code can be found in Appendix D.

III METAL AND OXIDE FUEL COMPARISON (V.2)

Because of the favorable experience of EBR-II with metallic fuel and some potential advantages of metallic fuel for a burner reactor that is recycling minor actinides, the reference design for this study employs metallic fuel (13). Internationally, however, oxide fuel is recognized as at least the near-term preferred fuel option for sodium-cooled fast reactors (10) (31). Thus, the trade-off to be considered is whether an oxide-fueled core would have better or worse safety characteristics and what the relative cost would be of generating electricity. Most of the analysis work described in this section relates to a comparison of accident scenarios and their relative consequences for the two different types of fuel design. Response to accident scenarios can have a direct impact on the capital cost of a nuclear power plant if expensive mitigative systems are required. Fuel cycle costs are likely to be a greater fraction of power generation costs in cycles involving some form of reprocessing and recycling than they are for the current generation of once-through nuclear power plants. There are substantial differences in reprocessing technologies for the oxide and metallic fuels, but there is very limited information on the cost of the pyroprocessing process used for metallic fuels. Fuel type can indirectly affect thermodynamic efficiency related to allowable core outlet temperature, as well as system availability.

Hence, as part of the risk-informed examination of the SFR, a trade-off case study of the in-core performance of metal- and oxide-based TRU bearing fuels is examined. Due to large uncertainties associated with the cost of electrochemical reprocessing as primarily used for metallic fuel, and aqueous reprocessing as primarily used for oxide fuel, as well as their impacts on fuel cycle costs, a definitive cost-benefit comparison cannot be completed at this time. Instead, this case study focuses on in-core differences that should be considered when comparing metal and oxide fuel performance. Table 7 overviews the categories used to compare metal and oxide fuel. A discussion of the ranking rationale for each criterion can be found in Section III.2.

III.1 Introduction

U.S. and Korean reactor designers, such as GE, ANL and the Korean Atomic Energy Research Institute (KAERI), tout a number of benefits of using a metallic fuel in the SFR (13) (2) (32). These benefits include metal fuel's:

- hard neutron spectrum for improved transmutation and breeding characteristics,
- high thermal conductivity (and thus low stored energy in the fuel) for faster accident response,
- aversion to re-criticality during postulated beyond-design-basis Energetic-Scenarios and
- predicted lower manufacturing and reprocessing costs when incorporating minor actinides for recycling.

French and Japanese reactor designers believe that oxide fuel provides a comparable number of benefits and that it should continue to be employed until more advanced carbide fuels are developed. These benefits include oxide fuel's:

- softer neutron spectrum for reduced radiation damage to cladding and other structural components,
- larger Doppler and smaller sodium density reactivity coefficients for reduced impact of large reactivity excursions,
- large experience base of oxide fuels from LWRs, FFTF, Phénix, Superphénix, and many other SFR's and
- existing reprocessing and fabrication capabilities of MOX Pu bearing fuels.

Comparison studies between oxide and metal fuel have primarily examined their response to low-probability, beyond-design-basis accidents which include failures of the reactor protection systems (33) (20). These studies show that the short thermal time constant of metallic fuel, resulting from the high thermal conductivity of the fuel, sodium bond, and cladding, allows for thermal expansion of the control rod drive lines and core support plates to passively terminate the transient quickly. Oxide fuel has a relatively long thermal time constant, due to the low conductivity of the fuel and the fuel/cladding gap, which, coupled with the positive reactivity introduced as the fuel cools, tends to extend the length of transients. Extended transients are not desired because the extra energy generated must be removed, often through safety grade heat removal systems which add cost and complexity to the reactor design. Until the reactor power equals the heat removal rate, overall system temperatures increase. These observations indicate that metal cores may have a smaller conditional probability of core damage states or sodium boiling because they have lower primary coolant equilibrium temperatures for a majority of transients. However, considering the low values of the frequencies of these scenarios as estimated by the designers (typically $<10^{-8}$/yr or less), in a highly risk-informed licensing process, such as the NUREG-1860 approach, response to severe accidents of this type might not be a major factor in the selection of fuel type (1). A summary of various transient properties and responses of metal and oxide fuel to low-probability transients are listed in Table 6.

It has been demonstrated through operation of previous reactors (e.g., EBR II, PHENIX) that both metal and oxide fuel can be used successfully in SFRs. The primary cost or benefits that can be derived from the fuel choice are in manufacturing, reprocessing, specific power, burnup, and conversion ratio. Fuel performance after a fuel disruption event could also be a discriminating factor, if deemed necessary by the regulator.

Table 6 – Oxide and Metal Fuel Comparison (33) (20) (34)

Fuel Type / General Properties	**(ULOF) Unprotected Loss-of-Flow (Failure of Primary Pumps)**	**(UTOP) Unprotected Transient Over-Power (Control Rod Withdrawal)**	**(ULOHS) Unprotected Loss-of-Heat-Sink (Loss of Steam Generators)**	**Cladding Considerations Applicable to all Transients**
Metal • High conductivity • Fast thermal response • Low stored energy in fuel • Small shutdown reactivity insertion • Hard neutron Spectrum • Power coefficient vested mainly in coolant	<u>Key Points</u> Short flow halving times possible due to: • Fast thermal response • Low stored energy in fuel • Small shutdown reactivity insertion Sodium boiling probability is extremely low (<<10^{-4}/event)	<u>Key Points</u> Initial transient • Small Doppler initially allows for elevated system temperatures • Expected reactivity insertions leave large margin to potential damage states Low probability of core damage if primary pumps trip due to high system temperature.	Key Points Faster Power Reduction • Fast thermal response • Strong negative reactivity o Radial expansion o Control Rod Drive Line Expansion • Low (+) Doppler effect as fuel cools Lower long term equilibrium temperatures achieved	• FCMI low due to soft fuel • FCCI (Eutectic Formation) starts between 650-725°C o Rate of eutectic formation does not significantly contribute cladding breach below 900°C • Low melting point eutectics will not freeze in coolant channel • No exothermic fuel-coolant reaction
Oxide • Low conductivity • Slow thermal response • Large stored energy in the fuel • Large shutdown reactivity insertion • Relatively soft neutron spectrum • Power coefficient mainly vested in fuel	<u>Key Points</u> Long flow halving times required due to: • Long thermal response • Large stored energy in fuel • Small shutdown reactivity insertion Core must be designed to avoid sodium boiling	Key Points Initial transient • Large Doppler dampens transient power spike quickly • Expected insertions leave very large margin to potential damage states High probability sodium boiling and/or core damage if primary pumps trip due to high system temperature.	Key Points Slower Power Reduction • Strong (+) Doppler effect as fuel cools delays shutdown • Slow thermal response Structural problems may occur due to • High sustained equilibrium temperatures • Long time scales	• FCMI primary failure mode due to hard fuel • FCCI erosion of cladding occurs over long time periods o Not a concern during transients • Cladding breach should be avoided o Exothermic fuel-coolant chemical reactions

In this assessment, design basis events are those that establish the design requirements for safety related systems, structures, and components. Historically, systems were designed to assure that these accidents would not result in severe fuel damage or uncoolable geometry (8) (35). Events that result in conditions that are outside the envelope of the design basis event conditions are referred to as beyond design basis events. These events have the potential to result in severe fuel damage. For sodium-cooled fast reactors, there is a subcategory of beyond design basis events that could result in energetic disruption of the core. We refer to these as Energetic Scenarios (ES). The potential for severe fuel damage events to lead to ES depends in part on the manner in which molten fuel debris transports after fuel failure. If the fuel debris forms blockages within the core region allowing fuel material to collect, there is a greater potential for recriticality than if the fuel debris is swept from the core region (36).

Table 7 – Metal and Oxide Fuel Comparison
1 = favoring metal, 5 = favoring oxide, 3 = neutral.

General Category	Specific Category	Rank
Transient Performance	Events without fuel damage	3
	Severe fuel damage events without potential for ES	1
	Severe fuel damage events with potential for ES	2
Operating Constraints	Maximum Coolant Outlet Temperature (without ODS clad)	3
	Maximum Coolant Outlet Temperature (with ODS clad)	4
	Maximum Achievable Burnup	4

III.2 General Assessment

The relative performance of metal and oxide fuel has been examined by fast reactor designers since the 1960s (13). The following section outlines the operating constraints for metal and oxide fuel and then describes historical and current safety characteristics of metal and oxide fuel. The safety cases for metal and oxide fuels will then be compared using the criteria set forth in NUREG-1860.

In the NUREG-1860 approach, licensing basis events (LBEs) are developed by grouping accident scenarios according to common characteristics, including their potential offsite consequences. Although LBEs are in many respects analogous to Design Basis Accidents or

Design Basis Events, as used in current licensing practice, an LBE can involve any degree of fuel damage. If the consequences are greater than 500 rem, the licensee must demonstrate that either the mean frequency of such an event is less than 10^{-8}/ry or the 95th percentile is less than 10^{-7}/ry.

III.2.A Operating Constraints

The proposed core outlet temperatures for the next generation sodium reactors indicate a potential temperature limitation for metallic cores. General Electric's S-PRISM and the Westinghouse SFR design are both proposing metallic fuel with a fairly low core outlet temperature (510-530°C). JSFR and EFR are both oxide fueled cores and propose operation at a higher core outlet temperature, around 550°C. This indicates that, considering only thermal efficiency, the SFRs employing metal fuel are currently 0.5% less efficient and thus have a 1.25% higher busbar electricity cost (see the Thermodynamic Efficiency Case Study (Section V.II) for more details). Table 8 summarizes the core outlet temperature for 4 currently proposed sodium reactors. A summary of the cladding options and limitation discussed in this section can be found in Table 9.

Table 8- Comparison of Proposed Outlet Temperatures for Oxide and Metal Fueled SFRs (7) (10)

Design	Fuel Type	T_{out} (°C)
S-PRISM	Metal	510
Westinghouse	Metal	530
JSFR	Oxide	550
EFR	Oxide	545

Table 9 - SFR Cladding Summary

Cladding	*Classification*	*Temperature Limit*	*Burnup Limit*
HT9	Martensitic	640°C	200 dpa
PNC-FMS	Martensitic	650°C	150-200 dpa
D9	Austenitic	675°C	100 dpa
15-15Ti	Austenitic	675°C	130 dpa
PNC1520	Austenitic	675°C	160 dpa
ODS	ODS	700°C	>200 dpa

Current SFR core outlet temperatures appear to be limited by cladding performance. Martensitic steels such as HT-9[2] are currently favored by US and Korean designers for both metal and oxide fuels due to their low swelling at high burnups (> 200dpa, 20 at%). This low swelling comes at the cost of creep resistance, which limits HT-9 cladding temperatures to below 620-640°C (37). While the IFR program stopped fuel testing in the mid 1990s, continued research into martensitic steels has continued in France and Japan. One of the most promising evolutions of HT-9 is the Japanese PNC-FMS[3]. PNC-FMS shows the same low swelling rate as HT-9 (PNC-FMS has been irradiated to 150dpa), exhibits improved creep resistance, as can be seen from Figure 16, and can be operated at a cladding mid-wall temperature of 650°C. Above this temperature, coarsening of carbides and nitrides in the cladding rapidly decreases cladding performance and may lead to cladding failure (38).

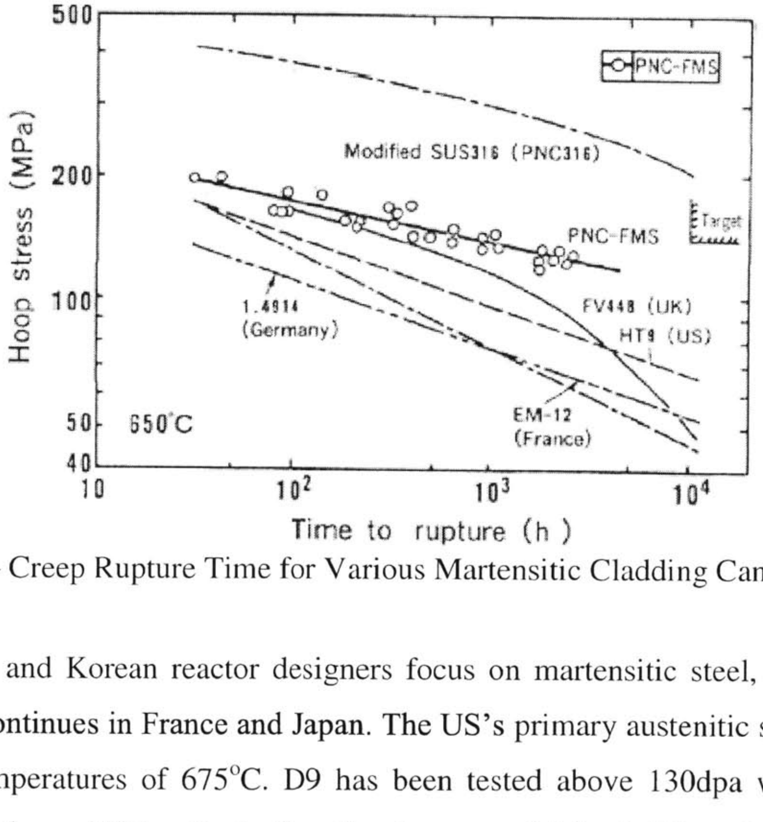

Figure 16– Creep Rupture Time for Various Martensitic Cladding Candidates (38)

While US and Korean reactor designers focus on martensitic steel, work on advanced austenitic steels continues in France and Japan. The US's primary austenitic steel, D9[4], achieved peak cladding temperatures of 675°C. D9 has been tested above 130dpa without failure, but reduced ductility above 100dpa limits the attractiveness of this cladding. Swelling limits other promising austenitic steels, such as 15-15Ti[5] and PNC1520[6], to 130 to 160dpa respectively,

---

[2] HT9 composition: 0.2C-12Cr-0.6Ni-1.0Mo-0.5W-0.3V-0.38Si-0.6Mn

[3] PNC-FMS composition: 0.15C-11Cr-0.5Ni-0.5Mo-2W-0.2V-0.05Nb-0.05Si-0.5Mn-0.05N

[4] D9 composition: 0.05C-14Cr-15Ni-1.5Mo-0.9Si-1.7Mn-0.23Ti, 50ppm Boron

[5] 15-15Ti composition: 0.1C-15Cr-15Ni-1.2Mo-0.6Si-1.5Mn-0.4Ti-0.03P, 50ppm Boron

which is below the desired 200dpa goal (38). A comparison of the swelling characteristics of martensitic and austenitic cladding tested in EBR-II can be seen in Figure 17.

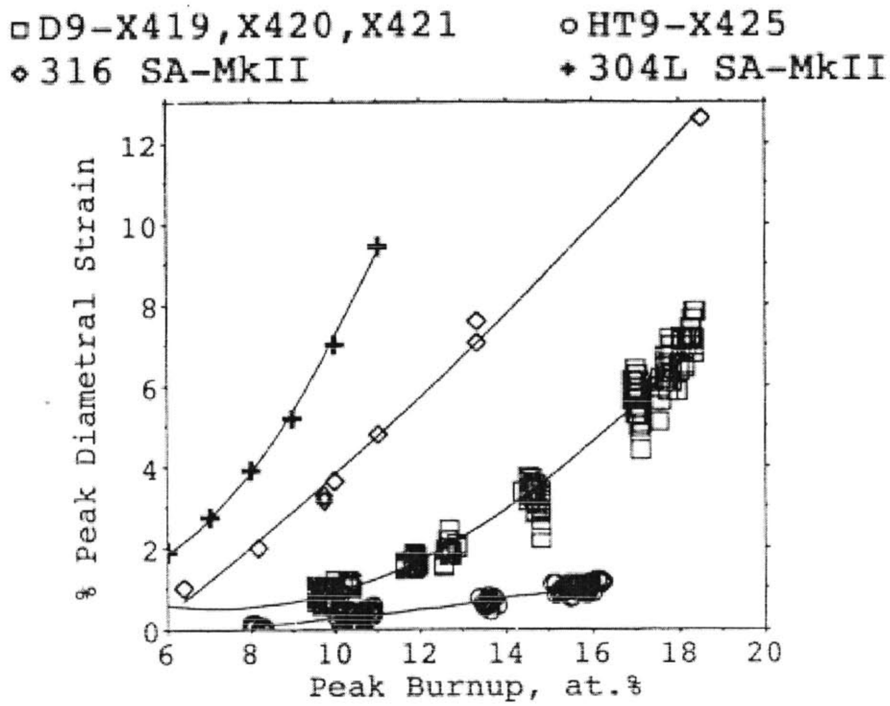

Figure 17– EBR-II Swelling Experiments for Potential IFR Driver Fuel (39)

The JSFR design hinges upon the development of ODS[7] cladding, which promises to operate maintain sufficient creep resistance beyond 200dpa and above a peak cladding temperature of 700°C by adding ceramic molecules, typically Y_2O_3, to the cladding (40). Early tests from FFTF and BOR 60 currently show good creep and swelling behavior up to 750°C, but the testing database for this cladding is limited and only extends up to 115dpa. Continued testing of this cladding is currently scheduled in JOYO to provide a licensing basis for replacing MONJU's driver cladding with ODS. The primary technical barrier for adoption of the ODS cladding is economic fabrication methods including welding of the end plug to the fuel pin (38).

With the proper smear density to reduce fuel/cladding-Mechanical-Interactions (FCMI) any of the above cladding options can be utilized for both oxide and metal fuels (13) (37). Metal fuels have an additional temperature limitation in that they form a low melting point

---

[6] PNC1520 composition: 0.05C-15Cr-20Ni-2.5Mo-0.8Si-1.7Mn-0.025Ti-0.1Nb-0.025P, 40ppm Boron

[7] ODS composition: 0.053C-10.78Cr-7.72Mo-0.02Si-0.015Mn-0.46Ti-0.1Y2O3-0.0622O-0.009N-0.001S

eutectic with iron-based cladding materials. The eutectic formation has two properties of interest: the liquidus temperature and rate of eutectic formation. Both these properties are complex functions of actinide content, cladding type, zirconium content, burnup and linear power, but even for the most limiting case examined by ANL (41), U-26%Pu-10%Zr, the liquidus temperature of 650°C remains above the creep failure temperature for martensitic cladding. Thus, metal and oxide fuel should have the same operating temperature limits for martensitic cladding. Whether or not metal fuel will limit the operating temperature for austenitic or ODS steels depends on the composition of the fuel and clad, and will be discussed in the next section. The addition of a liner between the cladding and the metal fuel has the potential of completely preventing eutectic formation, thus allowing metal and oxide fuel operating conditions to be primarily governed by cladding performance. This elimination of eutectic formation can come with safety implications, as will be discussed in the transient performance Section III.3b, of this case study.

While most of the fuel/cladding chemical interactions (FCCI) have been almost completely resolved through a lowered oxygen-to-heavy-metal ratio (42), the same is not true with metal fuel due to the abrupt end of the IFR program in 1994. The following sub-sections will overview the current state of knowledge for metallic fuel FCCI.

(i) Cladding Temperature Limit Implications of the Metallic fuel/cladding Eutectic Formation

A complex underlying phenomenology determines the eutectic liquidus temperature. The combination of cladding and fuel constituents creates a wide variability in the liquidus temperature, as can be seen in Table 10. Liquidus temperature predictions become more difficult with the addition of lanthanides and rare earth fission products. Thus, the only method for determining the liquidus temperature is through experimentation, which leaves the analyst vulnerable to the effects of limited data.

Table 10- Liquidus Temperatures from Direct-Couple Data After 300-700 Hours at Temperature (41)

	Melting Temperature (°C)			
	304	316	HT9	D9
U-8Pu-10Zr	>760	790	740	750
U-19Pu-10Zr	>780	790	>780	>730
U-26Pu-10Zr	-	<775	650	650
U-15Pu-11Zr	>800	>800	>800	>800

During the IFR program, direct-couple (a.k.a. diffusion-couple but this thesis will use direct-couple for consistency) testing was one of the methods employed to determine the liquidus temperature for metallic fuel/cladding combinations. The schematic in Figure 18 illustrates the changes observed during fuel/cladding restructuring in fresh fuel which the liquidus temperatures reported in Table 10 attempt to define. Initially, interstitial atoms such as carbon, oxygen, nickel, chromium, and especially nitrogen migrate into the fuel. These atoms have an affinity for zirconium and form a zirconium-rich layer between the fuel and the cladding. This zirconium layer acts as an imperfect barrier to iron, uranium, and plutonium migration. Some melting is expected in the zirconium-depleted fuel region, although the partially-melted fuel has been observed to transform into a load bearing foam which has little safety impact. On the other side of the zirconium-rich region, melting is expected as uranium and plutonium start to form a eutectic with the iron in the cladding. The stainless steels 304 and 316 both have a high- nitrogen concentration, which is credited for causing the higher liquidus temperatures seen for these claddings in Table 10. The high affinity between nitrogen and zirconium is believed to promote the formation of a thick zirconium diffusion barrier between the fuel and cladding. Additional tests have been conducted in which a nitrogen-rich layer has been applied between the fuel and cladding in an attempt to force a zirconium-rich layer to form more effectively in HT9 fuels. Since this barrier is imperfect, it is theoretically possible that, if the sample is heated for an extremely long period of time, enough iron, uranium, and plutonium migration will occur to lower the liquidus temperature of stainless steels 304 and 316 further. Unfortunately, furnace testing was only conducted up to 700 hours and thus it is impossible to determine what would have happened under further testing (41).

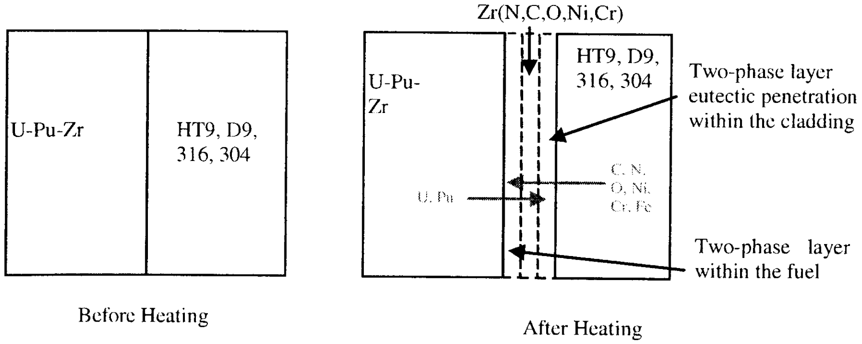

Figure 18- Schematic of Direct-Couple Fuel/Cladding Restructuring after Heating (41)

Since the IFR program ended, there has been additional direct-couple testing conducted in both the US and Korea. The direct-couple testing in the US primarily examines the effects of plutonium bearing metal fuel on potential high temperature cladding, such as ODS, T112[8] and 800H[9], at their peak design temperatures (700°C). In order to determine the effect of fission products on FCCI without access to irradiated fuel, two fuel forms were used: U-19Pu-10Zr and U-19Pu-9Zr-2Nd-2.5Mo-2.5Ru. The neodymium was added to represent lanthanide diffusion and chemical behaviors, and molybdenum and ruthenium are added to represent noble metal diffusion and chemical behaviors. Samples were tested for 25 hours and then cooled and examined with SEM. The fresh fuel samples showed the expected high zirconium layer and no liquid phase for the advanced cladding tested. The samples with the synthetic fission products lacked the high zirconium layer after 25 hours and extensive diffusion occurred between the fuel and the cladding. Additionally, ODS showed extensive liquid phase transformation, while no conclusive evidence for liquid phases was found for 800H, the only other steel tested with the synthetic fission product fuel (43) (44).

The KAERI has also been using direct-couple tests to examine potential diffusion barriers for 25 hours at 800°C. These barriers are applied by vapor deposition of either zirconium, (Cr-Ni alloy–Zr) or Ti-(Cr-Ni alloy–Zr) between the U-10Zr and HT9. The zirconium forms a coherent diffusion barrier while Ti, Cr, Ni forms a non-coherent precipitate layer which combines with the zirconium to form a highly effective secondary barrier against FCCI and drastically reduces

---

[8] T112 composition: 0.011C-10.54Cr-0.32Mo-0.15Si-0.62Mn-0.32O-0.54Nb-0.39Ni-0.19V-0.63Al

[9] 800H composition: 0.069C-20.42Cr-0.13Si-0.76Mn-31.59Ni-0.50Al-0.57Ti-0.42Cu-0.014P-0.001S

cladding wastage (45). The extent to which these barriers will hold up under irradiation is currently unknown and should be investigated in the future.

We can conclude from these recent direct-couple tests that ODS steel does not undergo liquid phase transition at 700°C with fresh fuel, partially due to the high zirconium region that is allowed to form. The addition of "fission products" prevents this high zirconium layer and extensive liquid phase transition is seen for ODS clad, although other high temperature steels do not undergo liquid phase transition. The effect of rapid zirconium layer formation and gradual fission product buildup, as would be seen in a reactor, is unknown at this time. It is possible that the high zirconium layer would reduce lanthanide buildup in the clad, raising the liquidus temperature. As ODS cladding is designed to be operated at high temperatures, special attention should be given to both high temperature-low linear power behavior, as well as the ability of vapor deposit diffusion barriers, such as those examined by KAERI, to prevent fission product buildup in the clad.

While the direct-couple tests explain the fresh fuel, or simulated burned fuel diffusion characteristics at elevated temperatures, they do not include the effects of long term temperature gradients and gradual lanthanide buildup with burnup. It should be noted that for most irradiated fuel tests, the fuel/cladding interface temperature is typically low, < 600°C, the plutonium content is medium-to-low, <19 wt% Pu, and then the fuel rod segment is heated post-irradiation for 1 to 36 hours in order to gauge transient FCCI behavior. Even so, it is possible to gain some insight on how burnup will affect the liquidus temperatures reported in Table 10. Due to the low operating temperatures, the high zirconium buffer region takes a long time to form an effective barrier, allowing uranium, plutonium and iron migration to dominate the liquidus temperatures. At higher burnups, lanthanides have had a chance to penetrate deep into the cladding and dominate FCCI. By this time, a high zirconium layer has had a chance to form thus retarding additional diffusion which might lower the liquidus temperature further. Once this zirconium layer has formed, the liquidus temperature is determined by iron which has already penetrated into the fuel and lanthanides and actinides which have penetrated into the clad. The existing testing indicates that the liquidus temperature from irradiated fuel decreases with burn-up, as the liquidus temperature for U-19wt%Pu-Zr HT9 fuel dropped to 650°C at 11% burnup (34) (46) (47).

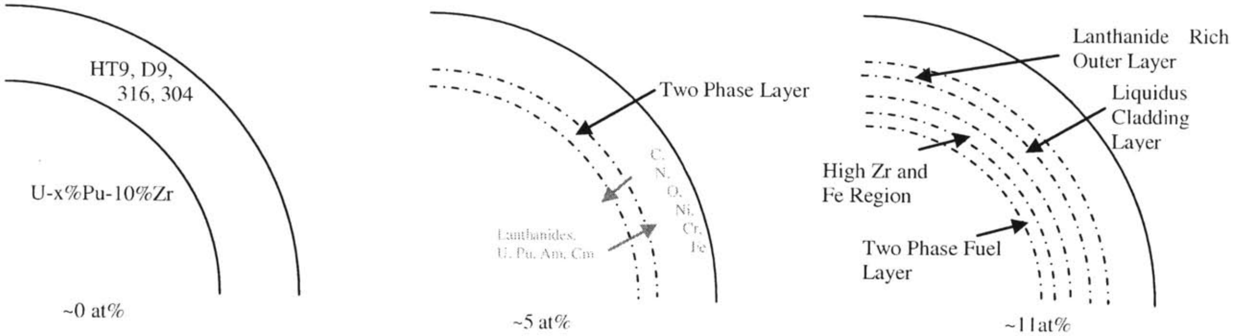

Figure 19- Schematic of Fuel(U-19%Pu-10%Zr)/Cladding Restructuring with Burnup (34)

The degree to which the liquidus temperature decreases with burnup seems to be a function of linear power, which controls the rate of lanthanides build up in the cladding (controlled by burnup and linear power) with respect to the rate of the protective zirconium layer formation (controlled by time at temperature), as shown in Figure 19. The high thermal conductivity of sodium ensures that the peak cladding temperature occurs at the top of the core, where the linear heat rate is the lowest. The linear heat rate dictates the temperature gradient in the fuel, which is the primary driving force for lanthanide migration into the cladding. Because the linear heat rate is at a minimum at the top of the core, the lower temperature gradients provide less of a driving force for lanthanides to enter the cladding. Lanthanides dominate FCCI at high burnup, so the liquidus temperature is the highest where the lanthanide concentration is the lowest, at the top of the core. Short core designs, i.e., EBR-II, have fairly flat axial power distributions and thus this trend is not easily seen in the EBR-II fuel tests. FFTF was designed with a taller core and the D9 cladding IFR-1 lead test assembly demonstrated the variation of liquidus temperature from linear heat rate. Because there was only one metal fuel test assembly in FFTF and little available high burnup furnace data from EBRII, it is difficult to completely separate out the effects of burnup from those of linear power within a given assembly for D9 clad. Still, combining the FFTF D9 data with the EBR-II HT9 data does support a linear heat rate dependency on liquidus temperature, as can be seen in Figure 20.

To further examine the dependency of liquidus temperature on linear heat rate shown in Figure 20, two curves have been plotted on both the HT9 and D9 graphs. The first curve is the conservative liquidus temperature curve (solid). This curve is plotted as a step function and connects the tests conducted at the highest linear power for a given temperature in which no liquefaction is experienced at a lower temperature. Thus, the 14.7kW/ft, 675°C HT9 EBR-II test is not included in this curve, since multiple tests conducted at combinations of equal or lower temperatures and linear powers show that liquefaction should occur in this region. Whether or not this curve is actually conservative can only be determined with further fuel testing. The optimistic curve (dotted) connects the most extreme tests, in terms of linear power and test-temperature, which are with non-liquefaction tests in which no experimental results are inconstant with the curve. Thus, for the HT9 EBR-II tests, the optimistic curve connects the test at 11.7kW/ft, 700°C with the test at 15.3kW/ft, 650°C. It should be noted that the conservative curve is only conservative when compared to the optimistic curve because longer time-at-temperature tests may yield liquefaction below this curve. The optimistic and conservative curves are only an indication of a possible trend, and further fuel testing needs to be conducted at much longer time-at-temperatures before these curves can be validated.

Unfortunately, due to the short heating times of these furnace tests it is impossible to definitively know the steady state liquidus temperature for either cladding at high burnup. Thus, to be conservative, many core designers limit their peak cladding temperature to 650°C regardless of linear power. While this might be a practical assumption in the short term, additional fuels testing may allow the peak cladding temperature to be raised to 700°C or greater depending on linear power at the top of the core for advanced cladding, such as ODS. Currently, no database for metallic fuel with ODS clad exists. Thus it is impossible to determine if ODS will be more or less susceptible to eutectic penetration than HT9 or D9 cladding. Beyond the limited database of high burnup fuel/cladding interactions, the unknown interplay between the ceramic Y_2O_3, which exists in ODS cladding but not in traditional steels, and the metallic fuel makes any attempt to extrapolate a eutectic temperature impossible (34) (46) (47) (41).

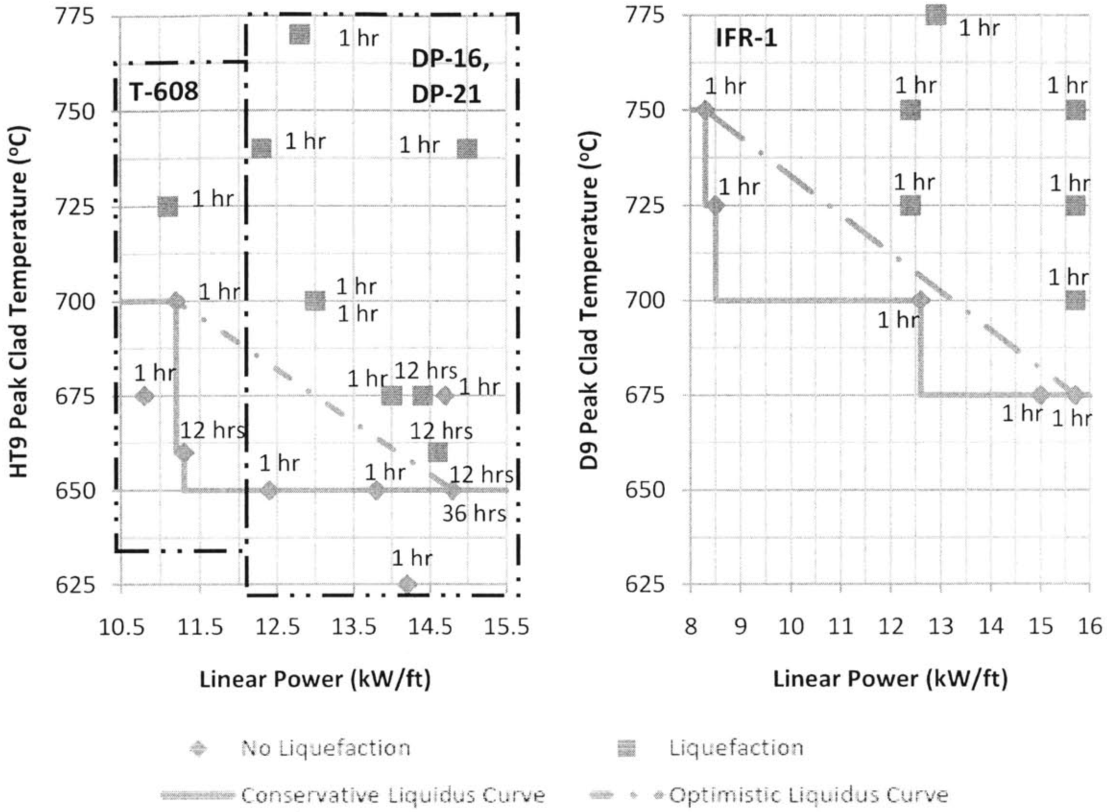

Figure 20– Liquidus Temperature Variations with Linear Power for U-19%Pu-10%Zr. HT9 cladding irradiated in EBR-II to 10.4±0.7 at% burnup (left). D9 cladding irradiated in FFTF to 9.4 at% burnup (right). Times refer to furnace hold time at indicated temperature. Tests resulting in liquefaction (melting) are indicated by diamonds, tests resulting in no liquefaction are indicated by squares. (34) (46) (47)

Some reactor designers have taken the metal fuel liquidus temperature to be 650°C regardless of fuel composition, cladding choice or linear power, thus imposing a 50°C temperature penalty compared to ODS cladding oxide fuel (3) (48). This temperature penalty seems to be imposed either due to the liquidus temperatures of U-26Pu-10Zr fuels found in direct-couple tests, or due to the 650°C liquidus temperatures found in the high linear power tests described by Cohen (34). While Cohen reports the FCCI results of the high burnup-high linear power elements DP-17, DP-21, he did not report results of the higher burnup but lower linear power element T-608. The T-608 element showed less cladding wastage and a higher liquidus temperature than either of the higher linear power elements. This element was examined at the same time as the DP tests to determine the effects of linear power on FCCI and the test results can be found in the Annual IFR Progress Report from 1993. When the T-608 data for HT9 cladding is coupled with the IFR-1 test data for D9 cladding, there seems to be evidence to support the notion that a bounding 650°C temperature limit may be overly conservative. Further irradiation test data will be needed to resolve this issue. Both sets of liquefaction data are plotted in Figure 20. The following quote, from the 1993 IFR annual progress report, emphasizes the required conservative nature of setting the liquidus temperature limit given the lack of data (46):

> *"Even though the data show that the eutectic threshold temperature is higher for fresh fuel...a eutectic threshold temperature of 1200°F (650°C) has been applied irrespective of burnup, cladding type or exact quantity of plutonium or other actinides in the fuel. The reason for adopting this position is in order to bound the effects of fission product (especially lanthanides)and actinide carryover which will be experienced in current unknown amounts when the fuel is recycled through the preprocessing and the recycled fuel returned to EBR-II, -i.e., to set conservative criteria prior to the availability of data..."*

Thus, in order to operate cladding above 650°C, additional fuel testing would be required. Regardless, additional testing would be required to operate at temperatures above 650°C because the primary candidate cladding for metal fuel, HT-9, is creep limited below 650°C. The large variability in fuel/cladding combinations would require extensive fuel testing for high temperature cladding candidates, and this testing should include high temperature, low linear power tests to prevent unnecessary exclusion of the high temperature operation.

(ii)Operating Conditions Conclusions

Taking into account all of the available cladding limits, primarily due to creep and fuel/cladding eutectic, the following guidelines can be formulated:

- Due to the large dependence of the fuel/cladding liquidus temperature on cladding choice, it is impossible to set a eutectic limit for a cladding without empirical data.
- For U.S. tested cladding, i.e. SS304, SS316, D9, HT9, and variations of U.S. tested cladding which most likely have similar eutectic behavior, i.e., PNC-FMS, 15-15Ti, creep limits will limit cladding performance, not eutectic liquefaction. Thus, the value of 3 (neutral) is given to outlet temperature (without an ODS clad) category in Table 5.

- With metal fuel, high Pu regions of the core, i.e., >20 at%, may or may not require restricted cladding temperatures due to burnup effects when using U.S. tested cladding other than SS316 since no high burnup eutectic data exist and direct-couple tests show an initially low liquidus temperature. If deploying advanced cladding, such as ODS, high Pu regions may be restricted to a peak cladding temperature of 650°C unless additional zirconium is added to the fuel matrix to increase the liquidus temperature or a diffusion barrier is employed to prevent eutectic formation. Thus, the value of 4 (slightly favoring oxide) is given to outlet temperature with ODS cladding category in Table 7.
- Due to a lack of high burnup metallic fuel data, the value of 4 (slightly favoring oxide) is given to the achievable burnup category in Table 5. Lead test assemblies from EBR-II show the potential for HT9 to be burned past 20 at%, but not enough data exist at this time to form a licensing basis beyond 11 at% burnup.

Additionally, Chapter V of this thesis overviews how the rate of fuel/cladding eutectic formation can predicted more accurately than traditional modeling correlations, both of which assume that the formation rate is only dependent upon the temperature of the fuel/cladding interface. New correlations are developed using multivariable regression, and model uncertainty is used to create uncertainty bounds for existing and new predictive correlations.

III.2.B Transient Response

The fuel in a sodium reactor is not arranged in the most reactive configuration. Thus accidents which change the geometry or remove coolant have the potential to cause runaway reactivity excursions. Excursions which lead to the release of fuel outside the cladding are referred to as core disruptive accidents (CDAs). If these excursions produce mechanical energy due to sodium boiling or fuel vaporization, they are referred to as Energetic Scenarios (ES) and may have enough energy to damage the vessel head and thus provide a pathway to radiation release. The following sections outline the historical and present response to ESs for metal and oxide fuel.

(i) Overview of Energetic Scenarios

CDAs are low-probability hypothetical accidents that result in a core geometry change. CDAs are of concern in fast reactors because the fuel is generally not arranged in its most reactive configuration and core compaction can lead to large reactivity insertions. If the net reactivity insertion is larger than \$1, the resulting prompt reactivity excursion may allow the fuel to vaporize and the resulting pressure shock waves will cause the core to disassemble. If the CDA reaches the point of fuel vaporization, it is referred to as an ES (49).

The "work energy" is the maximum amount of work done on the reactor vessel resulting from ESs (49). There is no appreciable work energy from non-ESs because the fuel does not vaporize and sizeable pressure waves within the vessel are avoided. Structural components, such as the reactor vessel and containment, must be able to withstand the work energy if the public is to be protected against these very low probability accidents. Making ESs highly unlikely may allow for the possibility of reduced design requirements for the containment and reactor vessel.

(ii) Traditional Energetic Scenario Modeling

Early ES analyses were conducted using the Bethe-Tait methodology. This procedure removes all of the coolant from the core and assumes that the core collapses on itself through gravity. The corresponding reactivity insertion vaporizes the fuel until the core disassembles. Many negative feedback mechanisms such as core expansion or removal of fuel during the accident are neglected. Using this methodology, reactivity ramp rates of \$60/s were hypothesized yielding extremely large work energy values. As the scientific community began to understand more about the SFR core behavior and became more certain about feedback mechanisms, the work energy values for SFR cores exponentially decreased, as can be seen in Figure 21. As a result it is almost impossible to compare work energy values from different historical studies meaningfully.

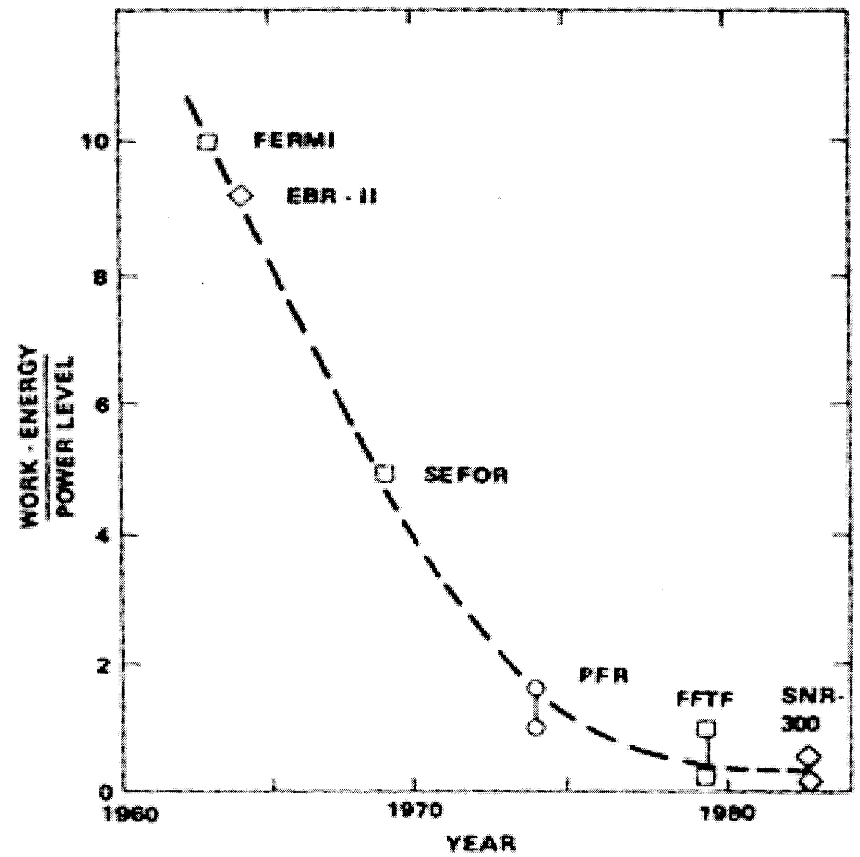

Figure 21– Decreasing Trend in Predicted Normalized Work Energy for SFRs from 1960 to 1985 (49)

Most current ES studies assume an unprotected transient and ignore specific feedbacks in order to force the fuel vaporization. These studies have been performed as recently as 2002 and provide some insight into how metal and oxide fuels behave during ESs. In an analysis by Singh of an Unprotected Loss of Flow Accident initiating an ES, metal fuel released less work energy than oxide fuel per fraction of the core that was melted before fuel vaporization occurred (36). This result was attributed to the larger negative Doppler power feedback in the metal fuel and the neglecting of negative feedbacks derived from fuel movement. Even though metal fuel has a smaller Doppler temperature coefficient than the oxide fuel, its low specific heat allows for a stronger negative feedback per unit power than the oxide fuel, which takes more energy to raise its temperature.

(iii)Mechanisms Preventing Metals Fuels from experiencing Energetic Scenarios

Many metallic fuel proponents take exception to the traditional view that any fuel type can undergo an ES. The basis for their view is the following hypothesis: inherent feedback and metallic fuel motion and sweep-out will stop accidents in the CDA phase. Actinides and Lanthanides in metallic fuel can form a low melting point eutectic with the cladding starting at 650°C, which makes the cladding more vulnerable to creep stresses. During the pre-disassembly phase of an ES at high cladding temperatures (>900°C) the eutectic will quickly lead to failure of the cladding, releasing molten fuel into the coolant. However, the low fuel melting temperature of the metallic fuel (~1080°C) will ensure that any flow paths clogged by re-solidified fuel will unblock as the sodium in the blocked pathway re-melts the fuel. Under full flow conditions with the pump pressure slightly pressurizing the sodium, the eutectic will typically breach the cladding before substantial coolant bulk boiling occurs, stopping the transient before the positive sodium void coefficient can cause an additional power excursion. However, under low flow conditions without the pressure head from the pump, the temperature of sodium can increase to the boiling point of 881°C, indicating that some boiling in the hot channel may occur before the eutectic breaches the cladding wall. SAS4A results indicate that in this time period, the axial movement of fuel within the cladding leads to a rapid decrease in reactivity that counteracts the reactivity insertion from sodium boiling. If the molten fuel leaving failed fuel is swept out of the core, the negative reactivity produced by losing fuel from the core will cause the reactor to quickly shut down before fuel vaporization could occur (50).

In a loss of flow event, the coolant will not have the driving force to carry away the molten fuel in streamers. A minor energetic release can occur when, after the molten fuel leaves the cladding due to a driving force from fission gases in the plenum and gases dissolved in the fuel, some of the fuel travels through the core, thus possibly causing prompt criticality. The potential for prompt criticality is the greatest in an initial core loading where no high-burnup pins exist, thus allowing for the initial cladding failures to occur with minimal fission gas pressure to drive the fuel out of the core. SAS4a simulations have determined that, during highly conservative simulations, the resulting thermal energy from this power spike will not exceed 50MJs before enough fuel leaves the core to cause the reactor to shut down and stop additional melting. Additionally, a 300°C margin to fuel vaporization was maintained in all simulations, thereby limiting work energy to vaporized sodium bubbles (51). This energy level is too small to cause damage to the vessel, which would lead to measureable offsite consequences (52). Studies that have examined the amount and distribution of fuel collecting on the bottom of the vessel have shown that re-criticality should be avoided with large margins (50) (51). Further testing of metal fuel's post cladding failure behavior at low flow rates will be required to verify these simulations.

Some proposed metallic fueled reactor designs, such as the S-PRISM, are not designed with an additional in-core ES mitigation system based on the perception of inherent prevention of ESs. By removing ESs from the containment design constraints, the current machinery dome may be able to be replaced with a more flexible and less costly containment design, such as the one proposed for S-PRISM (35). This containment would have to contain potential sodium spills, seismic events, and guard against airplane crashes and other missile impacts. These design goals may be achievable through a minimally re-enforced thick concrete structure, thus allowing for more flexibility in the containment design and implementation, which could save construction costs.

Some reactor designers have proposed the addition of a Vanadium liner between the metal fuel and cladding to prevent eutectic formation at high temperatures. These designers wish to utilize advanced austenitic or ODS cladding to achieve high outlet temperatures and increase thermal efficiency (4). This approach would likely remove the eutectic fuel removal pathway from the metal fuel safety case, although additional testing needs to be performed to determine if the Vanadium liner deteriorates above 900°C where eutectic formation enters the safety case. Even if the liner were to deteriorate quickly at these temperatures, it is probable that the liner would impede the exodus of the fuel from the clad. This could decrease the rate at which negative reactivity is inserted into the reactor, slowing shutdown and increasing the chance of fuel vaporization, and thus energetic releases.

(iv)Mechanisms Preventing Oxide Fuels from experiencing Energetic Scenarios

There is evidence that oxide fuels may also be able to benefit from fuel removal as a way to prevent ESs. SIMMER III is a code package originally created by LANL and further developed at the Forschungszentrum Karlsruhe and the Japan Nuclear Cycle Development

Institute. SIMMER III performs a more mechanistic analysis of fuel motion out of the core during ESs than SAS4a. SIMMER simulations, with supporting experiments, have shown that a significant portion of the molten oxide core (upwards of 50%) can potentially be removed from the core through the control rod guide tubes before fuel vaporization occurs. This process requires the molten oxide fuel to first breach the cladding and then intra-assembly ducts before finally leaving the core. These barriers may delay oxide fuel removal from the core to the extent that there is some energy release but not to the extent predicted by traditional analysis (53) (54) (55).

The potential of ESs in oxide cores has led some proposed SFR designs, such as the JSFR, to consider additional systems to mitigate their consequences. The JSFR has two such additional systems: a core catcher and inter-assembly streaming channels. During a severe accident oxide fuel could slump to the bottom of the vessel and form a critical geometry in that region, leading to fuel vaporization (10). In order to prevent the oxide fuel from experiencing re-criticality, the JSFR incorporates a core catcher that is intended to spread the molten fuel in a coolable subcritical geometry. Core catchers add expense, especially considering the low probability of their use. If ESs resulting in potential re-criticality can be removed from design considerations, the core catcher could be excluded from design.

The JSFR is also considering the inclusion of streaming channels within the fuel assemblies (Figure 22). These assemblies would sacrifice fuel pins in order to provide a space for molten oxide fuel to leave the core during a severe accident. The streaming of the fuel out of the core would shut the reactor down before the oxide started to vaporize and produce significant work energy (40). However, by removing fuel from the streaming assemblies there is either a fuel cycle penalty or penalty of lower power density since additional assemblies are required to compensate for the streaming paths.

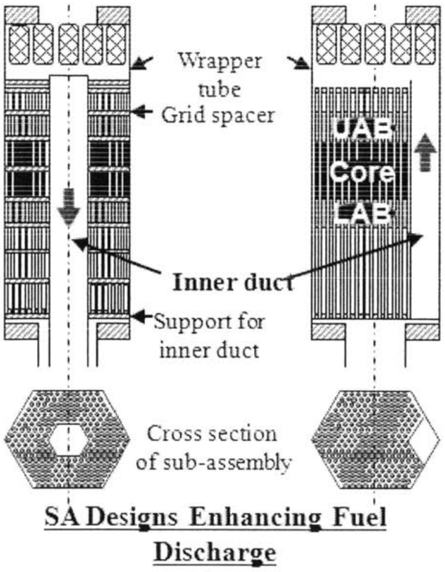

Figure 22– Possible JSFR Streaming Assembly Design (40)

(v) Comparison of Metal and Oxide-Fueled Designs

This section will compare the safety performance of metal and oxide cores for a spectrum of accident scenarios. The consequences of design basis events, postulated accidents to which the single-failure criterion is applied, have essentially the same consequences for the two different types of core. They also have very similar margins to severe accident conditions. Events without severe fuel damage in Table 7 are given a value of 3 (neutral) Beyond Design Basis Events are any events that exceed the design basis conditions. They may or may not lead to severe fuel damage. Similarly, severe fuel damage may or may not lead to an ES.

For historical reasons, SFR accident analyses have focused on a set of Beyond Design Basis Events referred to as unprotected accidents. In this case, unprotected means scenarios that include failure of the reactor protection system. Because of sodium's excellent heat transfer properties and the unpressurized nature of SFR reactor coolant systems, it is difficult to identify scenarios that result in fuel damage, if the reactor protection system works. From a risk standpoint, unprotected sequences are not necessarily risk significant, because of their low probabilities. It is important to also recognize that severe fuel damage can occur for other scenarios in which the reactor protection system functions. For example, the Fermi 1 accident indicates the importance of design features to prevent core damage from flow blockage. Three general categories of unprotected accidents will be discussed:

- Unprotected Transient Overpower (UTOP)
- Unprotected Loss of Flow (ULOF)
- Unprotected Loss of Heat Sink (ULOHS)

There are two typical proposed initiators of an unprotected transient overpower. One cause is a malfunction of the reactor protection system which withdraws the control rods to their stops which may or may not be misaligned to allow for varying degrees of reactivity insertion. These transients favor metal fuel because the slow method of reactivity insertion allows the delayed feedbacks of control rod driveline and core radial expansion to help reduce the peak power experienced during the transient. The other initiator is due to sodium voiding within the core. While this initiator is more difficult to physically justify, it favors oxide fuel's stronger Doppler coefficient and larger margin to fuel melting. For extremely large reactivity insertions which raise oxide fuel past the point of melting, oxide fuel has a difficult time escaping the core to remove reactivity thus posing the potential for ESs (36). Metal fuel's rapid fuel/cladding eutectic formation rate at high temperatures allows it to remove liquid fuel from the core quickly, thus ending the transient (51) (13). If metal fuel is forced to remain in place by a liner or massive flow blockage, metal fuel has the potential to undergo an ES as well (36).

Unprotected loss of flow accidents also come in two different categories: ULOF with or without pump coastdown. Pump coastdown can come from inertia from a mechanical pump or from a flywheel attached to an EM pump and is tailored to sufficiently minimize the rate of flow reduction to allow the reactor to power down via reactivity feedbacks. Due to the large operating temperature of an oxide fuel and the slow thermal time constant to remove the stored energy, oxide cores are typically designed to achieve a longer flow halving time than metal cores. A ULOF without coastdown is the most commonly modeled way for an oxide core to experience an ES. The fuel/cladding eutectic formation typically prevents metal cores from experiencing ES under these circumstances, but under certain assumptions ULOFs without coastdown could potentially result in ES for metal fuel (36) (51) (20) (33).

The last major unprotected accident category is the unprotected loss of heat sink. These accidents could for example involve failure of the condenser pumps, which removes the primary heat sink. The reactor continues to operate at power, which slowly reduces as the system temperature rises. The only heat removal path available to the reactor is the safety grade decay heat removal system. The low operating temperature of metal fuel allows the reactor to shut down and the system to stabilize with large margins to sodium boiling and creep failure of the structural supports. Oxide fuels, with their high operating temperatures, take longer to reduce power causing more energy to be deposited in the primary system. This can result in high system temperatures which can threaten the core structural supports or even result in sodium boiling (20) (33).

When examining inherent reactivity response to beyond design basis accidents, metal fuel emerges as a strong favorite. Because of metal fuel's consistently better accident response, except for extremely large and quick reactivity insertions where the fuel is confined by a cladding with a barrier that prevents eutectic formation, the severe fuel damage event without potential for ES category is assigned the value of 1. The severe fuel damage event with the potential for ES category is assigned the value of 2 because metal fuel still outperforms oxide fuel in all but the most extreme cases.

III.3 Technical Evaluation

The NUREG-1860 safety case for a generic SFR core is made in Section IV and extended to higher temperatures for metal and oxide fuel in the Thermodynamic Efficiency case study. Thus, the basic safety case for metal and oxide fuels is described in Chapter V and (14); consequently the overall safety case will not be described here. In lieu of a full safety case, the following topics will be discussed:

1. Relative accident response for bounding accidents
    a. UTOP comparison for metal and oxide fuel
    b. ULOF comparison for metal and oxide fuel
2. Steady state liquidus limit for U-19Pu-10Zr for an unspecified high-temperature cladding at 11at% burnup.

III.3.A Relative Accident Response for Bounding Licensing Basis Events

This section will compare the relative performance of metal and oxide fuel for the UTOP and ULOF sequences. To simplify the comparison of fuel types, only the 510°C and 554°C steady state core average outlet temperatures are examined for the metal and oxide fuel comparison. These temperatures were chosen since they represent the current and maximum potential core outlet temperatures of metallic fueled SFRs (see Chapter IV for more details). In order to determine the probability of cladding failure and/or sodium boiling, the importance sampling method described in Section II.4 was used to create hundreds of RELAP5-3D simulations of metal fuel and oxide fuel performance for both transients.

(i) Evaluation of Transient Uncertainties for Metal and Oxide Fuel

In order to estimate the probability of failure for Transient Overpower (TOP) and Loss of Flow (LOF) LBEs, many simulations have been conducted with uncertain parameters sampled from underlying epistemic distributions. For both oxide and metal cores experiencing TOP and LOF events, ANL studied the epistemic reactivity coefficient uncertainties for SFR cores. They report the epistemic uncertainties as normal distributions with the following standard deviations (25):

- Doppler ($\sigma_{Dop} = 20\% \ \alpha_{Dop}$)
- Na density ($\sigma_{Na} = 20\% \ \alpha_{Na}$)
- Axial expansion ($\sigma_{AE} = 30\% \ \alpha_{AE}$)
- Core radial expansion ($\sigma_{CRE} = 20\% \ \alpha_{CRE}$)
- Control rod drive line expansion ($\sigma_{CRDL} = 20\% \ \alpha_{CRDL}$)

Due to a combination of lack of knowledge and difficulty of simulation, many important uncertainties are not included in the following analysis. Because these uncertainties are not modeled, conservative values are assumed in an attempt to provide a conservative estimate of the conditional failure probabilities. Some of the excluded uncertainties that should be included in future analysis include:

- Reactivity insertion rate
- Thermal conductivity of fuel and clad
- Creep and eutectic formation rates

- Power peaking factors

(ii) Statistical Methods Used to Predict Release Frequencies for Metal and Oxide Fuel

This section summarizes the information found in II.4 and II.5 and is only intended to help the reader understand how the failure probabilities are calculated in Sections *iii* and *iv*.

Pool type sodium reactors are designed to survive most unprotected transients without cladding rupture. To avoid running a prohibitive number of RELAP5 simulations, the sampling distributions should be biased in a way which forces sampling of larger, and thus more limiting, reactivity coefficients while providing an unbiased estimate of the failure probabilities. By biasing the sampling procedure through importance sampling, each simulation is no longer assigned the same weight when calculating failure probabilities.

The mean and variance of the failure probability calculated through Importance Sampling (IS) can be found through Eq. III.1 and Eq.III.2,

$$E[\hat{p}] = \frac{1}{N}\left[\sum_{i=1}^{N}\left\{w_i(\rho)\left(\prod_{j=1}^{M} w_i\left(\alpha_{j_i}\right)\right)F\left(\left\{\rho_i, \alpha_{dop_i}, \dots, \alpha_{CRE_i}\right\}\right)\right\}\right] \qquad \text{III.1}$$

$$\begin{aligned} &Var(E[\hat{p}]) \\ &= \frac{N}{N-1}\left[\frac{1}{N}\sum_{i=1}^{N}\left\{w_i(\rho)\left(\prod_{j=1}^{M} w_i\left(\alpha_{j_i}\right)\right)F\left(\left\{\rho_i, \alpha_{dop_i}, \dots, \alpha_{CRE_i}\right\}\right)\right\}^2\right. \\ &\left. - E[\hat{p}]^2\right] \end{aligned} \qquad \text{III.2}$$

where $w_i\left(\alpha_{j_i}\right)$ is the weight of the j^{th} importance reactivity coefficient and M is the total number of importance sampled reactivity coefficients (23).

Because the TNF has requirements on both the mean and the 95th percentile of the radiation release, and thus cladding failure, distributions around the cladding failure probabilities are required. The likelihood function for cladding failure is binomial: either the cladding fails or remains intact. The prior and posterior distributions for cladding failure take the form of the beta distribution. These distributions are expressed by Eq. III.3 and Eq. III.4, respectively (22).

$$L(x|N,p) = \binom{N}{x} p^x (1-p)^{N-x} \qquad \text{III.3}$$

$$\pi(p|q,r) = \frac{\Gamma(q+r)}{\Gamma(r)\Gamma(p)} p^{q-1}(1-p)^{r-1} \qquad \text{III.4}$$

$L(x|N,p)$ is the likelihood of x failures in N trials, p is the probability of failure, $\Gamma(.)$ is the gamma function, and q and r are the shape parameters of the beta distribution.

This method has been described in more detail in the general methodology section of this thesis, Section II.5.

(iii) UTOP

This section will outline the relative performance of oxide and metal fuel to the bounding licensing basis UTOP event, as described in the thermodynamic efficiency case study (Chapter IV.2). In this account, the time dependant progression of system temperature for both fuels will be examined, focusing on steady state temperatures reached at the end of the transient. It should be noted that the following analysis was conducted using the reactivity behavior of metal and oxide TRU fuel with the same uncertainties and statistical sampling described in the thermodynamic efficiency case study.

In order to model the UTOP, the following assumptions were made. First, the reactor power and control system malfunctions and corrects for a false low power indication by raising the control rods to their stops. These stops are assumed to be previously misaligned by the reactor operator, allowing reactivity insertion to between \$0.7 and \$0.9 instead of the nominal \$0.3 limit. The prompt reactivity feedbacks, i.e., Doppler (-), sodium density (+), and the delayed reactivity feedbacks, i.e., control rod driveline expansion (-) and core radial expansion (-), all respond to counteract the initial reactivity insertion. This initial response is labeled as Section A in Figure 24 through Figure 29. Next, the inlet temperature starts to rise, thus increasing the temperature of the entire core, including the coolant, fuel, control rod driveline and fuel assembly spacers. Because the overall temperature feedback of both the oxide and the metal cores are negative, negative reactivity continues to build up thus reducing thermal power levels. This inlet temperature rise is exacerbated because NUREG-1860 does not allow credit to be taken for non-safety grade systems during accident analysis. Thus, the primary heat sink was disabled by tripping the condenser pump at the start of the transient; leaving only decay heat removal operational. This power decrease is labeled Section B. The final stage of the accident occurs when the cold pool heats up to 535°C, or 579°C for the hotter core, which trips EM pumps to prevent overheating. The pump trip effectively turns what is already a UTOP-ULOHS into a ULOF as well. The progression of this transient is illustrated in Figure 23. As heat removal from the core transitions from forced convection to natural circulation, the reactor decreases power dramatically leading to one of the following end states:

- The reactor power decreases to decay heat levels and the decay heat removal system successfully provides long term cooling.
- The reactor power decreases to decay heat levels and the decay heat removal system successfully provides long term cooling, but not before thermal creep causes cladding failure.
- The reactor power does not decrease fast enough, allowing peak sodium temperatures to reach their full-flow boiling point, which is approximately 925°C due to the pressure head of the pumps. From the onset of hot channel sodium boiling it can be assumed that minor core damage occurs, but RELAP5-3D does not have the capability to accurately model the accident progression beyond this point.
- The reactor power does not decrease fast enough; allowing channel averaged sodium temperatures to reach their boiling point. From the onset of boiling in the core outlet it can be assumed that major core damage occurs, but RELAP5-3D does not have the capability to accurately model the accident progression beyond this point.

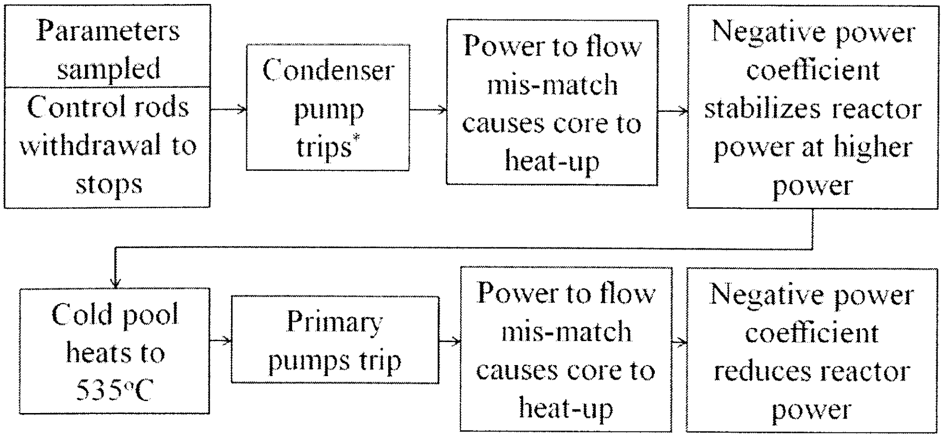

*Non-safety grade components cannot be taken credit for in safety analysis

Figure 23 - Block diagram of UTOP LBE Progression.

Section A in Figure 24 through Figure 29 covers the initial phase of the transient, which is the response to the reactivity insertion. The reactivity insertion rate is dictated by the maximum speed of the control rod driveline motors, limiting the reactivity insertion rate to \$0.16/s. At this speed, energy is able to transfer into the coolant quickly enough that the metal core's stronger control rod driveline and core radial expansion feedbacks are able to limit peak power and reactivity insertion to below that of the oxide core. Had the insertion rate been much quicker, the oxide core's slightly stronger Doppler coefficient$\left(\rho_{Doppler}^{Oxide} = -0.12\frac{c}{s} > \rho_{Doppler}^{Metal} = -0.10\frac{c}{s}\right)$, would have caused the immediate power increase to be smaller than the metal core, although the stabilized power level for the metal fuel would have been lower than for the oxide fuel. In summary, the immediate impact of the initial transient is that the fuel and coolant temperatures increase more dramatically for the oxide fuel than for the metal fuel in this range.

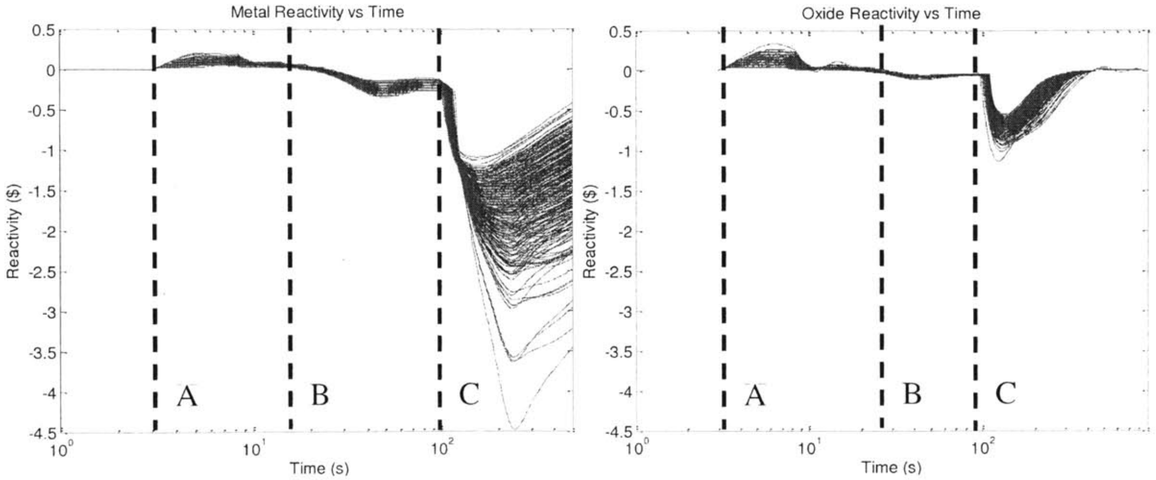

Figure 24-Metal (left) and Oxide (right) Reactivity Response to LBE UTOP Divided into Three Sections: A) Response to initial power increase, B) Feedback from inlet temperature rise, C) Response to pump trip

Section B in Figure 24 through Figure 27 covers the pool heat-up phase of the transient, which is the response to the loss of primary heat removal. Due to the oxide core's higher post UTOP power level, inlet temperature effects start to dominate the oxide core's response to the transient more dramatically than for the metal core. Due to the relatively low fuel temperature in metal fuel, the negative feedback effects from additional core expansion and driveline insertion are only counteracted by a weak Doppler swing as the fuel cools approximately 200°C due to decreased thermal power. In contrast, oxide fuel cools 400-600°C during this period, adding 2 to 3 times more positive reactivity than metal fuel, which acts to counteract the negative reactivity from core and control rod expansions as the inlet temperature continues to rise.

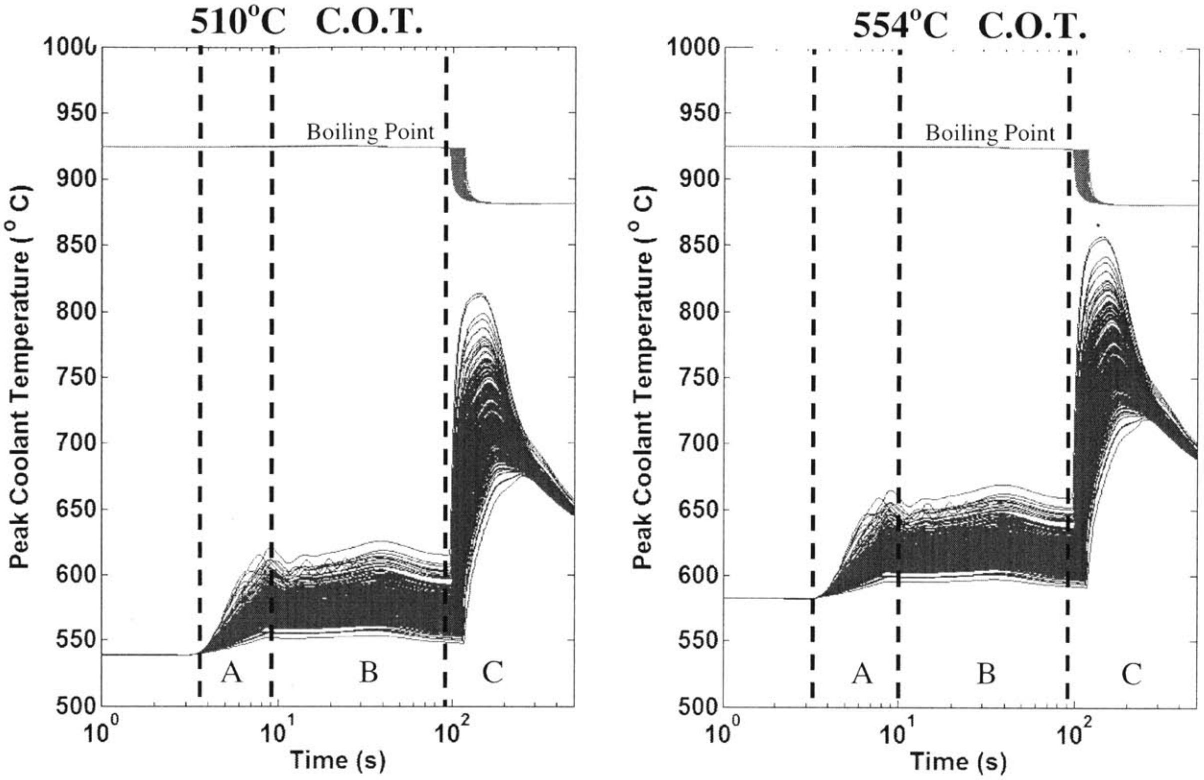

Figure 25 - Metal Hot Channel Temperature Response to UTOP
Divided into Three Sections: A) Response to initial power increase, B) Feedback from inlet temperature rise, C) Response to pump trip. C.O.T. refers to the initial Core Outlet Temperature.

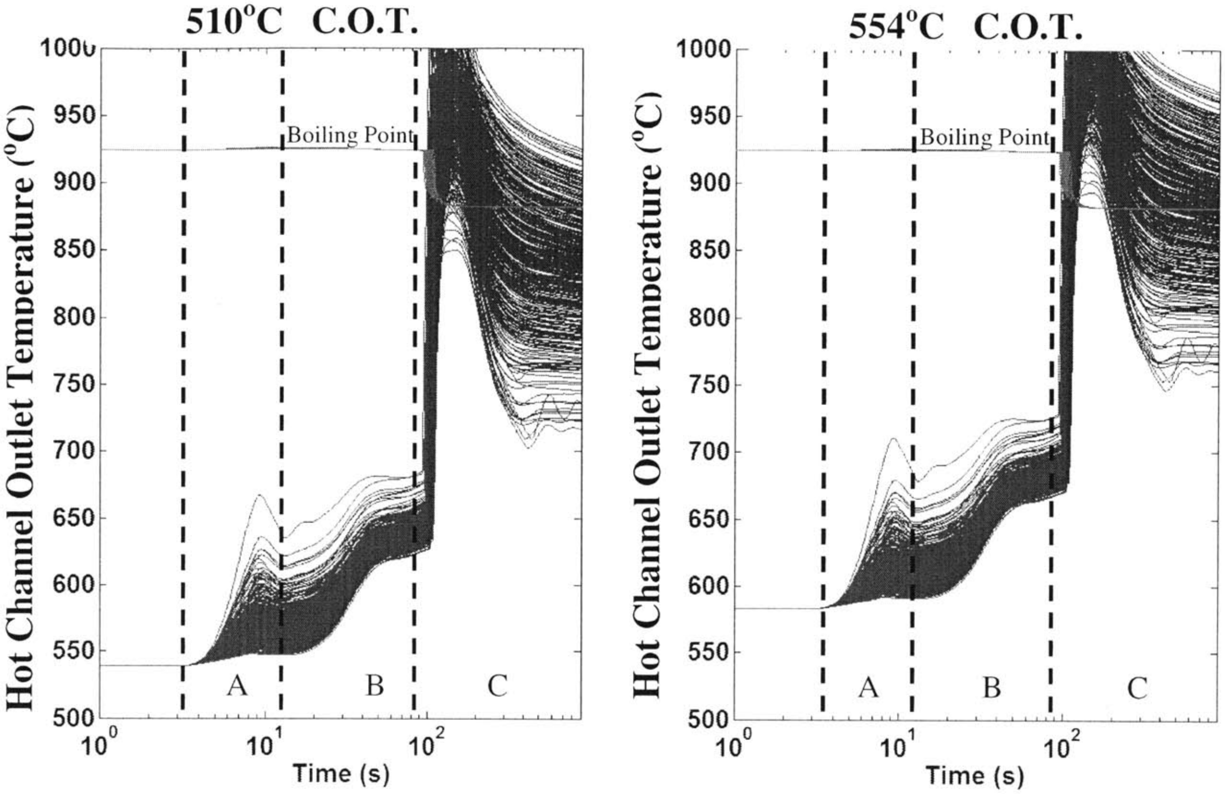

Figure 26 - Oxide Hot Channel Coolant Temperature Response to UTOP
Divided into Three Sections: A) Response to initial power increase, B) Feedback from inlet temperature rise, C) Response to pump trip. C.O.T. refers to the initial Core Outlet Temperature.

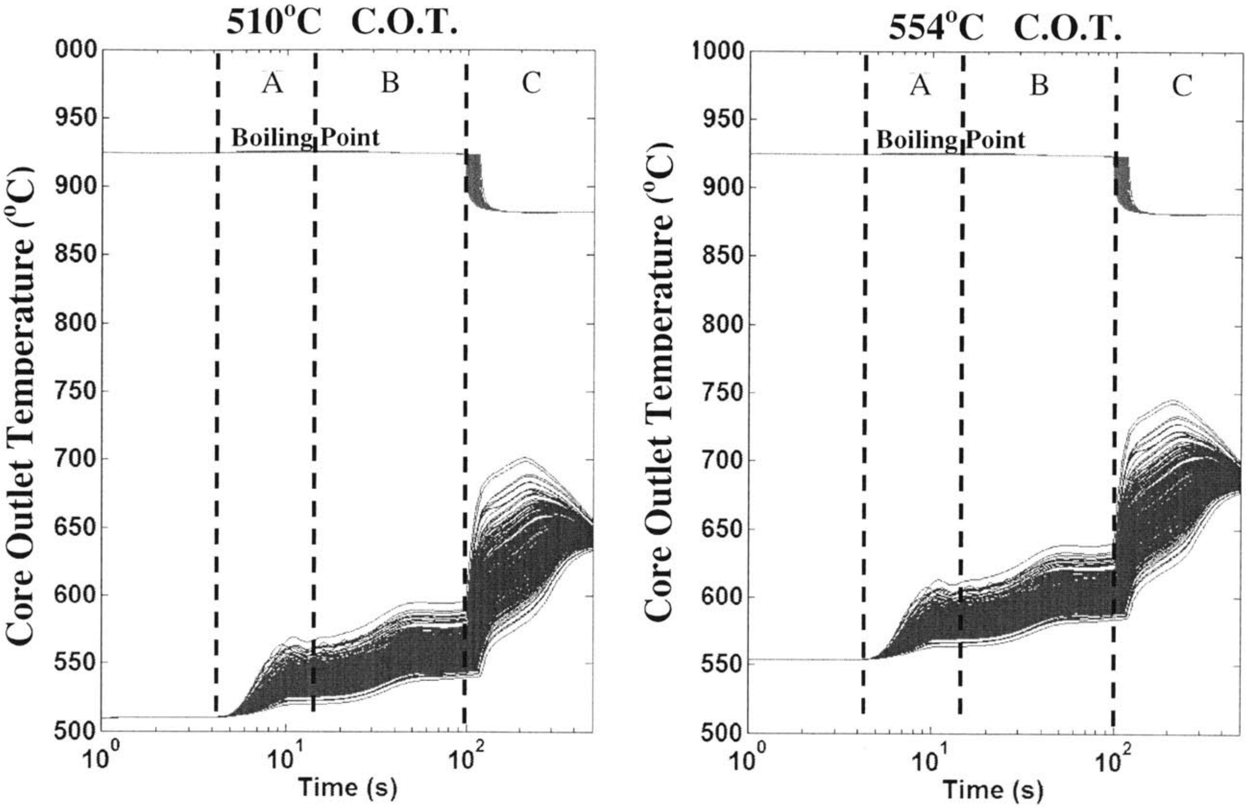

Figure 27 - Metal Core Outlet Temperature Response to UTOP
Divided into Three Sections: A) Response to initial power increase, B) Feedback from inlet temperature rise, C) Response to pump trip. C.O.T. refers to the initial Core Outlet Temperature.

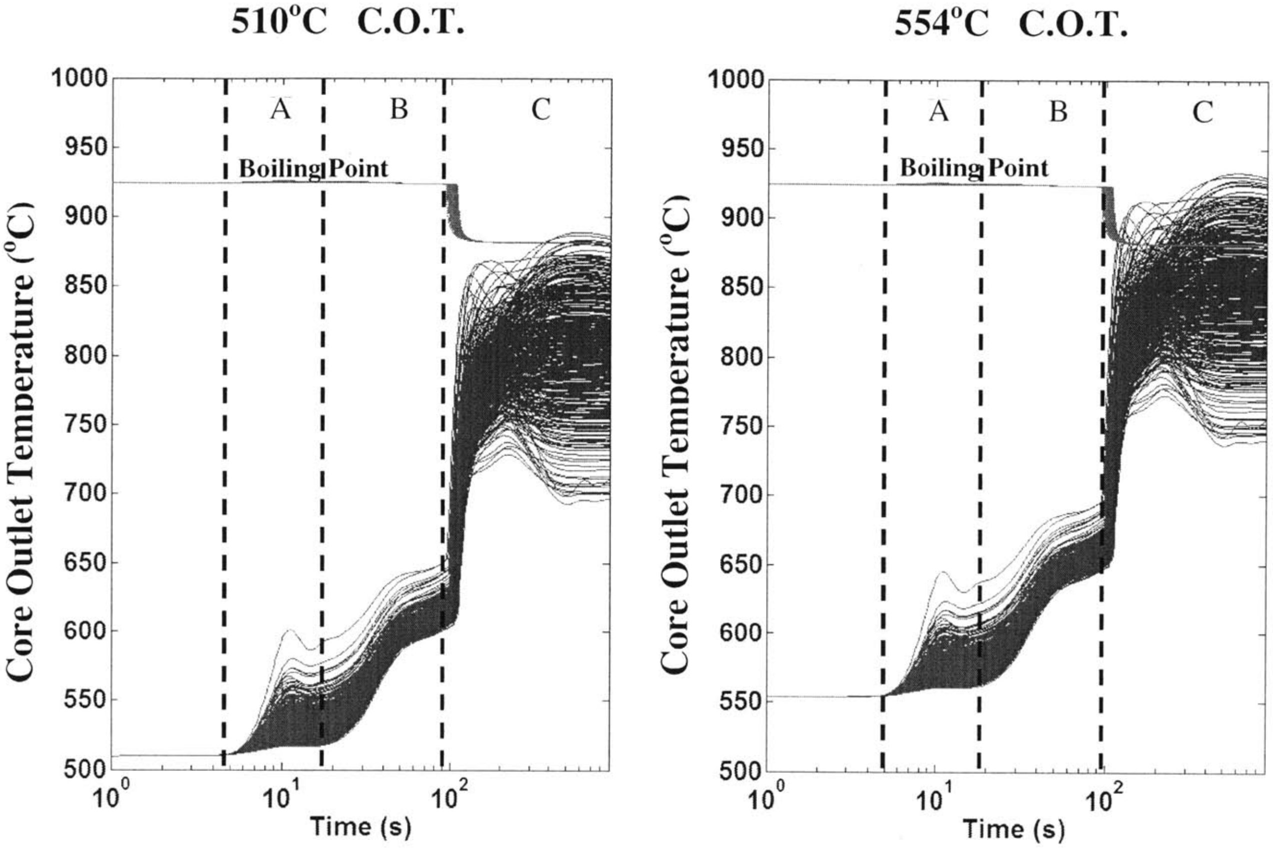

Figure 28-Oxide Core Outlet Temperature Response to UTOP Divided into Three Sections: A) Response to initial power increase, B) Feedback from inlet temperature rise, C) Response to pump trip. C.O.T. refers to the initial Core Outlet Temperature.

Section C in Figure 24 through Figure 27 covers the transition to natural circulation phase of the transient, which is the response to the loss of primary coolant pumps. This phase is initiated when the EM pumps reach their trip point and turn off, providing only coastdown flow and natural circulation to cool the core. The thermal power then drops until the coolant and the fuel are near thermal equilibrium. The oxide fuel has to cool an additional ~700°C to near equilibrium with the coolant temperature. Unfortunately, the process of reaching a fuel/coolant equilibrium temperature results in raising the coolant temperature past the boiling point in the hot channel in the majority of simulations and past the boiling point in the core outlet in a small fraction of simulations. As RELAP5 does not model sodium boiling, it is possible that the positive reactivity from hot channel sodium voiding would have pushed some of the non-core averaged boiling simulations to experience core averaged boiling. For metal fuel, the fuel and coolant temperatures stabilize near 650-700°C with large margins to hot channel or core sodium boiling. For oxide fuel, fuel temperatures start to level off between 800 and 1000°C and the coolant temperatures level off between 750 and 950°C. Thus, with oxide fuel there is little to no margin to hot channel or core-wide boiling. This temperature difference is caused because some of the oxide simulations terminate before the reactor power transitions completely to decay heat. The residual power is low and able to be removed by the DRACS, but prevents the fuel and coolant temperatures from equalizing.

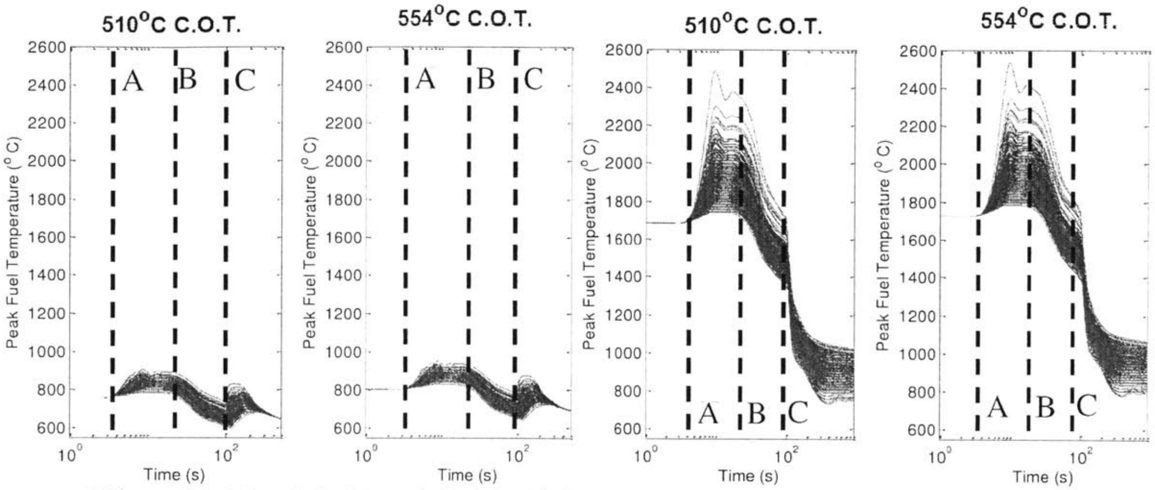

Figure 29-Metal (left) and Oxide (right) Peak Fuel Temperature Response to UTOP Divided into Three Sections: A) Response to initial power increase, B) Feedback from inlet temperature rise, C) Response to pump trip

Metal fuel's response to the UTOP transient is benign, with cladding failure and sodium boiling avoided in all simulations for 510°C and 554°C. Thus, a failure probability cannot be calculated for metal fuel at these temperatures. Because oxide fuel simulations resulted in cladding failure and sodium boiling, the mean and 95th percentiles can be directly calculated. These values are reported in Table 11.

Table 11 – Oxide UTOP Failure Probabilities

Core Outlet Temperature	Failure Path	Mean Pr(Failure|UTOP)	95th Percentile Pr(Failure|UTOP)
510°C	Cladding Rupture	0.995	0.999
510°C	Hot Channel Boiling	0.991	0.997
510°C	Core Average Boiling	3.3x10-5	2.9x10-5
554°C	Cladding Rupture	< 1.0	< 1.0
554°C	Hot Channel Boiling	< 1.0	< 1.0
554°C	Core Average Boiling	0.089	0.11

While the thermodynamic efficiency case study, Chapter IV, shows that both metal and oxide cores meet the regulatory structure of NUREG-1860 when the UTOP conditional probability of failure is applied to bound the TOP accident response, the metal core does so in a much more benign fashion than the oxide core. The oxide core is only able to satisfy the Frequency Consequence Curve because of the benign offsite release of the full core boiling end state and the low initiating frequency of the TOP event. While unprotected transients have initiating frequencies lower than 10^{-7}/yr, and thus would not be a traditional LBE, these transients may be selected as a deterministic LBE by the NRC. Under these circumstances, additional scrutiny would be given to the oxide fuel's response considering the high likelihood of sodium boiling.

(iv) ULOF (USBO)

This section will outline the relative performance of oxide and metal fuel in the bounding licensing basis ULOF event, as described in the thermodynamic efficiency case study (Chapter IV.2). In this account, the time dependent progression of both fuels will be examined, focusing on steady state temperatures reached at the end of the transient. It should be noted that the following analysis was conducted using the reactivity behavior of metal and oxide TRU fuel with the same uncertainties and statistical sampling described in the thermodynamic efficiency case study.

In order to model the ULOF, the following assumptions were made. First, all four primary reactor coolant pumps trip, coasting down from forced to natural circulation using the pump's internal inertia. It is assumed that the reactor protection system fails, preventing the control rods from inserting into the reactor, which would quickly reduce reactor power. Instead, the reactor begins to decrease thermal power as the prompt reactivity feedbacks, i.e., Doppler, sodium density, and the delayed reactivity feedbacks, i.e., Control Rod Driveline Expansion and Core Radial Expansion., all respond to counteract the heating of the core. Next, the inlet temperature starts to rise, adding additional negative reactivity and reducing thermal output. This temperature rise is exacerbated because NUREG-1860 does not allow credit to be taken for non-safety grade systems during accident analysis. Thus, the primary heat sink was disabled by tripping the condenser pump at the start of the transient; leaving only decay heat removal operational. At this point, the ULOF is identical to a unprotected station blackout (USBO). This transient is described in pictorially in Figure 23. As heat removal from the core transitions from forced convection to natural circulation, the reactor decreases power dramatically leading to one of the following end states:

- The reactor power decreases to decay heat levels and the decay heat removal system successfully provides long term cooling.
- The reactor power decreases to decay heat levels and the decay heat removal system successfully provides long term cooling, but not before thermal creep causes cladding failure.
- The reactor power does not decrease fast enough; allowing peak sodium temperatures to reach their full flow boiling point, which is elevated due to the pump pressure head. From the onset of boiling in the hot channel it can be assumed that minor core damage occurs, but RELAP5-3D does not have the capability to accurately model the accident progression beyond this point.
- The reactor power does not decrease fast enough; allowing bulk sodium temperatures to reach their boiling point. From the onset of boiling in the core outlet it can be assumed that major core damage occurs, but RELAP5-3D does not have the capability to accurately model the accident progression beyond this point.

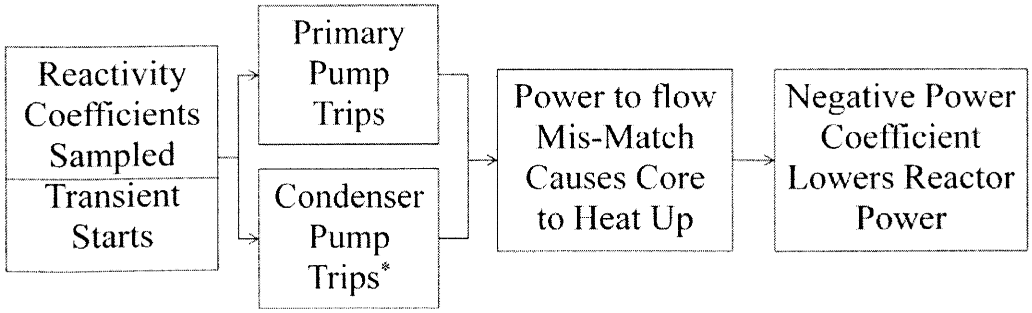

*Non-safety grade components cannot be taken credit for in safety analysis
Figure 30- Block diagram of USBO LBE Progression.

Figure 31 through Figure 34 are pertinent time dependent parameter plots for metal and oxide fuel performance during the USBO. From Figure 31 and Figure 32, it can be seen that metal fuel has a stronger inherent negative reactivity effect during the course of the transient. This can be attributed to the relatively small fuel temperature swing experience by metal fuel, Figure 33, when compared to oxide fuel, Figure 34. Oxide fuel has a stronger negative Doppler coefficient than metal fuel, thus a large amount of positive reactivity is inserted into the core as the fuel cools. While the total reactivity in the oxide core remains negative, the oxide core takes longer from fission power levels to transition to decay heat power levels than the metal core, yielding universally hotter system temperatures. These hotter temperatures can be seen from the peak and bulk coolant temperature plots in Figure 35 through Figure 38.

Metal fuel experiences coolant boiling in the hot channel in only two simulations at 554°C, whereas over a quarter of the oxide fuel simulations experience coolant boiling in the hot channel at 554°C. It should be noted that the core outlet temperatures for the oxide fuel simulations are still increasing with time at the end of the simulations. While it may be tempting to continue these simulations over a longer time interval, this would pose a fruitless endeavor. From Figure 36, it can be seen that the peak coolant temperatures have stabilized by 120-150 seconds into the transient. The bulk coolant temperatures are unlikely to increase past the peak coolant temperatures for a given simulation, and the results at this point are already non-conservative as RELAP5-3D does not handle sodium boiling correctly. Thus, even though some of the peak coolant temperatures have already passed the boiling point in this RELAP simulation, no additional positive reactivity is inserted due to sodium voiding. Attempting to extend the simulation thus turns into an exercise in interpreting false data. The failure probabilities for metal and oxide fuel for the USBO accident can be found in Table 12.

Table 12 – Estimated Failure Probabilities for Metal and Oxide Fuel during a USBO

Core Outlet	Fuel Type	Boiling Location	Mean Pr(Boiling I USBO)	95th Percentile Pr(Boiling I USBO)
510°C	Metallic	Hot Channel	$< 1.8\text{x}10^{-4**}$	N/A
554°C	Metallic	Hot Channel	$1.8\text{x}10^{-4**}$	N/A
510°C	Oxide	Hot Channel	$6.2\text{x}10^{-5}$	$1.7\text{x}10^{-4}$
554°C	Oxide	Hot Channel	0.046	0.067
510°C	Oxide	Core Outlet	$<3.7\text{x}10^{-4}$	<0.002
554°C	Oxide	Core Outlet	$3.7\text{x}10^{-4}$	0.002

* Refers to sum of the weights of simulations resulting in Sodium Boiling

** This failure probability has not converged. Actual failure probability is likely higher than this value

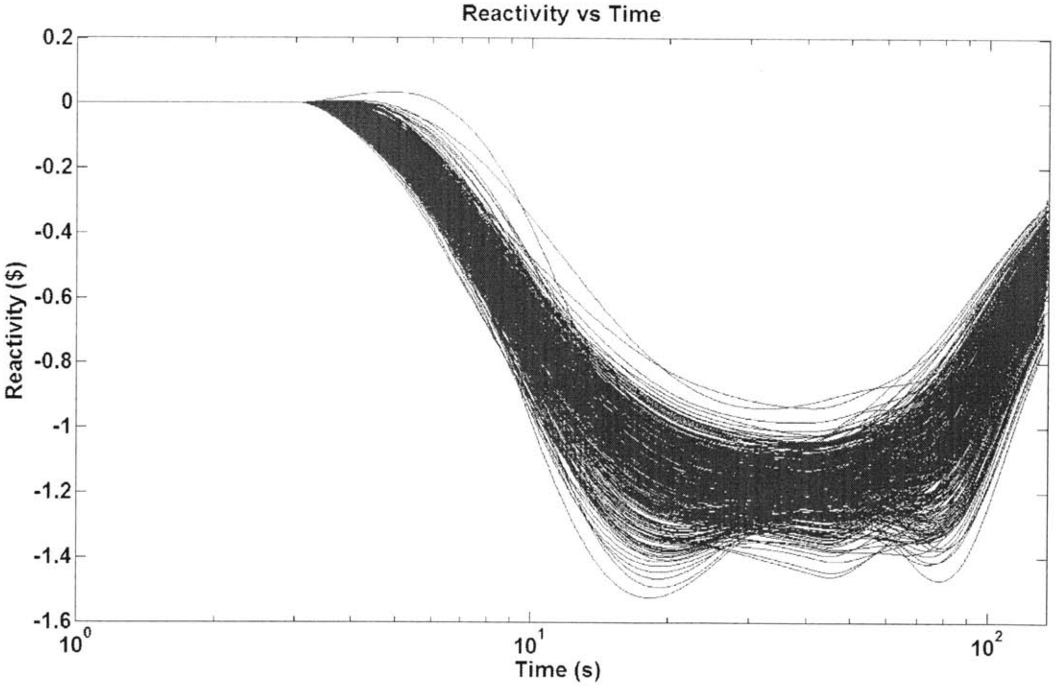

Figure 31 – USBO Time Dependent Reactivity for Metallic Fuel

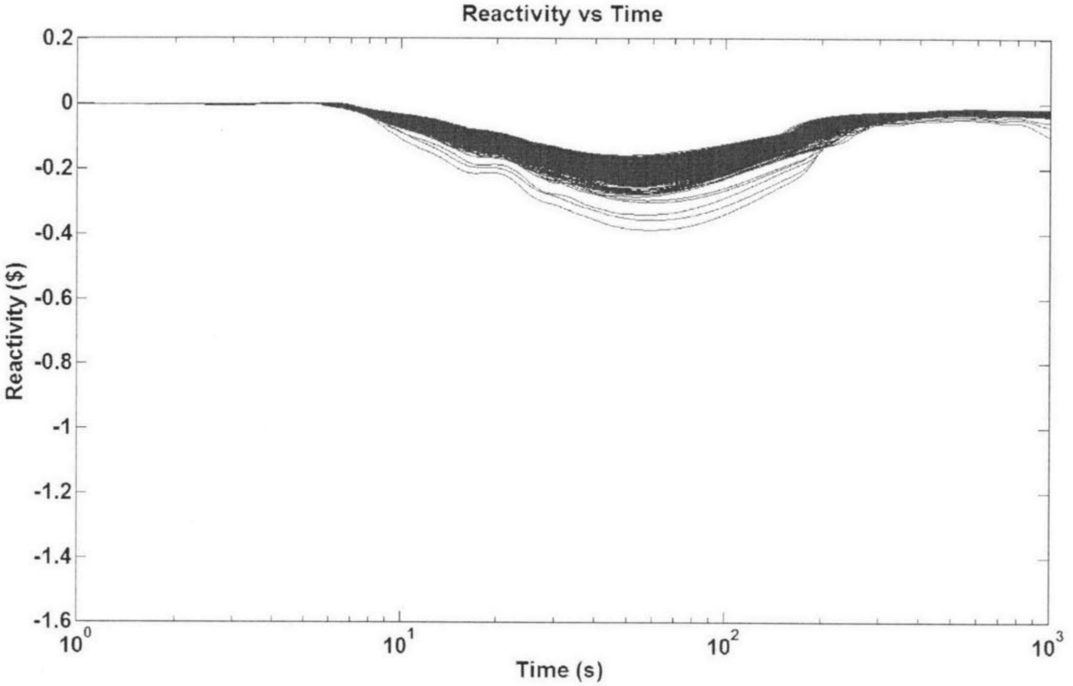

Figure 32 – USBO Time Dependent Reactivity for Oxide Fuel

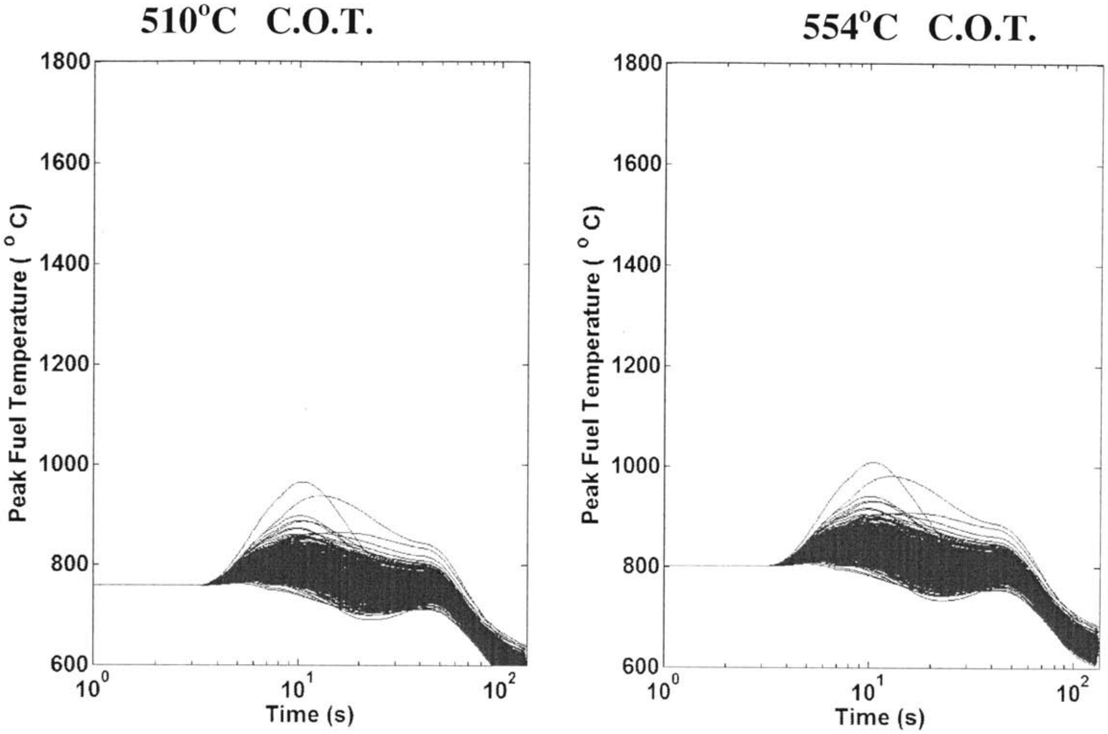
510°C C.O.T.

554°C C.O.T.

Figure 33 – USBO Peak Fuel Temperature for Metal Fuel

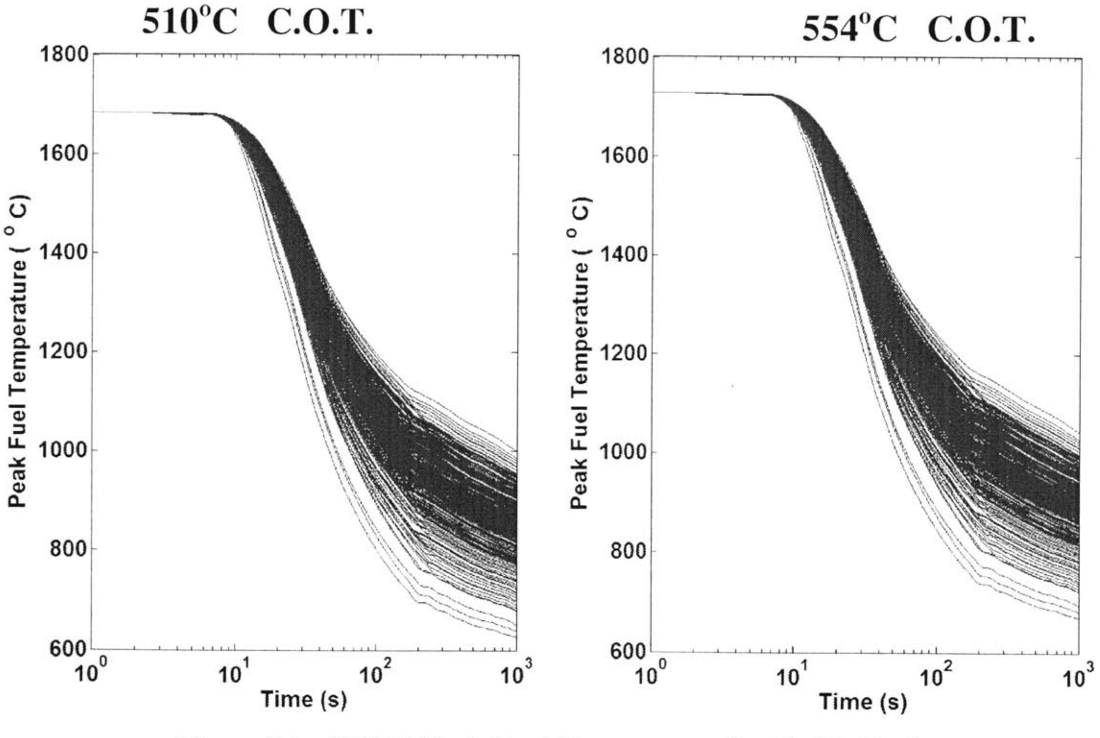
510°C C.O.T.

554°C C.O.T.

Figure 34 – USBO Peak Fuel Temperature for Oxide Fuel

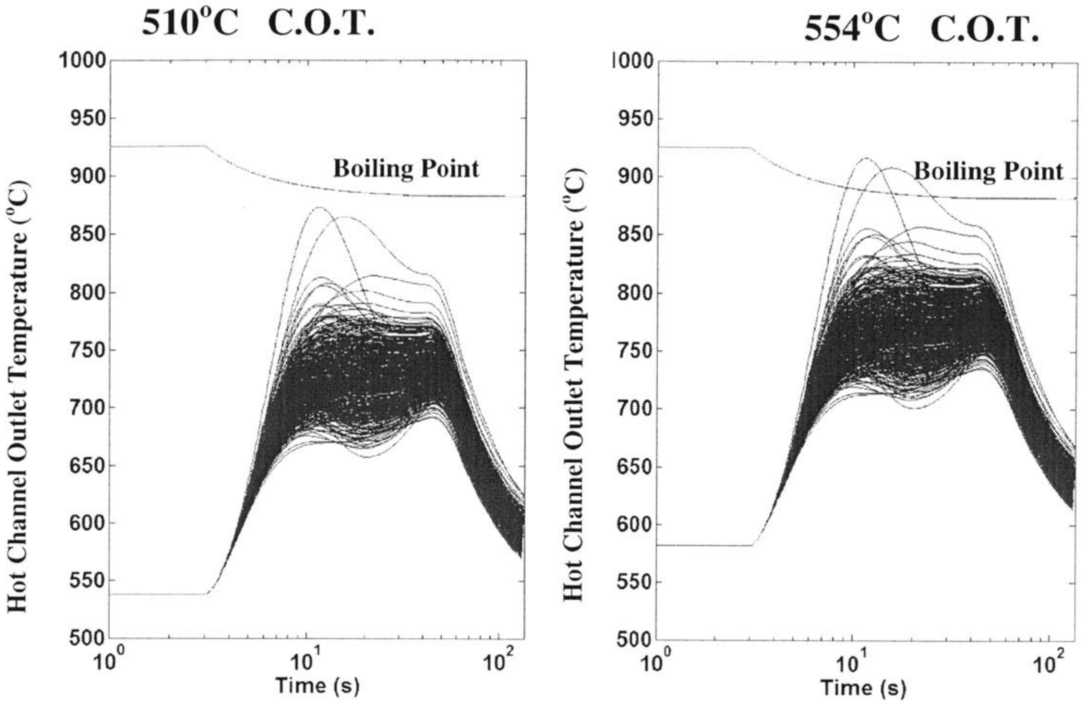

Figure 35 – USBO Hot Channel Outlet Temperature for Metal Fuel

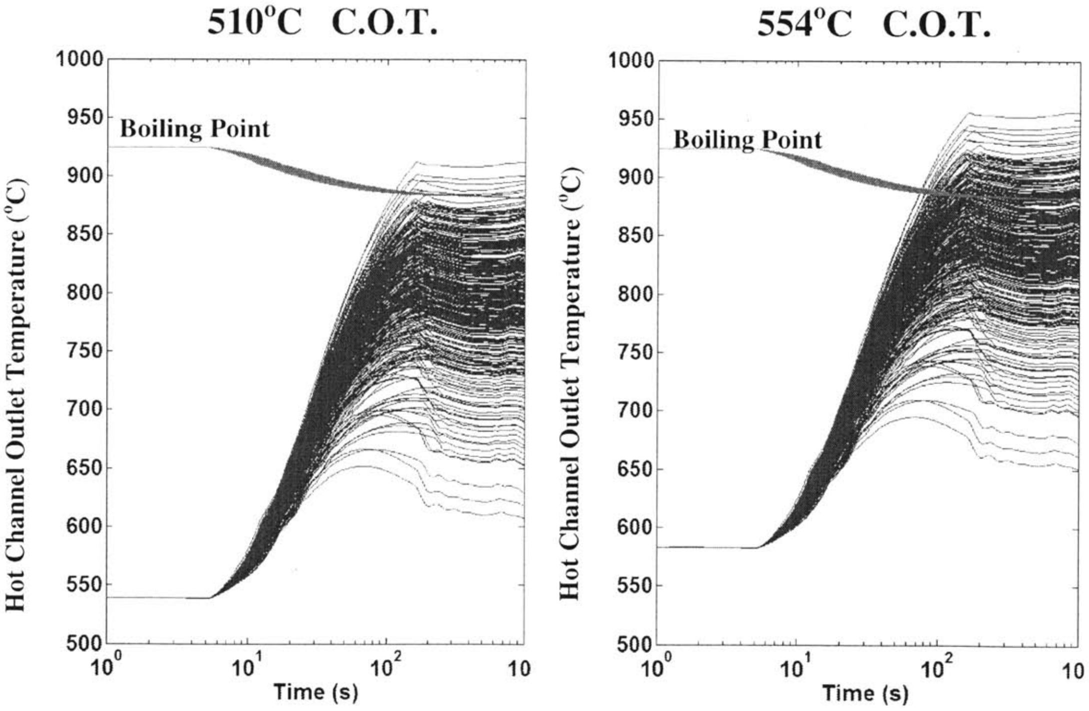

Figure 36 - USBO Hot Channel Outlet Temperature for for Oxide Fuel

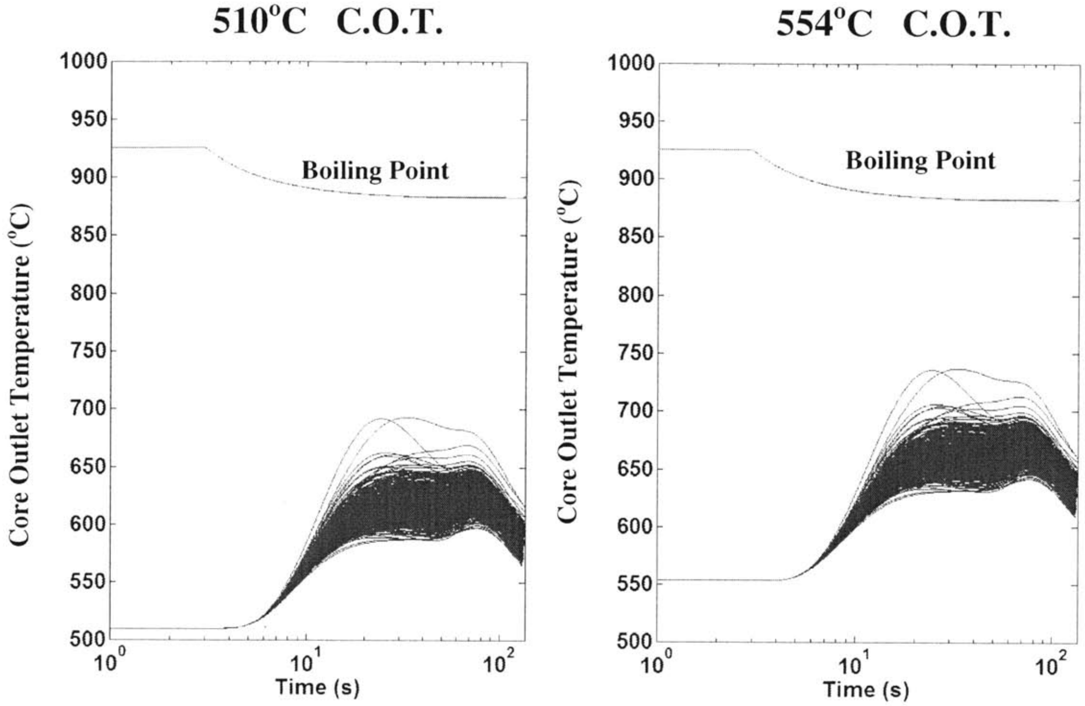
510°C C.O.T.

554°C C.O.T.

Figure 37 – USBO Core Outlet Temperature for Metal Fuel compared

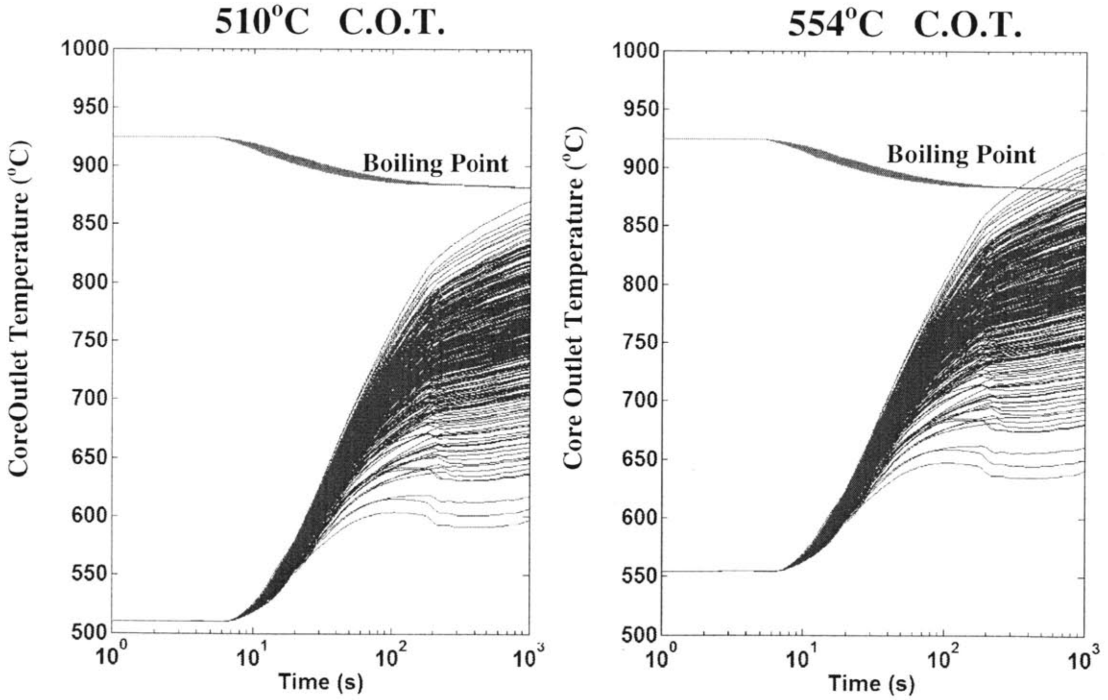
510°C C.O.T.

554°C C.O.T.

Figure 38 – USBO Core Outlet Coolant Temperature for Oxide Fuel

While the thermodynamic efficiency case study, Chapter IV, shows that both metal and oxide cores meet the regulatory structure of NUREG-1860 when the USBO conditional probability of failure is applied to bound the LOF accident response, the metal core does so in a much more benign fashion than the oxide core. The oxide core is only able to satisfy the Frequency Consequence Curve because of the benign offsite release of the full core boiling end state. While unprotected transients have initiating frequencies lower than 10-7/yr, and thus would not be a traditional LBE, these transients may be selected as a deterministic LBE by the NRC. Under these circumstances, additional scrutiny would be given to the oxide fuel's response considering the high likelihood of sodium boiling.

III.3.B Determination of Metal Fuel Liquidus Temperature Limitations at 11at% Burnup

Due to the relatively low liquidus temperature found in high burnup U-19Pu-10Zr fuel with HT9 clad, it has been suggested that the peak cladding temperature limit for this fuel is 650°C (32) (34). This conservative limit was applied due to the results of Cohen's analysis of 11.1 at% burnup metallic fuel, the results of which can be seen in Figure 20. EBR-II, due in part to a short core, has a relatively flat flux profile and most irradiations conducted were designed with linear powers that bound the outer envelope of the IFR design space. Typical SFRs have much lower linear powers, almost by a factor of 2, and thus liquidus limits found at 15kW/ft may not apply to reactor designs with a peak linear power of 8.5kW/ft. EBR-II tests plotted in Figure V.3.7 hint at the potential for a higher liquidus temperature for linear powers below 11kW/ft and the potential for a correlation between linear power and liquidus temperature was supported by the IFR-1 test assembly with D9 cladding U-19Pu-10Zr. The following analysis determines whether liquidus temperature would prevent HT9 cladding U-19Pu-10Zr from reaching ODS creep temperature limits of 700°C. This assumes that ODS steel will not form a lower liquidus temperature with metal fuel than HT9 clad, an assumption that cannot be verified without ODS cladding metal fuel testing.

Figure 39 shows the nominal and axial temperature profiles for the hot channel of an 85cm tall 0.7 conversion ratio core. The hot channel was designed with the nominal linear power profile in Figure 39, a nominal hot channel temperature rise of 185°C, and the inlet temperature is set to allow the 2-σ **peak cladding temperature to be** 700°C. Hot channel factors are applied in the same manner as in the thermodynamic efficiency case study.

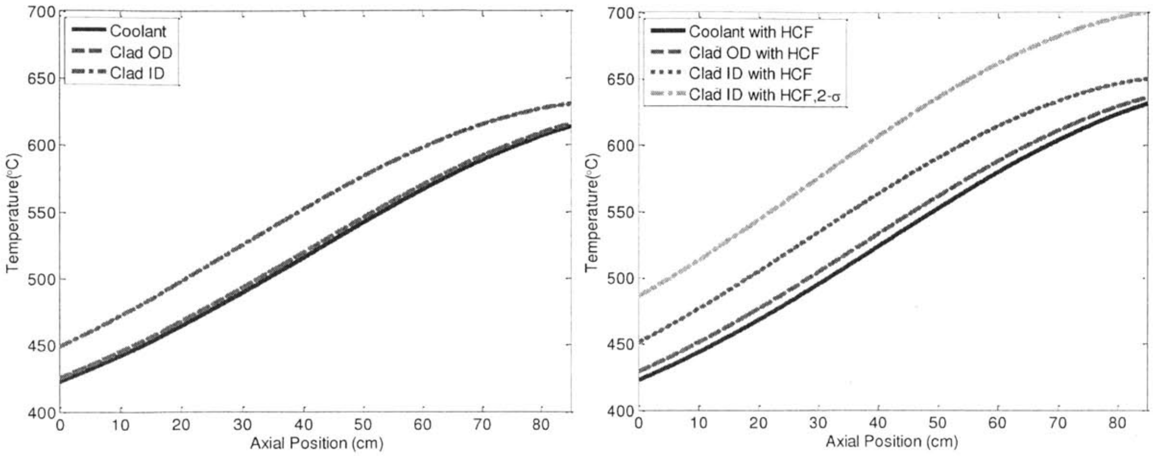

Figure 39- Axial Temperature Profiles for a Representative Metallic Core. Nominal values are shown on the left and hot channel factors values are shown on the right.

The peak axial power, 8.8kW/ft, is less than the EBR-II data shown in Figure 20. Thus, applying the EBR-II data directly would imply a liquidus temperature limit of 700°C throughout the core. Because of the lack of data in Figure 20, and in order to see the effect of axially varying liquidus temperature on potential peak cladding temperatures, a conservative 30% axial overpower value was used to determine the liquidus temperature, as can be seen in Figure 40. As can be seen, the margin to liquidus temperature decreases in the peak axial power regions, but the margin does not decrease to zero until the top of the core. If 650°C was used as a constant liquidus temperature for this core, the top 35% of the cladding would be experiencing eutectic erosion of the clad, as can be seen in Figure 41.

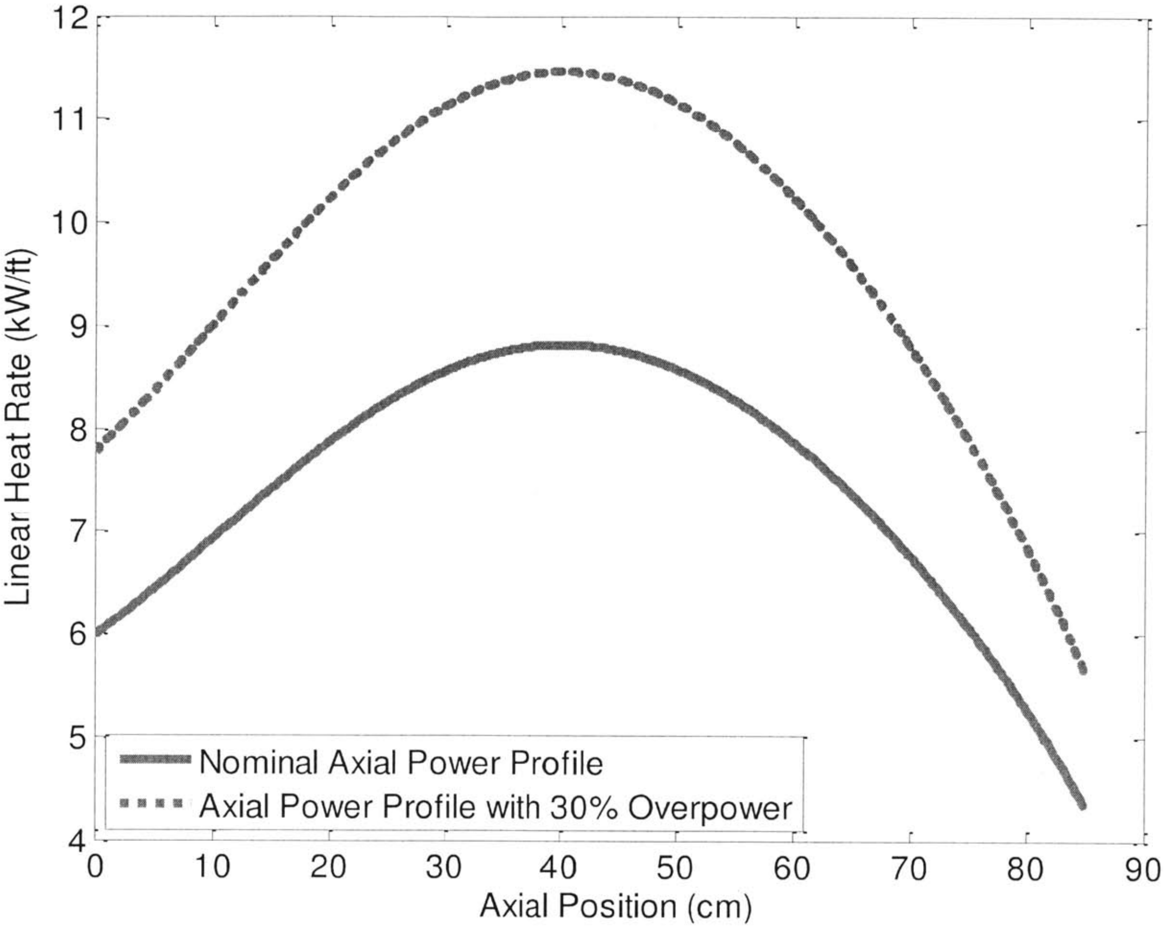

Figure 40- Axial Power Profile for Representative Metallic Core.
130% overpower used to provide a conservative estimate of the liquidus temperature

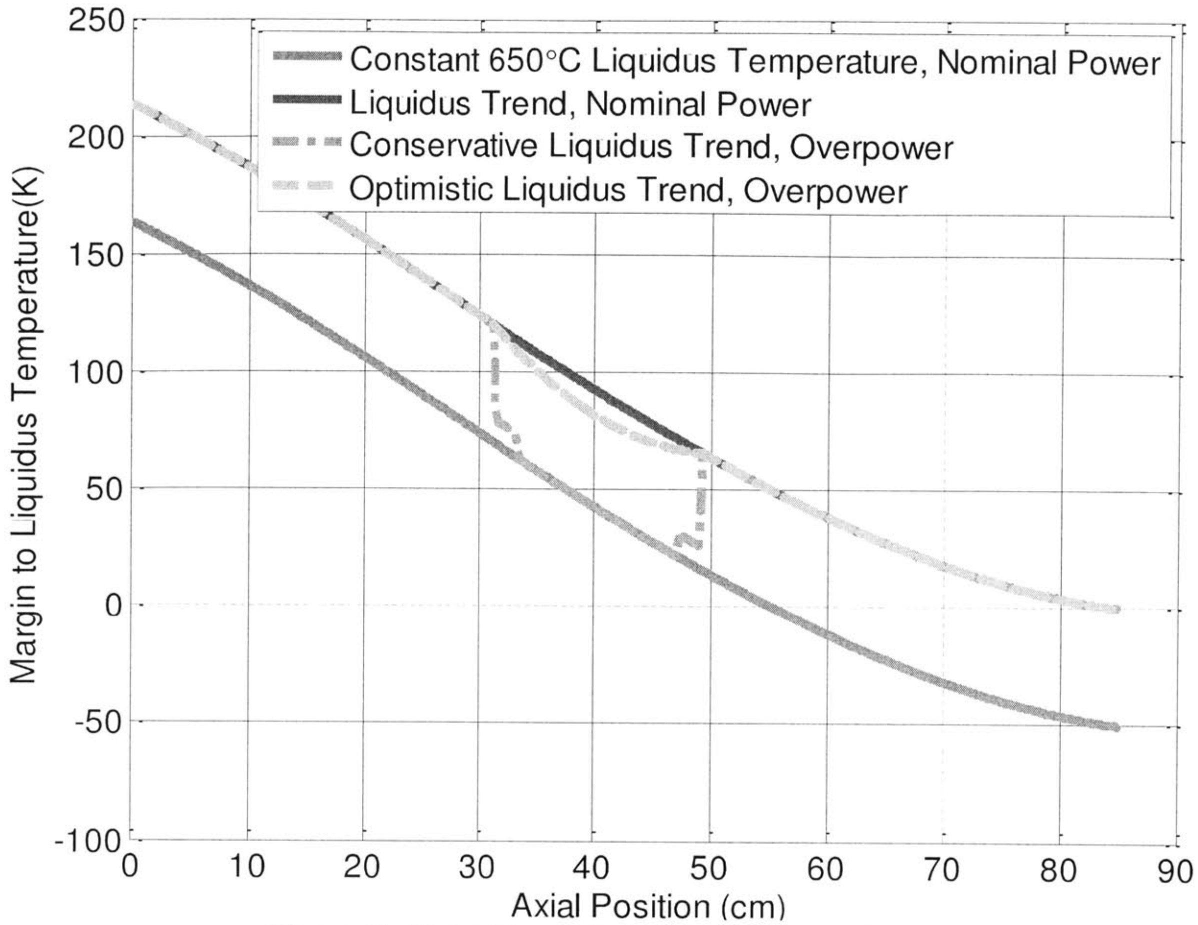

Figure 41- Axial Margin to Liquidus Temperature.
130% overpower used to provide a conservative estimate of the liquidus temperature

The preceding analysis shows that even though high linear power HT9 cladding U-19Pu-10Zr can undergo liquefaction above 650°C, the potential exists to operate lower linear power regions at higher temperatures. Currently this discussion is limited because only limited data exists at lower linear power levels for HT9 clad U-19Pu-10Zr. Additionally, martensitic cladding experiences creep rupture above 650°C without eutectic thinning making the ability to avoid eutectic formation above 650°C irrelevant. This analysis should only be used to guide future metallic fuel research to examine both low and high linear power levels for advanced fuels which may be able to operate above 650°C.

III.4 Economic Evaluations

In general, capital cost tends to be the largest element of power generation cost. In Nitta's analysis of SFR costs, the cost of the containment structure for a full containment system is indicated to represent 4.7% of the capital cost of the plant (56). Thus, the ability to select a less robust containment could have a significant economic advantage for one fuel type over another. On the other hand, if the need to protect against external threats requires a robust containment anyway, the differential cost of protecting against Energetic Events could be minimal.

Power plant efficiency can have a substantial effect on capital cost as indicated in Chapter IV of this thesis. At the current state of cladding development, both metal and oxide fuel have the same core outlet temperature limits and potential burnup limits, which are primarily set by choice of cladding. The differences in the approach to reprocessing for oxide and metal fuels are substantial. It was not within the scope of this thesis to attempt to estimate the cost of a pyroprocessing facility for metal fuel to compare against the aqueous processes used for oxide fuels. Each type of process has its advantages. At this point, we cannot associate an economic advantage to either.

III.5 Conclusions

Additional fuel testing will be required to create a licensing basis for irradiating U-Pu-Zr fuel past 11 at%, but lead test assemblies showed that metallic fuel has the potential of being irradiated beyond 20 at% burnup with HT-9 clad. A full economic and fuel cycle comparison was not included for this case study because of a lack of reliable information on reprocessing costs, but both fuel forms have the potential for high temperature and high burnup performance and are believed to be licensable under the NUREG-1860 licensing structure. Additionally, the lack of radioactive material release limits below a mean frequency of 10^{-8}/yr, or a 95th percentile of 10^{-7}/yr, may allow for ESs to be removed from the design basis and allow for a reduced pressure containment such as proposed by S-PRISM. The savings from moving to reduced pressure containment may allow for a 4.7% savings of the total capital cost for the SFR.

IV THERMODYNAMIC EFFICIENCY (V.3)

Improving the efficiency of a design or process is often considered the Holy Grail for designers and engineers. If a project's economic competitiveness is questioned, efficiency gains are seen as a way to increase reduce capital cost by raising power output while using the same basic structures and inputs as the original design. With an electricity generating facility, increasing the thermodynamic efficiency increases the electricity produced with ideally minimum impact on fuel, capital, and operation and maintenance costs. The following section examines how thermodynamic efficiency may be increased in the Sodium Fast Reactor (SFR) through a combination of:

- increasing the core outlet temperature for metal and oxide fuel,
- removing the intermediate loop,
- replacing shell and tube heat exchangers with Printed Circuit Heat Exchangers (PCHEs) (57),
- switching from a Rankine to a Supercritical-CO2 power conversion cycle.

IV.1 Introduction

This case study examines how to maximize the economic benefit from implementing various combinations of the four design alternatives above to raise thermodynamic efficiency for the SFR. These potential modifications are initially studied in series, but once their individual technical feasibility and safety constraints are analyzed, combinations of these alternatives will be analyzed. Finally, the economic impacts of the design alternatives are analyzed to determine their effect on the busbar cost of the SFR.

The most direct way of increasing thermodynamic efficiency is to raise the core outlet temperature. In an ideal Carnot power conversion cycle, the thermodynamic efficiency, η, is related to the absolute temperature of the heat source, T_h, and the heat sink, T_c, by Eq.IV.1.

$$\eta = 1 - \frac{T_c}{T_h} \qquad \text{IV.1}$$

While in practice Carnot efficiencies can never be achieved, the basic trends indicated by the Carnot cycle can be generalized to other power conversion cycles. Specifically, in order to increase thermal efficiency, the designer needs to increase the temperature of the heat source or decrease the temperature of the heat sink. The heat sink temperature is typically an exogenous variable, often dictated by geographical location, cooling tower design and weather cycles, and thus is hard for the designer to adjust. In contrast, one of the key design variables chosen by the reactor designer is the core outlet temperature. As Eq. IV.1 suggests, increasing the core outlet temperature will increase the thermodynamic efficiency.

It should be noted that for a direct cycle, the core outlet and turbine inlet temperatures are equal. However, for an indirect cycle the T_h of interest is not the core outlet temperature but the turbine inlet temperature. These two temperatures differ due to energy losses to the environment in the primary, intermediate, and power conversion loop piping as well as inefficiencies in heat exchanger designs. One of the important locations where energy is lost in the system is in the intermediate heat transfer loop. The intermediate loop is used in the existing SFR designs to keep the primary radioactive sodium separated from the water of the steam Rankine power cycle. This separation is done in order to avoid a sodium-water exothermic reaction with the radioactive primary sodium coolant in the event of a steam generator tube rupture.

By raising the core outlet temperature and reducing temperature losses in the system, the turbine inlet temperature is elevated, yielding an efficiency increase that is a function of the Power Conversion System (PCS) employed. This case study will examine variations in core outlet temperature, heat exchanger type, and choice of PCS, as well as the potential for the elimination of the intermediate loop, as shown in Figure 42.

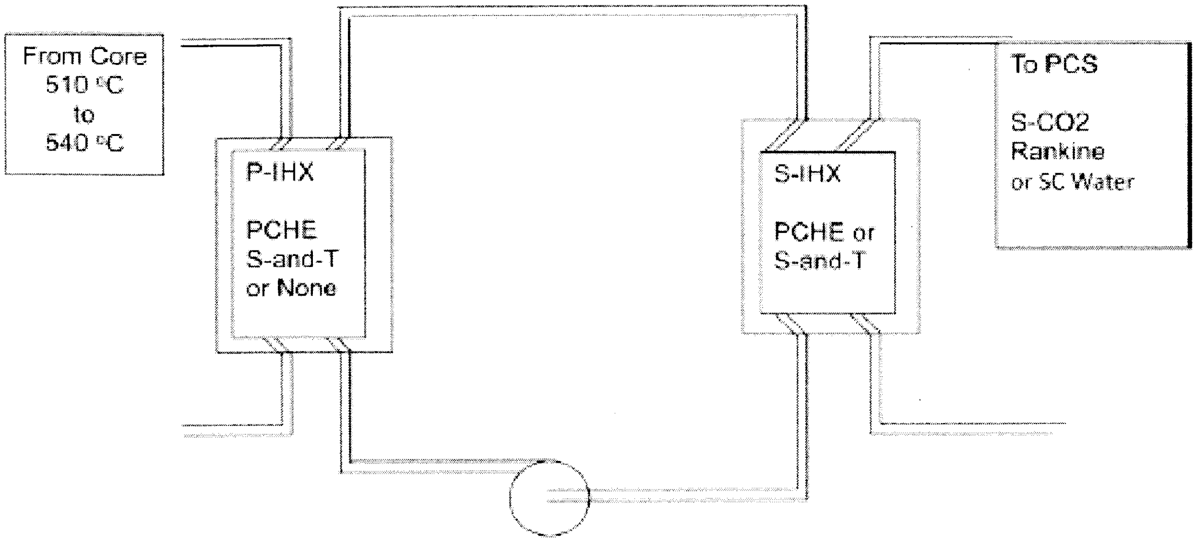

Figure 42-The Arrangement of Components in the SFR Balance of Plant and the Options Available for each Component. S-and-T refers to Shell and Tube Heat Exchangers and SC Water refers to the supercritical water power conversion cycle (58).

These choices are summarized in analogy to a fault tree in accident space, as shown in Figure 43.

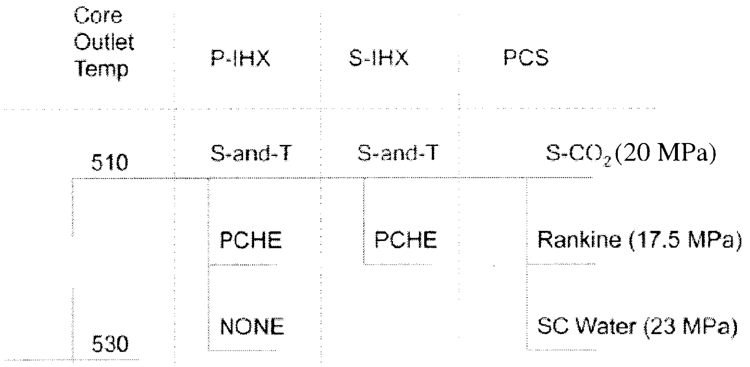

Figure 43- The Design Choices Affecting Efficiency that are Considered in this Study. All design options examined for 510°C are repeated for 530°C (58).

Figure 43 is intended to reflect the range of options for developing a balance of plant for an SFR. The primary IHX could be a PCHE or a shell-and-tube design, or the intermediate loop could be eliminated. The secondary IHX could be either PCHE or shell-and-tube, and the PCS could be a S-CO$_2$, conventional Rankine, or supercritical water cycle. The range of system pressures in the steam cycle can also vary substantially. In this study, two core outlet temperatures will be compared: 510°C and 530°C and the steam cycles will be assumed to operate at 15.5 MPa and 23 MPa (supercritical), with the results extrapolated to higher temperatures.

IV.2 General Assessment

Before the detailed safety and economic consequences of the design modifications can be addressed, a general assessment of the safety constraints for the 4 design alternatives must be considered. The constraints for the 4 proposed design modifications are:

- core temperature and radioactive material release limits for metal and oxide fuel,
- design restrictions caused by removing the intermediate loop,
- limits for PCHE implementation,
- limits to S-CO_2 power conversion cycle implementation.

IV.2.A Core Temperature and Radioactive Material Release Limits for Metal and Oxide Fuel

The core outlet temperature is limited by steady state cladding limits, transient limits on core structural temperature, and temperature limits on the vessel and sodium piping. The following sections detail these limits.

(i) Steady State Fuel-Clad Temperature Limits for Metal and Oxide Fuel

Steady state cladding temperature limits are designed to ensure that fuel will be highly reliable under expected conditions. Typically, this is done by ensuring that the 2σ hot channel factor cladding temperatures are below material limits of the clad. HT-9 is a martensitic alloy commonly chosen by the IFR/ALMR/PRISM program in the US for both their oxide and metal core designs and the KALIMER program in Korea for their metal core design (50) (32). HT-9 is typically chosen due to its low swelling under long term irradiation compared to austenitic cladding materials, e.g. D9 and SS-316 (41). Unfortunately, this reduced swelling is achieved at the cost of increased thermal creep at high temperatures.

To limit thermal creep, HT-9 is typically limited to steady state cladding mid-wall temperatures below 640°C (38) (59). The other operating limit for any steel cladding used with metallic fuel is due to the fuel-clad eutectic formation. Eutectic formation has been experienced in metallic pins at peak cladding temperatures above 650°C at high burnup (34). For steady state operations, this inner wall cladding limit typically corresponds to a cladding mid-wall limit of 645-648°C. Thus, HT-9 is thermal creep limited, which applies the same limit to both oxide and metal fuel. If the cladding was chosen based on high temperature performance instead of high burnup performance, metallic fuels would still be limited to the 645°C cladding mid-wall temperature range due to eutectic formation, unless a protective liner was employed, while oxide fuel would be able to successfully reach higher temperatures.

(ii)Transient Temperature and Release Limits For Metal and Oxide Fuel

Transients that have the potential to limit the outlet coolant temperature for the SFR are broadly defined in two categories:

- Transient OverPower (TOP)
- Loss Of Flow (LOF)

When determining transient limits in conjunction with NUREG-1860, a designer needs to consider events that will trigger the onset of additional radiation release. Even in hermetically sealed vessels, leakage of less than 0.1% of cover-gas per day to the containment is expected, so it is assumed that any fuel failure will contribute to some, albeit small, offsite consequences (60) (61). According to Denning et. al., a reactor vessel plenum overpressure of greater than 1MPa may result in failure of the primary system seal, which can release activated sodium into the containment. A 1MPa overpressure of the vessel head may occur during channel averaged sodium boiling and/or failure of over a 3rd of the core fuel pins if a design does not have a Vessel Plenum Overpressure Relief System (VPORS). It is likely that a VPORS would be incorporated in the vessel head to prevent such a seal failure, but inclusion of such as system may be optional. The following analysis will consider both options. It is unlikely that an internal event, even an energetic scenario, will be able to produce enough energy to fail the primary pressure boundary, which is a more severe end state than failing a seal on the primary system (55) (46). External events, such as earthquakes and aircraft impacts, are the most likely causes of containment and/ or primary system failure. From Denning et. al., Table 13 gives the 95th percentile end states used when calculating LBEs.

Table 13- 95th Percentile End States for RELAP5 Transients (61)

End State Label	**Criteria**	**95th % Dose for FCC curve**	
		VPORS	No VPORS
Minor Fuel Damage	Clad Damage Fraction > 1.0	<< 0.001 rem	<< 0.001 rem
Fuel Damage	Fuel Temperature > 1120°C Hot Channel Sodium Boiling > 925°C	<< 0.001 rem	<< 0.001 rem
Sodium Boiling	Core Outlet Sodium Temperature > 925°C	<< 0.001 rem	0.22 rem
Energetic Scenario	Structural Supports Fail Inlet Temperature >730oC	<< 0.001 rem	4.0 rem

(iii) Piping and Vessel Temperature Limits

The core outlet temperature has been proposed up to 575°C, the core outlet temperature designated for the BN-1800 design which uses Cr 18 Ni 9 steel for vessel, piping and heat exchanger materials (10). In general, the temperature limits for structural steels are still being assessed. During the design of the Prototype Fast Breeder Reactor, 316L(N) SS was chosen for components operating at temperatures higher than 500°C due to its high creep resistance. 304L(N) SS was chosen for the remainder of the plant because 304L(N) is 20% less expensive than 304L(N). This cost estimation takes into account that 304L(N) piping tends to be 15% thicker than 316L(N), and thus more 304L(N) is needed for the same amount of piping (62).

IV.2.B Design Restrictions Caused by Removing the Intermediate Loop

For a pool design, elimination of the intermediate loop requires placement of the primary to power conversion cycle heat exchangers inside the pool. This has consequences in both safety considerations and sizing of the heat exchangers within the vessel. As a safety concern, designers are commonly cautious regarding placement of a steam generator or large CO_2 plenum inside a pool of sodium, even if it is double-walled. The failure of the heat exchanger plenum could constitute a single failure leading to core damage due to the positive reactivity insertion resulting from coolant voiding. Some designs have created double pool levels which prevent such a gas bubble from entering the core (63). The impracticality of eliminating the intermediate loop in a pool design was also the result of the very tight space for the Secondary-IHX within the reactor vessel. By using the dimensions of the base case Primary-IHX as the maximum dimensions of the single IHX for this case, the heat transfer to the PCS is severely limited. Steam generators and S-CO_2 heat exchangers require more heat transfer area than the small heat exchanger can provide. Consequently, the option of eliminating the intermediate loop is considered to be practical only for loop-type SFRs.

IV.2.C Limits for PCHE Implementation

HEATRIC^{TM} Printed Circuit Heat Exchangers (PCHEs) are considered as a replacement for both the intermediate loop heat exchanger and the steam generator (57). They are the heat exchanger of choice when considering compactness and ruggedness. PCHEs are formed by diffusion bonding plates with etched channels. Alternating plates for hot and cold fluids allow very large heat transfer area in a relatively compact volume.

The overall performance of PCHEs is of interest because steam generator tube leaks have been problems for several SFRs. The small channel diameter and the robust design of PCHEs should reduce the frequency and severity of steam generator leaks. Also, every shell-and-tube design used in this study is modeled as a double-walled tube with a helium gap. The use of double walled tubes or hybrid PCHEs will improve the availability of the entire reactor system. At this time, PCHEs can be implemented as a viable alternative to shell and tube heat exchangers with no limiting conditions within the expected SFR operating range (58).

IV.2.D Limits to S-CO_2 Power Conversion Cycle Implementation

According to the Gen-IV Component Design and Balance of Plant Project Management Board, six challenges remain to be solved before the S-CO_2 cycle is ready for commercial deployment (64).

1. A commercial scale (defined as greater than 600MWth) demonstration plant must be built
2. Proper scaling of all necessary system parameters need to be demonstrated
3. Appropriate stability and control of the cycle needs to be demonstrated near the critical point of CO_2.
4. Transient performance must be verified (i.e., rapid power transients or reactor SCRAM)
5. Sodium-CO_2 chemical interactions must be better understood

6. Long-term material compatibility between structural materials and S-CO_2 must be confirmed.

Work in many of these areas has been performed at MIT. As mentioned above, modeling of the S-CO_2 cycle still requires validation, especially in the development of control techniques for transient operation. Significant progress has recently been made in transient modeling, but additional work will have to enter the experimental realm (65). A full recompression cycle test loop is required in order to test the performance of the cycle under system transients.

Compact turbomachinery is a benefit of the S-CO_2 recompression cycle, but more detailed studies of the expected costs must be performed in order to quantify the economic advantage of this cycle beyond that achieved from efficiency improvements alone. Cost estimates for turbomachinery and heat exchangers will allow for comparisons with Rankine and supercritical water cycles. Then, the entire economic benefit of the S-CO_2 cycle can be understood. As a first order economics estimate, the S-CO2 cycle should require 1/6 the raw materials as an equivalent Rankine power conversion cycle, thus an n^{th}-of-a-kind S-CO2 cycle can be taken to be $1/6^{th}$ the cost of an equivalent Rankine cycle (12).

The corrosion of stainless steels in an S-CO_2 environment must be investigated further. Corrosion will affect the lifetime and reliability of heat exchangers and the failure modes of every PCS component. The AGR program has operated S-CO_2 cycles reliably at outlet temperatures of up to 650°C, but at a 4.3 MPa operating pressure. The S-CO_2 power conversion cycle for an SFR would likely operate at 20MPa, increasing creep, fatigue, and corrosion rates. Early work in the field indicates that operating temperatures should not go above 700°C because dissociation of the S-CO_2 at these temperatures may lead to corrosion of the turbine blade and structural components (66).

IV.3 Technical Evaluation

This section will illustrate how the preceding 4 design alternatives can be examined within NUREG-1860's Frequency Consequence Curve (FCC). The initial design alternative of raising core outlet temperature will be examined using RELAP5 simulations for both metal and oxide fuel types (17). Removing the intermediate loop is commented on but not analyzed because a detailed design, comprising both plant layout and potential accident sequences, was not available for analysis. Switching to a S-CO_2 cycle without removing the intermediate loop does not require a detailed safety evaluation because NUREG-1860's FCC only considers the response of safety grade components. Thus, the S-CO_2 cycle will perform exactly like a Rankine cycle for the safety analysis. Since the power conversion system is non-safety grade, any design changes to these systems have no direct impact in the response to Licensing Basis Events (LBEs).

In order to raise the core outlet temperature, the fuel rod must be shown to be reliable at the elevated temperature. Hence all relevant LBEs must be shown to lie within the acceptable region of the FCC, and the operating temperature must be below vessel and piping limits. The following sections outline the analysis required to ensure that these limits are satisfied.

IV.3.A Determining the Steady State Core Outlet Temperature for Metal and Oxide Fuel

The fuel cladding is the most vital and one of the most stressed components in the reactor. The cladding forms the second barrier to radiation release, making the reliability of the cladding safety significant. At the same time, the cladding is located in the middle of the reactor core; exposed to high levels of radiation damage, stressed by fission gas, deformed by fuel/cladding chemical and mechanical interactions and operated at temperatures above the onset of thermal creep. For all of these reasons, statistical and deterministic safety margins are used to ensure that adequate margin is provided between the operating conditions and the cladding failure regime. Many methods have been developed to combine these margins and set operating limits, but the most commonly accepted method is the horizontal method, which separates direct and statistical uncertainties and combines them separately (16) (15) (47), discussed in Section II.2. By employing the horizontal method on a metal and oxide fueled pool type reactor with HT-9 cladding, the maximum allowable steady state operating temperature for each of these fuel types is determined.

Using the 640°C cladding mid-wall temperature limit from HT-9 and assuming the same linear powers for metal and oxide fuel, it can be seen from Figure 44 that the maximum core

44 that the maximum core outlet temperature from a fuel reliability standpoint is a little under 550°C for both core designs. Since creep is a function of both temperature and pressure, the creep temperature limit may be increased if the plenum pressure can be significantly decreased, although this is effort left to future work. It should be noted that the Russian BN-1800 proposes a nitride fueled core that has a proposed core outlet temperature of 575°C. Unfortunately, no additional justifications were given to show how this outlet temperature is achievable (i.e., no cladding type or peak temperatures were provided) (9). The removal of the pellet cladding eccentricity direct and statistical uncertainties for the metallic fuel did not cause a significant reduction in the corresponding 2σ peak cladding temperatures when compared with oxide fuel. This outlet temperature is in line with the standard core outlet temperatures of most currently proposed SFR designs for oxide fuel (10). The importance of incorporating hot channel factors should be emphasized, because not including these safety factors would cause a designer to believe that the HT-9 creep limit would correspond to a feasible steady state core outlet temperature of 607°C, as can be seen in Figure 44. This analysis uses the horizontal methodology detailed in Section II.2 and the supporting spreadsheets can be found in Appendix E.

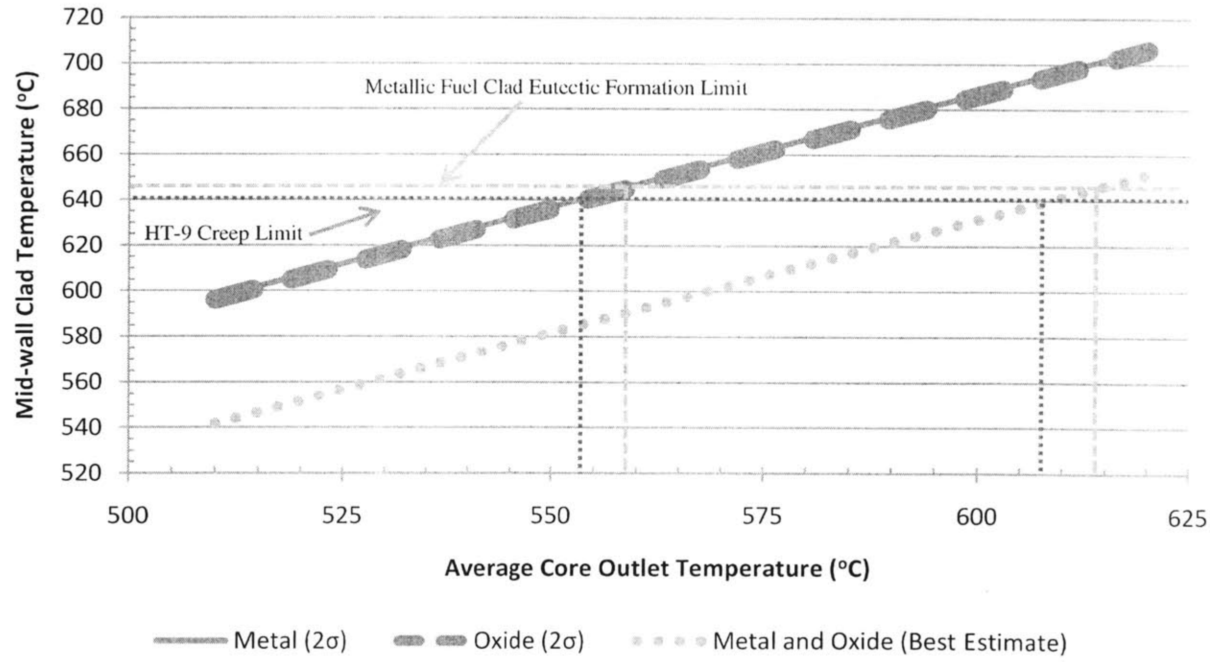

Figure 44- Steady State Limits and Corresponding Core Outlet Temperatures for HT-9. Because HT-9 is creep limited, the core outlet temperature for both metal and oxide fuel is 554°C. The conventional 650°C fuel/cladding eutectic limit for metallic fuel is also given. For typical linear power designs, this temperature limit may be as high as 700°C (see Figure 20).

IV.3.B Determining the Transient Core Outlet Temperature for Metal and Oxide Fuel

In order to demonstrate that raising the core outlet temperature will satisfy the transient requirements set forth in NUREG-1860, both the mean and 95th percentile of the frequency and magnitude of radiation release for a given LBE are required. Calculation of radioactivity release can be difficult, but for extremely low probability accidents, where the mean frequency of core damage is below the FCC frequency threshold of 10^{-8}/yr and/or the 95th percentile is below 10^{-7}/yr, there is no release limit. Thus, if the core damage frequency can be established to be below the threshold frequency, the system response is considered acceptable without dose calculations, and any additional analysis required by the NRC will be considered beyond design basis. If this requirement is too stringent or would cause the designer to add additional systems and thus increasing costs, then dose estimates will be required for the associated end states of those sequences. For an SFR with a broken primary system seal and a functioning containment operating at its designed leak rates, the highest radiation release state is 4 rem (61), which falls within the unacceptable region at release frequencies larger than 10^{-4}/yr. The optimal configuration of design parameters can be selected through the following procedure:

1. Determine the largest of the mean and 95th percentile frequency of radiation release for the most limiting LBE.
2. Adjust the core outlet temperature and add or remove redundant safety features until the radiation release frequency and magnitude is within the acceptable region of the FCC.
3. Check to ensure that the changes to the reactor configuration did not inadvertently place LBEs, which originally had lower failure probabilities, into the unacceptable region above the FCC. If so, repeat Part 2 with the new limiting accident group.

(i) Evaluation of Transient Uncertainties for Metal and Oxide Fuel

The UTOP and ULOF transient uncertainties are described in Section III.A part (i).

(ii) Statistical Methods Used to Predict Release Frequencies for Metal and Oxide Fuel

The statistical methods used to predict mean and 95th percentile radioactive material release frequencies can be found in Section III.A part (ii).

(iii)Licensing Basis Event Transients for Metal and Oxide Fuel

For the sodium fast reactor, three general categories of transient exist that can challenge the integrity of the primary system:

- Transient Overpowers (TOP)
- Loss of Flow (LOF)
- Loss of Heat Sink (LOHS)

The FCC is only evaluated for safety grade components. Since the primary heat sink is not safety grade, it cannot be taken credit for while attempting to meet the TNF. Thus, there are only two categories of LBEs which will be examined to determine the temperature limits of the SFR:

- Transient Overpower with Loss of Heat Sink (TOP/LOHS)
- Loss of Flow with Loss of Heat Sink (LOF/LOHS)

(iii.a) Transient Overpower with Loss of Heat Sink for Metal and Oxide Fuel

TOPs are one of the primary transients analyzed for sodium reactors (20) (33). The following discussion will detail how TOP analysis is conducted for a proposed LBE. In addition, the effects of core outlet temperature on the TOP LBE analysis are also discussed. Because all events are treated as LOHS accidents in the FCC, TOP/LOHS sequences have the same initiating frequency as TOP sequences and will be referred to as TOP for simplicity.

(iii.a.1) Transient Overpower Initiator Frequencies

In general, any TOP can be defined by answering three questions:

1. What is the total reactivity being inserted into the reactor?
2. What is the rate of reactivity insertion during the transient?
3. What is the frequency of achieving this combination of total reactivity and reactivity insertion ramp rate?

Determining the answers to these questions is difficult due to the low probability of a large power excursion. Because the ALMR PRA is the most up-to-date SFR PRA available, the ALMR reactivity insertion distribution was used to determine the magnitude and the rate of reactivity insertion. In the ALMR PRA, the cause of reactivity insertion is a malfunctioning reactivity controller system that registers a low core power level. Thus, the computer pulls the control rods out of the core until they reach their control rod stops, which are set to allow for a maximum reactivity insertion of 30¢. For larger reactivity insertions, misalignment of the control rod stops is assumed to be due to human error with the resulting reactivity insertion distribution presented in Table 14.

Table 14- ALMR TOP Reactivity Insertion Distributions (67)

Frequency of TOPs	Reactivity Insertions	Reactivity Insertion Rate
3x10^{-5}/yr	\$0.3-0.5	\$0.03/s
2x10^{-6}/yr	\$0.5-0.7	\$0.03/s
1x10^{-7}/yr	\$0.7-0.9	\$0.03/s

It should be noted that the frequencies in Table 14 are dependent on the core conversion ratio. Lower conversion ratios increase the cycle reactivity swing, causing the differential control rod worth to be larger for burner reactors than for unity conversion ratio closed cycle reactors. The differences in the frequencies in Table 14 come from spatial misalignment of the control rod stops, with any given misalignment becoming more severe because the differential rod worth increases in magnitude. Conveniently, the SFR RELAP5-3D model and the ALMR PRA both describe an approximately 0.7 conversion ratio burner reactor, allowing use of the reported frequencies without modification.

In general, the ALMR PRA provides a realistic approach to reactivity control in a burner reactor design since the control rod stops limit the amount of reactivity available for TOPs. Larger reactivates can be achieved if the control rod stop breaks, but the conditional probability of the rod stop flange breaking can be assumed to be *de minimis*.

Finally, as previously mentioned, by assuming the primary system and containment both leak at their respective design basis rates, the worst potential 95th percentile estimate of radiation release is 3.0 rem. This release level is acceptable at frequencies below 10^{-4}/yr, and thus any conditional failure probability applied to the lowest TOP initiating frequency, at $3x10^{-5}$/yr, will produce an LBE point in the acceptable region. The following analysis is presented for two reasons. First, NUREG-1860 requires the calculation of LBE points. Second, future reduction in containment requirements may lead to larger release states for external events, which are not considered in this study. With these motivations, the following TOP analysis is conducted.

(iii.a.2) Bounding The Transient Overpower

Unprotected transients are defined as transients where the reaction protection system fails to insert the control rods into the core. These events are normally not included in LBEs since the failure probability of the Reactor Protection System (RPS) is small enough to push unprotected accidents under the 10^{-7}/yr mean frequency FCC cutoff. For example, the failure probability for the RPS during a TOP is 3×10^{-5}/demand and is 1×10^{-7}/demand for all other transients (67). The high reliability of the RPS means that only protected TOPs and LOFs need to be analyzed. While this greatly simplifies the number of transients that need to be protected against with safety grade systems, most SFRs are extremely robust to transients, and calculating a failure probability for protected transients can be difficult. In general, any protected transient is going to be less severe than its unprotected counterpart, so if a failure probability is estimated for an unprotected transient then it can be reasonably assumed that the protected transient has a lower probability of failure.

Thus, the \$0.7-\$0.9 reactivity insertion bin was analyzed as an Unprotected TOP (UTOP) to determine a bounding probability of failure for a TOP. For TOPs, it can be assumed that probability of cladding failure increases as the magnitude of reactivity insertion increases, keeping all other variables constant. This inequality is written in Eq.IV.2.

$$\begin{aligned}&\Pr(\text{Clad Failure}|\$0.3-\$0.5\ \text{TOP})\\ &\quad<\Pr(\text{Clad Failure}|\$0.5-\$0.7\ \text{TOP})\\ &\quad<\Pr(\text{Clad Failure}|\$0.7-\$0.9\ \text{TOP})\end{aligned} \qquad \text{IV.2}$$

The same relations exist for unprotected transient overpowers, as is written in Eq.IV.3
.

$$\begin{aligned}&\Pr(\text{Clad Failure}|\$0.3-\$0.5\ \text{UTOP})\\ &\quad<\Pr(\text{Clad Failure}|\$0.5-\$0.7\ \text{UTOP})\\ &\quad<\Pr(\text{Clad Failure}|\$0.7-\$0.9\ \text{UTOP})\end{aligned} \qquad \text{IV.3}$$

Since an unprotected accident is an accident where the Reactor Protection System (RPS) fails to function, the probability of cladding failure for a protected transient overpower with \$X of reactivity inserted is always smaller than for an unprotected transient overpower of with \$X of reactivity, as is represented in Eq.IV.4.

$$\Pr(\text{Clad Failure}|\$X\ \text{TOP}) < \Pr(\text{Clad Failure}|\$X\ \text{UTOP}) \qquad \text{IV.4}$$

Thus, Eq.IV.5 gives a general inequality bounding the frequency of cladding failure for \$0.3 – \$0.5 TOPs.

$$\begin{aligned} &f(\text{Clad Failure}|\$0.3-\$0.5\ \text{TOP}) \\ &\quad = f(\$0.3-\$0.5\ \text{TOP}) * \Pr(\text{Clad Failure}|\ \$0.3-\$0.5\ \text{TOP}) \qquad \text{IV.5} \\ &\quad < f(\$0.3-\$0.5\ \text{TOP}) * \Pr(\text{Clad Failure}|\$0.7-\$0.9\ \text{UTOP}) \end{aligned}$$

If failures still cannot be calculated by increasing reactivity insertions or moving from protected to unprotected transients, then examining the accident at higher steady state temperatures may be considered. Thermal creep increases in a logarithmic fashion with temperature increases, thus evaluating the accident at a higher outlet temperature is guaranteed to increase the probability of failure. If the resulting hybrid LBE falls into the acceptable region of the FCC curve, then no further action is required. If the hybrid LBE falls into the unacceptable region of the FCC curve, then a less severe bounding accident, employing a greater number of simulations, must be designed and employed to bound the accident response.

(iii.a.3) TOP Results for Metal and Oxide Fuel

In the \$0.7-\$0.9 TOP event, the control rods withdraw from the core until they reach the control rod stops which have been misplaced to allow for a \$0.7-\$0.9 reactivity insertion. When the outlet temperature rises above 560°C, the reactor protection system should trip, causing the secondary control rods to insert into the core and shut down the reactor. All bounding accidents assume that the SCRAM system has failed and thus the TOP continues with only passive feedbacks used to shut the reactor down. Since all LBEs are assumed to be LOHS LBEs, the cold pool quickly heats up. When the cool pool reaches 510°C, the main coolant pumps trip to protect themselves, causing the accident to additionally become a loss of flow accident. With the pumps off, the coolant flow decreases faster than reactor power, thus causing the fuel, clad, and coolant to heat up. This heatup can lead to cladding rupture or local coolant boiling unless natural circulation can keep the system temperatures low enough to prevent creep rupture of the clad.

The calculated cladding creep rupture probabilities of the $0.7-$0.9 UTOP analysis are listed in Table 15a for core outlet temperatures of 510°C, 554°C, and 595°C. Note that 595°C is above the thermal creep limit set in Section IV.3a, and thus is only used to bound the accident response. The 595°C core outlet temperature was chosen to allow enough failures from the metallic fuel to be simulated in order to stabilize the mean and 95th percentile estimates of conditional cladding failure. For oxide fuel, the protective shutdown of the pumps produces extremely high cladding temperatures, causing substantial creep rupture at almost all evaluated outlet temperatures. The failure weight listed in Table 15a is used as the value of x with the prior value for q assumed to be zero and the total number of simulations is taken as N with the prior r assumed to be zero.

Table 15a - $0.7-$0.9 UTOP Creep Rupture Statistical Summary for Metal and Oxide Fuel

Core Outlet	Fuel Type	# of Simulations	Failure* Weight	Mean Pr(Clad Rupture | UTOP)	95th Percentile Pr(Clad Rupture | UTOP)
510°C	Metallic	280	0.0	<< 3.2×10^{-4}	<< 1.9×10^{-3}
554°C	Metallic	280	0.0	<< 3.2×10^{-4}	<< 1.9×10^{-3}
595°C	Metallic	280	0.09	3.2×10^{-4}	1.9×10^{-3}
510°C	Oxide	400	398.2	0.995	0.999
554°C	Oxide	400	400.0	<1.0	<1.0
595°C	Oxide	400	400.0	<1.0	<1.0

*Refers to sum of the weights of simulations resulting in cladding rupture

Additionally, many of the oxide TOP simulations result in hot channel and core outlet sodium boiling, both end states for potential radiation release listed in Table 13. Table 15b lists the number of simulations, total failure weight, mean and 95th percentile of the conditional probability of local and bulk sodium boiling given a $0.7-$0.9 UTOP. No boiling was produced by the simulation for the metallic cores with steady state core outlet temperatures ranging from 510°C to 595°C.

Table 15b - \$0.7-\$0.9 UTOP Sodium Boiling Simulation Summary for Oxide Fuel

Core Outlet	Boiling Location	# of Simulations	Failure Weight*	Mean Pr(Boiling | UTOP)	95th Percentile Pr(Boiling | UTOP)
510°C	H.C.B.**	400	159.0	0.40	0.44
554°C	H.C.B.	400	396.3	0.991	0.998
595°C	H.C.B.	400	400.0	<1.0	<1.0
510°C	C.A.B.**	400	0.0	$<<6.1\text{x}10^{-5}$	$<<1.6\text{x}10^{-4}$
554°C	C.A.B.	400	0.0184	$6.1\text{x}10^{-5}$	$1.6\text{x}10^{-4}$
595°C	C.A.B.	400	34.8	0.12	0.15

* Refers to sum of the weights of simulations resulting in boiling

** H.C.B.=Hot Channel Boiling, C.A.B.=Core Outlet Boiling

(iii.a.4) TOP LBEs on the FCC for Metal and Oxide Fuels

Table 15 details the probability distributions for creep rupture, local sodium boiling and bulk sodium boiling for the TOP/UTOP transients. Because the aforementioned distributions arise from binomial evidence, which only indicates the exceedance of a threshold value, overlaps between distributions are taken into account. For example, large scale boiling is always preceded by boiling in the hot channel, thus the probability distribution of arriving at the hot channel boiling end state must factor out the simulations that result in core outlet boiling, as written in Eq. IV.6. To factor out the overlapping probability, the probability of core outlet and hot channel boiling is defined as the product of the probability of core outlet boiling given hot channel boiling and hot channel boiling, as is written in Eq. IV.7, where the probability of core outlet boiling and core outlet and hot channel boiling are known and the probability of hot channel boiling given core outlet boiling is unity.

$$\begin{aligned} &Pr(Core\ Outlet\ and\ Hot\ Channel) \\ &\qquad = Pr(Core\ Outlet|Hot\ Channel\ Boiling) \\ &\qquad\quad * Pr(Core\ Outlet\ Boiling) \end{aligned} \qquad \text{IV.6}$$

Then the probability of hot channel boiling given no core outlet sodium boiling can be calculated using the decomposition rule in Eq. IV.11, where the horizontal bar indicates that the event did not occur.

$$
\begin{aligned}
&Pr(\mathit{Hot\ Channel\ Boililng}) = \\
&\qquad Pr(\mathit{Hot\ Channel\ Boiling}|\mathit{Core\ Outlet\ Boiling}) \\
&\qquad\quad * Pr(\mathit{Core\ Outlet\ Boiling}) \\
&\qquad + Pr(\mathit{Hot\ Channel\ Boiling}|\overline{\mathit{Core\ Outlet\ Boiling}}) \\
&\qquad\quad * Pr(\overline{\mathit{Core\ Outlet\ Boiling}})
\end{aligned} \qquad \text{IV.7}
$$

Using these equations, the probability distribution of the less severe end state, hot channel boiling without core outlet boiling, can be backed out from the probability distributions around both hot channel boiling and core outlet boiling. To create a distribution around the less severe end state, Monte Carlo methods must be used to sample from the distributions defined in Table 15. The same technique can be used to separate out the probability of creep rupture without local boiling from the probability of creep rupture with hot channel boiling and the probability of hot channel boiling.

Figure 45 shows the UTOP LBEs plotted on the Frequency Consequence Curve. Because of the low initiating frequency for this transient, all end states fall underneath the FCC cutoff. Thus, a VPORS will not be required to mitigate the consequences of a UTOP for either fuel choice. Both oxide and metal cores respond adequately to TOP at outlet temperatures at least up to 595°C. The LBE release frequencies were calculated by multiplying the UTOP initiating frequency by the conditional probability of arriving at an end state shown in Table 16. It should be noted that the probability of Hot Channel Boiling (H.C.B.) goes down for oxide fuel between 554°C and 595°C because some simulations that were H.C.B. entered the Core Average Boiling (C.A.B.) end state at the higher temperature.

Table 16 – Summary of Conditional End State Probabilities (mean/95th%)

	OK	C.F.	H.C.B.	C.A.B.
Metal 595°C	0.9997/-	$3\text{x}10^{-4}/2\text{x}10^{-3}$	-	-
Oxide 510°C	$5\text{x}10^{-3}/0.011$	0.51/0.55	0.49/0.53	-/-
Oxide 554°C	-/-	$9\text{x}10^{-3}/0.018$	0.990/0.997	$5\text{x}10^{-5}/9\text{x}10^{-3}$
Oxide 595°C	-/-	-/-	0.92/0.93	0.087/0.11

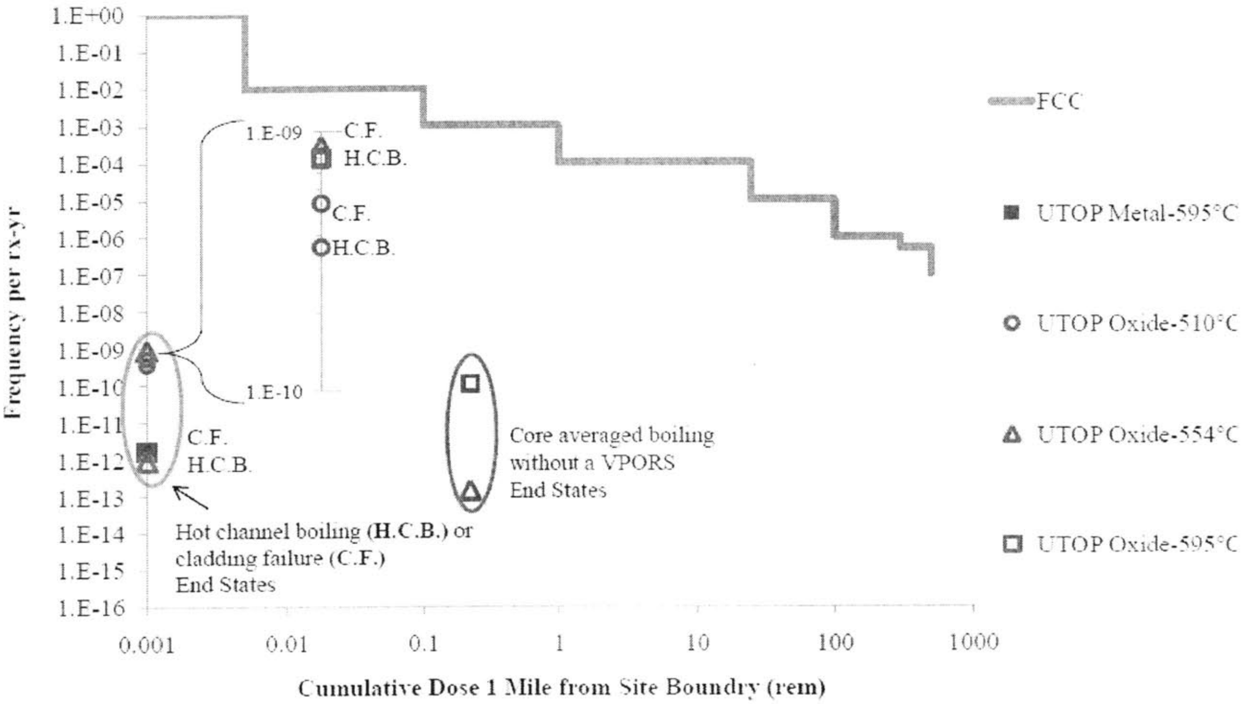

Figure 45– Frequency Consequence Curve with UTOP LBE Points Plotted for Metal and Oxide Fuel at a Variety of Core Outlet Temperatures.

(iii.b) Loss of Flow with Loss of Heat Sink for Metal and Oxide Fuel

Loss Of Flow (LOF) accidents are challenging sequences for the sodium reactor, and are often studied as a precursor to energetic core distributive accidents (54) (55) (36). While the small SCRAM failure probability for accidents not initiated by the RPS (~10^{-7}/demand) pushes these accidents below the TNF cutoff frequency, loss of primary coolant flow still has the potential to cause minor core damage (67). The following sections outline the possible initiators and LBE analysis for LOF events at both a 510°C and 550°C core outlet temperature. Because all events are treated as LOHS accidents in the FCC, LOF/LOHS sequences have the same initiating frequency as LOF sequences and will be referred to as LOF for simplicity.

(iii.b.1)Loss of Flow Initiator Frequencies

The loss-of-flow accident sequences enumerated in the ALMR PRA are listed in

(67). Three accident sequences have initiating frequencies that are greater than the 10^{-7}/yr TNF cutoff:

- Failure of 1 to 2 pumps (assumed failure of two pumps of four for conservatism)
- Station blackout event resulting in the loss of all pumps
- Failure of 2 pumps and their coastdown motors.

Of these events, failure of 1-2 pumps and station blackout events both require importance sampling to determine whether or not the likelihood of cladding failure is on the order of 10^{-5} to 10^{-7}/demand. Failure of 2 pumps and their coastdown motors only requires that the failure probability be below 0.1 to reach the frequency cutoff, which can be determined without importance sampling.

Table 17 - Loss-of-Flow Accident Frequencies for the ALMR. (67)

	Initiating Frequency (yr^{-1})*	Required Probability of Cladding Rupture**
1-2 pumps fail	0.5	2.00×10^{-7}
SBO	0.007	1.43×10^{-5}
2 pumps fail w/o C.D. Motors	6.5×10^{-7}	0.154
SBO w/o 2 C.D. Motors	9.1×10^{-9}	1.00
SBO w/o 4 CD Motors	4.73×10^{-10}	1.00

* Initiating Frequency refers to the frequency of pump failures, station blackout events (SBO), and coastdown (CD) Motor failures.

** The Required Probability of cladding Rupture refers to the failure probability needed to place cladding failure below the 10^{-7}/yr TNF threshold.

The metallic reactor design is designed to have a pump coastdown halving time of 5s, which is typical of metal cores. The oxide core is designed to have a 20s flow halving time to prevent large power-to-flow mis-matches which have the potential to cause short term sodium boiling due to the large stored energy of the oxide fuel. Other probabilistic analyses have indicated that flow coastdown can be represented as a normal distribution with a standard deviation set to 10% of the nominal value (11). This probabilistic representation of pump coastdown characteristics is used in the following analysis.

(iii.b.2) Bounding the Loss of Flow

Just as with the loss of flow analysis, the unreliabilities for protected accidents are too small to calculate directly using the statistical techniques outlined in Section ii of this chapter. Thus surrogate bounding accidents are designed to provide an upper bound to the probability of failure. If the hybrid LBE falls into the acceptable region of the FCC curve, then no further action is required. If the hybrid LBE falls into the unacceptable region of the FCC curve, then a less severe bounding accident has to be designed and employed to bound the accident response.

(iii.b.3) Station Blackout Results for Metal and Oxide Fuel

Of the three LOF accidents, Station BlackOut (SBO) is the only accident which leads to cladding failure at frequencies above the TNF cutoff. In the station blackout event, a/c power to all pumps in the plant is simultaneously lost. All bounding accidents assume that the SCRAM system has failed and thus the SBO becomes an Unprotected SBO (USBO) and continues with only passive feedbacks used to shut the reactor down. Since all LBEs are assumed to be LOHS LBEs, the cold pool quickly heats up. Without the pumps, natural circulation is required to remove the heat generated in the fuel. When the power to flow ratio rises above 1.3, the reactor protection system should trip, causing the control rods to insert into the core and shut down the reactor. All bounding accidents assume that the SCRAM system has failed and thus the SBO continues with only passive feedbacks used to shut the reactor down. With the pumps off, the coolant flow decreases faster than reactor power, thus causing the fuel, clad, and coolant to heat up. This heatup can lead to cladding rupture or local coolant boiling unless natural circulation can keep the system temperatures low enough to prevent creep rupture of the clad.

The results of the USBO analysis are seen in Table 18a for core outlet temperatures of 510°C, 554°C, and 620°C. Note that 620°C is above the thermal creep limit set in Section IV.3.A, and thus is only used to bound the accident response. 620°C was chosen because enough failures were calculated for the metallic fuel at this core outlet temperature to stabilize the mean and 95th percentile estimates of cladding failure. It should be noted that oxide cores are designed to have a longer flow coastdown than metallic cores, which should make the loss of flow transient less damaging, but the forced loss of non-safety grade heat sink causes the longer coastdown time to extend the transient. The additional power generated can only be removed by the decay heat removal system, and thus the oxide core experiences higher long term temperatures than the metallic cores.

Table 18a – USBO Creep Rupture Statistical Summary for Metal and Oxide Fuel

Core Outlet	Fuel Type	# of Simulations	Failure* Weight	Mean Pr(Clad Rupture I USBO)	95th Percentile Pr(Clad Rupture I USBO)
510°C	Metallic	405	0.0	$<< 2.6\times10^{-5}$	$<< 1.1\times10^{-5}$
554°C	Metallic	405	0.0	$<< 2.6\times10^{-5}$	$<< 1.1\times10^{-5}$
620°C	Metallic	405	0.008	2.6×10^{-5}	1.1×10^{-5}
510°C	Oxide	350	137.9	0.39	0.43
554°C	Oxide	350	342.3	0.978	0.988
620°C	Oxide	350	349.3	0.998	0.999

* Refers to sum of the weights of simulations resulting in cladding rupture

Additionally, many of the oxide unprotected SBO simulations result in local and bulk sodium boiling; both end states for potential radiation release listed in Table 13. Table 18b lists the number of simulations, total failure weight, mean and 95th percentile of the conditional probability of local and bulk sodium boiling given an unprotected SBO. A statistically significant number of boiling simulations was not simulated for the metallic cores with steady state core outlet temperatures ranging from 510°C to 554°C, but the probability of local boiling for a core outlet temperature of 620°C was calculable. No metal fuel simulations result in bulk boiling, but the probability of bulk boiling should be less than the probability of local boiling.

Table 18b - USBO Sodium Boiling Simulation Summary for Metal and Oxide Fuel

Core Outlet	Fuel Type	Boiling Location	# of Simulations	Failure* Weight	Mean Pr(Boiling I USBO)	95th Percentile Pr(Boiling I USBO)
510°C	Metallic	H.C.B.***	405	$< 1.8\times10^{-4}$**	$< 4.4\times10^{-4}$**	N/A
554°C	Metallic	H.C.B.	405	1.8×10^{-4}**	1.8×10^{-4}**	N/A
620°C	Metallic	H.C.B.	405	26.2	0.065	0.086
510°C	Oxide	H.C.B.	350	0.022	6.2×10^{-5}	1.7×10^{-4}
554°C	Oxide	H.C.B.	350	16.3	0.046	0.067
620°C	Oxide	H.C.B.	350	148	0.42	0.46
510°C	Oxide	C.A.B.***	350	< 0.13	$<3.7\times10^{-4}$	<0.002
554°C	Oxide	C.A.B.	350	0.13	3.7×10^{-4}	0.002
620°C	Oxide	C.A.B.	350	26.2	0.075	0.10

* Refers to sum of the weights of simulations resulting in Sodium Boiling

** This failure probability has not converged. Actual failure probability is likely higher than this value

*** H.C.B.=Hot Channel Boiling, C.A.B.=Core Average Boiling

(iii.b.4) Station Blackout Results

Figure 46 shows the USBO LBEs plotted on the Frequency Consequence Curve. While both oxide and metal cores respond adequately to USBOs at outlet temperatures up to 620°C, the metal core provides much greater margin to the FCC than the oxide core. It should be noted that hybrid LBE methodology would still allow for oxide fuel to operate at a steady state core outlet temperature of 554°C without a VPORS as only 0.2% of the oxide simulations reach bulk boiling at this temperature. When combined with the 0.007/yr initiating frequency for the LOF, the frequency of radioactive material release for this highly conservative hybrid methodology is still below the FCC frequency limit ($1.4\text{x}10^{-5}$/yr < $1\text{x}10^{-3}$/yr).

The LBE release frequencies were calculated by multiplying the SBO initiating frequency by the conditional probability of arriving at an end state shown in Table 19. The probability of arriving at an end state are calculated by using Eq. IV.6 and Eq. IV.7 and thus exclude simulations which also include a more severe end state. It should be noted that the probability of Cladding Failure (C.F.) goes down for oxide fuel between 554°C and 620°C because some simulations that were C.F entered the Hot Channel Boiling (H.C.B.) end state at the higher temperature.

Table 19 – Summary of Conditional End State Probabilities (mean/95th percentile)

	OK	C.F.	H.C.B.	C.A.B.
Metal 620°C	0.94/0.95	-/-	0.065/0.086	-/-
Oxide 510°C	0.61/0.65	0.39/0.44	$6\text{x}10^{-4}/3\text{x}10^{-3}$	-/-
Oxide 554°C	0.022/0.036	0.93/0.95	0.046/0.066	$5\text{x}10^{-5}/9\text{x}10^{-3}$
Oxide 620°C	0.002/0.007	0.58/0.62	0.35/0.39	0.07/0.10

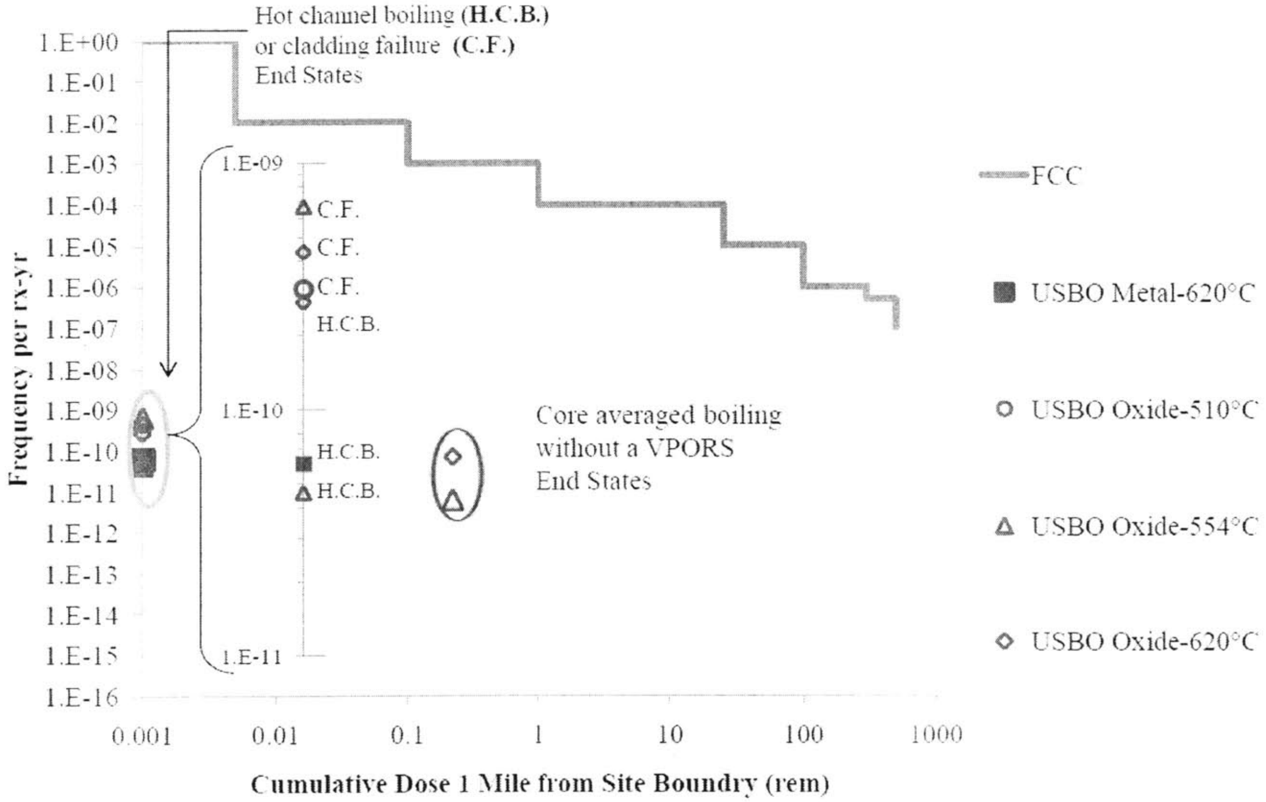

Figure 46– Frequency Consequence Curve with USBO Points Plotted for Metal and Oxide Fuel at a Variety of Core Outlet Temperatures.

(iv) Summary of Safety Analysis Limits on Core Outlet Temperature

The UTOP points and USBO LBEs illustrate that even with highly unreliable, or highly uncertain, reactor protection systems, the TNF should allow operating temperatures less than or equal to 550°C for both metal and oxide fuel. Thus, the core outlet temperature should be set at the steady state limit of 550°C.

IV.3.C Safety Analysis of Vessel and Piping for Elevated Temperatures

In a pool type reactor, all piped sodium is in the intermediate loop and thus non-radioactive. Thus, sodium pipe leaks are not governed by the FCC and no formal safety analysis is conducted in this case study. In general, even non-radioactive sodium leaks have caused close regulatory scrutiny and sodium pipes will be rigorously analyzed to ensure reliability. This report did not perform a detailed safety study on thermal stresses applied to the vessel and piping materials.

IV.3.D Safety Impacts of Removing the Intermediate Loop

The primary safety impacts concerning the primary cycle are that, in the event of a heat exchanger or steam generator break, the steam or other working gas may:

- enter the core causing a reactivity excursion due to the positive sodium void worth of SFR cores
- pressurize the primary vessel causing a break in the vessel head or seal leakage

These consequences are all but eliminated with an intermediate loop, because the intermediate loop is non-radioactive and provides an additional boundary to the primary system. Eliminating the intermediate loop is only practical for loop-type designs. Eliminating the intermediate loop, though effective in increasing efficiency, has safety implications, and there are other options for increasing efficiency without additional safety concerns. If the intermediate loop were eliminated in the pool design, the SFR will be in violation of NUREG-1860 because rupture of the IHX plenum could constitute a single failure that could lead to core damage (1). In the loop design, primary sodium must be pumped out of the vessel and into the IHX via primary sodium piping. The loop design introduces the large LOCA as a credible accident sequence, and therefore must be evaluated for its safety consequences in the PRA.

IV.3.E Safety Impacts of Switching to PCHEs

Due to robustness of PCHEs, no detailed safety analysis was conducted for PCHEs compared to standard shell and tube heat exchangers.

IV.3.F Safety Impacts of Switching from a Rankine to a S-CO_2 Power Conversion System

As the balance of plant is non-safety related, no detailed safety analysis was conducted for the S-CO_2 cycle compared to the Rankine cycle. The potential need for a redan system to prevent gas from entering the core if the intermediate loop is removed has been discussed in Section IV.3.D.

IV.4 Economic Benefit and Ranking of Design Alternatives

This section presents an analysis of how each of the design modifications affects the thermodynamic efficiency of the plant. Then, any efficiency changes will be analyzed to examine the effect on the levelized cost of electricity.

IV.4.A Design Alternatives Analyzed for Efficiency Impacts

Section IV.4.A reviews the results of an efficiency study conducted by Ludington in support of NERI contract (DE-FG07-07ID14888), the same contract which supports this thesis. A detailed description of the underlying analysis can be found in (58). The option space described in Figure 42 has been tabulated in Table 20. Twenty-four cases were examined, but only 18 are displayed in Table 20. The last six cases (numbers 19-24) correspond to the elimination of the intermediate loop for a pool design, which was determined to be impractical for safety and efficiency reasons.

Table 20 - Cases Considered for the Thermodynamic Efficiency Study. PCHE refers to Printed Circuit Heat Exchangers and S-and-T refers to Shell and Tube Heat Exchangers (58).

Case Number	P-IHX	S-IHX	Type	PCS
1	PCHE	PCHE	Pool/Loop	Water (15.5 MPa)
2	PCHE	PCHE	Pool/Loop	CO_2
3	PCHE	PCHE	Pool/Loop	Water (23 MPa)
4	PCHE	S-and-T	Pool/Loop	Water (15.5 MPa)
5	PCHE	S-and-T	Pool/Loop	CO_2
6	PCHE	S-and-T	Pool/Loop	Water (23 MPa)
7	S-and-T	PCHE	Pool/Loop	Water (15.5 MPa)
8	S-and-T	PCHE	Pool/Loop	CO_2
9	S-and-T	PCHE	Pool/Loop	Water (23 MPa)
10	S-and-T	S-and-T	Pool/Loop	Water (15.5 MPa)
11	S-and-T	S-and-T	Pool/Loop	CO_2
12	S-and-T	S-and-T	Pool/Loop	Water (23 MPa)
13	----------	PCHE	Loop Only	Water (15.5 MPa)
14	----------	PCHE	Loop Only	CO_2
15	----------	PCHE	Loop Only	Water (23 MPa)
16	----------	S-and-T	Loop Only	Water (15.5 MPa)
17	----------	S-and-T	Loop Only	CO_2
18	----------	S-and-T	Loop Only	Water (23 MPa)

Table 20 shows the results of the efficiency comparison for a constant core outlet temperature of 510°C and 530°C. The temperature listed in Table 20 is the turbine inlet temperature.

Table 21 - Efficiency Comparison of SFR Cases for a Core Outlet Temperature of 510°C and 530°C

	510°C Core Outlet Temperature		Δ Efficiency	530°C Core Outlet Temperature		Δ Efficiency*
Case Number	T (turbine inlet) ($^{\circ}$C)	Efficiency (%)	From Case 10 @ 510°C	T (turbine inlet) ($^{\circ}$C)	Efficiency (%)	From Case 10 @ 510°C
1	504.4	40.7	0.4	525.6	41.2	1.5
2	501.9	41.1	0.8	522	41.9	2.6
3	503.1	~41.2	0.9	526.1	~41.8	2.2
4	505.2	40.7	0.4	526	41.2	1.5
5	500.4	41.1	0.8	520.3	42	2.8
6	475.9	~40.4	0.1	505.9	~41.3	2.1
7	486.4	40.3	0.0	505	40.7	0.9
8	483.1	40.1	- 0.2	502.5	41.1	2.0
9	487.5	~40.8	0.5	507.1	~41.3	1.6
10	486.2	40.3	0.0	506.6	40.7	0.9
11	481.2	40.1	- 0.2	500.9	41.1	2.0
12	433.5	~38.8	- 1.5	477.6	40.5	2.2
13	507.4	40.8	0.5	525.6	41.2	1.4
14	504.2	41.2	0.9	524.1	42	2.7
15	509.8	~41.4	1.1	529.7	~41.9	2.2
16	508.4	40.8	0.5	527.6	41.2	1.4
17	502.6	41.2	0.9	522.4	42.1	2.9
18	473.6	~40.3	0.0	507.5	~41.3	2.2

*The effect of temperature changes on efficiency is linearly extrapolated to 550°C.

The reference case (case 10) is an efficiency improvement over the base SFR design due to the enlarged heat transfer surface of a straight tube steam generator. Beyond this efficiency increase, it is a possible to gain an extra 2.0 % efficiency by using the S-CO_2 cycle and increasing the core outlet temperature to 530°C. If core outlet temperature is restricted to 510°C, the efficiency can be improved by about 0.9 % if S-CO_2 or supercritical water cycles are used and the P-IHX is changed to a PCHE design or eliminated altogether.

IV.4.B Evaluating Economic Impact of Efficiency Increases

Increasing the core outlet temperature increases the plant thermal efficiency, which in turn reduces the per MW cost of the reactor. Using generic cost equations to estimate costs for a nuclear reactor, it can be seen that every component of the busbar cost, e (mills/kWhre), of a nuclear reactor (capital, fuel, and O&M) is inversely proportional to the plant thermal efficiency, η (12). Thus, the effect of varying the plant efficiency by a small amount can be approximated through Eq. IV.8.

$$\frac{\delta e_{capital}}{e_{capital}} = -\frac{\delta\eta}{\eta}, \frac{\delta e_{fuel}}{e_{fuel}} = -\frac{\delta\eta}{\eta}, \frac{\delta e_{O\&M}}{e_{O\&M}} = -\frac{\delta\eta}{\eta} \qquad \text{IV.8}$$

Assuming an initial thermal efficiency of approximately 40% (5), 1% efficiency increase will result in a fractional efficiency increase of 0.025 (0.01/0.4). Capital, fuel, and O&M costs all decrease proportionally with efficiency increases, decreasing the busbar cost by 2.5%.

(i)Raising the Core Outlet Temperature to 554°C for Metal and Oxide Fuel

For the base design with a Rankine steam cycle and standard shell and tube heat exchangers an a core outlet temperature of 510°C, Case 10 in the previous analysis, efficiency increased with outlet temperature at a rate of approximately 0.025%/°C. Thus, increasing the core outlet temperature to its steady state limit of 550°C will produce a 0.9% increase in thermal efficiency. Using the rule of thumb defined above, this efficiency increase correlates to a 2.2% decrease in busbar electricity cost.

(ii)Efficiency Impacts of Removing the Intermediate Loop

Next, the impact of removing the intermediate loop, a.k.a. Case 16, is considered. As mentioned earlier, this design alternative is only feasible from a safety case with a loop type design. It should be noted that the cost of a loop reactor is assumed to be the same as the cost of a pool reactor for this analysis. Starting from the base design with a Rankine steam cycle and standard shell and tube heat exchanger, removing the intermediate loop, while keeping a shell and tube steam generator, allows for a 0.5% efficiency increase. Looking only at the effect of efficiency and taking the cost of both designs to be constant, this single change can thus decrease the busbar electricity cost by approximately 1.25%.

(iii)Efficiency Impacts of Replacing Shell and Tube Heat Exchangers with PCHEs

Next, the impact of switching heat exchanger designs to PCHEs, a.k.a. Case 1, is considered. Starting from the base design with a Rankine steam cycle and standard shell and tube heat exchanger, the PCHEs reduce temperature loss in the heat exchangers, thus increasing efficiency by 0.4%. Looking only at the effect of efficiency and taking the cost of both designs to be constant, this single change can thus decrease the busbar electricity cost by approximately 1%.

The relative costs of PCHEs and shell-and-tube heat exchangers will need to be thoroughly studied, in order to understand the long term benefit of choosing one design over the other. The performance of PCHEs relative to their cost is also important, and information on the failure modes and repair costs for all components need to be obtained, or at least estimated in the absence of experience.

(iv)Efficiency Impacts of Moving to a S-CO_2 Power Conversion System

Next, the impact of moving to the S-CO_2 cycle, a.k.a. Case 11, is considered. Starting from the base design with a Rankine steam cycle and standard shell and tube heat exchanger, the turbine inlet temperature is too low to benefit from switching to a S-CO2 cycle. In fact, a 0.2% decrease in efficiency is expected, although this difference may be within the model uncertainties of the codes used. Thus, from an efficiency standpoint, there is not a reason to move to a S-CO_2 cycle under these conditions. This design alternative will be revisited in Section IV.5 when the S-CO_2 cycle is combined with higher outlet temperatures.

The potential for reduced capital cost with the S-CO_2 cycle must also be noted. Previous work indicates that a S-CO_2 power conversion cycle would require six times less material than a traditional Rankine cycle (12). When applied through G4ECONS, the estimated cost of the secondary side decreases by a third. When cost savings is propagated through the entire plant, a savings of 12% of the direct capital cost can be expected. Since capital costs are roughly 71% of busbar costs, a 12% reduction in capital costs yields a 8.5% reduction in busbar costs. The effect of capital cost savings on busbar costs were estimated by Christopher Nitta in support of NERI contract (DE-FG07-07ID14888). A detailed description of the underlying analysis can be found in (56).

Taken in total, replacing the Rankine cycle with a S-CO_2 power conversion cycle will yield an expected 8.4% busbar cost reduction. This number considers both the 8.5% decrease in busbar due to capital and the 0.5% increase in efficiency.

(v)Ranking Design Alternatives

Table 22 ranks the economic impact of the design alternatives. As can be seen, switching to the S-CO_2 cycle is the most effective method of reducing busbar and capital cost. It should be noted that the S-CO_2 busbar saving did not arise from increasing efficiency, which was the original motivation for examining the cycle in this case study, but due to reduction in the capital cost of the S-CO_2 power conversion cycle.

Table 22– Ranking Design Alternatives Based on Decrease in Busbar Cost

Design Alternative	Case #	Rank	Decrease in Busbar Cost
Raising Outlet Temperature to 554°C	10	2	-2.8%
Removing Intermediate Loop	16	3	-1.25%*
Adopting PCHEs	1	4	-1%
S-CO_2 power conversion cycle	11	1	-8.4%

* Does not include capital cost savings from removing intermediate loop

IV.5 Further Potential Improvements Based on Available Margins

None of these design options are mutually exclusive and thus they can be combined to achieve an even greater efficiency increase. For brevity, the following design option combinations will be considered:

1. Raising the core outlet temperature, changing both primary and secondary heat exchangers to PCHEs, and adopting the S-CO_2 power conversion cycle
2. Combining the design options in option 1 with removing the intermediate loop.

IV.5.A Adopting All Proposed Design Alternatives Except Removing the Intermediate Loop

Removing the intermediate loop is controversial and thus this section examines the potential efficiency gains that can be made without removing the intermediate loop. This modification corresponds to Case 2 in Table 21. Case 2 suggests that efficiency will increase with core outlet temperature by 0.04%/°C, thus arriving at a 42.9% thermodynamic efficiency when the core outlet temperature is taken to 554°C. As the base case thermodynamic efficiency was 40.3%, by raising the core outlet temperature, changing both primary and secondary heat exchangers to PCHEs, and adopting the S-CO_2 power conversion cycle, thermodynamic efficiency was increased by 2.6%. Using the rule of thumb derived earlier, a 2.6% increase in thermodynamic efficiency corresponds to a 6.5% reduction in busbar costs.

Taken together with the direct cost savings from adopting the S-CO_2 cycle, adopting these alternatives will yield a 14.4% cost reduction. This number considers both the 8.5% decrease in busbar due to capital and the 6.5% decrease in the adjusted busbar cost due to efficiency gains.

IV.5.B Adopting All Proposed Design Alternatives

This section examines the potential efficiency gains that can be made by adopting all of the proposed design modifications. This modification corresponds to Case 14 in Table 21. Case 14 suggests that efficiency will increase with core outlet temperature by 0.04%/°C, thus arriving at a 43.0% thermodynamic efficiency when the core outlet temperature is taken to 554°C. As the base case thermodynamic efficiency was 40.3%, by raising the core outlet temperature, changing both primary and secondary heat exchangers to PCHEs, and adopting the S-CO_2 power conversion cycle, thermodynamic efficiency was increased by 2.7%. Using the rule of thumb derived earlier, a 2.7% increase in thermodynamic efficiency corresponds to a 6.8% reduction in busbar cost of electricity.

Taken together with the direct cost savings from adopting the S-CO_2 cycle, adopting these alternatives will yield a 14.5% cost reduction. This number considers both the 8.5% decrease in busbar cost due to capital and the 6.6% decrease in the adjusted busbar cost due to efficiency gains.

IV.5.C Ranking All Design Alternatives

Table 23 ranks the economic impact of the design alternatives. As can be seen, combining all of the design alternatives produces the greatest reduction in busbar cost (Rank 1). It should be noted that the case of all the design alternatives except for removing the intermediate loop is almost as effective at reducing busbar costs, and considering the added cost associated with the increased regulatory burden of removing the intermediate loop, removing the intermediate loop may not confer a significant economic incentive.

Table 23 – Ranking Design Alternatives Based on Decrease in Busbar Cost

Design Alternative	Case #	Rank	Decrease in Busbar Cost
Raising Outlet Temperature to 550°C	10	3	-2.8%
Removing Intermediate Loop	16	4	-1.25%*
Adopting PCHEs	1	5	-1%
S-CO_2 power conversion cycle	11	6	-8.4%
All Alternatives but Removing the I.L.	2	2	-14.4%
All Design Alternatives	14	1	-14.5%*

* Does not include capital cost savings from removing intermediate loop

IV.6 Assessment and Conclusions

By moving the licensing process focus to a predominately risk informed regulatory structure supported by deterministic requirements, the TNF can change the way SFR designers approach ensuring reactor safety. Emphasis is shifted away from protecting against extremely low probability accidents and toward ensuring the lowest core damage probability for more likely accidents such as protected Transient Overpowers and Loss of Flow accidents.

The proposed methodology for evaluating design alternatives takes advantage of the unique probabilistic aspects of the TNF to reduce the cost of the SFR. Steady state cladding temperature limits prevent HT-9 cladding for metal or oxide fuel from moving far beyond 550°C, and all major internal LBEs are satisfied for these temperatures. In regard to increasing thermodynamic efficiency, there is no practical difference between metal and oxide fuels within NUREG-1860. No additional system constraints exist to prevent the outlet temperature from moving to 550°C. Combined with removing the intermediate loop, changing to PCHE heat exchangers, and moving to a S-CO_2 power conversion cycle, busbar costs can be expected to decrease by 14.5%. It should be noted that when all of the design alternatives are implemented, removing the intermediate loop does not confer a significant amount of efficiency gain, and a 14.4% reduction in busbar costs can be expected with the intermediate loop in place.

V IMPROVED MODELING OF THE RATE OF METAL FUEL/CLADDING EUTECTIC FORMATION RATE

In metal fuel with an iron based cladding, the fuel and cladding constituents diffuse into each other forming a low melting point fuel/clad eutectic at high temperatures. The solid-to-liquid phase transition temperature (or liquidus temperature) for this eutectic formation varies from 650°C to 775°C, depending on the fuel and cladding combination. Above the liquidus temperature the rate of further fuel/clad eutectic formation increases by orders of magnitude. The liquid fuel/clad eutectic acts to thin the clad, thus reducing the load bearing capabilities of cladding. This cladding thinning has two implications:

1. Under typical beyond-design-basis transients, i.e. Unprotected Transient Overpower (UTOP), Unprotected Loss of Flow (ULOF) and Unprotected Loss of Heat Sink (ULOHS), the eutectic formation reduces cladding reliability by decreasing cladding thickness, thus accelerating thermal creep by increasing fission pressure induced stress on the remaining load bearing cladding.
2. Under extremely low probability beyond-design-basis transients, which would typically lead prompt criticality and then fuel vaporization, i.e. instantaneous removal of all sodium from the core region or sudden loss of flow in some designs, rapid eutectic penetration will allow the eutectic formation to breach the cladding and the molten fuel to quickly leave the core region before enough energy is release to cause fuel vaporization (51).

Due to these safety issues, the phenomenon governing the fuel/clad eutectic has been experimentally examined since the 1960s. For simplicity, these experiments have been segmented into four general categories for further discussion: uranium dripping tests, EBR-II safety tests, EBR-II furnace tests, and FFTF furnace tests (34) (68) (69) (46) (47) (70) (Tsai H. , 1990) (71). From these tests, observations have quantitatively been made concerning potential dependencies on the rate of eutectic formation. In order to quantify these dependencies, correlations are made from the test database which takes into account first and second order interactions between potential variables. Finally, model uncertainty is used to judge the predictive nature of current and newly proposed predictive relationships.

V.1 Fuel/Clad Eutectic Database

This section conducts an overview of the metallic fuel/cladding eutectic experiments conducted from the 1960s to 1994 which were designed to examine the rate of liquid phase eutectic penetration into the cladding during accident sequences. In addition to reviewing the quantitative test results, qualitative dependencies on the rate of eutectic formation determined from these experiments are explored. Potential dependencies on the liquidus temperature are examined, especially in regard to high-burnup fuel. Because constituent diffusion rates increase by orders of magnitude after the solid-to-liquid phase transition (46), eutectic penetration can effectively be neglected below the liquidus temperature.

V.1.A Methodology

Currently, the fuel/cladding eutectic penetration rate tests are distributed over many papers in the open literature and the underlying fuel specifications for each test, such as initial plutonium enrichment, beginning of life (BOL) linear power and burnup, also span many references. This review will differentiate between each major category of eutectic testing as described in Section (i). The initial conditions for the fuel before and during each test are described in Section (ii). Additionally, one of the parameters of interest, BOL linear power, was typically not explicitly provided in the open literature and thus was estimated from similar tests. The procedure for this estimation is described in Section (iii).

(i) Parameters of Interest

The fuel/cladding eutectic experiments were conducted over 40 years. During that time, different fuel forms, cladding options, and experimental procedures were used as technology improved and sodium reactor designs matured. The range of fuel/cladding eutectic experiments can be divided into four general categories:

1. Uranium Dripping Tests – 306SS test slugs were dipped into molten uranium to determine eutectic penetration rates,
2. EBR-II Safety Tests – In-reactor tests where the sodium flow rate was purposely restricted in an assembly to cause higher than nominal temperatures to enable eutectic formation,

3. EBR-II Furnace Tests – UZr and UPuZr fuels were irradiated in EBR-II over a range of claddings, plutonium enrichments, burnups, and linear powers and subsequent eutectic tests were conducted in a high temperature furnace,
4. FFTF Furnace Tests – A full length IFR Driver Fuel pin, U 19%PU 10% Zr, was irradiated in FFTF to 9.5at% burnup and subsequent eutectic tests were conducted in a high temperature furnace.

(ii) Parameters of Interest

Since the 1960s, metallic fuel proponents have been running experiments to determine the safety implications of the formation of fuel/cladding eutectic. These experiments have demonstrated that cladding choice, fuel composition, burnup, initial plutonium loading, linear power, test temperature and time at test temperature all influence the rate of fuel/cladding eutectic formation. It is interesting to note that the steady state irradiation temperature of the fuel and cladding were not found to significantly affect the rate of eutectic formation during off-normal conditions (34). The ranges for the variables examined during the metallic fuel testing program are presented in Table 24.

Table 24 - Tested Parameters of Governing Fuel/cladding Eutectic Formation

Parameter	*Options*
Cladding composition	316SS, D9, HT9
Fuel composition	U, UZr, UPuZr
Burnup	(0-17at%)
Initial Pu Loading	(0-26wt%Pu)
BOL Linear Power	(0-15.7 kW/ft)
Test Temperature	650°C -1100°C
Time at Test Temperature	0-24hrs

(iii) EBR-II Linear Power Estimation

By the 1990s, Integral Fast Reactor (IFR) fuels researchers determined that both the fuel/cladding eutectic liquidus temperature and the rate of formation depend on the steady state linear power for that portion of the pin. Unfortunately, earlier studies omitted either the BOL or burnup-averaged linear power of the test sections. For most tests, enough evidence exists to estimate the steady state linear power of the test segments, albeit with large uncertainties.

Through knowledge transfer efforts conducted by ANL and INL, the axial position (72) and peak linear power (37) for a majority of the test sections are available. This information can be combined with a normalized power profile created using 27 data points from the DP-16, DP-17 and DP-21 samples in the X441 EBR-II test assembly (46). These data points are plotted in Figure 47 and the resulting 6th order polynomial fit with a R^2 of 0.98 is presented in Eq. V.1. It should be noted that this fit only applies to EBR-II test pins and still has unresolved errors associated with the fitting data. Predictive errors may exceed 10% of the estimated linear power, especially in the bottom half of the assembly where the fitting data is sparse. Linear power estimates determined using this fit will be noted with the superscript ^{fit} in this paper.

$$P'\left(\frac{x}{L}\right) = 33\left(\frac{x}{L}\right)^6 - 120\left(\frac{x}{L}\right)^5 + 180\left(\frac{x}{L}\right)^4 - 130\left(\frac{x}{L}\right)^3 + 48\left(\frac{x}{L}\right)^2 - 9.8\left(\frac{x}{L}\right) + 1.38 \qquad \text{V.1}$$

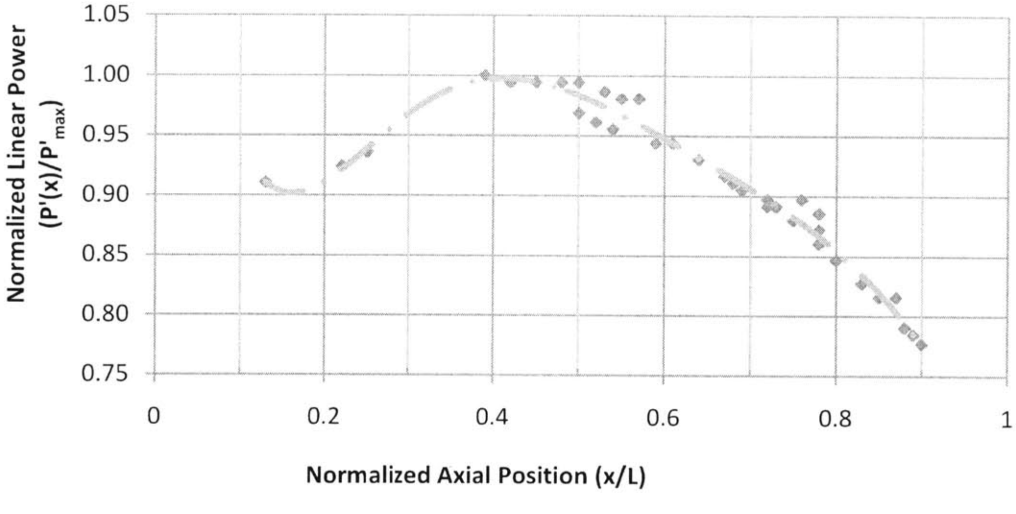

Figure 47 - Linear Power Profile for the DP-16, DP-17 and DP-21 Samples in the X441 EBR-II Test Assembly. (34)

V.1.B Fuel/Clad Eutectic Data

The following section overviews the experiments conducted in each of the four general fuel testing categories. Trends and dependencies correlated to the fuel/cladding eutectic formation during each testing period are discussed and the test results of interest are displayed in tables for each section.

(i) Uranium Dripping Tests

The uranium dripping tests were conducted to support severe accident analysis for the first loading of EBR-II (73) metallic driver fuel. Uranium metal melts at 1235°C but the U-Fe system can form two low melting point eutectics, U-77at%Fe which melts at 1080°C and U-34at%Fe which melts at 725°C. The kinetics of these three systems should be different, thus all three systems were examined. The dipping tests involved heating the molten uranium system to within 5°C of the desired test temperature and then dipping a pre-heated 760 μm (±5%) 304SS test sample into the uranium system bath. The sample was held in the bath until the eutectic penetrated through the entire thickness of the sample, at which point the sample was removed.

Because the U-34at%Fe system has the lowest melting point, it is the most safety significant dataset. The pure uranium melt data shows slightly faster penetration (within 15%) than the U-34at%Fe results while the U-77at%Fe penetration rates were two orders of magnitude slower than the U-34at%Fe results. Because of the lower eutectic formation temperature, the U-34at%Fe system dataset was chosen to represent expected eutectic behavior for the Bauer correlation which is used in safety analysis codes such as SAS4A (19).

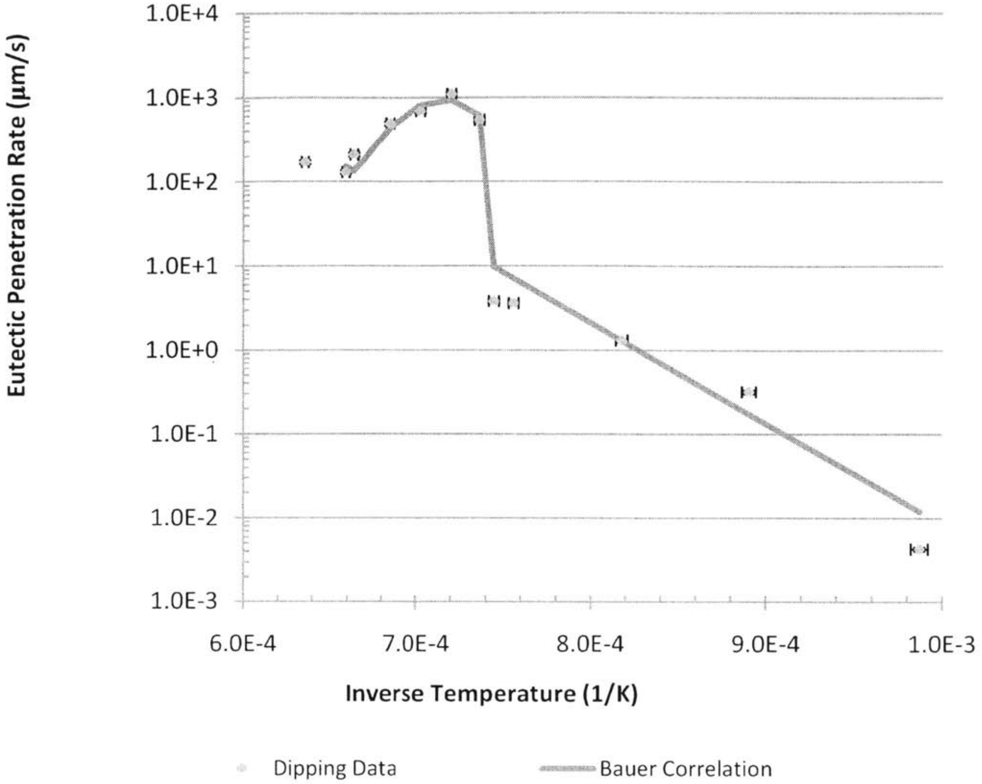

Figure 48 - Uranium Drip Test Penetration Rates for the U-34at%Fe Eutectic System with Experimental Error Bars

As can be seen from Figure 48, the eutectic penetration rate increases in an Arrhenius manner with increasing temperature between 725°C and 1080°C ($9.9\text{x}10^{-4}K^{-1}$ and $7.4\text{x}10^{-4}K^{-1}$). Above this temperature, the UFe_2 layer between the cladding and the liquid front disappears allowing for accelerated eutectic penetration. These eutectic penetration rates are listed in Table 25. Additional melt experiments above 1100°C with Type 430SS and Armco iron confirm that the breakdown of the UFe_2 layer is not cladding dependent (74).

Table 25 - Uranium Drip Test Eutectic Penetration Data between Uranium and SS304 (73)

Temperature (°C)	Penetration Rate (µm/s)
740	0.0043
850	0.32
950	1.3
1050	3.6
1070	3.8
1085	540
1115	1100
1150	690

1187	490
1233	210
1244	130
1300	170

(ii) EBR-II Safety Tests

The Mark-I driver fuel for EBR-II, and the subsequent Mark-II driver fuel, was composed of 95 wt% uranium and 5 wt% fissium alloy, a collection of noble metals left in the fuel after the melt-refining and injection casting process (13). Early eutectic tests were conducted by heating pre-irradiated fuel elements in a high temperature furnace until cladding rupture occurred. It was assumed that eutectic penetration was the only failure mechanism, and thus failure only occurred due to complete eutectic penetration of the cladding. Thus while reporting effective eutectic penetration rates, these studies actually reported an integral damage quantity which the studies suggest are a combination of eutectic penetration with thermal creep, fission gas pressure and irradiation damage (75).

The first EBR-II driver fuel tests which used Scanning Electron Microscope (SEM) images to determine the eutectic penetration of irradiated cladding came during qualification tests before EBR-II could conduct its Loss-of-Flow and Loss-of-Heat-Sink without SCRAM tests (70). In the qualification experiment, the XY-22 assembly was orificed to restrict sodium flow enough to create a peak cladding temperature of 600°C when the reactor was operating at 24MW$_{th}$. The control rods were then quickly withdrawn to raise reactor power to 45MWth. The reactor maintained this power for 2520 seconds until a fuel pin breach was detected and the reactor was quickly powered down. The results of this test are presented in Table 26. It should be noted that the amount of eutectic penetration during the test decreases with increasing burnup and the two high burnup test sections showed no liquid phase formation. This test indicates that eutectic penetration becomes less of a concern with higher burnup fuel, a result which was confirmed during later IFR fuel testing. Unfortunately, neither the burnup-averaged linear power nor the axial positions of the test elements were provided. This omission makes it impossible to determine if linear power dependencies exist for this test.

Table 26 -EBR-II Driver Fuel Test Results for UFs with 316SS Cladding and a Peak Linear Power of 7.62 kW/ft (70)

Assembly/ Element	Average Test Temperature (°C)	Penetration Rate (μm/s)	Burnup (at%)	Eutectic Formation?
XY-22/ E-23	769	0.040	0.0	Yes
XY-22/E-33	778	0.030	2.42	Yes
XY-22/E-24	793	0.020	3.95	Yes
XY-22/ E-32	759	0.005	7.5	No
XY-22/ E-16	793	0.005	7.69	No

(iii)EBR-II Furnace Tests

The majority of ANL fuels testing in the 1980s and 1990s was devoted to qualifying UZr and UPuZr fuel for use in the IFR program. Thus, a majority of the fuel/cladding eutectic formation testing was also conducted for these fuels. These tests extended over the largest span of parameters including burnups up to 17at% and plutonium enrichments up to 26wt%. This section will first cover UZr fuels and then move on to plutonium bearing fuels.

UZr fuels were the next evolution of metallic fuel after the UFs EBR-II driver fuel. Zirconium was added to the uranium to help stabilize the alloy, reduce irradiation induced swelling and act as a diffusion barrier (13). Most of the fuel/cladding eutectic data for this fuel was derived from pins irradiated in EBR-II test assemblies. Once the desired burnup was reached, the pins were removed from EBR-II and transferred to the Fuel Behavior Testing Apparatus (FBTA) to be chopped into test sections and placed in a high temperature furnace for elevated temperature testing. After the high temperature testing was complete, the samples were examined using a SEM which determines the penetration depth in a sample to within 10μm (76). This uncertainty is primarily due to axial variation in the sample and is not limited by the SEM system. Figure 49 shows the basic trends of the UZr FBTA tests. Due to the limited dataset very few concrete conclusions can be made, but two points should be noted (46) (71):

1. The effect of burnup on the rate of eutectic penetration is not simple. From Figure 49, it can be seen that increasing burnup for UZr with 316SS cladding appears to decrease eutectic penetration rates from 750°C to 850°C by a constant factor with little change in the penetration rate's sensitivity to temperature. UZr with D9 cladding exhibits more

complex behavior, with burnup decreasing high temperature eutectic penetration rates and increasing low temperature eutectic penetration rates.

2. The phenomenon governing the liquidus temperature also seems to be complex. No UZr pin experienced eutectic formation below 725°C, the eutectic point for the binary U-Fe system, and the 88-11 test showed no eutectic formation at 750°C. While longer tests may yield lower eutectic temperatures, it is reasonable to assume that the liquidus temperature is also a complex function of cladding type, burnup, linear power and fuel composition.

Table 27 summarizes the UZr fuels tests. Many of the eutectic penetration rates were extracted from poor quality log-log plots and thus may only be accurate to within ±10% of the listed penetration rates. Figure 49 only plots fuel/cladding tests where the temperature dependency of a given cladding type and burnup is available.

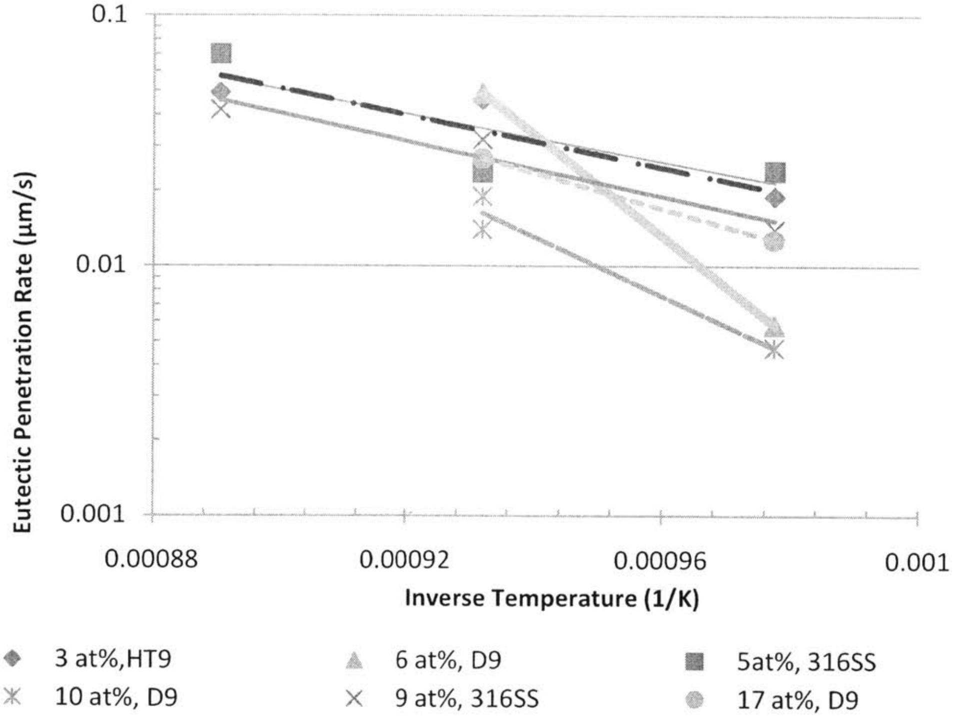

Figure 49 - Trends for UZr FBTA 1-hr Eutectic Penetration Rate Tests

The main objective of the fuels testing program was to qualify IFR driver fuel which would have would have to incorporate initial TRansUranic (TRU) isotope loading. In order to qualify TRU fuels, ANL first had to qualify Pu bearing fuels. The tests conducted in support of qualifying Pu fuels are summarized in Table 28 and

Table 29. It should be noted that test 90-01 was identified by ANL as an outlier (71) and thus conclusions drawn from this data point should be made with caution. This test element experienced excessive swelling near the mid-plane of the pin, allowing the fuel to expand to meet the new inner cladding surface. This expansion caused the high zirconium buffer layer between the inner, low zirconium fuel and the cladding to break down. Thus, low zirconium fuel was allowed to interact directly with the cladding and excessive fuel/cladding interaction was experienced. In order to verify that test 90-01 is not representative of typical fuel behavior, an additional sample was tested at the same temperature (750°C) from a higher elevation in the pin. That additional test, 90-02, was more consistent with the existing fuel/cladding eutectic database.

Table 27 - EBR-II UZr Fuel/Cladding Eutectic Test Summary[10]

Assembly/ Test No.	**Test Temperature (°C)**	**Burnup (at%)**	**Cladding Type**	**Axial Position (x/L)**	**Linear Power (kW/ft)$^{\text{fit}}$**	**Test Length (hours)**	**Penetration Rate (μm/s)**	**Eutectic Formation?**
X425/88-02	850	3*	HT9	0.87	11.8	1	0.049	Yes
X425/88-04	800	3	HT9	0.46	14.6	1	0.046	Yes
X425/88-05	750	3	HT9	0.48	14.5	1	0.019	Yes
X425/88-06	700	3	HT9	0.52	14.2	1	0.046	No
X425/88-13	725	3	HT9	0.56	14.5	1	0.019	No
X423/89-06	750	5	316SS	0.52	12.7	1	0.024	Yes
X423/89-08	850	5	316SS	0.45	12.9	1	0.070	Yes
X423/89-13	800	5	316SS	0.61	12.4	0.2	0.013**	Yes
X423/89-13	800	5	316SS	0.58	12.4	0.4	0.013**	Yes
X423/89-05	800	5	316SS	0.55	12.6	1	0.025**	Yes
X423/89-15	800	5	316SS	0.64	12.1	2	0.008**	Yes
X423/89-16	800	5	316SS	0.67	12.0	4	0.005**	Yes
X420/88-09	725	6	D9	0.89	8.6	1	0.002	No
X420/88-08	750	6	D9	0.91	8.4	1	0.0058	Yes
X420/88-07	800	6	D9	0.93	8.2	1	0.049	Yes
X429/88-20	800	8	HT9	0.27	12.4	0.13	0.028**	Yes
X429/88-21	800	8	HT9	0.30	12.6	0.25	0.032**	Yes
X429/88-19	800	8	HT9	0.25	12.2	0.5	0.022**	Yes
X429/88-18	800	8	HT9	0.2	11.9	1	0.029**	Yes
X429/88-17	800	8	HT9	0.23	12.0	2	0.027**	Yes
X421/89-02	800	9	316SS	0.48	11.9	1	0.032	Yes
X421/89-03	850	9	316SS	0.52	11.7	1	0.042	Yes
X421/89-04	750	9	316SS	0.45	11.9	1	0.014	Yes
X420/88-11	750	10	D9	0.76	10.5	1	0.0047	No
X421/88-12	800	10	D9	0.78	10.4	1	0.014	Yes
X421/88-14	800	10	D9	0.74	10.7	1	0.019	Yes
X421/90-08	725	17	D9	0.78	10.9	1	0.001	No
X421/90-07	750	17	D9	0.82	10.1	1	0.013	Yes

***Fuel/Clad gap had not closed prior to high temperature testing. **Corrected penetration rates to remove instantaneous liquefaction due to steady state diffusion. *** It is unclear if this test is 90-04, 90-05 or 90-06 with corresponding $^{x}/_{L}$ locations of 0.51, 0.87 and 0.53.**

---

[10] Extracted by the autor from: (72) (71) (41) (41)

Table 28 - EBR-II UPuZr Fuel/Cladding Eutectic Test Data Summary[11]

Assembly/ Element	Test Temperature (°C)	Plutonium Loading (wt% Pu)	Burnup (at%)	Cladding Type	Axial Position (x/L)	Linear Power (kW/ft)	Test Length (hours)	Penetration Rate (µm/s)	Eutectic Formation ?
X420/86-66	800	19	2.3	D9	N/A*	11.0*	0.083	0.043	Yes
X420/86-56	920	19	2.3	D9	N/A*	11.0*	0.083	0.14	Yes
X420/86-59	975	19	2.3	D9	N/A*	11.0*	0.083	0.42	Yes
X420/86-54	1000	19	2.3	D9	N/A*	11.0*	0.083	0.68	Yes
X420/86-55	1100	19	2.3	D9	N/A*	11.0*	0.083	2.9	Yes
X430/90-17	800	26	2.3	HT9	0.80	12.8 $^{\text{fit}}$	1	0.015	Yes
X425/87-74	700	19	3	HT9	0.69	13.4 $^{\text{fit}}$	1	0	No
X425/87-75	750	19	3	HT9	0.71	13.2 $^{\text{fit}}$	1	0.014	Yes
X425/87-76	780	19	3	HT9	0.74	13.3 $^{\text{fit}}$	1	0.017	Yes
X423/88-22	700	26	4.7	316SS	0.54	12.6 $^{\text{fit}}$	1	0	No
X423/88-23	750	26	4.7	316SS	0.60	12.3 $^{\text{fit}}$	1	0	No
X423/88-24	800	26	4.7	316SS	0.57	12.5 $^{\text{fit}}$	1	0.009	Yes
X423/88-26	850	26	4.7	316SS	0.63	12.2 $^{\text{fit}}$	1	0.0021	Yes
X423/89-12	800	26	4.7	316SS	0.80	11.1 $^{\text{fit}}$	0.4	0.017	Yes
X423/89-09	800	26	4.7	316SS	0.70	11.8 $^{\text{fit}}$	1	0.010	Yes
X423/89-10	800	26	4.7	316SS	0.73	11.6 $^{\text{fit}}$	2	0.0079	Yes
X423/89-11	800	26	4.7	316SS	0.78	11.3 $^{\text{fit}}$	4	0.0051	Yes
X423/88-25	670	26	4.7	316SS	0.45	12.9 $^{\text{fit}}$	7	0	No
X423/88-28	710	26	4.7	316SS	0.4	13.0 $^{\text{fit}}$	7	0	No
X423/88-27	740	26	4.7	316SS	0.48	12.9 $^{\text{fit}}$	7	0	No
X423/89-01	770	26	4.7	316SS	0.42	13.0 $^{\text{fit}}$	7	0	No
X441/92-05	725	19	5.6	HT9	0.48	14.8 $^{\text{fit}}$	7	0.0029**	Yes
X441/92-03	740	19	5.5	HT9	0.57	14.3 $^{\text{fit}}$	1	0**	No
X441/92-18	750	19	5	HT9	0.76	13.1 $^{\text{fit}}$	1	0.0011**	Yes
X441/91-09	770	19	5.6	HT9	0.39	14.9 $^{\text{fit}}$	1	0.0075**	Yes
X441/91-15	740	19	9.2	HT9	0.89	11.7 $^{\text{fit}}$	1	0.013**	Yes
X441/92-08	800	19	5.6	HT9	0.42	14.9 $^{\text{fit}}$	0.1	0.0050**	Yes
X441/92-07	800	19	5.6	HT9	0.45	14.9 $^{\text{fit}}$	0.5	0.043**	Yes
X441/91-01	800	19	5.5	HT9	0.55	14.4 $^{\text{fit}}$	1	0.030**	Yes

***Axial positions were not available for these tests. Peak BOL linear heat rates are reported. **Corrected penetration rates to remove instantaneous liquefaction due to steady state diffusion.** (34)

---

[11] Extracted by the author from: (69) (46) (47) (34) (72) (71) (37) (41) (68)

Table 29 - EBR-II UPuZr Fuel/Cladding Eutectic Test Data Summary (Cont.)[12]

Assembly/ Element	**Test Temper-ature (°C)**	**Plutonium Loading (wt% Pu)**	**Burnup (at%)**	**Cladding Type**	**Axial Position (x/L)**	**Linear Power (kW/ft)**	**Test Length (hours)**	**Penet-ration Rate (µm/s)**	**Eutectic Form-ation ?**
X441/92-06	800	19	5.6	HT9	0.50	14.7 $^{\text{fit}}$	2	0.020**	Yes
X441/91-33	625	19	10.7	HT9	0.69	13.6 $^{\text{fit}}$	1	0.0022**	No
X441/91-31	650	19	10.4	HT9	0.75	13.2 $^{\text{fit}}$	1	0.0046**	No
X441/91-19	650	19	9.3	HT9	0.88	11.9 $^{\text{fit}}$	1	0**	No
X441/91-02	675	19	11.0	HT9	0.25	14.0 $^{\text{fit}}$	1	0**	No
X441/91-32	650	19	11.1	HT9	0.61	14.1 $^{\text{fit}}$	12	0.0003**	No
X441/91-36	660	19	10.9	HT9	0.64	13.9 $^{\text{fit}}$	12	0.0013**	Yes
X441/91-34	675	19	10.8	HT9	0.67	13.7 $^{\text{fit}}$	12	0.0027**	Yes
X441/91-35	650	19	11.1	HT9	0.59	14.2 $^{\text{fit}}$	36	0.0004**	No
X441/91-29	700	19	9.7	HT9	0.83	12.5 $^{\text{fit}}$	1	0.0067**	Yes
X441/91-16	770	19	9.8	HT9	0.85	12.2 $^{\text{fit}}$	1	0.0088**	Yes
X441/91-17	700	19	9.8	HT9	0.83	12.5 $^{\text{fit}}$	1	0.0067**	Yes
X441/91-12	800	19	10.8	HT9	0.68	13.7 $^{\text{fit}}$	0.1	0.0**	Yes
X441/91-13	800	19	10.6	HT9	0.72	13.4 $^{\text{fit}}$	0.5	0.012**	Yes
X441/91-28	800	19	11.3	HT9	0.52	14.6 $^{\text{fit}}$	0.5	0.014**	Yes
X441/91-11	800	19	10.0	HT9	0.8	12.8 $^{\text{fit}}$	1	0.012**	Yes
X441/91-14	800	19	10.5	HT9	0.73	13.3 $^{\text{fit}}$	2	0.0064**	Yes
X441/91-31	675	19	10.5	HT9	0.72	13.4 $^{\text{fit}}$	1	0.0087	Yes
N/A/A-850	675	19	11.2	D9	0.76	14.6	1	0.028	No
N/A/A-850	700	19	11.2	D9	0.83	13.8	1	0.030	Yes
N/A/A-850	723	19	11.2	D9	0.73	15.0	1	0.03	Yes
X441/91-18	740	19	11.3	HT9	0.54	14.5 $^{\text{fit}}$	1	0.011	Yes
Pin T-608^{x}	675	19	12.6	HT9	0.76	10.8	1	0	No
Pin T-608^{x}	700	19	13.0	HT9	0.71	11.2	1	0.0006	No
Pin T-608^{x}	725	19	12.8	HT9	0.73	11.1	1	0	Yes
Pin T-608^{x}	660	19	13.1	HT9	0.69	11.3	12	0.0002	No
X421/90-02	750	19	17	D9	0.87	9.6 $^{\text{fit}}$	1	0.015	Yes
X421/90-03	800	19	17	D9	0.84	9.9 $^{\text{fit}}$	1	0.022	Yes
X421/ 90-01^{+}	***750***	***19***	***17***	***D9***	***0.5***	***11.8*** $^{\text{fit}}$	***1***	***0.050***	***Yes***

****Corrected penetration rates to remove instantaneous liquefaction due to steady state diffusion.** (34) **x Assembly or test number not provided, thus the element number is provided. +This data point is an outlier in the FBTA database.** (72)

The degree to which the liquidus temperature decreases with burnup is thought to be a function of linear power, which controls the rate of lanthanide build up in the cladding

---

[12] Extracted by the author from: (69) (46) (47) (34) (72) (71) (37) (41)

(controlled by burnup and linear power) with respect to the rate of the protective zirconium layer formation (controlled by time at temperature). The high thermal conductivity of sodium ensures that the peak cladding temperature occurs at the top of the core, where the linear heat rate is the lowest. The linear heat rate dictates the temperature gradient in the fuel, which is the primary driving force for lanthanide migration into the cladding. Because the linear heat rate is at a minimum at the top of the core, the lower temperature gradients provide less of a driving force for lanthanides to enter the cladding. Lanthanides dominate FCCI at high burnup, so the liquidus temperature is the highest where the lanthanide concentration is the lowest, at the top of the core. Short core designs, i.e., EBR-II, have fairly flat axial power distributions and thus this trend is not easily seen in the EBR-II fuel tests. Unfortunately, due to the short heating times of these furnace tests it is impossible to definitively know the steady state liquidus temperature for any of the cladding options at high burnup.

(iv)FFTF Furnace Tests

The Fast Flux Test Facility (FFTF) was an oxide driver fueled testing reactor that more closely replicates the power and temperature profile of a typical IFR design. Thus, the IFR-1 lead test assembly was irradiated in FFTF to ensure that the EBR-II fuel/cladding eutectic database would apply to other reactor designs. The results of the IFR-1 assembly tests are listed in Table 30. FFTF, like many commercial reactor designs, has a peak cladding temperature at the top of the core and a peak linear power in the mid-section of the reactor. Thus, the IFR-I tests were also designed to determine if the liquidus temperature was a function of linear power. As can be seen from Table 30, the liquidus temperature was found to increase with decreasing linear power.

Table 30 - FBTA FFTF UPuZr Fuel/Cladding Eutectic Test Data Summary (47)

Assembly	Test Temper-ature (°C)	Plutonium Loading (wt% Pu)	Burnup (at%)	Cladding Type	Axial Position (x/L)	Linear Power (kW/ft)	Penetration Rate (μm/s)	Eutectic Formation?
IFR-1	675	19	9.4	D9	0.56	15.7	0.011	No
IFR-1	700	19	9.4	D9	0.57	15.7	0.011	Yes
IFR-1	700	19	9.4	D9	0.55	15.7	0.017	Yes
IFR-1	725	19	9.4	D9	0.52	15.7	0.026	Yes
IFR-1	750	19	9.4	D9	0.53	15.7	0.027	Yes
IFR-1	700	19	9.4	D9	0.74	15.7	0.011	No
IFR-1	725	19	9.4	D9	0.75	12.4	0.013	Yes
IFR-1	750	19	9.4	D9	0.72	12.4	0.018	Yes
IFR-1	775	19	9.4	D9	0.73	12.9	0.024	Yes
IFR-1	725	19	9.4	D9	0.72	8.5	0.012	No
IFR-1	750	19	9.4	D9	0.73	8.3	0.0036	No

V.2 Overview of Existing Models

Figure 50 shows the available 1-hour averaged fuel/cladding eutectic formation data (69) (46) (47) (68) (34) (73) (72) (71) (70). The rate of fuel/cladding eutectic formation is governed by an Arrhenius equation, such as Eq. V.2, thus a transformation of the data is required to apply a linear fit.

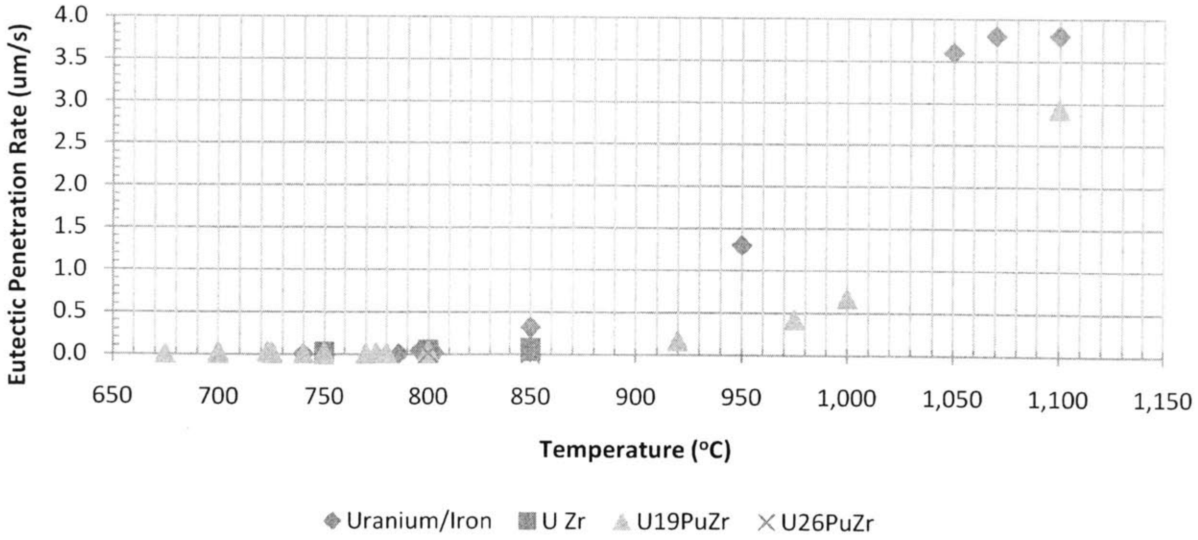

Figure 50– Untransformed Fuel/Cladding Eutectic Formation Data

Predictive models that depend exclusively on temperature are the only publicly available eutectic formation models and ignore other explanatory variables recognized to be important (47). The basic eutectic formation model is created by taking a new variable Y, which is a log transformation of the eutectic formation rate, and bounding the data with a highly conservative linear fit of a new variable X1, which is an inverse transform of the temperature data. The transformed data, seen in Figure 51, clearly exhibits more linearity than the untransformed data.

$$R = A\,e^{\frac{B}{T}}\ \left(\frac{\mu m}{s}\right) \qquad \text{V.2}$$

Eq. V.2 can be rewritten as Eq. V.3:

$$ln\left(\frac{R}{A}\right) = \frac{B}{T} \qquad \text{V.3}$$

Introducing the new variable defined in Eq. V.4,

$$Y = ln\left(\frac{R}{A}\right) \qquad \text{V.4}$$

and Eq. V.5,

$$X1 = \frac{1}{T} \qquad \text{V.5}$$

yields the linear Eq. V.6.

$$Y = B * X1 \qquad \text{V.6}$$

Currently, the fuel/cladding eutectic rate is modeled by the 1 variable Bauer correlation (Eq.V.7). This correlation was created using uranium melt tests in 1962 and was never updated with additional data developed during the IFR program. The ANL correlation (Eq. V.8) (72), while not used in the SFR safety analysis code SAS4a (19), is another 1 variable correlation referenced by the ANL's fuel testing program as a potential bounding correlation to the ternary fuel/cladding penetration rates between 650°C to 800°C. These correlations are listed below:

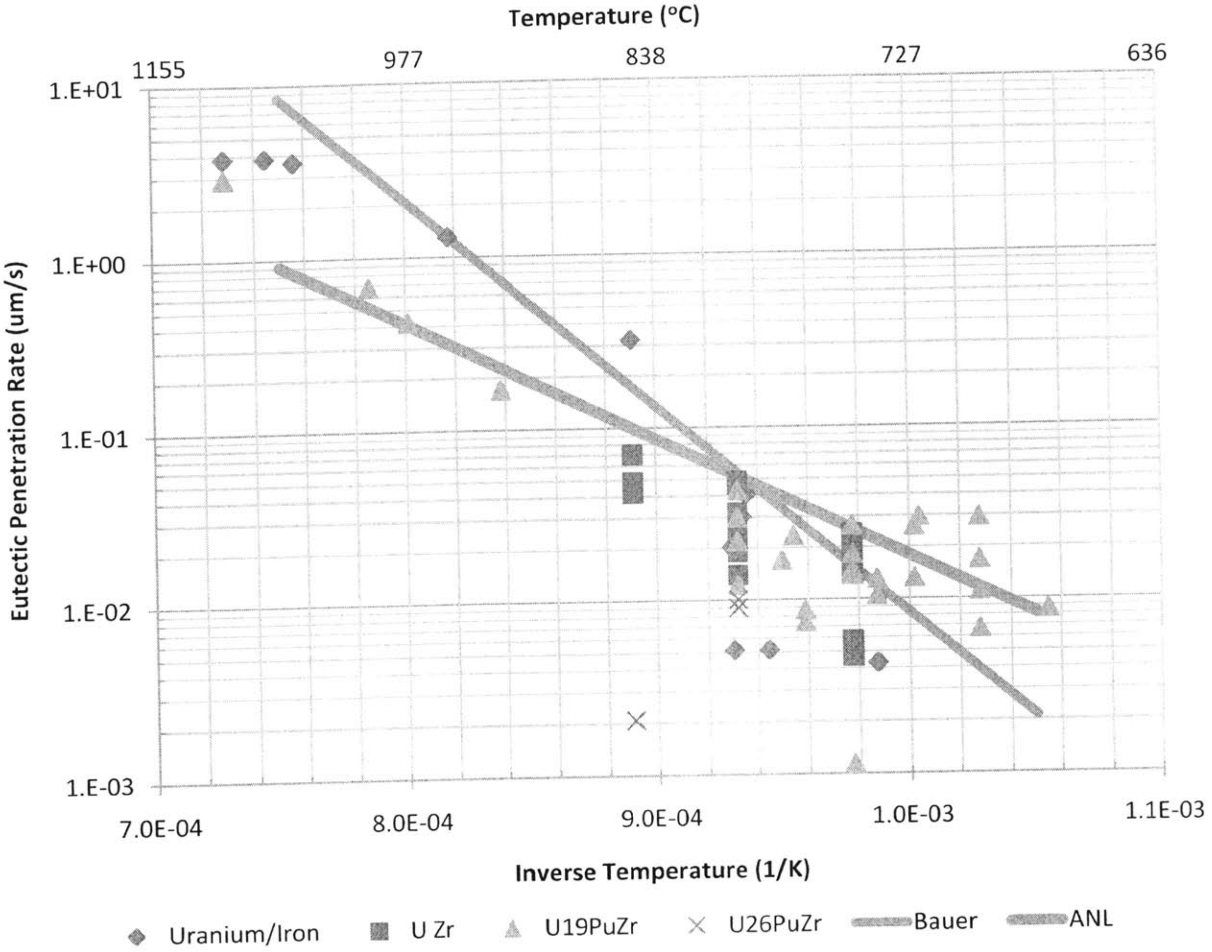

Figure 51– Transformed Fuel/Cladding Eutectic Formation Data

Bauer correlation:

$$\dot{r} = \exp(22.847 - 27624\,InvT)\left(\frac{\mu m}{s}\right) \quad \text{V.7}$$

ANL correlation:

$$\dot{r} = \exp(11.646 - 15665\,InvT)\left(\frac{\mu m}{s}\right) \quad \text{V.8}$$

V.3 Creation and Verification of New Models using Multivariable Linear Regression

Because it would be useful for reactor designers to understand how design options, i.e. fuel type, cladding type and fuel enrichment, and operational parameters, i.e. fuel/cladding interfacial temperate and burnup, affect the rate of fuel/cladding eutectic formation, a database of fuel/cladding eutectic penetration rates was collected and multivariable regression correlations were fit to the data. The fuel/cladding eutectic formation data are limited and what data exists spans over the variables listed in Table 31. The database examined includes 61 data points and is divided using stratified random sampling into two groups, with 80% of the data used in the training group to fit new correlations using the statistical code JMP (28), and 20% of the data are used to verify the models. Stratified random sampling is employed in order to ensure that all types of data are equally represented in both the training and validation data sets. The predictive worth of each of the correlations is determined by using the correlations to predict the verification data.

Table 31 - Regression Variable Types and Symbols.
Categorical variables take the value of 1 if true and 0 if false. Continuous variables are valid in the range given.

Variable	*Type*	*Symbol*
Cladding composition (SS-316, HT9, D9)	Categorical	SS, D9 (HT9 treated implicit)
Fuel composition (UZr or UPuZr, UF_i or U)	Categorical	Zr (U treated implicit)
Burnup (0-17at%)	Continuous	Bu
Enrichment (0-26wt%Pu)	Continuous	En
BOL Linear Power (0-15.7 kW/ft)	Continuous	P
Inverse Temperature (1.05×10^{-3}-7.28×10^{-2} K^{-1})	Continuous	InvT

Except for the inverse temperature term, these explanatory variables shift the y intercept fit up or down depending on the state of the fuel pin at the beginning of the transient. In order to determine how fuel form, burnup, enrichment or linear power change the temperature sensitivity of the correlation in $\left(\frac{\frac{\mu m}{s}}{\left(\frac{1}{K}\right)}\right)$, interaction terms must be considered. An interaction term is a term where two or more explanatory variables appear in the same term with one fitting coefficient.

The final linear model takes the form of Eq. V.9, and then the variables are transformed back into their original units. Of course, all of these variables will not be statistically significant and many will be weeded out in the final model to preserve degrees of freedom.

$$Y = InT\,(A + B * SS + C * D9 + D * Zr + E * Bu + F * En + G * P) + H * HT9 + I * D9 + J * Zr + K * Bu + L * En + M * P + N \qquad \text{V.9}$$

From the fuel/cladding eutectic training data, two correlations were created. The 1st order interactions correlation showed statistically significant dependencies between the fuel/cladding eutectic formation rate and fuel/cladding interfacial temperature, plutonium enrichment, linear power, cladding type, and a first order interaction between burnup and linear power. Bolded terms indicate variables in which the 95th percentile error bars extend beyond zero, and thus statistically may not exist. Many sources cite a known dependence on eutectic penetration rate with fuel composition but, as can be seen from Eq. V.10, the 1st order model did not resolve a dependence. Thus, Eq. V.11 incorporates the 2nd order interaction terms into the regression model in an attempt to resolve this dependency, although at the cost of severely reducing the statistical certainties around the constant and inverse temperature terms. These two correlations are shown below.

First order interactions correlation (R^2_{adj} =0.80):

$$\begin{aligned}\dot{r} = \exp(&10.0 - 17800\, InvT - 0.051\, En - \boldsymbol{0.026\, Bu} + 0.27\, P \\ &+2657\, [InvT - 9.4x10^{-4}]\, [P - 10.9] + 0.046\, [Bu - 6.73]\, [P - 10.9] \\ &+SS\, [\boldsymbol{-0.004} + 19900\, \{InvT - 9.4x10^{-4}\}] \\ &+D9\, [0.77 + 0.65\, \{En - 9.2\} - 0.35\, \{P - 10.8\}])\end{aligned} \tag{V.10}$$

Second order interactions correlation (R^2_{adj} =0.84):

$$\begin{aligned}\dot{r} = \exp(&\boldsymbol{11.4 - 13800\, InvT} - 0.03\, En - 0.5\, Bu \\ &+14000\, [InvT - 9.4x10^{-4}][Bu - 6.73] \\ &+Zr\, [1.3 + 0.483\, \{Bu - 6.73\} + \boldsymbol{1500\{InvT - 9.4x10^{-4}\}} \\ &\quad -12500\{InvT - 9.4x10^{-4}\}\{Bu - 6.7\}] \\ &+D9\, [\boldsymbol{0.35} + 0.056\{En - 9.2\}] \\ &+SS\, [\boldsymbol{0.082} + 16000\, \{InvT - 9.4x10^{-4}\} \\ &\quad -9700\{InvT - 9.4x10^{-4}\}\{Bu - 6.7\}])\end{aligned} \tag{V.11}$$

$\dot{r}$ is the 1 hour averaged eutectic penetration rate measured in μm/s. R^2_{adj} is a goodness-of-fit measure adjusted to account for the loss of degrees-of-freedom from explanatory variables. Typically, only variables with a standard error of less than 5% are included in the regression model. If necessary, terms with greater than 5% statistical error are included to incorporate a statistically significant higher order term. These terms are bolded to denote their high statistical uncertainty.

While R^2_{adj} is a useful parameter to gauge the model's accuracy when applied to the training data, verification data is needed to determine the predictive accuracy of a model. Using the 13 data points set aside at the beginning of the analysis, shown in Table 32, the Bauer correlation, ANL correlation, and the 1st and 2nd order interaction regression models are used to predict the natural log transformation of the eutectic penetration rates. The natural log transformations of the penetration rates were used to compare model accuracy for two reasons:

1. By comparing the log transformation of the penetration rates, accuracy over all orders of magnitude is ensured. If the non-transformed penetration rates were used, the residuals of the faster penetration rates would take precedence over the smaller penetration rates.
2. The regression fits were conducted to minimize the sum of the square of the residuals of the log-transformation of the training, so evaluating the log-transformation of the verification data ensures consistency.

Table 32 – Validation Data

Test, Assembly #	**Temp (°C)**	**Rate (μm/s)**	**Enrichment (wt% Pu)**	**Burnup (at%)**	**Zr in Fuel?**	**Cladding Type**	**Power (kW/ft)**
Dipping	1100	3.8E+00	0	0	No	SS	0.0
E-33,XY-22	798	3.0E-02	0	2.42	No	SS	7.6
86-66,X420	800	4.3E-02	19	2.3	Yes	D9	11.0
88-04,X425	800	4.6E-02	0	3	Yes	HT9	14.6
87-76,X425	780	1.7E-02	19	3	Yes	HT9	13.0
88-24,X423	800	9.0E-03	26	4.7	Yes	SS	12.5
91-09,X441	770	7.5E-03	19	5.6	Yes	HT9	14.9
88-08,X420	750	5.8E-03	0	6	Yes	D9	8.4
88-20,X429	800	2.7E-02	0	8	Yes	HT9	12.4
91-15,X441	740	1.3E-02	19	9.2	Yes	HT9	11.7
IFR-1	700	1.7E-02	19	9.4	Yes	D9	15.7
88-14,X421	800	1.9E-02	0	10	Yes	D9	10.7
90-02,X421	750	1.5E-02	19	17	Yes	D9	9.6

As can be seen from Table 33, the 2nd order interaction correlation did the best job of predicting the data in the verification set, followed closely by the 1st order correlation. The Bauer and ANL correlations performed similarly to each other but were much less effective at predicting the verification data than either new correlation. The data in Table 30 is also presented graphically in Figure 52.

Table 33 - Natural Log Transformation of Predicted Penetration Rates, $\ln(\dot{r}[\frac{\mu m}{s}])$, Compared to Verification Data.

	Bauer Correlation		**ANL Correlation**		**1st Order Interactions**		**2nd Order Interactions**	
Experimental	Predicted	Predicted	Residual	Predicted	Predicted	Residual	Predicted	Residual
1.34	**2.73**	**-1.39**	**0.24**	**1.10**	**2.26**	**-0.93**	**2.25**	**-0.91**
-3.50	**-2.95**	**-0.55**	**-2.98**	**-0.52**	**-4.02**	**0.52**	**-3.83**	**0.33**
-3.14	**-2.90**	**-0.24**	**-2.95**	**-0.19**	**-3.31**	**0.18**	**-3.31**	**0.17**
-3.08	**-2.90**	**-0.18**	**-2.95**	**-0.13**	**-3.43**	**0.35**	**-3.49**	**0.41**
-4.07	**-3.39**	**-0.68**	**-3.23**	**-0.84**	**-4.74**	**0.66**	**-4.43**	**0.35**
-4.71	**-2.90**	**-1.81**	**-2.95**	**-1.75**	**-4.93**	**0.22**	**-5.01**	**0.30**
-4.89	**-3.64**	**-1.25**	**-3.37**	**-1.52**	**-4.14**	**-0.75**	**-4.56**	**-0.33**
-5.15	**-4.16**	**-0.99**	**-3.67**	**-1.48**	**-4.44**	**-0.71**	**-4.48**	**-0.67**
-3.61	**-2.90**	**-0.71**	**-2.95**	**-0.66**	**-3.40**	**-0.21**	**-3.64**	**0.03**
-4.33	**-4.42**	**0.09**	**-3.82**	**-0.51**	**-5.41**	**1.08**	**-4.77**	**0.44**
-4.08	**-5.54**	**1.46**	**-4.45**	**0.38**	**-3.81**	**-0.27**	**-4.32**	**0.24**
-3.96	**-2.90**	**-1.06**	**-2.95**	**-1.01**	**-3.77**	**-0.20**	**-3.98**	**0.02**
-4.20	**-4.16**	**-1.39**	**-3.67**	**-0.53**	**-5.08**	**0.88**	**-3.60**	**-0.60**
sum(Ri^2)		**12.4**		**11.9**		**4.94**		**2.5**

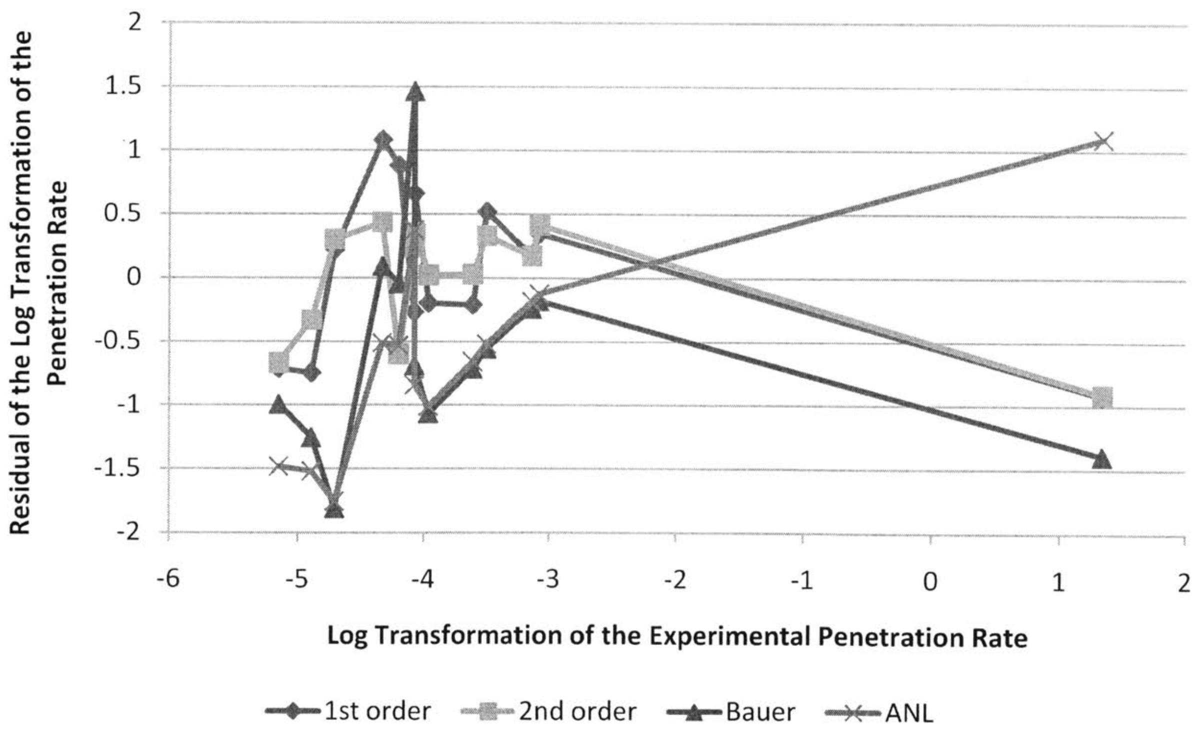

Figure 52 –Plot of the Residuals of the Verification Data for the Four Correlations

V.4 Point Estimate Simulated Transient Comparison

In order to gauge the impact of adopting the new correlations on transient calculations, a severe ULOF/LOHS was simulated. The realization analyzed in this study is the simulation with the highest average transient temperature from the RELAP5-3D simulated ULOF/LOHS calculations with an average core outlet temperature of 550°C. As can be seen from Figure 53, the peak cladding temperature increases quickly from 587°C to 910°C in 12 seconds and then slowly decreases as the inlet and outlet temperatures equalize. The second temperature perturbation at 45 seconds is caused by LOHS effects. Since the lowest experimentally determined liquidus temperature for metal fuel is 650°C, the analysis was stopped once peak cladding temperatures decreased below 650°C.

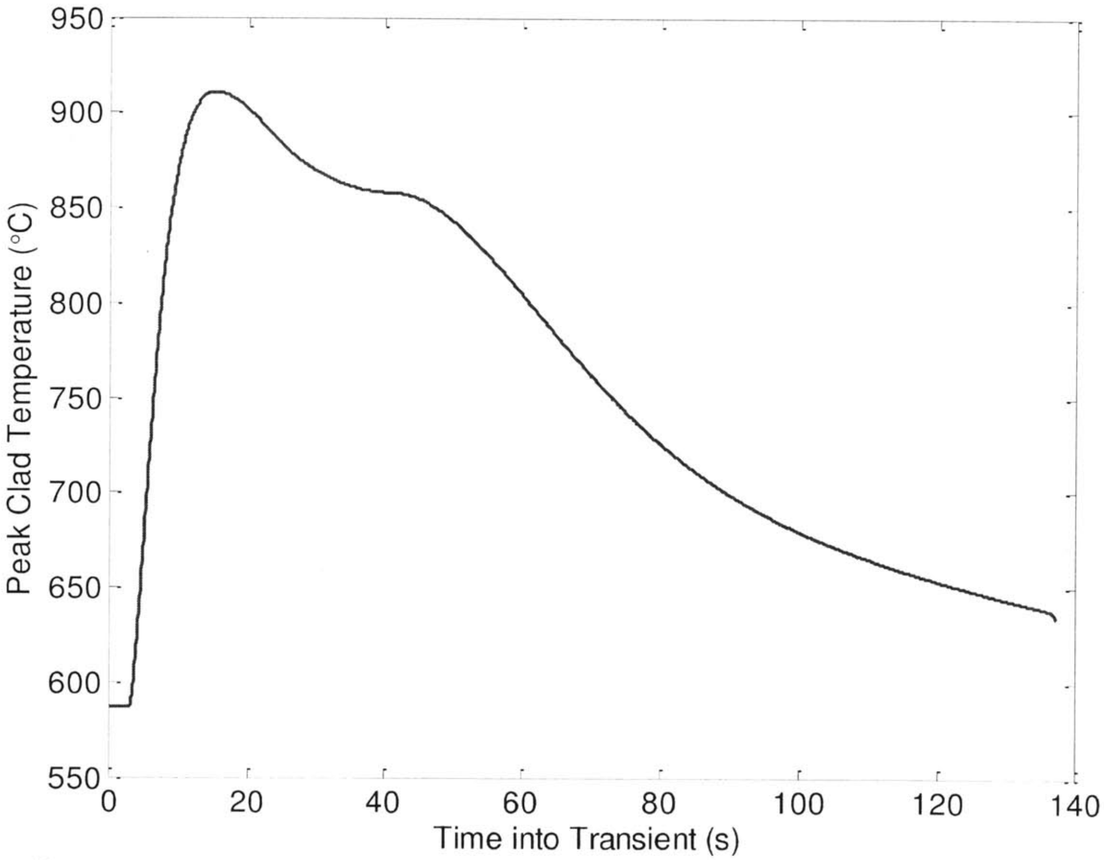

Figure 53- Peak Cladding Temperature for Metallic Fuel During a Simulated ULOF/LOHS

In order to use the two new correlations to predict the eutectic penetration depth, the state of the fuel pin is defined. For this analysis, it is assumed that the fuel in the hot channel is

10 wt% zirconium, was enriched to 19 wt% plutonium, has a steady state linear power of 8.8 kW/ft, is currently at 10 at% Bu and is clad with HT9. The predicted penetration depths for this fuel in this accident from the four correlations can be seen in Figure 54. It should be noted that the first order correlation predicts the lowest penetration depth, 0.6 μm, followed by the second order correlation, 1.7 μm, with the ANL and Bauer correlations predicting the highest penetration rates, at 7.6 μm and 15.4 μm respectively. It should be noted that the new correlations predict vastly reduced penetration depths than either of the existing correlations. This trend supports the notion that the Bauer and ANL correlations are intended to be bounding, conservative correlations, where as the new correlations are best estimate calculations.

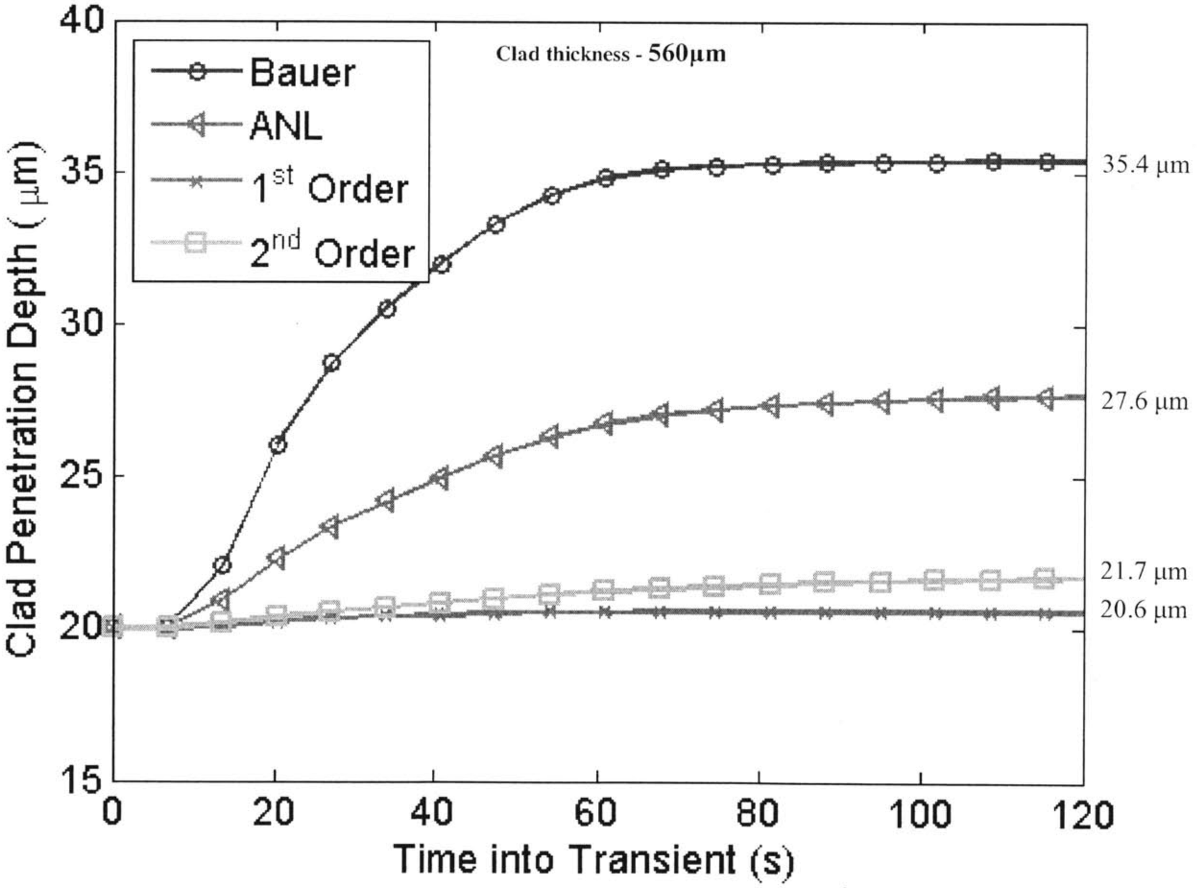

Figure 54- Eutectic Penetration Depth for the Bauer, ANL, 1st and 2nd order correlations. The dotted line at 560μm indicates a typical cladding thickness. "Instantaneous" penetration depth of 20μm assumed due to steady state diffusion effects.

In order to determine the effects of burnup and plutonium enrichment, a sensitivity analysis is conducted on both variables. Figure 55 shows the same transient as analyzed in Figure

54, but with the fuel burnup decreased to 5 at%. Figure 56 also shows the same transient as analyzed in Figure 53, but with the enrichment increased to 26 wt% plutonium. In both cases, the expected trends of higher enrichment and higher burnup leading to slightly lower penetration depths than seen in Figure 54 are exhibited in the new correlations (71) (34).

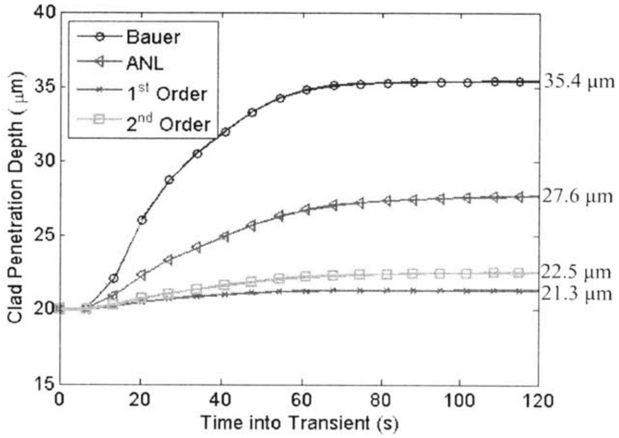

Figure 55 - Eutectic Penetration Depth for 5 at% Burnup Fuel with the Bauer, ANL, 1st and 2nd Order Correlations.

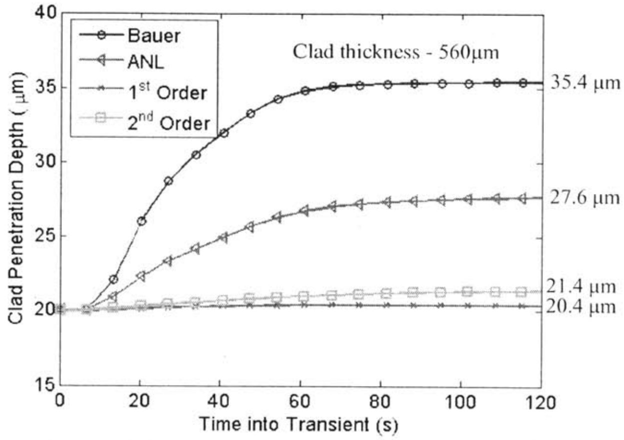

Figure 56- Eutectic penetration Depth for 26 wt% Fuel with the Bauer, ANL, 1st and 2nd Order Correlations.

From examining Figure 54, Figure 55 and Figure 56, it is interesting how much the current correlations over-predict the amount of eutectic formation during the transient. Current correlations over-predict the penetration thickness (15.4 μm compared to between 0.4 and 2.5 μm) by approximately an order of magnitude. Because most ANL benchmark tests experimentally compare time to cladding rupture, which is a function of creep and eutectic formation, to DEFORM5 predictions, it is possible that DEFORM5 is under-predicting creep rates to compensate for the over-prediction in eutectic wastage. Future work should re-analyze the integral tests with the new eutectic correlations to determine if the predictive capabilities of DEFORM5 improve, which would indicate that creep was properly handled and cladding failure prediction uncertainties were caused by inaccurate eutectic modeling, or if the predictive capabilities degrade, which would indicate that creep was adjusted to compensate for inaccurate eutectic predictions.

V.5 Model Uncertainty

This section will utilize the model uncertainty methodology outlined in Section II.7 on the correlations described in V.2 and V.3.

Previous applications of this model error methodology have assumed the validation ratio to be log-normally distributed, a distribution which also complies with both of the previous stated conditions. To determine if the validation ratio can be modeled as a lognormal distribution, the Lilliefors test was applied to the natural-log transformation of the validation ratio for each of the models (24). The Lilliefors test is a 2-sided goodness-of-fit test which compares the maximum difference between the empirical cumulative distribution of the validation ratio to a normal distribution with the mean and standard deviation of the input data. By inputting the natural log transformation of the validation ratios to the Lilliefors test, the Lilliefors test is tricked into determining if the underlying data is lognormally distributed. The results of the Lilliefors test for the four distributions of interest can be seen in Table 32. The null hypothesis which is tested in the Lilliefors test is that the validation ratio data is normally distributed. If the test returns a p-value of less than 0.05 the hypothesis is rejected, or stated differently, the test shows greater than a 95% confidence that the data was not derived from a normal distribution. Thus, the validation ratio cannot be modeled lognormally. In any hypothesis test, p-values greater than 0.05 do not prove that the underlying distribution is normal but merely that there is not enough evidence to suggest otherwise. The Lilliefors test does not report p-values greater than 0.5 or less than 0.001.

It should be noted that while the 1st and 2nd order interaction equations can only use the 13 validation data points listed in Table 32, the Bauer and ANL correlations have more validation data as these correlations were created with less training data. The number of validation data points available to each distribution is listed in Table 34. All correlations pass the Lilliefors test at a 5% confidence level and thus it is acceptable to use the lognormal distribution to model the validation ratio.

Table 34– Results of the Lilliefors test on the Natural Log Transformation of the Validation Ratios for the 4 Fuel/Cladding Eutectic Correlations.

Category	Bauer Correlation	ANL Correlation	1st Order Interactions	2nd Order Interactions
# of Validation Points	54	61	13	13
p-value	0.50	0.15	0.50	0.07
Lognormally Distributed?	Yes	Yes	Yes	Yes

Now that Table 34 has confirmed that the validation ratio can be modeled as a log-normal distribution, model uncertainty distributions can be created for the predictive relationships. Section V.5.A uses the model uncertainty methodology outlined in Section II.7 to create unique uncertainty distributions for both the new and old predictive relationships. Section V.5.B applies these distributions to the transient examined in Section V.4 by plotting the 90% confidence interval for each correlation.

V.5.A Solving the Model Uncertainty Equations

Solving Eq. II.28 through Eq.II.33 is difficult to do analytically because of the difficulty in integrating over multiple lognormal distributions. Thus, a combination of Monte Carlo (MC) Methods and numerical integration was employed as necessary.

First, Eq. II.29-II.33 are solved. Using MC, values of b_m and s_m are randomly sampled from Eq.II.30 and used to evaluate the likelihood of the evidence R^* through Eq.II.29. A 3-D surface of points, with b_m and s_m in the x-y plane and the calculated likelihood in the z-plane, is then created. This surface is the un-normalized portion of Eq. II.31 and can be seen in Figure 57.

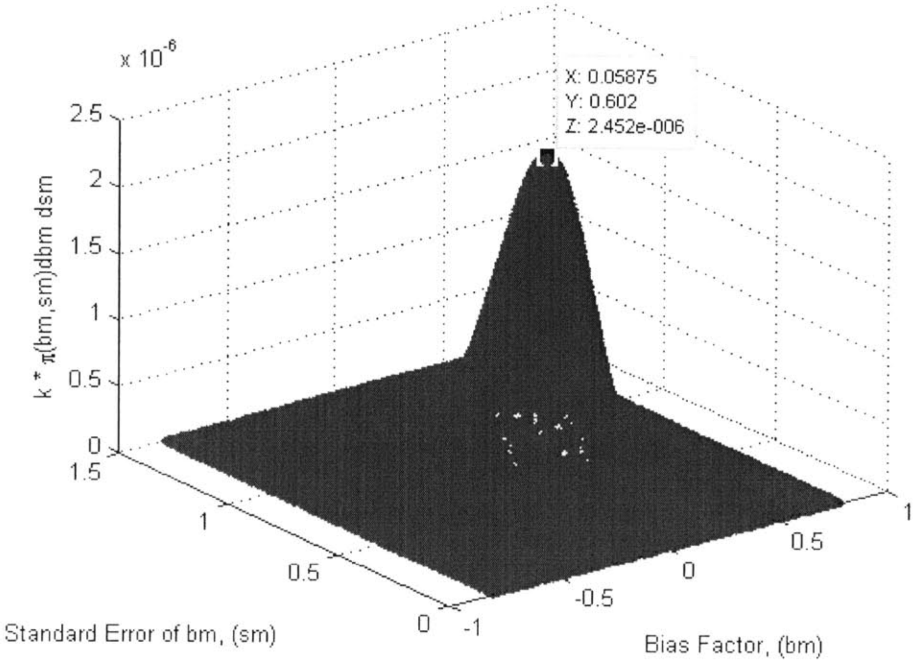

Figure 57– Un-normalized Posterior Distribution Resulting from MC sampling for the 1st Order Fuel/Cladding Eutectic Correlation with 10^5 Random Samples.

Once enough data points have been sampled to cover the state space sufficiently, MATLAB's griddata function can interpolate z-values (probability density) on a uniformly spaced x-y grid (b and s_m) (24). Once the posterior distribution has been re-organized on a uniform grid of adequate spatial resolution, it is possible to numerically integrate the distribution to calculate the normalization constant k. At this point, the full joint probability is known and can be seen plotted in Figure 58.

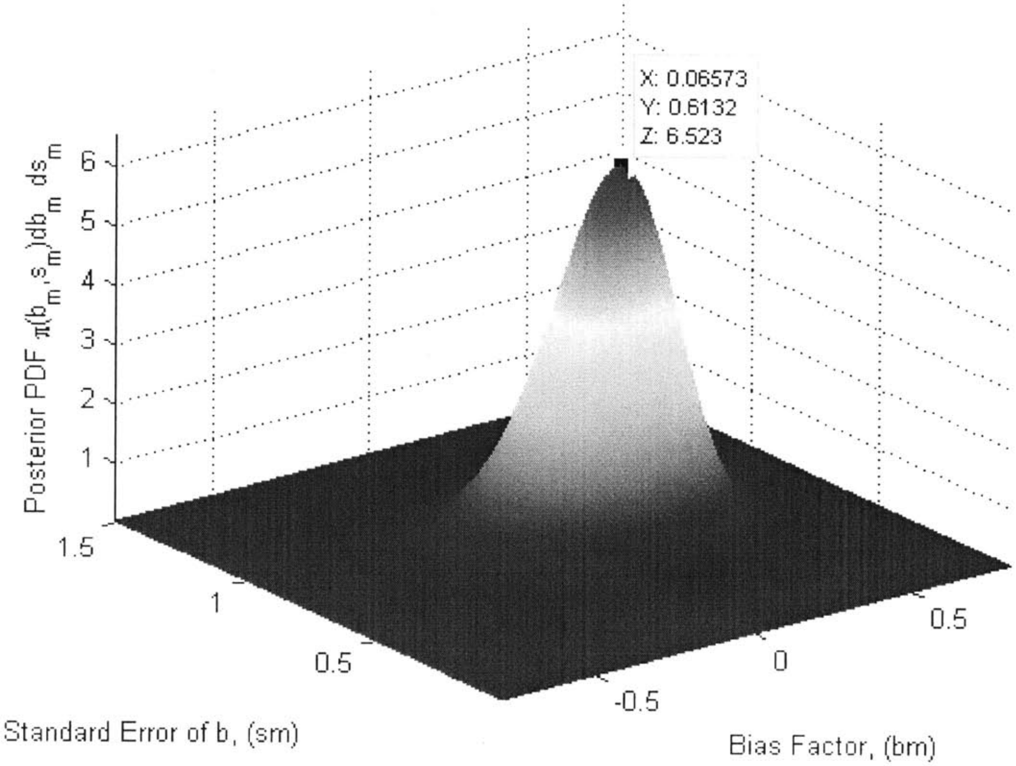

Figure 58– Normalized Posterior Distribution Resulting from MC sampling for the 1st Order Fuel/Cladding Eutectic Correlation with 10^5 Random Samples.

Marginal distributions of b_m and s_m, Figure 59 and Figure 60, can be calculated from the joint distribution through Eq. V.11 and Eq. V.12. The marginal distributions examined for each variable separately may show insight into the epistemic uncertainties of b_m and s_m which may be hard to determine from a 3-D plot. From Figure 59, the 1st order correlation marginal distribution of b_m indicates that the model slightly over-predicts the experimental data because the maximum likelihood of the bias factor is slightly positive. For the log-normal distribution, e^{b_m} and $e^{b_m+\frac{1}{2}s_m^2}$ are the 50th percentile and mean of the validation ratio distribution.

$$\pi(b_m|R^*) = \int_{s_m} \pi(b_m, s_m|R^*)ds_m \qquad \text{V.12}$$

$$\pi(s_m|R^*) = \int_{b_m} \pi(b_m, s_m|R^*)db_m \qquad \text{V.13}$$

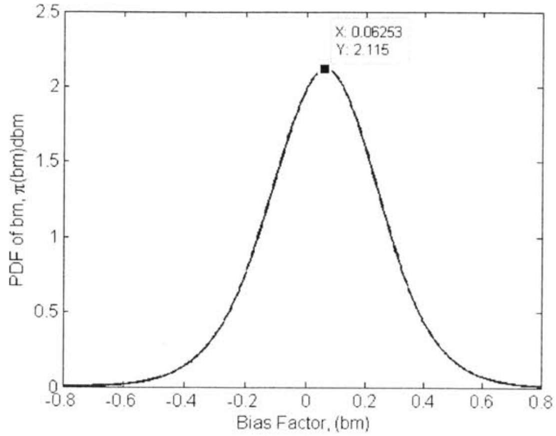

Figure 59 – Marginal Distribution for the Bias Factor, b_m, of the 1st Order Fuel/Cladding Eutectic Correlation.

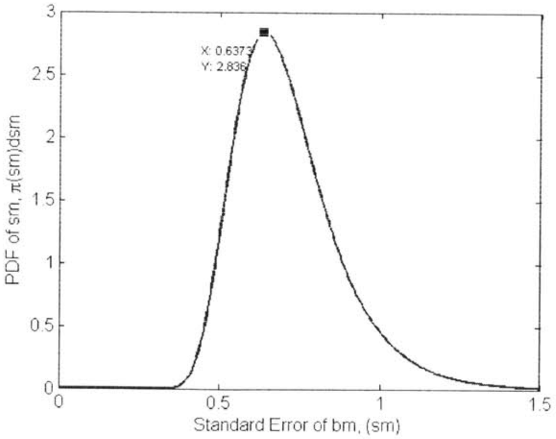

Figure 60 – Marginal Distribution for the Standard Error of Bias Factor, s_m, of the 1st Order Fuel/Cladding Eutectic Correlation.

The 5th, 50th, 95th and mean values for the b_m and s_m for each correlation are listed in Table 35. The 1st and 2nd order correlations predict the validation data better than the Bauer and ANL correlations, thus the bias factors for the new correlations are closer to zero. The large negative bias factors for the Bauer and ANL correlation indicate that they over-predict the rate of eutectic formation. The higher s_m values for the existing correlations are indicative of a higher degree of randomness in the validation ratio, a randomness which is expected as these correlations do not attempt to adjust for many dependent variables.

Table 35– Epistemic Uncertainty in b_m and s_m Predictions for the Bauer, ANL, 1st order, and 2nd Order Correlations.

	Bauer Correlation		**ANL Correlation**		**1st Order Interactions**		**2nd Order Interactions**	
	b_m	s_m	b_m	s_m	b_m	s_m	b_m	s_m
5th	-0.78	0.99	-0.81	0.94	-0.27	0.50	-0.26	0.36
50th	-0.52	1.15	-0.58	1.09	0.062	0.69	-0.19	0.49
mean	-0.51	1.16	-0.57	1.10	0.063	0.72	-0.17	0.51
95th	-0.26	1.37	-0.35	1.27	0.40	1.02	0.22	0.74

Returning to the validation ratio distribution, Eq. II.28 can be transformed into Eq. V.14 by substituting the likelihood function from Eq.II.32 and the uniform prior distribution, $\pi_0(R) = \mathrm{U}(10^{-6}, 35)$.

$$\pi(R|R^{*},M) = \begin{cases} \dfrac{1}{k}\iint_{b_m,s_m} \dfrac{\frac{1}{\sqrt{2\pi}R\,s_m} e^{\left(-\frac{1}{2}*\frac{\ln(R)-b_m}{s_m^2}\right)} \pi(b_m,s_m|R^{*})db_m ds_m}{35-10^{-6}} dR, 0 \leq R \leq 8 \\ 0, \qquad else \end{cases} \qquad \text{V.14}$$

By combining constants the posterior distribution and abbreviating the lognormal distribution into the functional name, $LN(R|b_m,s_m)$, Eq. V.14 can be simplified to Eq. V.15.

$$\pi(R|R^{*},M) = \begin{cases} \dfrac{1}{k'}\iint_{b_m,s_m} LN(R|b_m,s_m)\pi(b_m,s_m|R^{*})db_m ds_m\, dR, & 0 \leq R \leq 8 \\ 0, & else \end{cases} \qquad \text{V.15}$$

Thus, solving for the posterior distribution of the valuation ratio reduces to solving the double integral. While this integral can be solved using Metropolis Sampling Markov Chain Monte Carlo, it was easier to simply numerically integrate the function and normalize the resulting distribution. When approached from a numerical integration perspective, the validation ratio distribution can be thought of as a simple weighted average of all possible lognormal distributions, with the likelihood (weight) of various combinations of shape parameters determined from the joint distribution $\pi(b_m,s_m|R^{*})$. The probability distribution function and cumulative distribution function 1st order fuel/cladding eutectic correlation can be seen in Figure 61.

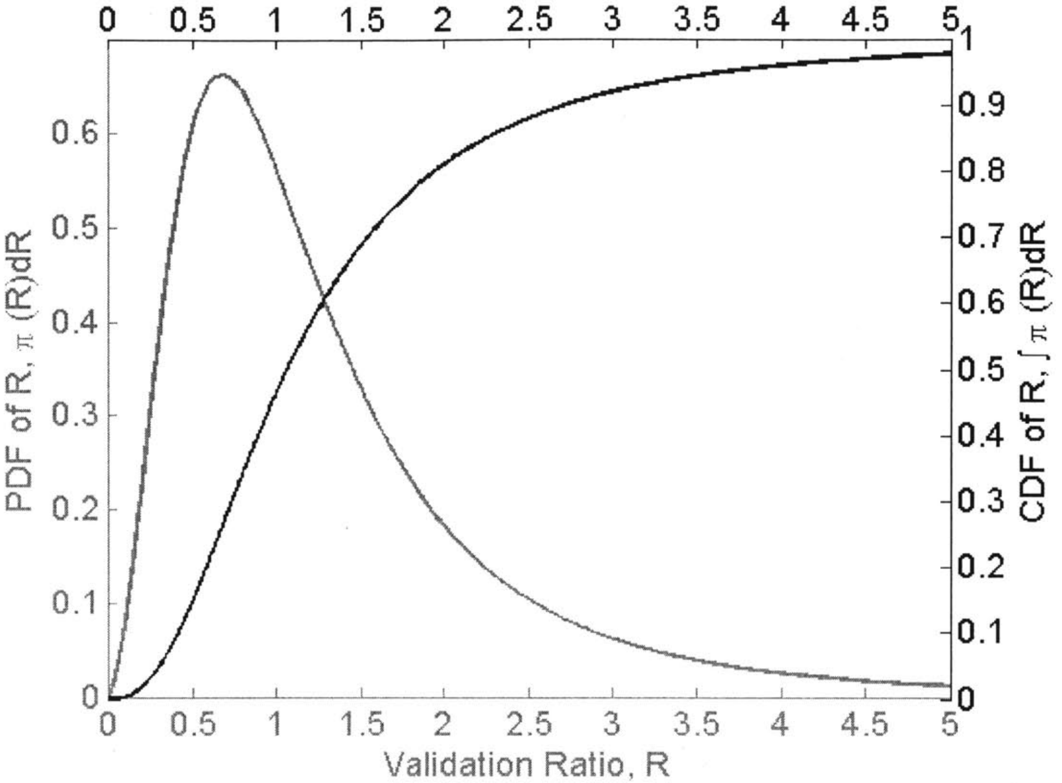

Figure 61– PDF (left) and CDF (right) of the Validation Ratio Distribution for the 1st order Fuel/Cladding Eutectic Correlation.

Table 36– Aleatory Uncertainty in R Predictions for the Bauer, ANL, 1st Order, and 2nd Order Correlations.

	Bauer Correlation	**ANL Correlation**	**1st Order Interactions**	**2nd Order Interactions**
5th	0.08	0.09	0.30	0.40
50th	0.60	0.56	1.06	0.98
mean	1.18	1.04	1.43	1.14
95th	4.10	3.47	3.66	2.39

Figure 62 through Figure 65 compares the empirical and computational cumulative distributions for all four correlation's validation factors. The cumulative distributions are an indication of the confidence that the real validation ratio is below the given value. Thus for the Bauer correlation, a cumulative distribution of 0.95, or the 95th percentile, indicates that 95% of the time the real validation ratio for an experiment will be less than the 95th percentile value of 4.1. The empirical distributions for the Bauer and ANL correlations are smoother than for the 1st and 2nd order interactions because there is more validation data for the simpler correlations. The lognormal posterior distributions agree well with the body of the data for all correlations, but the upper tails of the 1st and 2nd order correlation numerical distributions over-predict the 95th percentile of the empirical distributions. This apparent over-prediction is acceptable because 13 data points is not enough to have a reliable 95th percentile estimate from an empirical distribution. Additionally, the lognormal distribution predicts a conservative 95th percentile, which is desired from a safety/regulatory perspective.

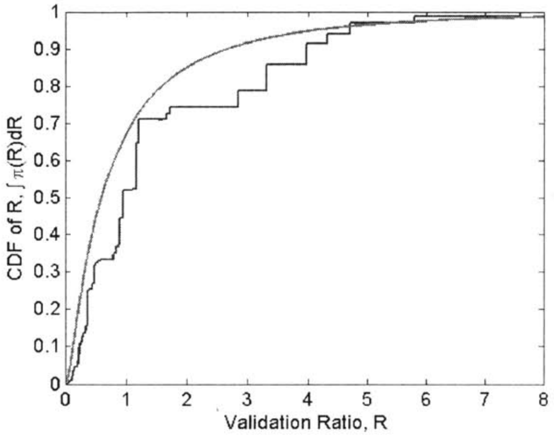

Figure 62 – Cumulative Distributions for the Bauer Correlation Validation Ratio. The Empirical Distribution is Jagged and the Lognormal Distribution is Smooth.

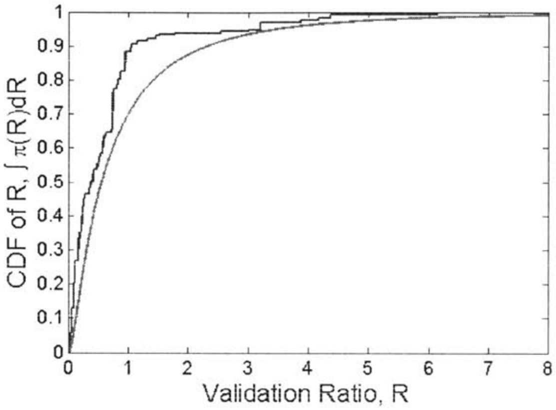

Figure 63– Cumulative Distributions for the ANL Correlation Validation Ratio. The Empirical Distribution is Jagged and the Lognormal Distribution is Smooth.

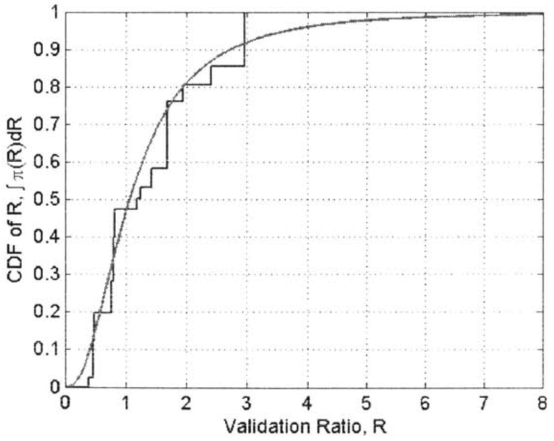

Figure 64– Cumulative Distributions for the 1st Order Correlation Validation Ratio. The Empirical Distribution is Jagged and the Lognormal Distribution is Smooth.

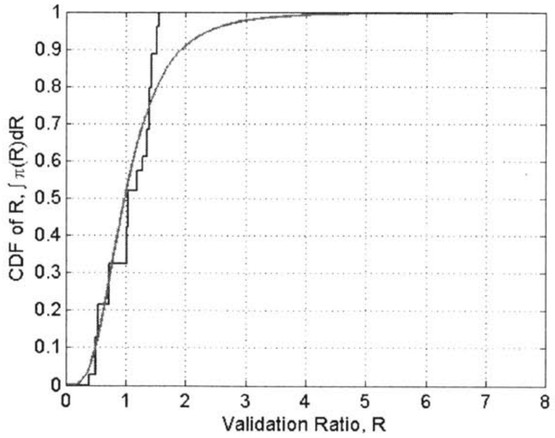

Figure 65– Cumulative Distributions for the 2nd Order Correlation Validation Ratio. The Empirical Distribution is Jagged and the Lognormal Distribution is Smooth.

The validation ratio probability and cumulative distribution functions are plotted in Figure 66. From Table 32 and Figure 66 and Figure 67, the Bauer and ANL correlations tended to over-predict the experimental results. This expectation is confirmed by the relatively small values of R at the maximum probability density. Additionally, the ANL correlation PDF is skewed slightly more to the right than the Bauer correlation PDF, which agrees with the empirical distributions shown in Figure 66 and Figure 67. The 1st and 2nd order correlations show better predictive ability as their validation ratio distributions are centered closer to 1.0. The 2nd order correlation is narrower and centered closer to 1.0 than the 1st order correlation, indicating the better predictive ability predicted by Table 32.

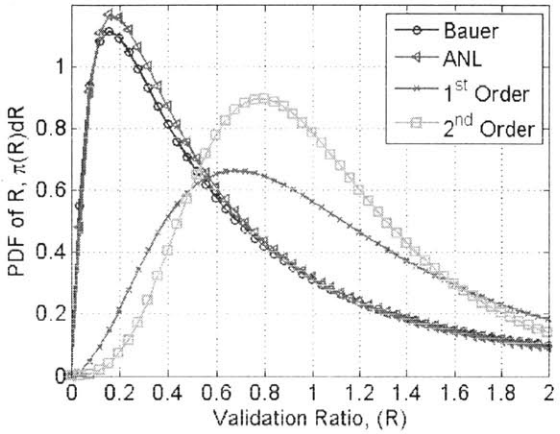

Figure 66– Probability Distribution Functions of the Validation Ratio for all Four Predictive Relationships.

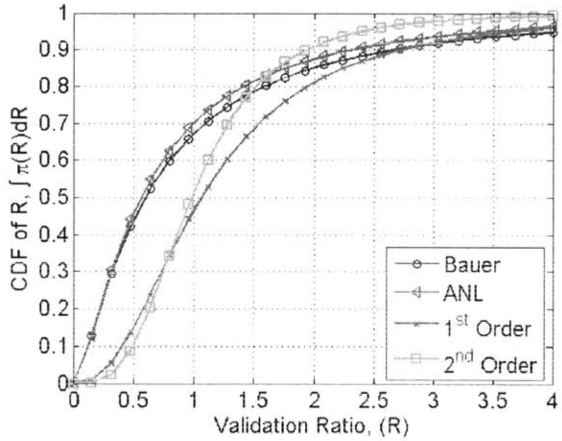

Figure 67– Cumulative Distribution Functions of the Validation Ratio for all Four Predictive Relationships.

V.5.B Simulated Transient Comparison with Model Uncertainties

One of the desired goals driving the creation of the model uncertainty distributions was to examine the confidence in the model predictions. By combining the transient analyzed in Figure 53 with the validation ratio distributions, the range of possible eutectic penetration depths can be examine. The solid lines in Figure 68 and Figure 69 are the same predictions as shown in Figure 54 (i.e., U 19%Pu 10%Zr fuel, 10at% burnup, HT9 clad, q'=8kW/ft). The four equations are plotted on two sub-figures for clarity, with the Bauer and 2nd order interaction correlation in Figure 68 and the ANL and 1st order correlation in Figure 69. The 5th and 95th percentile estimates from the Validation Ratio distributions are plotted as unconnected markers whose shape corresponds to original prediction.

While the Bauer and ANL correlations predict thicker (deeper) cladding penetrations than the 1st or 2nd order correlations, there is significant overlap in the distributions for all of the correlations. This overlap is expected because the Validation Ratio distributions were created with at least a fraction of the same data. Thus, the empirical validation ratios for all of the correlations should cause the distributions to be wide enough to provide for some overlap, assuming the test cases are inside the applicability range of the correlations. If the correlations are used outside of the training/validation data set, new effects and interactions may occur which may cause distributions to diverge greatly.

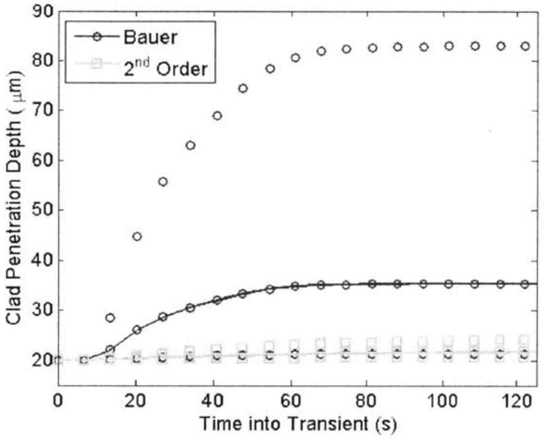

Figure 68 – Transient Eutectic Penetration for the Bauer (circle) and 2nd Order Interaction (square) Correlations. 5th and 95th percentile confidence bounds are represented by unconnected markers.

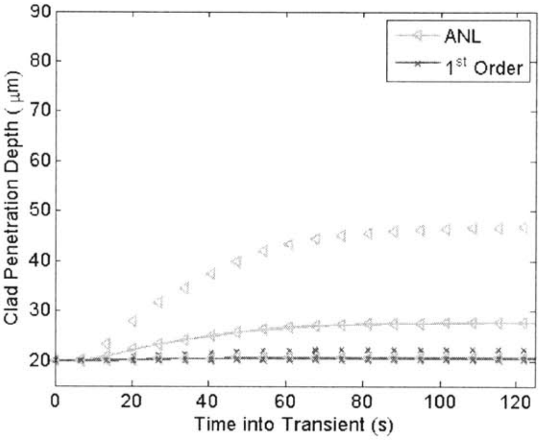

Figure 69– Transient Eutectic Penetration for the ANL (triangle) and 1st Order Interaction (cross) Correlations. 5th and 95th percentile confidence bounds are represented by unconnected markers.

Typically, regulations will put a limit on both the thickness of eutectic wastage and the cumulative damage fraction allowed during the transient. The fractional cladding damage is a normalized measure of the total damage absorbed by the clad, in this case through thermal and irradiation creep and eutectic wastage (19) (77). The fractional cladding damage can be defined by Eq. V.16:

$$FCD(\sigma, T, Bu, \dots) = \int_{t_{mini}}^{t_{max}} \frac{1}{t_f(\sigma, T, Bu, \dots)} dt_f \qquad \text{V.16}$$

where $t_f(\sigma, T, Bu, \ldots)$ is the time to cladding failure at a given stress, temperature, burnup, or any other number of potential variables which can weaken the cladding. Under this definition, a CDF=1.0 indicates that the cladding has breached. t_f is typically given through correlations such as those given in the DEFORM-5 module in SAS4A. Assuming a plenum pressure of 10MPa, which is reasonable for end of life metallic fuel pins, and that eutectic wastage acts only to thin the load bearing portion of the fuel pin, the cumulative damage fraction experienced over the course of the transient is calculated and plotted in Figure 70. As expected, the 1st and 2nd order correlations, which predicted eutectic penetration of less than 5%, are almost indistinguishable from the no-eutectic-formation base case. The substantial cladding erosion predicted by the Bauer correlation and the ANL correlation only increase the cumulative damage fraction by 3% and 8% respectively. The minimal contribution of eutectic to the cumulative damage fraction for HT9 has been observed elsewhere (68) (77), thus it is not surprising to experience creep limited cladding operation in this case.

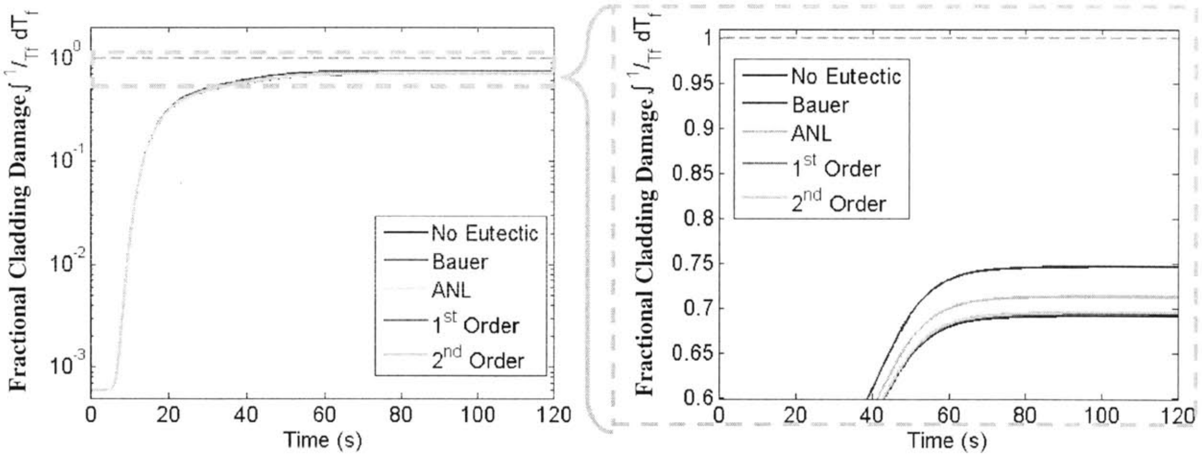

Figure 70– Best Estimates of the Failure Fraction for the ULOF/LOHS Transient for the Four Eutectic Equations and with no Eutectic Considered.
The right image shows a magnification of the cumulative damage fraction of at the end of the transient.

The regulator may desire the probability of cladding failure given the uncertainties in eutectic penetration correlations for the transient. First, we define the conditional cumulative cladding failure distribution function for a given correlation, $F(R)$, as in Eq. V.17.

$$F(R) = \begin{cases} 0, & CDF(\sigma, T, Bu, \ldots | R) < 1.0 \\ 1, & CDF(\sigma, T, Bu, \ldots | R) \geq 1.0 \end{cases} \tag{V.17}$$

Then the probability of cladding failure can be determined using Eq. V.18 which integrates Eq. V.17 over all possible values of R (77).

$$\pi(Clad\ Failure) = \int_R F(R)\ \pi(R|R^*)dR$$

As expected, the Bauer correlation has the highest probability of cladding rupture, followed by the ANL correlation. The 1st and 2nd order correlations predict small penetrations and tighter distributions, thus the probability of failure for these correlations are many orders of magnitude lower than the Bauer and ANL correlations. The probabilities of cladding failure given eutectic wastage uncertainties are given in Table 37. If the Bauer or ANL correlations are used, then the correlation model uncertainties should be combined with the uncertainties associated with thermal creep to determine the uncertainties around the time-to-failure and calculate the true probability of cladding failure for this transient realization. Conversely, if the 1st and 2nd order correlations are used, the contribution of the eutectic uncertainties can be ignored, as the extremely low individual contributions to cladding failure in Table 37 will most likely be dwarfed by the uncertainties in thermal creep and time to failure at these temperatures.

Table 37– Probability of Cladding Failure for the LOF/LOHS Transient Simulation given Uncertainties in Validation Ratio Predictions for the Bauer, ANL, 1st order, and 2nd Order Correlations.

	Bauer Correlation	**ANL Correlation**	**1st Order Interactions**	**2nd Order Interactions**
Probability Of Cladding Failure	4×10^{-2}	4×10^{-3}	8×10^{-12}	6×10^{-13}

V.6 Conclusion

The rate of fuel/cladding eutectic formation has historically been modeled as a simple function of temperature, in spite of 40 years of experimental evidence which supports additional dependencies such as fuel form, cladding type, burnup, enrichment, and linear power. New correlations which statistically resolve many of these dependencies were developed and their predictive uncertainties were quantified. It was shown that the current correlations over predict eutectic penetration for potential accident types. Additionally, for the accident analyzed, the uncertainties associated with new correlations are small enough as to be negligible when compared to other cladding failure uncertainties, such as creep rates or predicted time-to-cladding-failure.

VI CONCLUSION

This thesis is focused on reducing the cost of the SFR in a safe and responsible manner. The licensing framework described in NUREG-1860, a.k.a. the TNF, was used as a guide to set a regulatory safety framework within which design alternatives could be compared. This thesis focused on three primary topics:

- Alternate fuel forms,
- Thermodynamic efficiency,
- Improved modeling of the rate of metal fuel/cladding eutectic formation rate

VI.1.A Alternative Fuel Forms (Metal and Oxide)

Because of the favorable experience of EBR-II with metallic fuel and some potential advantages of metallic fuel for a burner reactor that is recycling minor actinides, the reference design for this study employs metallic fuel. Internationally, however, oxide fuel is recognized as at least the near-term preferred fuel option for sodium-cooled fast reactors. Thus, the trade-off to be considered is whether an oxide-fueled core would have better or worse safety characteristics than a metal-fueled core and what the relative cost between the two fuel types would be of generating electricity. Most of the analysis work described in this section relates to a comparison of accident scenarios and their relative consequences for the two different types of fuel design. Response to accident scenarios can have a direct impact on the capital cost of a nuclear power plant if expensive mitigative systems are required. Fuel cycle costs are likely to be a greater fraction of power generation costs in cycles involving some form of reprocessing and recycling than they are for the current generation of once-through nuclear power plants. There are substantial differences in reprocessing technologies for the oxide and metallic fuels, but there is very limited information on the cost of the pyroprocessing process used for metallic fuels. Fuel type can indirectly affect allowable core outlet temperature and hence thermodynamic efficiency. It can also affect system availability. Hence, the choice of fuel is a highly uncertain yet important economic driver of the SFR.

Due to large uncertainties associated with the cost of electrochemical reprocessing, as used for metallic fuel, and aqueous reprocessing, as used for oxide fuel, and their impacts on fuel cycle costs, a full cost-benefit comparison cannot be completed at this time. Instead, this case study focuses on in-core operational differences that should be considered between metal and oxide fuel. Table 7, reproduced below, overviews the categories used to compare metal and oxide fuel. In this assessment, design basis events are those that establish the design requirements for safety related systems, structures, and components. Historically, systems were designed to assure that these accidents would not result in severe fuel damage or uncoolable geometry. Events that result in conditions that are outside the envelope of the design basis event conditions are referred to as beyond-design-basis events. These events could result in severe fuel damage. For sodium cooled fast reactors, there is a subcategory of beyond-design-basis events that could result in energetic disruption of the core. These events are referred to as Energetic Scenarios (ES). The potential for severe fuel damage events to lead to ES depends in part on the manner in which molten fuel debris is transported after fuel failure. If the fuel debris forms blockages within the core region allowing fuel material to collect, there is a greater potential for re-criticality than if the fuel debris is swept from the core region.

Table 7–Metal and Oxide Fuel Comparison
1 = favoring metal, 5 = favoring oxide, 3 = neutral.

General Category	Specific Category	Rank
Transient Performance	Events without fuel damage	3
	Severe fuel damage events without potential for ES	1
	Severe fuel damage events with potential for ES	2
Operating Constraints	Maximum Coolant Outlet Temperature (without ODS clad)	3
	Maximum Coolant Outlet Temperature (with ODS clad)	4
	Maximum Achievable Burnup	4

The proposed core outlet temperatures for the next generation sodium reactors indicate a potential temperature limitation for metallic cores. General Electric's S-PRISM and the Westinghouse SFR design are both proposing metallic fuel with a fairly low core outlet temperature (510-530°C). JSFR and EFR are both oxide fueled cores and propose operation at a higher core outlet temperature, around 550°C. This indicates that, considering only thermal efficiency, the SFRs employing metal fuel are currently 0.5% less efficient and thus have a 1.25% higher busbar electricity cost (see the Thermodynamic Efficiency Case Study (Section V.II) for more details). A summary of the cladding options considered for SFR designs can be found in Table 9, reproduced below.

Table 9 –SFR Cladding Summary

Cladding	Classification	Temperature Limit	Burnup Limit
HT9	Martensitic	640°C	200 dpa
PNC-FMS	Martensitic	650°C	150-200 dpa
D9	Austenitic	675°C	100 dpa
15-15Ti	Austenitic	675°C	130 dpa
PNC1520	Austenitic	675°C	160 dpa
ODS	ODS	700°C	>200 dpa

Taking into account all of the available cladding limits, primarily due to creep and fuel/clad eutectic formation, the following guidelines can be formulated:

- It is impossible to set an overall eutectic limit for a cladding, because of the large dependence of the fuel/clad liquidus temperature on cladding choice.
- For U.S. tested cladding, i.e. SS304, SS316, D9, HT9, and variations of U.S. tested cladding which most likely have similar eutectic behavior, i.e., PNC-FMS, 15-15Ti, creep limits will limit cladding performance, not eutectic liquefaction.
- With metal fuel, high Pu regions of the core, i.e., >20 at%, may or may not require restricted cladding temperatures due to burnup effects when using U.S. tested cladding other than SS316 since no high burnup eutectic data exist and direct-couple tests show an initially low liquidus temperature. For advanced cladding, such as ODS, high Pu regions may be restricted to a peak cladding temperature of 650°C unless additional zirconium is added to the fuel matrix to increase the liquidus temperature or a diffusion barrier is employed to prevent eutectic formation.
- Lead test assemblies from EBR-II show the potential for HT9 clad fuel to be burned past 20 at%, but not enough data exist at this time to form a licensing basis beyond 11 at% burnup.

Plant thermal efficiency can have a substantial effect on capital cost. At the current state of cladding development, both metal and oxide fuel have the same core outlet temperature limits and potential burnup limits, which are primarily set by choice of cladding. The differences in the approaches to reprocessing for oxide and metal fuels are substantial. It was not within the scope of this study to attempt to estimate the cost of a pyroprocessing facility for metal fuel to compare against that of the aqueous processes used for oxide fuels.

Outside of thermal creep, the fuel/cladding eutectic liquidus temperature is sometimes viewed as the maximum achievable cladding temperature and thus a limit for future metal fuel operations. The fuel/cladding eutectic database indicates that the liquidus limit is highly cladding dependent and thus a robust eutectic testing program would need to be conducted before any advanced claddings are employed with commercial metallic fuel. Even with this caveat, the liquidus temperature identified for HT9 cladding, 650°C, is commonly viewed as a lower bound for the liquidus temperature. It should be noted, however, that this liquidus temperature was determined from high linear power EBR-II tests, typically between 12 to 15kW/ft. Typical metallic fueled SFR designs have a peak linear power between 8 and 9 kW/ft and are outside of the experimental database. It has been demonstrated in both EBR-II and FFTF that the liquidus temperature is a function of linear power, most likely due to the higher temperature gradients in the fuel associated with higher linear powers. Thus the 650°C liquidus temperature is most likely overly conservative. Additional fuel testing is need to determine if the 650°C liquidus temperature for 10 at% fuel can be expected in proposed SFR designs or if it is a product of conservative fuel testing.

The operational costs of metal or oxide fuel forms appear to be similar. Additional fuel testing will be required to create a licensing basis for burning U-Pu-Zr fuel past 11 at%, but lead test assemblies showed that metallic fuel has the potential of being burned past 20 at% burnup with HT-9 clad. A full economic and fuel cycle comparison was not performed for this case study because of a lack of reliable information on reprocessing costs, but both fuel forms have the potential for high temperature and high burnup performance and are believed to be licensable under the NUREG-1860 licensing structure. In general, capital cost tends to be the largest element of power generation cost. The cost savings that can be realized from moving to a less robust containment structure was indicated to be approximately 5% of the capital cost of the plant. Thus, the ability to select a less robust containment could have a significant economic advantage for one fuel type over another. On the other hand, if the need to protect against external threats requires a robust containment, the differential cost of protecting against Energetic Scenarios is likely minimal.

VI.1.B Design Alternatives Resulting in Improved Thermal Efficiency

Improving the thermodynamic efficiency of a design or process is often considered the Holy Grail for designers and engineers. Such efficiency gains are seen as a way to increase output while using the same basic structures and inputs as the original design. With an electricity generating facility, increasing the thermodynamic efficiency increases the electricity produced with minimum impact on fuel, capital, and operation and maintenance costs. The following case study examines how thermodynamic efficiency may be increased in the Sodium Fast Reactor (SFR) through a combination of:

- increasing the core outlet temperature above 510°C for metal and oxide fuel
- removing the intermediate loop
- replacing shell and tube heat exchangers with Printed Circuit Heat Exchangers (PCHEs)
- switching from a Rankine to a Supercritical-CO_2 power conversion cycle

In order to raise the core outlet temperature, the entire system including the vessel, the fuel rods, the primary piping and the steam generators, must be shown to be reliable at the elevated temperature. Hence all relevant Licensing Basis Events (LBEs) must be shown to lie within the acceptable region of the Frequency-Consequence-Curve (FCC). In order to satisfy vessel and piping limits without detailed technical evaluation, the hottest proposed core outlet temperature of 575°C was set as an upper temperature bound. This is the core outlet temperature proposed for the BN-1800 design, which uses Cr 18 Ni 9 steel for vessel, piping and heat exchanger materials (10). Steady state clad temperature limits are designed to ensure that fuel pin integrity will be highly reliable at the desired core temperatures. Typically, this is done by ensuring that the 2σ hot channel factor clad temperatures are below material limits of the clad (16). Using the 640°C clad mid-wall temperature limit from HT-9 (39), it can be shown that the maximum core outlet temperature from a fuel reliability standpoint is approximately 550°C for both metal and oxide core designs. This outlet temperature is in line with the standard core outlet temperatures of most currently proposed SFR designs for oxide fuel (10).

The safety implications of implementing the design alternatives must also be considered. The elimination of the intermediate loop is only considered to be licensable for loop-type SFRs because of the impracticality of managing large sodium/water interactions inside the primary vessel of the pool type configuration. PCHEs can be implemented as a viable alternative to shell and tube heat exchangers with no limiting conditions within the expected SFR operating range due to the robustness of the diffusion bonding manufacturing process (57).

The S-CO_2 cycle still requires validation, especially in the development of control techniques for transient operation. Significant progress has recently been made in transient modeling, but additional work will have to enter the experimental realm (Trinh, 2009). A full recompression cycle test loop is required to test the performance of the cycle under system transients. The corrosion of stainless steels in an S-CO_2 environment must be investigated further. Corrosion will affect the lifetime and reliability of heat exchangers and the failure modes of every PCS component. The British AGR program has operated S-CO_2 cycles reliably at outlet temperatures of up to 650°C, but only at a 4.3 MPa operating pressure. The S-CO_2 power conversion cycle for an SFR would likely operate at 20MPa, increasing creep, fatigue, and corrosion rates. Early work in the field indicates that operating temperatures should not go above 700°C because dissociation of the S-CO_2 at these temperatures may lead to corrosion of the turbine blade and structural components (66).

RELAP5-3D calculations for metal and oxide fuel show that internal LBEs are within the acceptable region of the Frequency Consequence curve for the steady state core outlet temperature limit of 550°C. With the same limiting core outlet temperature and plant design, these fuel forms should produce the same thermodynamic efficiencies.

The thermodynamic efficiencies were evaluated for plant designs with the following design space:

- 510°C and 530°C core outlet temperatures,
- PCHE and shell-and-tube heat exchangers,
- Intermediate loop and no intermediate loop,
- Rankine, supercritical water and supercritical CO2 power conversion cycles.

Transient analysis of both metal and oxide pool type SFRs indicate the FCC does not limit the reactor operating temperature. Thus, to maximize thermodynamic efficiency the SFR designer should use the highest allowable steady state core outlet temperature. Using the G4ECONs model, the cost saving potential of the design alternatives mentioned above were calculated and are reported in Table 23.

Table 23–Ranking Busbar Cost Savings for the Various Design Alternatives

Design Alternative	Decrease in Busbar Cost
Raising Outlet Temperature from 510°C to 550°C	-2.8%
Removing Intermediate Loop	-1.25%*
Adopting PCHEs	-1%
S-CO$_2$ power conversion cycle	-8.4%
All Alternatives but Removing the Intermediate Loop	-14.4%
All Design Alternatives	-14.5%*

* Does not include capital cost savings from removing intermediate loop

Steady state clad temperature limits prevent HT-9 clad for metal or oxide fuel from hotter than 550°C, and all major internal LBEs are satisfied for these temperatures. In regard to increasing thermodynamic efficiency, there is no practical difference between metal and oxide fuels with respect to the risk informed framework of NUREG-1860. No additional system constraints exist to prevent the outlet temperature from moving to 550°C. Combined with removing the intermediate loop, changing to PCHEs, and moving to a S-CO$_2$ power conversion cycle, busbar costs may decrease by 14.5%.

VI.1.C Improved Modeling of the Rate of the Metal Fuel/Cladding Eutectic Formation Rate

The fuel/cladding eutectic experiments were conducted over 40 years. During that time, different fuel forms, cladding options, and experimental procedures were used as technology improved and sodium reactor designs matured. The range of fuel/cladding eutectic experiments can be divided into four general categories:

1. Uranium Dripping Tests – 306SS test slugs were dipped into molten uranium to determine eutectic penetration rates,
2. EBR-II Safety Tests – In-reactor tests where the sodium flow rate was purposely restricted in an assembly to cause higher than nominal temperatures to enable eutectic formation,

3. EBR-II Furnace Tests – UZr and UPuZr fuels were irradiated in EBR-II over a range of claddings, plutonium enrichments, burnups, and linear powers and subsequent eutectic tests were conducted in a high temperature furnace,
4. FFTF Furnace Tests – A full length IFR Driver Fuel pin, U 19%PU 10% Zr, was irradiated in FFTF to 9.5at% burnup and subsequent eutectic tests were conducted in a high temperature furnace.

The rate of fuel/cladding eutectic formation has historically been modeled as a simple function of temperature, in spite of 40 years of experimental evidence which supports additional dependencies such as fuel form, cladding type, burnup, enrichment, and linear power. New correlations which statistically resolve many of these dependencies were developed and their predictive uncertainties were quantified. It was shown that the current correlations over predict eutectic penetration for potential accident types. Additionally, for the accident analyzed, the uncertainties associated with the new correlations are small enough as to be negligible when compared to other cladding failure uncertainties, such as creep rates or predicted time-to-cladding-failure.

VI.1.D General Conclusions

According to the TNF, both metal and oxide fuel are acceptable and should have the same operating limits without the use of tertiary shutdown systems. Some additional insights concerning fuel testing and selection are:

1. The only regulatory advantage possessed by oxide fuel is more robust international and national fuel testing databases. This advantage partially disappears when considering TRU fuel which has little oxide or metal fuel testing,
2. While potentially irrelevant from a regulatory perspective, metal fuel possess better inherent shutdown capabilities when compared to oxide fuel,
3. Future metal fuel testing should be conducted over the entire range of expected operating parameters. The initial fuel/cladding eutectic database focuses on linear powers which are as much as two times the peak linear powers proposed by S-PRISM and other metal reactor designs, which may force unnecessary conservatism on metallic fuel.

From Table 38, Busbar costs can be decreased by over 19% by optimizing thermodynamic efficiency, adopting a S-CO2 power conversion cycle, and moving to an S-PRISM-type low-pressure containment. The S-CO_2 power conversion cycle is still in the developmental stage. A large financial investment is needed before cost savings associated with this power conversion cycle can be achieved.

The accuracy of predicting fuel/cladding eutectic penetration rates is improved and the uncertainties in the new correlations are small enough to be neglected for most transients.

Table 38 – Achievable cost savings for the SFR through the application of Risk Information

Design Alternative	Rank	Decrease in Busbar Cost
Raising Outlet Temperature to 550°C	5	-2.8%
Removing Intermediate Loop	6	-1.3%*
Reducing Containment Requirements	4	-4.7
Adopting PCHEs	7	-1%
S-CO_2 power conversion cycle	3	-8.4%
All Alternatives but Removing the I.L.	2	-18.5%
All Design Alternatives	1	-19.5%

VI.1.E Recommendations for Future Work

This thesis identified a wide array of future work that should be conducted in support of sodium cooled fast reactor development.

Steady State Analysis

1. Additional high burnup U-19%Pu-10%Zr fuel with HT9 cladding high temperature eutectic testing should be conducted for fuel irradiated at linear powers consistent with typical metallic fueled SFR designs, approximately 8 to 9 kW/ft for peak conditions.
2. A rigorous structural analysis is needed focusing on the steady state temperature dependence of the reliability of primary and secondary piping, valves, primary vessel, and steam generators. Sodium/water reactions have plagued SFRs for their entire existence, sometimes causing them to be shut-down for years, as was the case with MONJU. As designers increase system temperatures in order to increase thermodynamic efficiency, they must assure that those economic gains will not be lost due to a decreased capacity factor.

3. The horizontal, semi-statistical hot channel factor methodology needs to be updated by assuming non-normal statistical uncertainties. Additionally, axial variations of the hot channel factors should be considered because creep constraints will occur at the maximum cladding temperature location at top of the pin, while eutectic constraints will occur at the peak linear power of the fuel pin. The potential to increase creep and eutectic cladding temperature limits by decreasing plenum pressure and accounting for linear power in the eutectic limit should also be examined.

Transient Analysis

1. An analysis of the co-variances of reactivity coefficients in SFR designs is needed. In this thesis, reactivity coefficients were treated as independent variables, but dependencies between these coefficients should exist. For example, a harder than expected spectrum will simultaneously cause the sodium density coefficient to increases and the Doppler coefficient to become less effective, thus potentially reducing inherent safety. A softer spectrum will cause the opposite effect. In order to more realistically model the probabilistic transient response, these dependencies should be incorporated, potentially as co-variances to the normal probability distributions which currently describe the reactivity coefficients.
2. Each RELAP5 simulation produces a range of outputs including time dependent temperature, pressure, flow rates, and Fractional Cladding Damages (FCDs) for various components. Each of these parameters will have a distribution due to the epistemic uncertainties, but for now only the FCD has been examined. In fact, because cladding failure is modeled as a Bernoulli sequence, the only information, or evidence, extracted from each simulation is whether or not the FCD exceeds 1.0. It is probable that some of the ignored information could be used to provide a more accurate estimate of the failure probability, but incorporating this evidence is left as future work.
3. The epistemic uncertainty distributions describing the SFR reactivity coefficients need to be re-examined. There is no reason to assume that these coefficients are normally distributed and this assumption is most likely incorrect. Special attention should be paid to the tails of the distributions, since failure of inherent safety will occur in this region. Any chosen distribution should ensure that a conservative failure probability will be reached.

VII WORKS CITED

1. NRC. (2007). *Feasibility Study for Development of a Risk-Informed, Performance Based Alternative to Plant Licensing.* **NUREG-1860**, Office of Nuclear Regulatory Research. Washington D.C.:NRC.
2. Boardman, C. E., Dubberley, A. E., & Hue, M. (2000). Optimizing the size of the Super-PRISM Reactor. ICONE.8, *#8003.* Baltimore, MD.
3. Mizuno, T., Ogawa, T., Naganuma, M., & Aida, T. (2005). Advanced Core Design Studies with Oxide and Metal Fuels for Next Generation Sodium Cooled Reactors. ICAPP'05, *#5195.* Seoul, Korea.
4. Dubberley, A., Wu, T., & Kubo, S. (2003). Appendix "C", Part II: S-PRISM Hight Burnup Metal-Fuel Core Designs. ICAPP'03, *#3142.* Cordoba, Spain.
5. Boardman, C. E., Dubberley, A. E., Carroll, D. G., Hue, M., Fanning, A. W., & Kwant, W. (2000). A Description of the S-PRISM Plant. ICONE8, *#8168.* Baltimore, MD.
6. Ivans, W. (2006). *The Current Nuclear Regulatory Environment: A PRISM Perspective.* **M.S. Thesis**, Department of Nuclear and Radiological Engineering. Gainesville, FL: University of Florida.
7. Energy Solutions. (2008). *GNEP Deployment Studies, Overall Summary Report, Rev. 1.*
8. Wigeland, R., & Cahalan, J. (2009). Fast Reactor Fuel Type and Reactor Safety Performance. GLOBAL'09, *#9445.* Paris, France.
9. Poplavsky, V., Tsibulia, A., & Kamaiev, A. B. (2004). BN-1800: A Next Generatioin Fast Breeder. *Nuclear Engineering International*, ***49*** (599), 20-24.
10. IAEA. (2006). *Fast Reactor Database 2006.* **IAEA-TECDOC-1531**. International Atomic Energy Agency.
11. Morris, E. (2007). Uncertainty in Unprotected Loss of Heat Sink, Loss of Flow, and Transient Overpower Accidents. **ANL-AFCI-205** . Argonne, IL: Argonne National Laboratory.
12. Dostal, Driscoll, & Hejzlar. (2004). *A Supercritical Carbon Dioxide Cycle for Next Generation Power Reactors.* **MIT-ANP-TR-100**, Department of Nuclear Science and Engineering. Cambridge, MA: MIT.
13. Chang, Y. I. (2007). Technical Rational for Metal Fuel in Fast Reactors. *Nuclear Engineering and Technology*, ***39*** (3), 162-170.
14. Johnson, B. C. (2010). *Application of the Technology Neutral Framework to Sodium-Cooled Fast Reactors.* **PhD Thesis**, Department of Nuclear Science and Engineering. Cambridge, MA: MIT.
15. Vilim, R. (1985). *Reactor Hot Spot Analysis.* **FRA-TM-152**. Chicago, IL: Argonne National Laboratory.
16. Carelli, M., & Friedland, A. (1980). Hot Channel Factors for Rod Temperature Calculation in LMFBR Assemblies. *Nuclear Engineering and Design*, ***62*,** 155-180.
17. RELAP5-3D Dev. Team. (2005). *RELAP5-3D© Code Manual Volume I: Code Structure, System Models and Solution Methods.* **INEEL-EXT-98-00834**. Idaho Falls, ID: Idaho National Laboratories.
18. Memmott, M. J. (2009). *Thermal-Hydraulic Analysis of Innovative Fuel Configurations for The Sodium Fast Reactor.* **MIT-NES-TR-007**, Department of Nuclear Science and Engineering. Cambridge, MA: MIT.

19. ANL. (1996). *The SAS4A/SASSYS-1 LMR Analysis Code System.* ANL-FRA-1996-3 Vol. 3, Reactor Analysis Division. Argonne, IL: Argonne National Laboratory.
20. Cahalan, J., Wigeland, R., Friedel, G., Kussmaul, G., Moreau, J., Perks, M., et al. (1992). Performance of Metal and Oxide Fuels During Accidents in Large Liquid Metal Cooled Reactors. International Topical Meeting on Fast Reactor Safety, *#700149*, pp. 73-82. Snowbird, UT.
21. Langewisch, D. R. (2009). *Uncertainty and Sensitivity Analysis for Long-Running Computer Codes: A Critical Review.* **MIT-NSP-TR-024**, Department of Nuclear Science and Engineering. Cambridge, MA: MIT.
22. Ang, H.-S., & Tang, W. (2007). **Probability Concepts in Engineering**. Wiley.
23. Robert, C., & Casella, G. (2004). **Monte Carlo Statistical Methods, 2nd Ed**. New York, NY: Springer.
24. MATHWORKS Inc. (2010). **MATLAB Users Manual**. Natick, MA: MATHWORKs.
25. Mueller, C., & Wade, D. (1988). Probabilities of Inherent Shutdown of Unprotected Events in Innovative Liquid Metal Reactors. ANS Topical Meeting on Safety of Next Generation Power Reactors, *#880506-3.* Seattle, WA.
26. Apostolakis, G., & Mosleh, A. (1979). Expert Opinion and Statistical Evidence: An Application to Reactor Core Melt Frequency. *Nuclear Science and Technology* , ***70***, 135-149.
27. Albright, S., Winston, W., & Zappe, C. (2009). **Data Analysis & Decision Making, Rev. 3**. Mason, OH: South-Western Cengage Learning.
28. SAS Institute Inc. (2007). **JMP Introductory Guide**, *Release 7.*
29. Droguett, E., & Mosleh, A. (2008). Bayesian Methodology for Model Uncertainty Using Model Performance Data. *Risk Analysis* , ***28*** (5), 1457-1476.
30. Azarkhail, M., Ontiveros, V., & Modarres, M. (2009). A Bayesian Framework for Model Uncertainty Considerations in Fire Simulation Codes. ICONE17, *#75684.* Brussels, Belgium.
31. Ichimiya, M., Mizuno, T., & Kotake, S. (2007). A Next Generation Sodium Cooled Fast Reactor Concept and its R&D Program. *Nuclear Engineering and Technology* , ***39*** (3), 171-186.
32. Kwon, H., Lee, D.-U., Lee, B.-O., Kim, Y. L., & Kim, Y.-S. (2003). Probabilistic Estimation of LMR Fuel Cladding Performance. *J. Korean Nuclear Society* ; ***35*** (2), 144-154.
33. Royl, P., Cahalan, J., Friedel, G., Kussmaul, G., Moreau, J., Perks, M., et al. (1990). Influence of Metal and Oxide Fuel Behavior on the ULOF Accident in 3500MWth Heterogeneous LMR Cores and Comparison with other Large Cores. International Topical Meeting on Fast Reactor Safety, *IV*, pp. 83-92. Snowbird, UT.
34. Cohen, A., Tsai, H., & Neimark, L. (1993). Fuel/cladding compatibility in U- 19Pu-10Zr/ HT9-clad fuel at elevated temperatures. *Journal of Nuclear Materials* (**204**), 244-251.
35. Boardman, C., Dubberley, A., Hui, M., & Iwashige, K. (2001). Containment Performance of S-PRISM under Severe BDB Conditions. ICONE9, *#943.* Nice, France.
36. Singh, O. (2002). Energetics of Core Disruptive Accident for Different Fuel for a Medium Sized Fast Reactor. *Journal of Nuclear Energy* , ***29***, 673-683.
37. Crawford, D. C., Porter, D. L., & Hayes, S. L. (2007). Fuels for sodium-cooled fast reactors: US perspective. *Journal of Nuclear Materials* (**371**), 202-231.

38. Cheon, J., Chan, B., Byoung, O., Raison, J., Mizuno, T., Delange, F., et al. (2009). Sodium Fast Reactor Evaluation: Core Materials. *Journal of Nuclear Materials* , ***392*** (2), 324-330.
39. Pahl, R., Porter, D., Crawford, D., & Walters, L. (1992). Irradiation behavior of metallic fast reactor fuels. *Journal of Nuclear Materials* , ***188***, 3-9.
40. Mizuno, T., Ogawa, T., Naganuma, M., & Aida, T. (2005). Advanced Oxide Fuel Core Design Study for SFR in the "Feasibility Study" in Japan. GLOBAL'05, *#434*. Tsukuba, Japan.
41. Hoffman, G., Walters, C., & Bauer, T. (1997). Metallic Fast Reactor Fuel. *Progress in Nuclear Energy* , ***31*** (1), 83-110.
42. Delage, F., Carmack, J., Lee, C., Mizuno, T., Raison, P., & Somers, J. (2009). SFR Status for Ongoing Research and Results: Advanced Fuels. GIF Symposium, (pp. 231-237). Paris, France.
43. Keiser, D., & Cole, J. (2005). Fuel/Cladding Compatibility in Metallic Nuclear Fuels. *TMS Letters* , *2*, 79-80.
44. Keiser, D., & Cole, J. (2009). An Assessment of Layer Development at the Fuel/Cladding Interface During Irradiation of Metallic SFR Fuel Elements. Mater. Res. Soc. Symp. Proc. , *1125*.
45. Kim, J., Ryu, H., Baek, J., Oh, S., Lee, B., Lee, C., et al. (2009). Performance of a Diffusion Barrier under a Fuel-Clad Chemical Interaction (FCCI). *Journal of Nuclear Materials* , ***39*** (4), 144-150.
46. Chang, Y. I., Walters, L. C., Laidler, J. J., Pedersen, D. R., & Wade, D. C. (1994). *Intergal Fast Reactor Program Annual Progress Report FY 1993.* **ANL-IFR-244**. Argonne, IL: Argonne National Laboratory.
47. Chang, Y. I., Walters, L. C., Laidler, J. J., Pedersen, D. R., & Wade, D. C. (1994). *Intergal Fast Reactor Program Annual Progress Report FY 1994.* **ANL-IFR-246**. Argonne: Argonne National Laboratory.
48. Sugino, K., Ogawa, T., Okano, Y., & Minzuno, T. (2005). Advanced Metal Fuel Core Design Study for SFR in the "Feasibility Study" in Japan. GLOBAL'05, *#399*. Tsukuba, Japan.
49. Walter, A., & Reynolds, A. (1981). **Fast Breeder Reactors**. New York: Pergamon Press.
50. Dubberley, A., Lipps, A., Boardman, C., & Wu, T. (2000). SuperPRISM Metal Core Margins To Severe Core Damage. ICONE 8, *#8001*. Baltimore, MD.
51. Morris, E., & Tenter, M. C. (1994). SAS4A Analysis of Abrupt Loss of Flow without SCRAM in Metallic Fueled Fast Reactors. International Topical Meeting on Sodium Fast Reactors Safety, *#81829A*. Obninsk, Russian Federation.
52. Tobita, Y., Morita, K., Kawada, K., Niwa, H., & Nonaka, N. (1999). Evaluation of CDA Energetics in the Prototype LMFBR with Latest Knowledge and Tools. ICONE7, *#7145*. Tokyo, Japan.
53. Kondo, S., Tobita, Y., Morita, K., Brear, D., Kamlyama, K., Yamano, H., et al. (1999). Current Status and Validation of the Simmer-III LMFR Safety Analysis Code. ICONE7, *#7249*. Tokyo, Japan.
54. Tobita, Y., Kondo, S., Yamano, H., Morita, K., Maschek, W., Coste, P., et al. (2006). The Development of SIMMER-III, an Advanced Computer Program for LMFR Safety Analysis, and Its Application to Sodium Experiments. *Nuclear Technology* , ***153***, 245-255.

55. Tobita, Y., Koji, M., Kawada, K., Niwa, H., & Nonaka, N. (1999). Evaluation of CDA Energetics in the Prototype LMFBR with Latest Knowledge and Tools. ICONE7, *#7145.* Tokyo, Japan.
56. Nitta, C. (2010). *Applying Risk Informed Methodologies To Improve the Economics of Sodium-Cooled Fast Reactors.* **S.M. Thesis**, Department of Nuclear Science and Engineering. Cambridge, MA: MIT.
57. Heatric (TM). (2009). Retrieved March 4, 2009, from www.heatric.com
58. Ludington, A. (2009). *Tools for Supercritical Carbon Dioxide Cycle Analysis and the Cycle's Applicability to Sodium Fast Reactors.* **S.M. Thesis**, Department of Nuclear Science and Engineering. Cambridge, MA: MIT.
59. Puigh, R. (1985). In-Reactor Creep of Selected Ferric Alloys. Effects of Radiation on Materials: Twelfth International Symposium, (pp. 7-18). Williamsburg, VA.
60. Kwant, W., & Boardman, C. (1992). PRISM-Liquid Metal Cooled Reactor Plant Design and Perfomance. *Nuclear Engineering and Design* , ***136***, 111-120.
61. Denning, R., Brunett, A., Grabaskas, D., Umbel, M., & Aldemir, T. (2010). Toward More Realistic Source Terms for Metallic-Fuel Sodium Reactors. *ICAPP'10, #10204.* San Diego, CA.
62. Mannan, S., Cheatal, S., Raj, B., & Bhoje, S. (2003). Selection of Materials for Prototype Fast Breeder Reactor. Transactions- Indian Institute of Metals, ***56 Part 2***, pp. 155-178. India.
63. Hejzlar, P., Boungiorno, J., Macdonald, P., & Todreas, N. (2004). Design Strategy and Constraints for Medium-Power Lead-Alloy-Coolded Actinide Burners. *Nuclear Technology* , ***147***, 321-341.
64. Sienicki, J., Moisseytsev, A., Cho, D., Thomas, M., Wright, S., Pickard, P., et al. (2010). International Collaboration on Development of the Supercritical Carbon Dioxide Brayton Cycle for Sodium-Cooled Fast Reactors under the Generation IV International Forum Component Design and Balance of Plant Project. ICAPP'2010, *#10048.* San Diego, CA.
65. Trinh, T. (2009). *Dynamic Response of the Supercritical CO2 Brayton Recompression Cycle to Various System Transients.* **S.M. Thesis**, Department of Nuclear Science and Engineering. Cambridge, MA: MIT.
66. Forrest, E., & Stefano, P. (2010). Alternative Power Cycles for Nuclear Power Plants. **Unpublished MIT Study** .
67. El-Sheikh, K. (1994). Probabilistic Risk Assessment of the Advanced Liquid Metal Reactor. **GEFR-00873** . San Diego, CA: GE Nuclear Energy.
68. Bauer, T., Wright, A., Robinson, W., & Klickman, A. (1987). Cladding Failure Margins for Metallic Fuel in the Integral Fast Reactor. SMiRT'87, *#880506-14.* Lausanne, Switzerland.
69. Chang, Y. I., Walters, L. C., Battles, J. E., Pedersen, D. R., & Wade, D. C. (1990). *Integral Fast Reactor Program Summary Progress Report FY1985-FY1989.* **ANL-IFR-125**. Argonne, IL: Argonne National Laboratory.
70. Lahm, C., Koenig, J., Betten, P., Bottcher, J., Lehto, W., & Seidel, B. (1987). EBR-II Driver Fuel Qualification For Loss-Of-Flow and Loss-Of-Heat-Sink Tests without SCRAM. *Nuclear Engineering and Design* (**101**), 25-34.
71. Tsai, H. (1991). Behavior of Low-burnup Fuels for the Integral Fast Reactor at Elevated Temperatures in Ex-Reactor Tests. Conference on Fast Reactors and Related Fuel Cycles, *#911001-17.* Kyoto, Japan.

72. Tsai, H. (1990). Fuel/Cladding Compatibility In Irradiated Metallic Fuel Pins at Elevated Temperatures. Proceedings of the 1990 International Fast Reactor Safety Meeting, *#900804-9.* Snowbird, Utah.
73. Walter, C., & Kelman, L. (1966). The Interaction of Iron with Molten Uranium. *Journal of Nuclear Materials* , ***20*** (3), 314-322.
74. Walter, C., & Kelman, L. (1962). Penetration Rate Studies of Stainless Steel by Molten Uranium and Uranium-Fissium Alloy. *Journal of Nuclear Materials* , ***6*** (3), 281-290.
75. Betten, P., Bottcher, J., & Siedel, B. (1983). Eutectic Penetration Times in Irradiated EBR-II Driver Fuel Elements. ANS Winter Meeting, *# 83104775.* San Francisco, CA.
76. Tsai, H. e Denman, M. Personal Communication. Email. 6 Aug. 2010.
77. Mueller, C., & Kramer, J. (1987). Cladding Failure Probability Modeling for Risk Evaluations of Fast Reactors. SMIRT9, *# 870812.* Lausanne, Switzerland.
78. Hejzlar, P., & Cho, D. (2008, October). Personal Communication. Argonne, IL: ANL.
79. Thermoflow, Inc. (2006). **STEAM PRO 16.0**.
80. Martin, P. (2008). French and United Kingdom Experience of High Burnup Mixed-Oxide Fuel in Sodium-Cooled Fast Breeder Reactors. *Journal of Nuclear Technology* , ***161***, 35-44.
81. Dostal, V. (2004). Medium Powered Lead-Alloy Fast Reactor Balance-of-Plant Options. *Nuclear Technology* , ***147*** (3), 388-405.
82. Chikazawa, Y., Kotake, S., & Sawada, S. (2011). Comparison of Advanced Fast Reactor Pool and Loop Configurations from the Viewpoint of Construction Cost. *Nuclear Engineering and Design* , ***241*** (1), 378-385.

VIII APPENDIX A – DEFORM5 FAILURE MODEL

For metallic fuel in Sodium Cooled Fast Reactors (SFRs), cladding failures during accident conditions are primarily caused by stress rupture. Stress rupture is induced by cladding thinning due to a combination of thermal creep and fuel/cladding eutectic formation. ANL has a variety of failure models which include both creep and eutectic which are included in SAS, the details of which can be found on pages 8-115 to 8-127 in ANL-FRA-1996-3 Volume 3 (19). This appendix seeks to summarize the primary ANL failure model, DEFORM5, and explain how it can be used to predict cladding failure. The methodology described in this Appendix is used in the Creep_Failure.m code of BEAGLE to predict clad failure.

A.1 Nomenclature

For simplicity, the following symbols and definitions will be used for all of the following equations in this paper:

Θ = Dorn Parameter = $t_r \exp(-Q/RT)$
t_r = Mean Rupture Time (hr)
Δt = Time step (s)
T = Cladding Temperature (K)
T_f = Failure Temperature (ksi)
T_a = Temperature at the fuel/cladding interface
T_{cut} = Input Eutectic Temperature (650°C)
$\dot{T}$ = heating rate
R = Universal gas Constant
Q = Specific Energy of Reaction = (cal / mole)

- 20%CW SS – Q = 53,508 cal/mole
- HT-9 – 70,170 cal/mole

$$\sigma_\theta = Hoop\ Stress = \frac{r_o^2 + r_i^2}{r_o^2 - r_i^2} P = \frac{P * R}{h}$$

σ^* = 135 ksi
r_o = outer cladding radius
r_i = inner cladding radius
h = cladding thickness
l = length of fuel pin
r = cladding midwall radius
P = Internal Gas Pressure– typical high burnup value is ~ 10MPa
P_b = Burst Pressure
LMP = Experimentally determined Larson-Miller parameter
B = Burnup (atom %)

$F_{f,n}$ = New Failure Fraction
$F_{f,o}$ = Fractional Cladding Damage
r_1 = outer boundary of old inner cladding cell
r_2 = outer boundary of old center cladding cell

A.2 ANL Failure Model (DEFORM-5)

Deform 5 calculates cladding failure due to both eutectic wastage of the inner wall and thinning of the cladding due to thermal creep as discussed in Section 1.2. DEFORM-5 calculates a static mean failure time for any given time step given average stresses (function of cladding radius and wall thickness) and cladding temperature. The fractional cladding damage (FCD) is then computed by dividing the length of the time step by the mean failure time for that time step, and summing over all previous time steps.

For eutectic formation, the wall thickness decreases at a rate governed by the following Arrhenius equation. This equation will be replaced with a distributed equation once the probabilistic model is completed.

$$\dot{r} = 10^{-6} * \exp\left(22.847 - \frac{27624}{T_a}\right) \qquad \text{A.1}$$

The equivalent creep rate is determined by:

$$\dot{\varepsilon}_{eq} = 5.1966x10^{10} * \left(\frac{\sigma_{eq}}{\sigma^*}\right)^{2.263} * e^{-\frac{36739}{T}} \qquad \text{A.2}$$

Where:

$$\sigma^* = 3.956x10^{-3} + 2.12x10^{11} * (1.144 - 4.856x10^4 * T) \quad (Pa) \qquad \text{A.3}$$

the rupture time is then calculated by:

$$t_r = \theta * e^{\frac{70170\frac{cal}{mole}}{*1.986\frac{cal}{mole*K}* T}} \qquad \text{A.4}$$

where the Dorn parameter θ can be found by:

$$\theta = e^{A+B*\ln \ln\frac{730MPa}{\sigma_{eq}}} \qquad \text{A.5}$$

$$A = -34.8 + \tanh\frac{\sigma - 200}{50} + C \tag{A.6}$$

$$B = \frac{12}{(1.5 + .5 * tanh\frac{\sigma - 200}{50})} \tag{A.7}$$

$$C = -\left(0.5\left[1 + tanh\frac{\sigma - 200}{50}\right]\right) * \left(0.75 * \left[1 + \tanh\frac{\dot{\mathrm{T}} - 58}{17}\right]\right) \tag{A.8}$$

where the damage fraction is calculated by:

$$\mathrm{F}_{\mathrm{f,n}} = \frac{\Delta \mathrm{t}^{\mathrm{i}}}{\mathrm{t_r}^{\mathrm{i}}} \tag{A.9}$$

and the total FCD is calculated by:

$$\mathrm{F}_{\mathrm{f,o}}^{\mathrm{i+1}} = \mathrm{F}_{\mathrm{f,o}}^{\mathrm{i}} + \mathrm{F}_{\mathrm{f,n}} \tag{A.10}$$

when $F_{f,o}$=1 the cladding is assumed failed. The EOL FCD value is predicted to be 0.0006 for S-PRISM fuel (4). This value was used as the initial FCD value for all Creep_Failure.m calculations.

A.3 Creep Rate Effect on Cladding Thickness

The creep model presented in section II.A.3 described how to calculate the equivalent creep rate for steady state and transient conditions. This section will describe how creep affects the cladding thickness in the RELAP5-3D post-processing model.

First, the primary stresses must be defined. The cladding will be analyzed using a thin shell approximation where:

$$\sigma_\theta = \frac{P * R}{h} \tag{A.11}$$

$$\sigma_z = \frac{P * R}{2 * h} \tag{A.12}$$

$$\sigma_z = -P \cong 0 \tag{A.13}$$

And the equivalent stress is defined as:

$$\sigma_{eq} = \sqrt{\frac{1}{2}\left[\sigma_\theta^2 + \sigma_z^2 + (\sigma_\theta - \sigma_z)^2\right]} = \sqrt{\frac{1.5}{2}} * \sigma_\theta \quad \text{A.14}$$

The preloaded strain in a thin shell approximated cylinder, neglecting thermal expansion, is then calculated by:

$$\epsilon_\theta = \frac{P * R}{2 * E * h}(2 - v) = \frac{\Delta r}{r} \quad \text{A.15}$$

$$\epsilon_z = \frac{P * R}{2 * E * h}(1 - 2v) = \frac{\Delta l}{l} \quad \text{A.16}$$

Radial strain is not calculated in the thin shell model, but as the radius and height increases, the thickness must decrease to conserve volume. The change in volume of the cladding can be expressed as:

$$(V + \Delta V) = 2 * \pi * (r + \Delta r) * (l + \Delta l) * (h + \Delta h) = 0 \quad \text{A.17}$$

A.18

After some arithmetic manipulation the change in thickness can be determined by:

$$\Delta h = -h * \left(1 - \frac{1}{(1 + \epsilon_\theta) * (1 + \epsilon_z)}\right) \quad \text{A.19}$$

Using the following relations, the t=0 radius, length, and cladding thickness can be calculated.

$$h^0 = h + \Delta h \quad \text{A.20}$$

$$l^0 = l + \Delta l \quad \text{A.21}$$

$$r^0 = r + \Delta r \qquad \text{A.22}$$

Then using the equivalent creep strain rate ($\dot{\epsilon}_{eq}$) from ANL and MIT correlations, the additional strain in the z and θ directions (r is not calculated due to the thin shell approximations) can be calculated by:

$$\Delta\epsilon_\theta = \frac{\Delta t * \dot{\epsilon}_{eq}}{\sigma_{eq}}\left[\sigma_\theta{}^i - \frac{1}{2}\sigma_z{}^i\right] = \frac{\Delta t * \dot{\epsilon}_{eq}}{\sigma_{eq}}\left[\frac{3}{4}\sigma_\theta{}^i\right] = \frac{\Delta r^i}{r^i} \qquad \text{A.23}$$

$$\Delta\epsilon_z = \frac{\Delta t * \dot{\epsilon}_{eq}}{\sigma_{eq}}\left[\sigma_z{}^i - \frac{1}{2}\sigma_\theta{}^i\right] = \frac{\Delta t * \dot{\epsilon}_{eq}}{\sigma_{eq}}\left[\frac{1}{2}\sigma_\theta{}^i - \frac{1}{2}\sigma_\theta{}^i\right] = 0 \qquad \text{A.24}$$

Where the i superscript indicates that the stresses are calculated with the ith time steps values for h_o, l_o, and r_o. The new thickness now only changes with radius as $\Delta\epsilon_z$ will always be 0.

$$\Delta h^i = -h^i * \left(1 - \frac{1}{(1 + \Delta\epsilon_\theta)}\right) \qquad \text{A.25}$$

Now the i+1th time parameters can be calculated by:

$$h^{i+1} = h^i + \Delta h^i \qquad \text{A.26}$$

$$r^{i+1} = r^i + \Delta r^i \qquad \text{A.27}$$

A.4 Validation Against SAS4a/DEFORM5 Calculations

Creep_Failure.m does not calculate transient plenum pressure changes, instead using a constant value for simplicity and speed. While a typical EOL plenum pressure for a metal fuel pin is approximately 10MPa (4), most of the cladding damage during the transient will occur at higher plenum pressure when high fuel temperature allows for further fission gas release. Thus, the a conservative constant pressure damage calculations should use a plenum pressure high enough to conservatively predict the time to failure estimates at all temperatures, within uncertainties (68). Using trial and error, a 14.3MPa plenum pressure conservatory predicts cladding failure times at all temperatures, as can be seen in Figure 71.

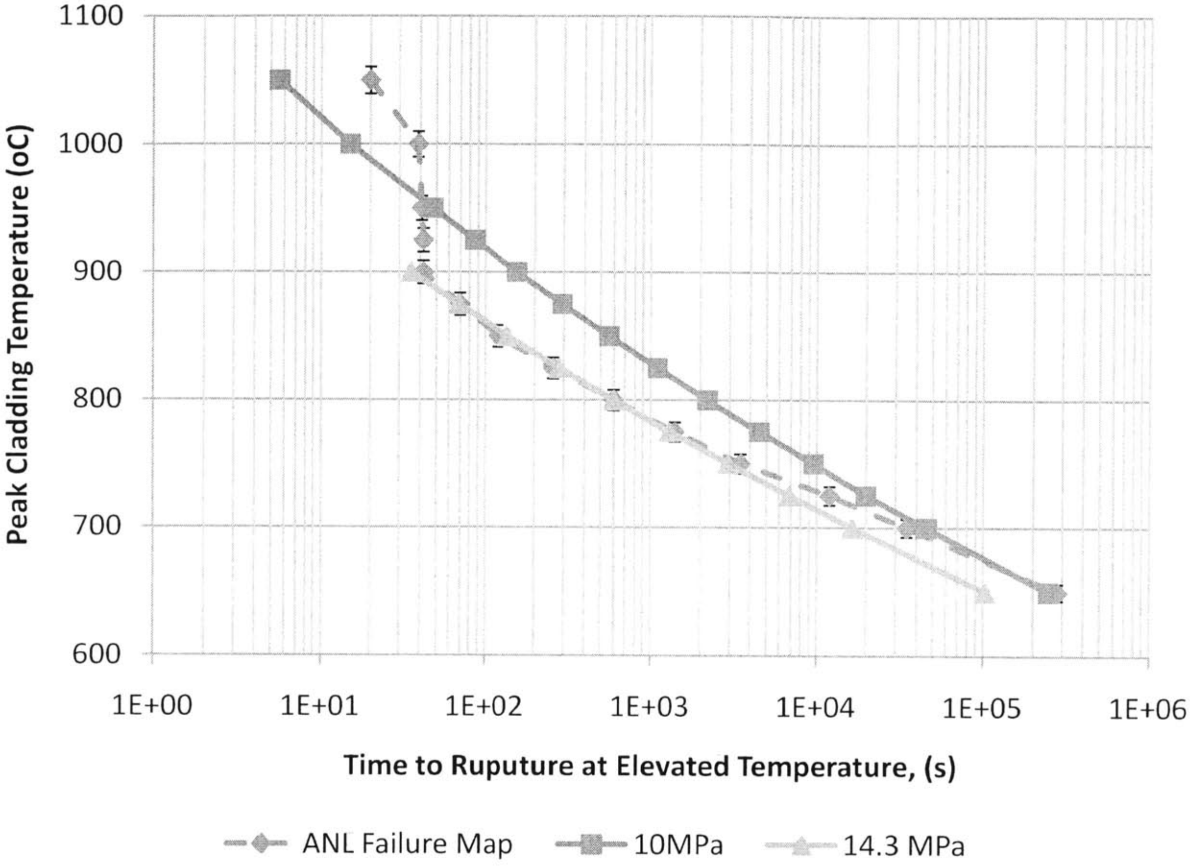

Figure 71 - Time to Cladding Failure.
Plotted as a Function of Cladding Temperature from ANL, constant 10MPa plenum pressure with DEFORM5, and constant 14.3MPa plenum pressure with DEFORM5 (68)

Figure 72 and Figure 73 show variable pressure and constant pressure failure times for 14.3MPa and 10MPa respectively. These figures also plot the Error Factor, defined as the constant pressure predicted time to cladding rupture divided by the variable pressure predicted time to cladding rupture. As can be seen, 10MPa shows better agreement at low temperatures and 14.3MPa shows better agreement at high temperatures.

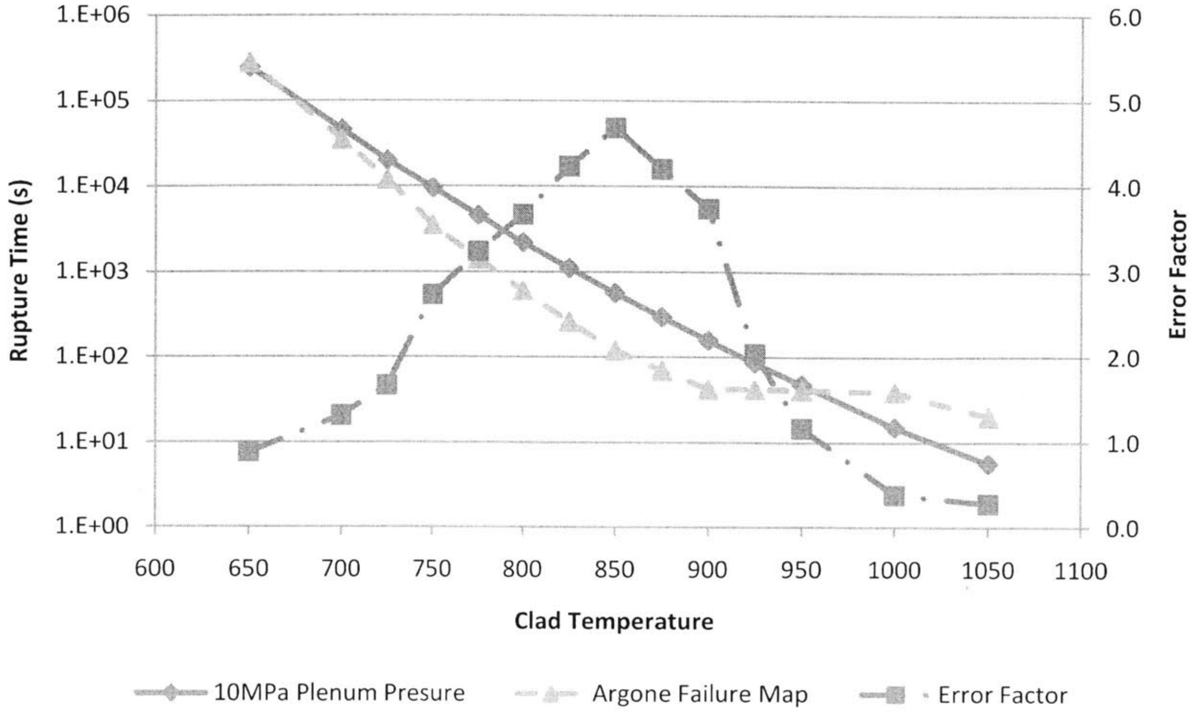

Figure 72 – Multiplicative Error between ANL Cladding Rupture Time and DEFORM5 Calculation with 10MPa Plenum Pressure

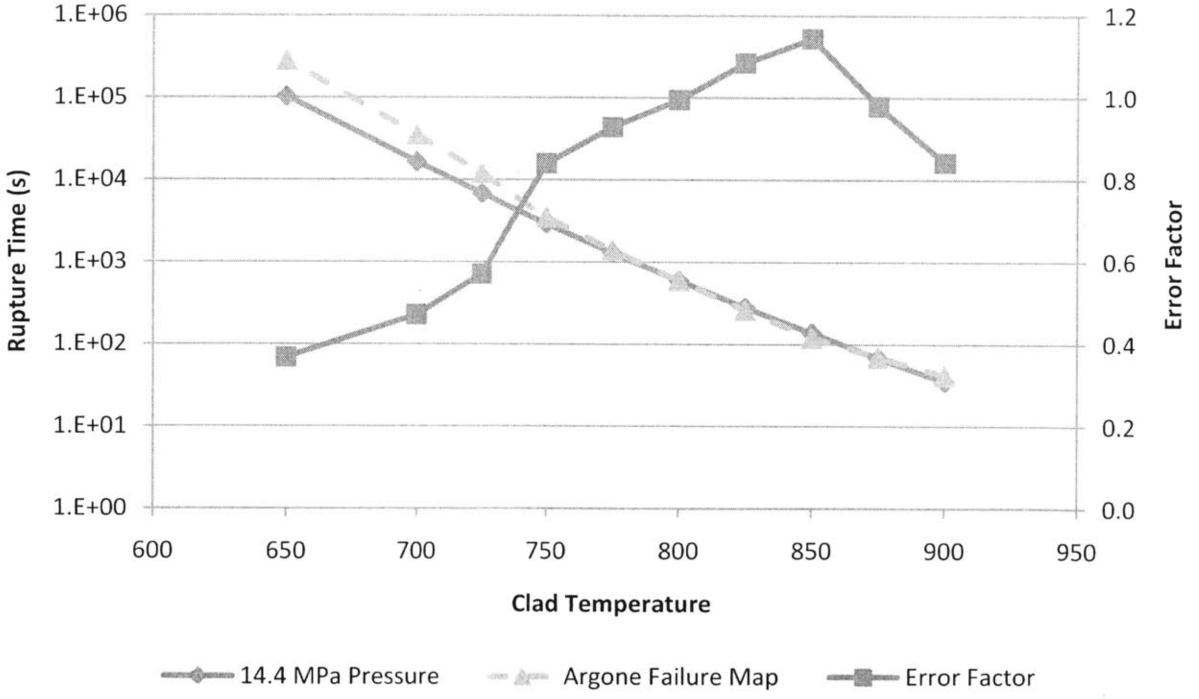

Figure 73- Multiplicative Error between ANL Cladding Rupture Time and DEFORM5 Calculation with 14.3MPa Plenum Pressure

A.4 Creep Conclusions

Using the methodology outlined in this appendix, the time to cladding failure can be approximated for a variety of transients. The cladding damage fraction model is typically considered a good estimation of failure time for high temperature transients ($T > 800^{o}C$), but may provide an overly conservative estimate for less challenging transients (77).

IX APPENDIX B – RELAP MODEL

Appendix B overviews the RELAP5-3D model in pictorial form. A full description of the RELAP5-3D model, including validation against the ABR-1000, can be found in Matthew Memmott's thesis (18). First, Figure 74 shows the primary loop. This loop connects the core to the intermediate heat exchangers and decay heat removal systems.

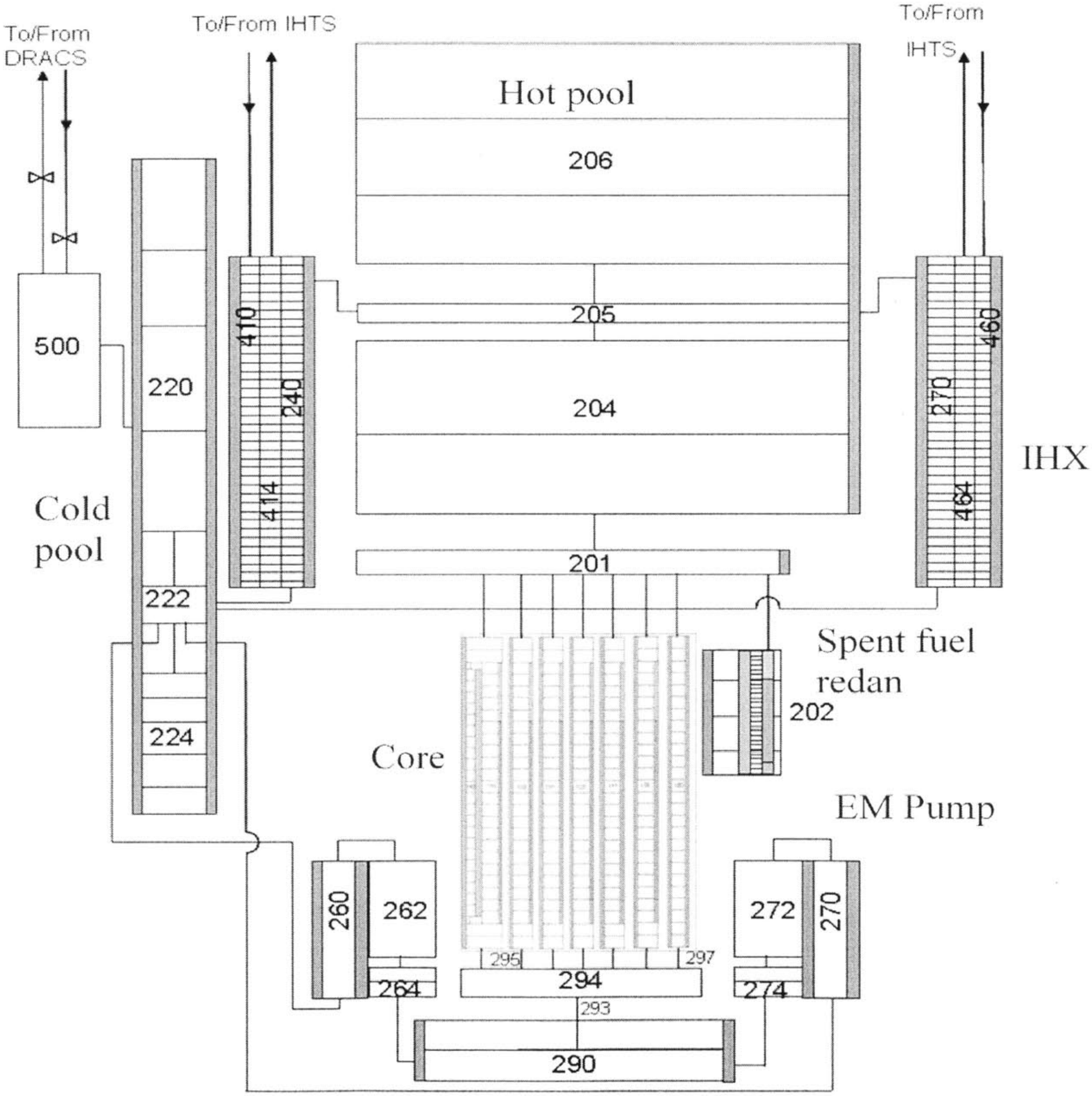

Figure 74 – Primary System of RELAP5-3D SFR Model

Figure 75 shows the reactor core model. Channel 190 represents the control assemblies, 180 represents core bypass, and channels 110, 131, 132, 123, 111, and 150 represent inner and outer fuel assemblies.

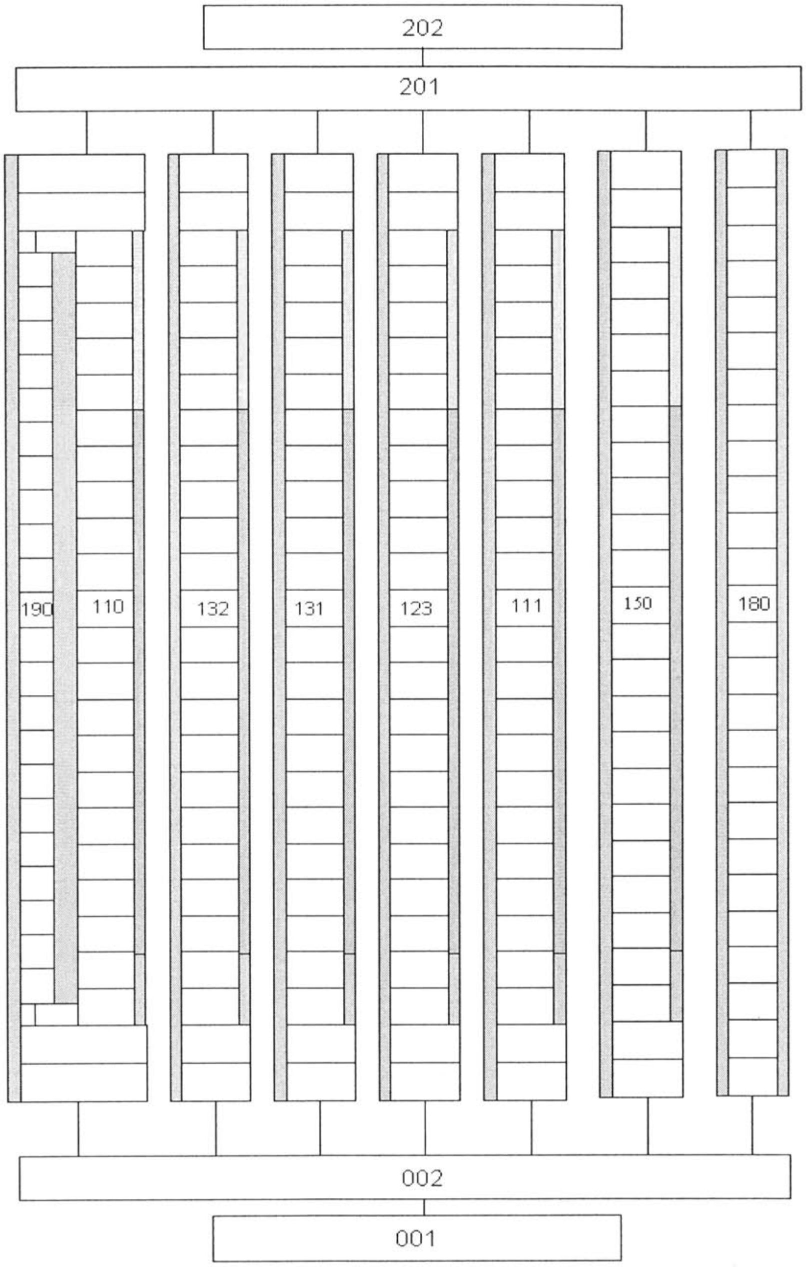

Figure 75– Core Layout of RELAP5-3D SFR Model

Figure 76 shows the intermediate loop of the ABR-1000. This loop connects the IHX to the steam generators. The balance of plant is represented by a response surface and thus is not shown.

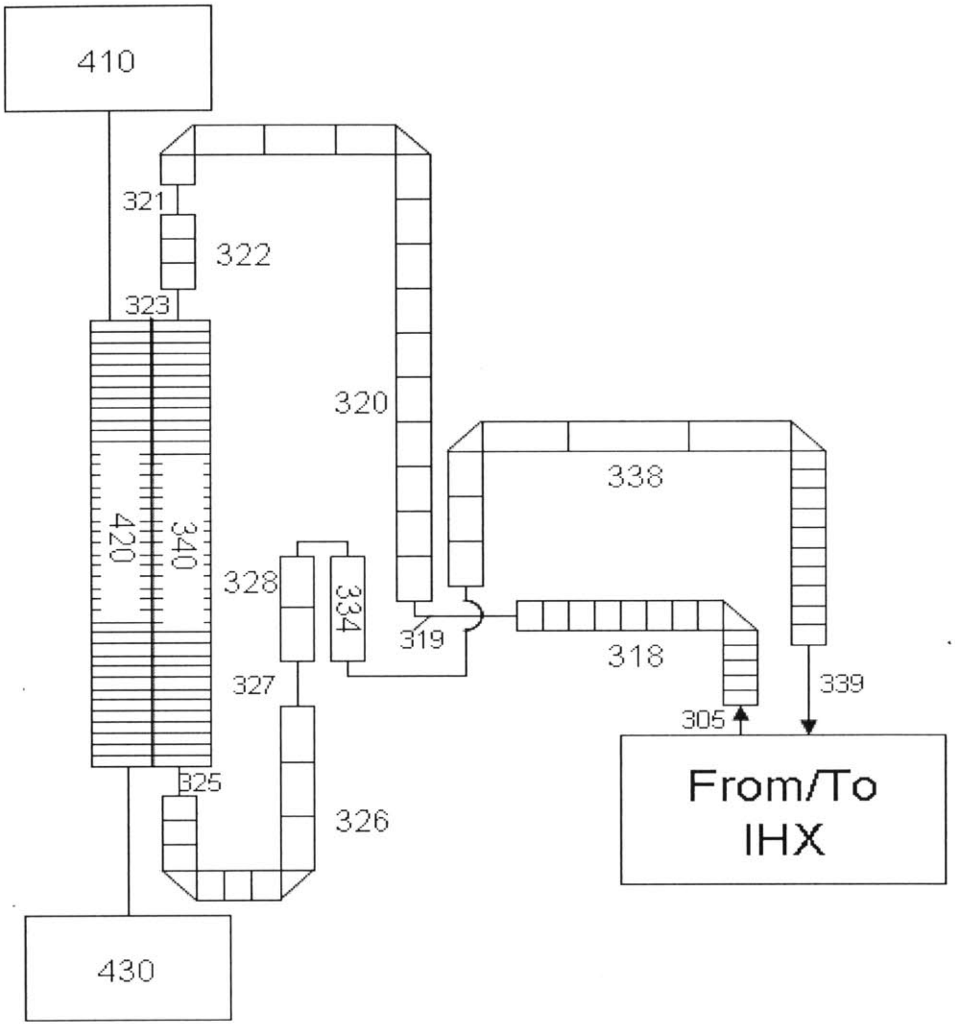

Figure 76– Intermediate Loop of RELAP5-3D SFR Model

Figure 77 shows the decay heat removal system. It connects the core to a NaK loop which removes energy to the environment through an additional heat exchanger.

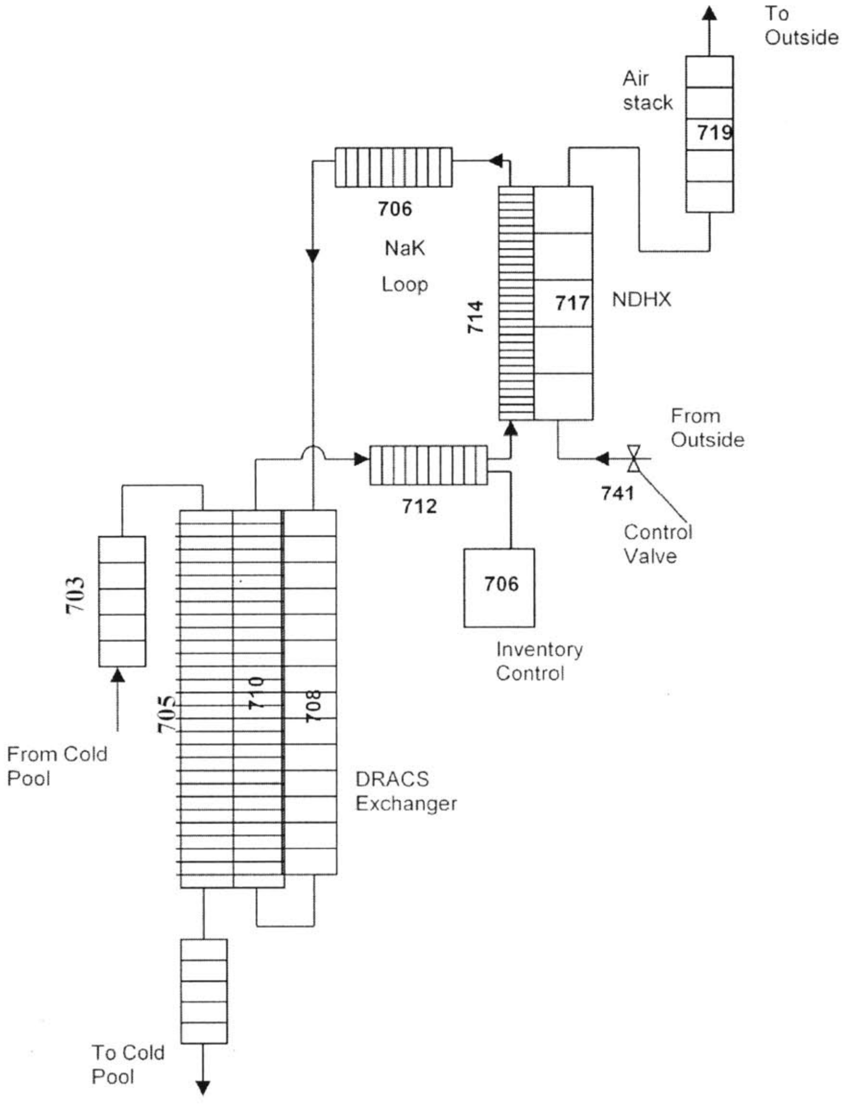

Figure 77 – Decay Heat Removal Loop of RELAP5-3D SFR Model

Table 39 compares the RELAP5-3D model parameters with the ABR-1000. It should be noted that the ABR-1000 report did not specify secondary sodium inventory, so it was originally assumed to be 533MT. It was later discovered that the secondary inventory was closer to 1000MT, but at that point most of the analysis conducted in this thesis was completed.

Table 39 – Comparison between RELAP5-3D Model and ABR-1000 Parameters

	Model	Report		Model	Report
Primary Inventory (MT)	1445	1309	**DRACS**		
Secondary Inventory (MT)	533	-	Na Tin (°C)	510	510
Primary Side			Na Tout (°C)	355.85	355
IHX Tin (°C)	508.19	510	NaK Tin (°C)	489.62	484
IHX Tout (°C)	353.85	355	NaK Tout (°C)	314.87	328
IHX ΔP Primary (kPa)	9.58	18.2	NaK H (m)	5.22	-
Core Tin (°C)	353.01	355	Air Tin (°C)	30	-
Core Tout (°C)	508.35	510	Air Tout (°C)	48.36	-
Core ΔP (MPa)	0.323	0.314	Stack H (m)	8.25	8.25
mdot (kg/s)	1267.7	1256	Stack A (m)	5	5
Secondary Side			Na mdot (kg/s)	12.6	12.6
IHX Tin (°C)	333.014	333	Nak mdot (kg/s)	17.5	17.5
IHX Tout (°C)	488.871	488	air mdot (kg/s)	110	-
IHX ΔP Secondary (kPa)	22.20	14.8	**PCS System**		
mdot (kg/s)	1253.5	1256	H2O Tin (°C)	216	216
SG Tin (°C)	488.837	477	H2O Tout (°C)	453.987	454
SG Tout (°C)	330.955	326	PCS Pressure (MPa)	16.7	455??

X APPENDIX C – RELAP UNCERTAINTY SCRIPTS AND CODES (BEAGLE)

This Appendix contains the codes and scripts used in the RELAP5-3D uncertainty propagation code BEAGLE. BEAGLE has three main stages:

1. RELAP Input Generator – Writes a user defined number of RELAP inputs and defines basic parameters and distributions from which to sample. This stage also allows for the option to conduct biased importance sampling.
2. RELAP Automation – Automates the process of running every RELAP file generated by the input generator.
3. RELAP Output Extraction – Reads every RELAP output and transforms minor edit variables into MATLAB objects.
4. Cladding Failure Calculation – Calculates transient induced cladding damage fractions and computes the statistical weight of the simulation resulting in failed cladding.

X.1 RELAP Input Genertor

The RELAP input generator has 3 primary scripts: Importance.m, Reactivity_Generator.m and Auto.m.

X.1.A Importance.m

```
function [num,wgt]=inp(random)
if random<=0.5
    num=0.0+rand*5/100;
    wgt=.1;
elseif random<=0.8
    num=0.05+rand*45/100;
    wgt=1.5;
else
    num=0.5+rand*50/100;
    wgt=2.5;
end
```

X.1.B Reactivity Generator.m

```
clear all
% close all
In_folder_name='C:/Users/Matt/Documents/RELAP/InputGen/importance/In';     %
The Folders must be made before running
Ou_folder_name='C:/Users/Matt/Documents/RELAP/InputGen/importance/Ou';     %
The Folders must be made before running
folders=8;
```

```
%%%%%%%%%%%%%%%%%%%%%%%%%%%%%%%%
%%  Generates the Parameters Used  In the UTOP Uncertainty Study
%%%%%%%%%%%%%%%%%%%%%%%%%%%%%%%%
runs=50;    %number of inputs to be created
inputs=1;  %if inputs=1 then the inputs will print, else they will not
plots=1;   %if inputs=1 then the inputs will print, else they will not

%%%%%%%%%%%%%%%%%%%%%%%%%%%%%%%
%%  Should the parameter be (mean), (random), or (2sigma off, in a bad way)
%%% 1=mean, 2=rand 3="2 sig"
doppler=2;              %%% Doppler
expansion=2;            %%% Expansion
sodiumdensity=2;        %%% Na Density
CRExpansion=2;          %%% CRE
CRDLExpansion=2;        %%% CRDLE

reactivity(1)=0.7;
reactivity(2)=0.9;
%%  Initialize Variables
wgt=zeros(6,runs);
tau=zeros(1,runs);
ax=zeros(1,runs);
dop=zeros(1,runs);
rho=zeros(6,runs);
sod111=zeros(5,runs);
sod123=zeros(5,runs);
sod150=zeros(5,runs);
mean=zeros(1,3);
sig=zeros(1,3);
sod=zeros(1,runs);
cre=zeros(2,runs);
crdle=zeros(2,runs);
wgtt=zeros(1,runs);
time=zeros(1,runs);
react=zeros(1,runs);
%%
for iii=1:folders
    figure(iii)
    %%%%%%%%%%%%%%%%%%%%%%%%%%%%%%%
    %%   Reactivity Values
    %%%%%%%%%%%%%%%%%%%%%%%%%%%%%%%
    if reactivity(1)~=0
        for i=1:runs
            [rnd,wgt(1,i)]=inp(rand);

            react(i)=reactivity(1)+(reactivity(2)-reactivity(1))*(1-rnd);
%%Reactivity value between $0.7 to $0.9

            rate=0.165;   %% $/s
            time(i)=react(i)/rate;   %% s
        end
    else
```

```
        for i=1:runs
            react(i)=reactivity(2);  %%Reactivity value between $0.7 to $0.9

            rate=0.165;   %% $/s
            time(i)=react(i)/rate;  %% s
        end
    end

    bound(1)=.3;
    bound(2)=.9;
    drho=(bound(2)-bound(1))/12;
    x=bound(1):drho:bound(2);

    %%%%%Plot
    if plots==1  % Only if plots=1, at top of file
        subplot(3,2,1)
        hist(react,x);
        title('Reactivity Insertion Distribution')
        xlabel('Reactivity Inserted ($)')
        ylabel('Number of Samples')
    end

    %%%%%%%%%%%%%%%%%%%%%%%%%%%%%
    %% Doppler
    %%%%%%%%%%%%%%%%%%%%%%%%%%%%%


%%%%%%%%%%%%%%%%%%%%%%%%%%%%%%%%%%%%%%%%%%%%%%%%%%%%%%%%%%%%%%%%%%%%%%%%%%%%%%
%%%%%%%%%%%%%%%%%%%%%%
    %%%%%%%%%  Calc Reference Doppler Temp

%%%%%%%%%%%%%%%%%%%%%%%%%%%%%%%%%%%%%%%%%%%%%%%%%%%%%%%%%%%%%%%%%%%%%%%%%%%%%%
%%%%%%%%%%%%%%%%%%%%%%
    temp150=[819.629,888.248,937.336,961.404,956.226];    %  Temperatures  in
150
    weight150=[0.001148,0.001547,0.001686,0.001547,0.001148];  %  Dop weight
in 150

    ave150=0;
    for i=1:5
        ave150=ave150+temp150(i)*weight150(i);    % Average Temp in 150
    end
    temp111=[798.65,862.28,909.86,935.63,935.26];
    weight111=[0.077075,0.103739,0.3113137,0.103739,0.077075];

    ave111=0;
    for i=1:5
        ave111=ave111+temp111(i)*weight111(i);
    end
    temp123=[789.8,850.8,897.7,924.5,926.9];
    weight123=[0.084119,0.113221,0.123478,0.1113221,0.084119];

    ave123=0;
    for i=1:5
        ave123=ave123+temp123(i)*weight123(i);
```

```
    end

    avetot=ave150+ave111+ave123;
    averho=-5.04+(5.04-7.56)/(1200-900)*(avetot-900);

    temp(1)=300;
    temp(2)=600;
    temp(3)=900;
    temp(4)=avetot;
    temp(5)=1125;
    temp(6)=3000;
%%
    temp(1)=300;
    temp(2)=600;
    temp(3)=900;
    temp(4)=avetot;
    temp(5)=1125;
    temp(6)=1275;

    Axial=-0.006;
    sigaxial=-Axial*.3;

    %%%%%%%%%%%%%%%%%%%%%%%%%%%%%%%%%%%%%%%%%%%%%%%%%%%%%%%%%%%%%%%
    %%%%    Alphas ($/k)
    %%%%%%%%%%%%%%%%%%%%%%%%%%%%%%%%%%%%%%%%%%%%%%%%%%%%%%%%%%%%%%%
            alpha(1)=-.3205e-2;   % 20% std
            alpha(2)=-.1587e-2;   % 20% std
            alpha(3)=-0.0912e-2; % 20% std
            alpha(4)=-.085e-2;     % 30% std -  Not calculated

    if doppler==1
        for ii=1:runs
            if expansion==1
                ax(ii)=Axial;
                alpha=alpha+ax(ii);
            elseif expansion==2
                ax(ii)=norminv(ranexp,Axial,sigaxial);
                alpha=alpha+ax(ii); % 30% std - Axial Expansion
            else
                ax(ii)=axial+2*sigaxial;
                alpha=alpha+ax(ii);
            end
            dop(ii)=alpha(3);
            rho(4,ii)=averho;
            rho(3,ii)=averho-alpha(3)*(avetot-900);
            rho(2,ii)=rho(3,ii)-alpha(2)*(900-600);
            rho(1,ii)=rho(2,ii)-alpha(1)*(600-300);
            rho(5,ii)=rho(3,ii)-alpha(3)*(900-1125);
            rho(6,ii)=rho(4,ii)-alpha(4)*(1125-1275);
        end
    elseif doppler==2
        for ii=1:runs
            [rnd,wgt(2,ii)]=inp(rand);
            randop=(1-rnd);  % All doppler values draw from the same Z value
            [rnd,wgt(3,ii)]=inp(rand);
            ranexp=(1-rnd);  % Z for axial expansion
```

```
            alpha(1)=norminv(randop,alpha(1),alpha(1)*-.2);   % 20% std
            alpha(2)=norminv(randop,alpha(2),alpha(2)*-.2);   % 20% std
            alpha(3)=norminv(randop,alpha(3),alpha(3)*-.2); % 20% std
            alpha(4)=norminv(randop,alpha(4),alpha(4)*-.3);     % 30% std -
Not calculated
            if expansion==1
                ax(ii)=Axial;
                alpha=alpha+ax(ii);
            elseif expansion==2
                ax(ii)=norminv(ranexp,Axial,sigaxial);
                alpha=alpha+ax(ii); % 30% std - Axial Expansion
            else
                ax(ii)=axial+2*sigaxial;
                alpha=alpha+ax(ii);
            end
            dop(ii)=alpha(3);
            rho(4,ii)=averho;
            rho(3,ii)=averho-alpha(3)*(avetot-900);
            rho(2,ii)=rho(3,ii)-alpha(2)*(900-600);
            rho(1,ii)=rho(2,ii)-alpha(1)*(600-300);
            rho(5,ii)=rho(3,ii)-alpha(3)*(900-1125);
            rho(6,ii)=rho(4,ii)-alpha(4)*(1125-1275);
        end
    else
        for ii=1:runs
            alpha(1)=alpha(1)+2*alpha(1)*.2;   % 20% std
            alpha(2)=alpha(2)+2*alpha(2)*.2;   % 20% std
            alpha(3)=alpha(3)+2*alpha(3)*.2; % 20% std
            alpha(4)=alpha(4)+2*alpha(4)*.2*.3;     % 30% std -  Not
calculated
            if expansion==1
                ax(ii)=Axial;
                alpha=alpha+ax(ii);
            elseif expansion==2
                ax(ii)=norminv(ranexp,Axial,sigaxial);
                alpha=alpha+ax(ii); % 30% std - Axial Expansion
            else
                ax(ii)=Axial+2*sigaxial;
                alpha=alpha+ax(ii);
            end
            dop(ii)=alpha(3);
            rho(4,ii)=averho;
            rho(3,ii)=averho-alpha(3)*(avetot-900);
            rho(2,ii)=rho(3,ii)-alpha(2)*(900-600);
            rho(1,ii)=rho(2,ii)-alpha(1)*(600-300);
            rho(5,ii)=rho(3,ii)-alpha(3)*(900-1125);
            rho(6,ii)=rho(4,ii)-alpha(4)*(1125-1275);
        end
    end


    if plots==1  % Only if plots=1, at top of file
        subplot(3,2,[5 6])
        plot(temp,rho,'*-')
        title('Doppler and Axial Expansion Distribution')
        xlabel('Temperature (K)')
```

```
        ylabel('Reactivity ($)')
    end

    %%%%%%%%%%%%%%%%%%%%%%%%%%%%%%%
    %%  Sodium Density
    %%%%%%%%%%%%%%%%%%%%%%%%%%%%%%%
    for ii=1:runs
        if sodiumdensity==1;    % use mean values
            %%%%%%%%
            %%% Region 111
            %%%%%%%%
            j=1;
            a=2.0533068e-2;    % Buckling type term
            mean(j)=1.2445e-4*.12/.17;    % Convert from Pu (Matt M.) to TRU
core (Matt D.)
            sig(j)=mean(j)*.16;  % 20% std
            peak111=mean(j);
            n=10;
            for i=1:5
                sod111(i,ii)=peak111*cos(a*(50-n));    % Create sodium density
distribution
                n=n+20;
            end

            %%%%%%%%
            %%% Region 123
            %%%%%%%%
            j=2;
            mean(j)=1.3583e-04*.12/.17;
            sig(j)=mean(j)*.16;  % 20% std
            peak123=mean(j);
            n=10;
            for i=1:5
                sod123(i,ii)=peak123*cos(a*(50-n));
                n=n+20;
            end

            %%%%%%%%
            %%% Region 150
            %%%%%%%%
            j=3;
            mean(j)=1.3583e-04*.12/.17;
            sig(j)=mean(j)*.16;  % 20% std
            peak150=mean(j);
            n=10;
            for i=1:5
                sod150(i,ii)=peak150*cos(a*(50-n));
                n=n+20;
            end

        elseif sodiumdensity==2;  % random values
            %%%%%%%%
            %%% Region 111
            %%%%%%%%
            j=1;
            a=2.0533068e-2;    % Buckling type term
```

```
            mean(j)=1.2445e-4*.12/.17;    % Convert from Pu (Matt M.) to TRU
core (Matt D.)
            sig(j)=mean(j)*.16;   % 20% std

            [rnd,wgt(4,ii)]=inp(rand);

            peak111=norminv((1-rnd),mean(j),sig(j));
            n=10;
            for i=1:5
                sod111(i,ii)=peak111*cos(a*(50-n));    % Create sodium density
distribution
                n=n+20;
            end

            %%%%%%%%
            %%% Region 123
            %%%%%%%%
            j=2;
            mean(j)=1.3583e-04*.12/.17;
            sig(j)=mean(j)*.16;   % 20% std

            peak123=norminv((1-rnd),mean(j),sig(j));
            n=10;
            for i=1:5
                sod123(i,ii)=peak123*cos(a*(50-n));
                n=n+20;
            end

            %%%%%%%%
            %%% Region 150
            %%%%%%%%
            j=3;
            mean(j)=1.3583e-04*.12/.17;
            sig(j)=mean(j)*.16;   % 20% std

            peak150=norminv((1-rnd),mean(j),sig(j));
            n=10;
            for i=1:5
                sod150(i,ii)=peak150*cos(a*(50-n));
                n=n+20;
            end
        else                  % 2 sig values
            %%%%%%%%
            %%% Region 111
            %%%%%%%%
            j=1;
            a=2.0533068e-2;   % Buckling type term
            mean(j)=1.2445e-4*.12/.17;    % Convert from Pu (Matt M.) to TRU
core (Matt D.)
            sig(j)=mean(j)*.16;   % 20% std
            peak111=mean(j)+2*sig(j);
            n=10;
            for i=1:5
                sod111(i,ii)=peak111*cos(a*(50-n));    % Create sodium density
distribution
                n=n+20;
```

```
            end

            %%%%%%%%
            %%% Region 123
            %%%%%%%%
            j=2;
            mean(j)=1.3583e-04*.12/.17;
            sig(j)=mean(j)*.16;  % 20% std
            peak123=mean(j)+2*sig(j);
            n=10;
            for i=1:5
                sod123(i,ii)=peak123*cos(a*(50-n));
                n=n+20;
            end

            %%%%%%%%
            %%% Region 150
            %%%%%%%%
            j=3;
            mean(j)=1.3583e-04*.12/.17;
            sig(j)=mean(j)*.16;  % 20% std
            peak150=mean(j)+2*sig(j);
            n=10;
            for i=1:5
                sod150(i,ii)=peak150*cos(a*(50-n));
                n=n+20;
            end
        end
        clear mean sig

        sod(ii)=sum(sod150(:,ii))+sum(sod123(:,ii))+sum(sod111(:,ii));  % add
all of the regional sodium density coeff.
    end

    bound(1)=mean(sod)-3*std(sod);
    bound(2)=mean(sod)+3*std(sod);
    dsod=(bound(2)-bound(1))/10;
    x=bound(1):dsod:bound(2);

    %%%%%Plot
    if plots==1  % Only if plots=1, at top of file
        subplot(3,2,2)
        hist(sod,x);
        title('Sodium Density Coefficient Distribution')
        xlabel('Sodium Density Coefficient ($/K)')
        ylabel('Number of Samples')
    end
    %%%%%%%%%%%%%%%%%%%%%%%%%%%%%%%%
    %%  Radial Expansion
    %%%%%%%%%%%%%%%%%%%%%%%%%%%%%%%%

    %%%  Coolant Temperature = 782.7311401 K

    averad=-0.0039;
    sigrad=-averad*.2;  % 20% std
```

```
    if CRExpansion==1
        for i=1:runs
            cre(1,i)=averad;   %  Reactivity Coefficient

            cre(2,i)=cre(1,i)*782.7311401;               %  Constant Term
        end
    elseif CRExpansion==2
        for i=1:runs
            [rnd,wgt(5,i)]=inp(rand);

            cre(1,i)=norminv((1-rnd),averad,sigrad);  %  Reactivity
Coefficient

            cre(2,i)=cre(1,i)*782.7311401;               %  Constant Term
        end
    else
        for i=1:runs
            cre(1,i)=averad+2*sigrad;  %  Reactivity Coefficient

            cre(2,i)=cre(1,i)*782.7311401;               %  Constant Term
        end
    end


    bound(1)=mean(cre(1,:))-3*std(cre(1,:));
    bound(2)=mean(cre(1,:))+3*std(cre(1,:));
    dcre=(bound(2)-bound(1))/10;
    x=bound(1):dcre:bound(2);

    if plots==1  % Only if plots=1, at top of file
        subplot(3,2,3)
        hist(cre(1,:),x);
        title('Core Radial Expansion Coefficient Distribution')
        xlabel('CRE Coefficient ($/K)')
        ylabel('Number of Samples')
    end
    %%%%%%%%%%%%%%%%%%%%%%%%%%%%%%%
    %%  CRDLE
    %%%%%%%%%%%%%%%%%%%%%%%%%%%%%%%

    avecrdle=-0.49;
    sigcrdle=-avecrdle*.2;  % 5% std
    if CRDLExpansion==1
    for i=1:runs
        crdle(1,i)=avecrdle;  %  Reactivity Coefficient

        crdle(2,i)=-crdle(1,i)*14.8797;              %  Constant Term
    end
    elseif CRDLExpansion==2
    for i=1:runs
        [rnd,wgt(6,i)]=inp(rand);

        crdle(1,i)=norminv((1-rnd),avecrdle,sigcrdle);  %  Reactivity
Coefficient
```

```
        crdle(2,i)=-crdle(1,i)*14.8797;           %  Constant Term
    end
    else
    for i=1:runs
        crdle(1,i)=avecrdle+2*sigcrdle;  %  Reactivity Coefficient

        crdle(2,i)=-crdle(1,i)*14.8797;           %  Constant Term
    end
    end


    bound(1)=mean(crdle(1,:))-3*std(crdle(1,:));
    bound(2)=mean(crdle(1,:))+3*std(crdle(1,:));
    dcrdle=(bound(2)-bound(1))/10;
    x=bound(1):dcrdle:bound(2);

    if plots==1  % Only if plots=1, at top of file
        subplot(3,2,4)
        hist(crdle(1,:),x);
        title('Control Rod Drive Line Expansion Coefficient Distribution')
        xlabel('CRDLE Coefficient ($/K)')
        ylabel('Number of Samples')
    end

    %%%%%%%%%%%%%%%%%%%%%%%%%%%%%%%%%%%%%%%
    %%  Write Inputs
    %%%%%%%%%%%%%%%%%%%%%%%%%%%%%%%%%%%%%%%
    if inputs==1  % Only if inputs=1, at top of file
        for i=1:runs
            name=sprintf('%s%d/run%03.0f.i',In_folder_name,iii,i);
%             if inputs~=1

wgtt(i)=wgt(1,i).*wgt(2,i).*wgt(3,i).*wgt(4,i).*wgt(5,i).*wgt(6,i);
%             else
%                 wgtt(i)=1;
%             end

Auto(name,react(i),time(i),temp,rho(:,i),sod111(:,i),sod123(:,i),sod150(:,i),
cre(:,i),crdle(:,i),wgtt)
        end

        name1=sprintf('%s%d/output.1',Ou_folder_name,iii);
        fid=fopen(name1,'w');

        fprintf(fid,'Run #,     React ($),    Axial,      Dop,        Sod,
CRE,         CRDLE\n');
        for i=1:runs
            sod(i)=sum(sod150(:,i))+sum(sod123(:,i))+sum(sod111(:,i));
            fprintf(fid,'%f    %f    %f    %f    %f    %f
%f\n',i,react(i),ax(i),dop(i),sod(i),cre(1,i),crdle(1,i));
        end
        fclose('all');
        if iii > 1
            load data
        end
```

```
        Par.react(iii,:)=react';
        Par.ax(iii,:)=ax';
        Par.dop(iii,:)=dop';
        Par.sod(iii,:)=sod';
        Par.cre(iii,:)=cre(1,:)';
        Par.crdle(iii,:)=crdle(1,:)';
        Par.wgt(iii,:)=wgtt';
        save data Par
    end

    %% test weighting
%     if inputs~=1

wgttot(1,:)=wgt(1,:).*wgt(2,:).*wgt(3,:).*wgt(4,:).*wgt(5,:).*wgt(6,:);
        sum(wgttot)
%     end
end
```

X.1.C Auto.m

```
function
xyz=auto(name,react,time,temp,rho,sod111,sod123,sod150,cre,crdle,wgt)
% Example Code for Printing Progress to the Command Window

%%%%%%%%%%%%%%%%%%%%%%%%%%%%%%%%%%%%%%%%%%%%%%%%%%%%%%%%%%%%%
%%%%%  Print
%%%%%%%%%%%%%%%%%%%%%%%%%%%%%%%%%%%%%%%%%%%%%%%%%%%%%%%%%%%%%
expansion=1;    % 1 if expansion is updated
runtime=500;     % # of seconds of runtime
ramptime=100+time;

fid=fopen(name,'w');
fprintf(fid,'= Primary Heat Transport System for ABR 1000 \n');
fprintf(fid,'*  Created from information found in ANL 1000 Design Report\n');
fprintf(fid,'*  (See file ABR1000.xls for geometric considerations,
assumptions, and            \n');
fprintf(fid,'*   Calculations)
\n');
fprintf(fid,'*  Last updated June 02,2009
\n');
fprintf(fid,'*  M.R Denman, M.J Memmott
\n');

fprintf(fid,'*****************************************************************
****************    \n');
fprintf(fid,'*  Distribution Parameters
\n');
fprintf(fid,'*****************************************************************
****************    \n');
fprintf(fid,'* Total Reactivity: %f Time: %f \n',react,time);
fprintf(fid,'* Doppler  %f %f \n',temp(1),rho(1));
fprintf(fid,'*          %f %f \n',temp(2),rho(2));
fprintf(fid,'*          %f %f \n',temp(3),rho(3));
```

```
fprintf(fid,'*          %f %f \n',temp(4),rho(4));
fprintf(fid,'*          %f %f \n',temp(5),rho(5));
fprintf(fid,'*          %f %f \n',temp(6),rho(6));
sod=sum(sod150(:))+sum(sod123(:))+sum(sod111(:));
fprintf(fid,'* Sodium   %f\n',sod);
fprintf(fid,'* CRE   %f    CRDLE    %f\n',cre(1),crdle(1));
fprintf(fid,'* weight   %f   \n',wgt);

fprintf(fid,'**************************************************************
***************    \n');
fprintf(fid,'* run setup
\n');
fprintf(fid,'**************************************************************
***************    \n');
fprintf(fid,'0000100               restart                    transnt \n');
fprintf(fid,'0000101            run\n');
fprintf(fid,'0000102              si                 si
\n');
fprintf(fid,'0000103 -1\n');
fprintf(fid,'0000105 1.0 2.0 1.e6
\n');
fprintf(fid,'0000107   1   1   1 \n');
fprintf(fid,'**************************************************************
****************\n');
fprintf(fid,'* Matt D Added Card\n');
fprintf(fid,'**************************************************************
****************\n');
fprintf(fid,'0000200 0     1\n');
fprintf(fid,'**************************************************************
****************\n');
% fprintf(fid,'0000201 %f 1.0e-7 0.007 00019   17  6000   60000\n',0.5);
%diagnostic run
fprintf(fid,'0000201 %f 1.0e-6 0.007 00019   17  6000 60000\n',ramptime);
fprintf(fid,'0000202 %f 1.0e-6 0.007 00019   200  6000   60000\n',runtime);




fprintf(fid,'*\n');
fprintf(fid,'*\n');

fprintf(fid,'******************************************************\n');
fprintf(fid,'*              minor edit variables                  *\n');
fprintf(fid,'******************************************************\n');
fprintf(fid,'$ Var. Parameter \n');
fprintf(fid,'301 mflowj 201010000 *Core Mass Flow Rate\n');
fprintf(fid,'302 cntrlvar 8800 *DRACS Power\n');
fprintf(fid,'303 pmpvel 262 *Primary Pump Velocity\n');
fprintf(fid,'304 tempf 2010000 *Core Inlet Temperature\n');
fprintf(fid,'305 tempf 4010000 *Core Outlet Temperature\n');
fprintf(fid,'306 cntrlvar 8150 *Max Coolant Temp \n');
fprintf(fid,'308 rktpow 0 *Reactor Power\n');
fprintf(fid,'309 tempf 150140000 *Hot Channel Outlet Temperature\n');
fprintf(fid,'310 cntrlvar 10 *Max Clad Temp\n');
```

```
fprintf(fid,'311 cntrlvar 11 *Max Fuel Temp\n');
fprintf(fid,'312 cntrlvar 8210 * Core Radial Expansion\n');
fprintf(fid,'313 cntrlvar 8211 * CRDLE \n');
fprintf(fid,'314 cntrlvar 8212 *Structural Expansion\n');
fprintf(fid,'315 cntrlvar 8213 * Axial Expansion \n');
fprintf(fid,'316 rkreac 0 * Reactivity\n');

fprintf(fid,'*\n');
fprintf(fid,'*\n');

fprintf(fid,'*   Thermal Conductivity  \n');
fprintf(fid,'20100300 tbl/fctn 1 1\n');
fprintf(fid,'20100301 310.93 14.143\n');
fprintf(fid,'20100302 533.15 17.632\n');
fprintf(fid,'20100303 699.82 20.249\n');
fprintf(fid,'20100304 810.93 21.994\n');
fprintf(fid,'20100305 1088.71 26.355\n');
fprintf(fid,'20100306 4088.71 26.355\n');
fprintf(fid,'*   Heat Capacity  \n');
fprintf(fid,'20100351 310.93 3.690e6\n');
fprintf(fid,'20100352 533.15 4.256e6\n');
fprintf(fid,'20100353 699.82 4.407e6\n');
fprintf(fid,'20100354 810.93 4.513e6\n');
fprintf(fid,'20100355 1088.71 4.913e6\n');
fprintf(fid,'20100356 4088.71 4.913e6\n');
fprintf(fid,'*\n');
fprintf(fid,'*\n');
%%%%%%%%%%%%%%%%%%%%%%%%%%%%%%%%%%%%%%%%%%%%%%%%%%%%%%%%%%%%%%%%%%%
%%%%%%%%%  UPDATE CRE and CRDLE
%%%%%%%%%%%%%%%%%%%%%%%%%%%%%%%%%%%%%%%%%%%%%%%%%%%%%%%%%%%%%%%%%%%

if expansion==1
    fprintf(fid,'*\n');
    fprintf(fid,'20582000 RADexp sum 1.0 %f 1\n',cre(2));
    fprintf(fid,'20582001 0.0 %f tempf 004010000\n',cre(1));
    fprintf(fid,'*\n');
    fprintf(fid,'20582010 CRDLexp sum 1.0 %f 1\n',-crdle(2));
    fprintf(fid,'20582011 0.0 1.0 cntrlvar 8205\n');
    fprintf(fid,'*\n');
    fprintf(fid,'20582050 CRDLcalc sum 1.0 %f 1\n',-crdle(2));
    fprintf(fid,'20582051 0.0 %f cntrlvar 8204\n',crdle(1));
    fprintf(fid,'*\n');

fprintf(fid,'***************************************************************
****************\n');
    fprintf(fid,'* Control Vars to Plot reactivity for each effect listed
above\n');

fprintf(fid,'***************************************************************
****************\n');
    fprintf(fid,'*\n');
    fprintf(fid,'20582100 radexp sum 1.0 0.0 1\n');
    fprintf(fid,'20582101 %f %f tempf 004010000\n',-1*cre(2),cre(1));
    fprintf(fid,'*\n');
    fprintf(fid,'20582110 CRDLexp sum 1.0 0.0 1\n');
    fprintf(fid,'20582111 %f 1.0 cntrlvar 8205\n',crdle(2));
```

```
    fprintf(fid,'*\n');
end

%%%%%%%%%%%%%%%%%%%%%%%%%%%%%%%%%%%%%%%%%%%%%%%%%%%%%%%%%%%%%%%%%%%
%%%%%%%%%  Transient Trips
%%%%%%%%%%%%%%%%%%%%%%%%%%%%%%%%%%%%%%%%%%%%%%%%%%%%%%%%%%%%%%%%%%%
fprintf(fid,'*****************************************************************
*****************\n');
fprintf(fid,'* Transient trips\n');
fprintf(fid,'*****************************************************************
*****************\n');
fprintf(fid,'*\n');
fprintf(fid,'20600000  expanded\n');
fprintf(fid,'20605010 time 0 ge null 0 800000.  1  *DRACS Valve Trip\n');
fprintf(fid,'20602620 tempf 2010000  ge null 0 785.  1  *Pump Trip\n');
fprintf(fid,'20609990 time 0 ge null 0 3.  1           *Decay Power
initiation \n')
fprintf(fid,'20601000 time 0 ge null 0 3.  1  *UTOP Initiation \n');
% fprintf(fid,'20606660 rktpow 0 ge null 0 1.19e9 1       *SCRAM on Power
\n')
fprintf(fid,'20606670 tempf 4010000 ge null 0 830. 1   *SCRAM on Temp \n')
% fprintf(fid,'20606680 cntrlvar 8216 ge null 0 1.3 1   *SCRAM on Temp \n')
fprintf(fid,'*\n');
fprintf(fid,'*\n');
%%%%%%%%%%%%%%%%%%%%%%%%%%%%%%%%%%%%%%%%%%%%%%%%%%%%%%%%%%%%%%%%%%%%%%%%%%%%%%
%%%%%%%%%%
%%%%%%%%%%  Reactivity Insertion
%%%%%%%%%%%%%%%%%%%%%%%%%%%%%%%%%%%%%%%%%%%%%%%%%%%%%%%%%%%%%%%%%%%%%%%%%%%%%%
%%%%%%%%%%
fprintf(fid,'*****************************************************************
*****************\n');
fprintf(fid,'* Reactivity Insertion Table\n');
fprintf(fid,'*****************************************************************
*****************\n');
fprintf(fid,'*\n');
fprintf(fid,'*\n');
fprintf(fid,'20299000          reac-t       100\n');
fprintf(fid,'20299001       0.0        0.0\n');
fprintf(fid,'20299002      %f        %f\n',time,react);
fprintf(fid,'20299003     100000.0     %f\n',react);
% fprintf(fid,'20299100      reac-t     666\n')
% fprintf(fid,'20299101      0.0        0.0\n')
% fprintf(fid,'20299102      1.0        0.0\n')
% fprintf(fid,'20299103      3.0        -6.0\n')
% fprintf(fid,'20299104      100000.    -6.0\n')
% fprintf(fid,'20299200      reac-t     667\n')
% fprintf(fid,'20299201      0.0        0.0\n')
% fprintf(fid,'20299202      1.0        0.0\n')
% fprintf(fid,'20299203      3.0        -6.0\n')
% fprintf(fid,'20299204      100000.    -6.0\n')
% fprintf(fid,'20299300      reac-t     668\n')
% fprintf(fid,'20299301      0.0        0.0\n')
% fprintf(fid,'20299302      1.0        0.0\n')
% fprintf(fid,'20299303      3.0        -6.0\n')
% fprintf(fid,'20299304      100000.    -6.0\n')
fprintf(fid,'*\n');
```

```
fprintf(fid,'*---------------------------------------------------------------
----------------\n')
fprintf(fid,'* SG Structure 1\n')
fprintf(fid,'*---------------------------------------------------------------
----------------\n')
fprintf(fid,'*\n')
fprintf(fid,'*\n')
fprintf(fid,'* The SG is simplified to provide the right inventory of steam
and sodium\n')
fprintf(fid,'* while still providing the right heat transfer without knowing
the actual\n')
fprintf(fid,'* design.  Thus, the SAMult was adjusted until these factors
matched.\n')
fprintf(fid,'*\n')
fprintf(fid,'*\n')
fprintf(fid,'*HtStr  axialN radialMP Geom  ss  LBcoor\n')
fprintf(fid,'13401000 50        5     1     1   .01\n')
fprintf(fid,'*       location  format (1= Intrvl#,RightCoord, 2=
MeshIntrvl,Intrvl#)\n')
fprintf(fid,'13401100 0 1\n')
fprintf(fid,'*       intrvl#  RightCoor\n')
fprintf(fid,'13401101 4 .0159\n')
fprintf(fid,'*       Compos# Intrvl#\n')
fprintf(fid,'13401201 003 4\n')
fprintf(fid,'*       Srce Intrvl#\n')
fprintf(fid,'13401301 0.  4\n')
fprintf(fid,'*       ITF\n')
fprintf(fid,'13401400 0\n')
fprintf(fid,'*         T(K)  mshpnt#\n')
fprintf(fid,'13401401 761.15  5\n')
fprintf(fid,'*         BCVol     Incr  BCType SACode  SAMult    HS#\n')
fprintf(fid,'13401501 0 0.     0.    0.  344.    50\n')
fprintf(fid,'13401601 410500000 -10000      1       1  344.000   50\n')
fprintf(fid,'*         PSType  Pf  DMH   DMHM  HS#\n')
fprintf(fid,'13401701 0 0. 0. 0. 50\n')
fprintf(fid,'*       words (0=9,1=12)\n')
fprintf(fid,'13401900 1\n')
fprintf(fid,'*         Dhe LeHf  leHr Lgsf Lgsr Kfwd Krev Fboil nclf   P/d
ff    #\n')
fprintf(fid,'13401901 0.0 100. 100.  0.    0.    0.    0.  1.0    0.     1.1
1.35   50\n')
%%%
fprintf(fid,'\n')
fprintf(fid,'****************************************************************
*****************\n')
fprintf(fid,'* Pump Coastdown Tables\n')
fprintf(fid,'****************************************************************
*****************\n')
fprintf(fid,'** For each of these EM pumps, 2 pumps are combined in series
for a total of 4 p\n')
fprintf(fid,'*\n')
fprintf(fid,'*hydro  name    type\n')
fprintf(fid,'2600000 pmplent snglvol\n')
fprintf(fid,'2600101 0.676071  1.6  0.0  0.0  90.  1.6  4.5e-5 0.2
0000000\n')
fprintf(fid,'2600200 0   202801.3 549470. 5255980. 0.\n')
fprintf(fid,'*\n')
```

```
fprintf(fid,'*\n')
fprintf(fid,'*hydro  name    type\n')
fprintf(fid,'2700000 pmplent snglvol\n')
fprintf(fid,'2700101 0.676071  1.6 0.0 0.0  90.  1.6  4.5e-5 0.2 0000000\n')
fprintf(fid,'2700200 0   198729.3 549470. 5255394. 0.\n')
fprintf(fid,'*\n')
fprintf(fid,'*\n')
fprintf(fid,'*\n')
fprintf(fid,'*For the pumps sized in the Argonne Report, the area is wrong!
For pumps of that\n')
fprintf(fid,'*a veloctiy of 400m/s through the pump duct is achieved.  AS a
result, a new are\n')
fprintf(fid,'*reflects the appropriate pressure drop of the system is
achieved by adjusting t\n')
fprintf(fid,'*until the pressure drop matches the pump area.  An alternative
to this is maint\n')
fprintf(fid,'*area which gives a veloctiy of ~ 4m/s, and adjusting the ks to
give an appropr\n')
fprintf(fid,'*In this model, Kwere approximated  sudden entrance/exit, and
the area was\n')
fprintf(fid,'*until an adequate pressure drop/flow rate was achieved.\n')
fprintf(fid,'* (Actual calculated area is 0.006154, adjusted is 0.405255)\n')
fprintf(fid,'*\n')
fprintf(fid,'*hydro  name    type\n')
fprintf(fid,'2620000 empumpl  pump\n')
fprintf(fid,'2620101 .405255 1.6 0.0 0.0 -90. -1.6 0000000\n')
fprintf(fid,'2620108 260010000 0.0 .5 .1 00000000 * these Ks are based upon a
flanged 180 re\n')
fprintf(fid,'2620109 264000000 0.0 1. .5 00000000\n')
fprintf(fid,'2620200 0   569575. 550428. 5279694. 0.\n')
fprintf(fid,'2620201 0 7.26608 8.03966 0. * 2556.006\n')
fprintf(fid,'2620202 0 7.26696 7.26696 0. * 2556.006\n')
fprintf(fid,'**********************************************************************
**************************\n')
fprintf(fid,'* Brinham pump, 1 phase, no 2 phase, no torque table used, time
dependant pump velocity index, trip on 262, reverse flow allowed  \n')
fprintf(fid,'2620301 -1 -1 -3 -1 -1 262 1 $ This is for variable pumping**
mrd 4/11\n')
fprintf(fid,'**********************************************************************
*************************\n')
% fprintf(fid,'*2620301 0 -1 -3 -1 -1 262 0 $ This is for pump table (gradual
startup)\n')
% fprintf(fid,'*2620302 251.32 1.0 2.96 91.02 18421.227 160.0 851.35 0. .1
21.53 21.53 0. 0. *t\n')
fprintf(fid,'2620302 251.32 1.  2.96 91.02 18421.227 160.0 851.35 0. .1 21.53
21.53 0. 0. *to\n')
% fprintf(fid,'*2626100 0\n')
% fprintf(fid,'*2626101 0.0 0.0\n')
% fprintf(fid,'*2626102 0.1 251.32\n')
% fprintf(fid,'*head curve, region 1\n')
% fprintf(fid,'2621100 1 1 0.0 .45263 *extrapolated value*\n')
% fprintf(fid,'2621101 .11904762  .46315789\n')
% fprintf(fid,'2621102 .15873016  .47368421\n')
% fprintf(fid,'2621103 .23809524  .51578947\n')
% fprintf(fid,'2621104 .31746032  .55263158\n')
% fprintf(fid,'2621105 .39682540  .60526316\n')
% fprintf(fid,'2621106 .47619048  .67105263\n')
```

```
% fprintf(fid,'2621107 .55555556  .73684211\n')
% fprintf(fid,'2621108 .63492063  .81578947\n')
% fprintf(fid,'2621109 .71428571  .90789474\n')
% fprintf(fid,'2621110 .79365079  1.0\n')
% fprintf(fid,'2621111 .87301587  1.10526316\n')
% fprintf(fid,'2621112 .95238095  1.14473684\n')
% fprintf(fid,'2621113 1.        1.\n')
% fprintf(fid,'*torque curve, region 1\n')
% fprintf(fid,'2621200 2 1 0.0 .51087174  *extrapolated value*\n')
% fprintf(fid,'2621201 .11904762  0.51522074\n')
% fprintf(fid,'2621202 .15873016  0.52191192\n')
% fprintf(fid,'2621203 .23809524  0.53278508\n')
% fprintf(fid,'2621204 .31746032  0.58790078\n')
% fprintf(fid,'2621205 .39682540  0.61423844\n')
% fprintf(fid,'2621206 .47619048  0.66071828\n')
% fprintf(fid,'2621207 .55555556  0.68588425\n')
% fprintf(fid,'2621208 .63492063  0.77036280\n')
% fprintf(fid,'2621209 .71428571  0.87528978\n')
% fprintf(fid,'2621210 .79365079  0.91817838\n')
% fprintf(fid,'2621211 .87301587  1.01924103\n')
% fprintf(fid,'2621212 .95238095  1.07018303\n')
% fprintf(fid,'2621213 1.        1.\n')
% fprintf(fid,'*head curve, region 2\n')
% fprintf(fid,'2621300 1 2 .89   .00016955 *extrapolated value*\n')
% fprintf(fid,'2621301 .9        .05328947 *extrapolated value*\n')
% fprintf(fid,'2621302 .91636364 .25412649\n')
% fprintf(fid,'2621303 .93333333 .48140351\n')
% fprintf(fid,'2621304 .96923077 .84052320\n')
% fprintf(fid,'*torque curve, region 2\n')
% fprintf(fid,'2621400 2 2 .86   .001851911 *extrapolated value*\n')
% fprintf(fid,'2621401 .89       .290312645 *extrapolated value*\n')
% fprintf(fid,'2621402 .9        .479506579 *extrapolated value*\n')
% fprintf(fid,'2621403 .91636364 .539000268\n')
% fprintf(fid,'2621404 .93333333 .626555263\n')
% fprintf(fid,'2621405 .96923077 .877865891\n')
% fprintf(fid,'*head curve, region 8  *extrapolated values*\n')
% fprintf(fid,'2621501 1 8 -1.0 .880611\n')
% fprintf(fid,'2621502 0.0 .880611\n')
% fprintf(fid,'*torque curve, region 8  *extrapolated values*\n')
% fprintf(fid,'2621601 2 8 -1.0 .846348\n')
% fprintf(fid,'2621602 0.0 .846348\n')
% fprintf(fid,'*head curve, region 3\n')
% fprintf(fid,'2621700 1 3 -1.0 0.45263\n')
% fprintf(fid,'2621701 0.0 0.45263\n')
% fprintf(fid,'*torque curve, region 3\n')
% fprintf(fid,'2621800 2 3 -1.0 0.51087174\n')
% fprintf(fid,'2621801 0.0 0.51087174\n')
% fprintf(fid,'*\n')
% fprintf(fid,'*For Some Strange Reason, region 4 is needed during startup,
so here is a guess\n')
% fprintf(fid,'*\n')
% fprintf(fid,'*head curve, region 4  *extrapolated values*\n')
% fprintf(fid,'2621900 1 4 -1.0 0.200\n')
% fprintf(fid,'2621901 0.0 .200\n')
% fprintf(fid,'*torque curve, region 4  *extrapolated values*\n')
% fprintf(fid,'2622000 2 4 -1.0 0.220\n')
% fprintf(fid,'2622001 0.0 .220\n')
```

```
% fprintf(fid,'************************mrd
4/11/09*****************************************************\n')
%
fprintf(fid,'**************************************************************
**********************\n')
%% 20 second halving time for oxide core
% tau=20;
% m(1)=253;
% t=linspace(0.1,50,20);
% for i=2:20
%      m(i)=m(1)/(1+1/tau*(t(i)-t(1)));
% end
%
%
%
%
%%%%%%%%%%%%%%%%%%%%%%%%%%%%%%%%%%%%%%%%%%%%%%%%%%%%%%%%%%%%%%%%%%%%%%%%%%%%%%%%%
%%%%%%%%%%%%%%%%%%%%%%%%%%%%
% fprintf(fid,'*    4 primary pumps break, coastdown\n')
%
%%%%%%%%%%%%%%%%%%%%%%%%%%%%%%%%%%%%%%%%%%%%%%%%%%%%%%%%%%%%%%%%%%%%%%%%%%%%%%%%%
%%%%%%%%%%%%%%%%%%%%%%%%%%
% fprintf(fid,' 2626101    -1.0    253.0            $ time =0, full flow\n')
% fprintf(fid,' 2626102     0.01   253.0\n')
% fprintf(fid,' 2626103     %f   %f\n',t(1),m(1))
% fprintf(fid,' 2626104     %f   %f\n',t(2),m(2))
% fprintf(fid,' 2626105     %f   %f\n',t(3),m(3))
% fprintf(fid,' 2626106     %f   %f\n',t(4),m(4))
% fprintf(fid,' 2626107     %f   %f\n',t(5),m(5))
% fprintf(fid,' 2626108     %f   %f\n',t(6),m(6))
% fprintf(fid,' 2626109     %f   %f\n',t(7),m(7))
% fprintf(fid,' 2626110     %f   %f\n',t(8),m(8))
% fprintf(fid,' 2626111     %f   %f\n',t(9),m(9))
% fprintf(fid,' 2626112     %f   %f\n',t(10),m(10))
% fprintf(fid,' 2626113     %f   %f\n',t(11),m(11))
% fprintf(fid,' 2626114     %f   %f\n',t(12),m(12))
% fprintf(fid,' 2626115     %f   %f\n',t(13),m(13))
% fprintf(fid,' 2626116     %f   %f\n',t(14),m(14))
% fprintf(fid,' 2626117     %f   %f\n',t(15),m(15))
% fprintf(fid,' 2626118     %f   %f\n',t(16),m(16))
% fprintf(fid,' 2626119     %f   %f\n',t(17),m(17))
% fprintf(fid,' 2626120     %f   %f\n',t(18),m(18))
% fprintf(fid,' 2626121     %f   %f\n',t(19),m(19))
% fprintf(fid,' 2626122     %f   %f\n',t(20),m(20))
% fprintf(fid,' 2626123     1000.0   0.1\n')
% %%%%%%%%%%%%%%%%%%%%%%%%%%%%%%%%%%%%%%%%%%%%%%%%%%%%%%%%%%%%%%%%%%%%%%%%%%
% fprintf(fid,'*\n')
%
fprintf(fid,'**************************************************************
**********************\n')
fprintf(fid,'*\n')
fprintf(fid,'*hydro  name    type\n')
fprintf(fid,'2720000 empump1  pump\n')
fprintf(fid,'2720101 .405255 1.6 0.0 0.0 -90. -1.6 0000000\n')
fprintf(fid,'2720108 270010000 0.0 .5 .1 00000000 * these Ks are based upon a
flanged 18 upo\n')
fprintf(fid,'2720109 274000000 0.0 1. .5 00000000\n')
```

```
fprintf(fid,'2720200 0   567583. 550431. 5279639. 0.\n')
fprintf(fid,'2720201 0 7.25373 8.02682 0. * 2551.66\n')
fprintf(fid,'2720202 0 7.25461 7.25461 0. * 2551.66\n')
fprintf(fid,'****************************************************************
*************************\n')
fprintf(fid,'* Brinham pump, 1 phase, no 2 phase, no torque table used,time
dependant pump velocity index, trip on 262, reverse flow allowed  \n')
fprintf(fid,'2720301 -1 -1 -3 -1 -1 262 1 $ This is for variable pumping*\n')
fprintf(fid,'****************************************************************
*************************\n')
% fprintf(fid,'*2720301 0 -1 -3 -1 -1 262 0 $ This is for pump table (gradual
startup) $\n')
% fprintf(fid,'*2720302 251.32 1.0 2.96 91.02 18421.227 160.0 851.35 0. .1
21.53 21.53 0. 0.  *\n')
fprintf(fid,'2720302 251.32 1.  2.96 91.02 18421.227 160.0 851.35 0. .1 21.53
21.53 0. 0.  *t\n')
% fprintf(fid,'*2726100 0\n')
% fprintf(fid,'*2726101 0.0 0.0\n')
% fprintf(fid,'*2726102 0.1 251.32\n')
% fprintf(fid,'*head curve, region 1\n')
% fprintf(fid,'2721100 1 1 0.0 .45263 *extrapolated value*\n')
% fprintf(fid,'2721101 .11904762  .46315789\n')
% fprintf(fid,'2721102 .15873016  .47368421\n')
% fprintf(fid,'2721103 .23809524  .51578947\n')
% fprintf(fid,'2721104 .31746032  .55263158\n')
% fprintf(fid,'2721105 .39682540  .60526316\n')
% fprintf(fid,'2721106 .47619048  .67105263\n')
% fprintf(fid,'2721107 .55555556  .73684211\n')
% fprintf(fid,'2721108 .63492063  .81578947\n')
% fprintf(fid,'2721109 .71428571  .90789474\n')
% fprintf(fid,'2721110 .79365079  1.0\n')
% fprintf(fid,'2721111 .87301587  1.10526316\n')
% fprintf(fid,'2721112 .95238095  1.14473684\n')
% fprintf(fid,'2721113 1.       1.\n')
% fprintf(fid,'*torque curve, region 1\n')
% fprintf(fid,'2721200 2 1 0.0 .51087174  *extrapolated value*\n')
% fprintf(fid,'2721201 .11904762  0.51522074\n')
% fprintf(fid,'2721202 .15873016  0.52191192\n')
% fprintf(fid,'2721203 .23809524  0.53278508\n')
% fprintf(fid,'2721204 .31746032  0.58790078\n')
% fprintf(fid,'2721205 .39682540  0.61423844\n')
% fprintf(fid,'2721206 .47619048  0.66071828\n')
% fprintf(fid,'2721207 .55555556  0.68588425\n')
% fprintf(fid,'2721208 .63492063  0.77036280\n')
% fprintf(fid,'2721209 .71428571  0.87528978\n')
% fprintf(fid,'2721210 .79365079  0.91817838\n')
% fprintf(fid,'2721211 .87301587  1.01924103\n')
% fprintf(fid,'2721212 .95238095  1.07018303\n')
% fprintf(fid,'2721213 1.       1.\n')
% fprintf(fid,'*head curve, region 2\n')
% fprintf(fid,'2721300 1 2 .89   .00016955 *extrapolated value*\n')
% fprintf(fid,'2721301 .9        .05328947 *extrapolated value*\n')
% fprintf(fid,'2721302 .91636364 .25412649\n')
% fprintf(fid,'2721303 .93333333 .48140351\n')
% fprintf(fid,'2721304 .96923077 .84052320\n')
% fprintf(fid,'*torque curve, region 2\n')
% fprintf(fid,'2721400 2 2 .86   .001851911 *extrapolated value*\n')
```

```
% fprintf(fid,'2721401 .89        .290312645 *extrapolated value*\n')
% fprintf(fid,'2721402 .9         .479506579 *extrapolated value*\n')
% fprintf(fid,'2721403 .91636364 .539000268\n')
% fprintf(fid,'2721404 .93333333 .626555263\n')
% fprintf(fid,'2721405 .96923077 .877865891\n')
% fprintf(fid,'*head curve, region 8  *extrapolated values*\n')
% fprintf(fid,'2721501 1 8 -1.0 .880611\n')
% fprintf(fid,'2721502 0.0 .880611\n')
% fprintf(fid,'*torque curve, region 8  *extrapolated values*\n')
% fprintf(fid,'2721601 2 8 -1.0 .846348\n')
% fprintf(fid,'2721602 0.0 .846348\n')
% fprintf(fid,'*head curve, region 3\n')
% fprintf(fid,'2721700 1 3 -1.0 0.45263\n')
% fprintf(fid,'2721701 0.0 0.45263\n')
% fprintf(fid,'*torque curve, region 3\n')
% fprintf(fid,'2721800 2 3 -1.0 0.51087174\n')
% fprintf(fid,'2721801 0.0 0.51087174\n')
% fprintf(fid,'*\n')
% fprintf(fid,'*\n')
% fprintf(fid,'*For Some Strange Reason, region 4 is needed during startup,
so here is a guess\n')
% fprintf(fid,'*\n')
% fprintf(fid,'*head curve, region 4  *extrapolated values*\n')
% fprintf(fid,'2721900 1 4 -1.0 0.200\n')
% fprintf(fid,'2721901 0.0 .600\n')
% fprintf(fid,'*torque curve, region 4  *extrapolated values*\n')
% fprintf(fid,'2722000 2 4 -1.0 0.220\n')
% fprintf(fid,'2722001 0.0 .220\n')
% fprintf(fid,'*\n')
% fprintf(fid,'*\n')
% %%   3 sec halving time
% fprintf(fid,'************************mrd
4/11/09***************************************************\n')
%
fprintf(fid,'****************************************************************
**********************\n')
% fprintf(fid,'*     2 primary pumps break, no coastdown\n')
% fprintf(fid,' 2726101      -1.0  253.0              $ time =0, full flow\n')
% fprintf(fid,' 2726102      0.01   253.0\n')
% fprintf(fid,' 2726103      %f   %f\n',t(1),m(1))
% fprintf(fid,' 2726104      %f   %f\n',t(2),m(2))
% fprintf(fid,' 2726105      %f   %f\n',t(3),m(3))
% fprintf(fid,' 2726106      %f   %f\n',t(4),m(4))
% fprintf(fid,' 2726107      %f   %f\n',t(5),m(5))
% fprintf(fid,' 2726108      %f   %f\n',t(6),m(6))
% fprintf(fid,' 2726109      %f   %f\n',t(7),m(7))
% fprintf(fid,' 2726110      %f   %f\n',t(8),m(8))
% fprintf(fid,' 2726111      %f   %f\n',t(9),m(9))
% fprintf(fid,' 2726112      %f   %f\n',t(10),m(10))
% fprintf(fid,' 2726113      %f   %f\n',t(11),m(11))
% fprintf(fid,' 2726114      %f   %f\n',t(12),m(12))
% fprintf(fid,' 2726115      %f   %f\n',t(13),m(13))
% fprintf(fid,' 2726116      %f   %f\n',t(14),m(14))
% fprintf(fid,' 2726117      %f   %f\n',t(15),m(15))
% fprintf(fid,' 2726118      %f   %f\n',t(16),m(16))
% fprintf(fid,' 2726119      %f   %f\n',t(17),m(17))
% fprintf(fid,' 2726120      %f   %f\n',t(18),m(18))
```

```
% fprintf(fid,' 2726121     %f   %f\n',t(19),m(19))
% fprintf(fid,' 2726122     %f   %f\n',t(20),m(20))
% fprintf(fid,' 2726123     1000.0 0.0\n')

%%%
%
fprintf(fid,'*****************************************************************
****************\n')
% fprintf(fid,'* Utilization of Fast Reactor Decay Power Curve\n')
%
fprintf(fid,'*****************************************************************
****************\n')
% fprintf(fid,'*\n')
% fprintf(fid,'20502000 rctrp tripunit 1.0 0.0 1\n')
% fprintf(fid,'20502001 999\n')
% fprintf(fid,'*\n')
% fprintf(fid,'20502010 invrctrp tripunit 1.0 1.0 1\n')
% fprintf(fid,'20502011 -999\n')
% fprintf(fid,'*                  \n')
% fprintf(fid,'20502020     tabdecy  function  1000.e6   70000000.      0 0
\n')
% fprintf(fid,'20502021     time     0     106 \n')
% fprintf(fid,'*\n')
% fprintf(fid,'20502030 codedcyP mult 1.0  70000000.0 1\n')
% fprintf(fid,'20502031 cntrlvar 201    rkgapow 0\n')
% fprintf(fid,'*\n')
% fprintf(fid,'20502040 fastdcyP mult 1.0 70000000. 1\n')
% fprintf(fid,'20502041 cntrlvar 200    cntrlvar 202\n')
% fprintf(fid,'*\n')
% fprintf(fid,'20502050 DPchoose     stdfnctn  1.0      70000000. 1
\n')
% fprintf(fid,'20502051  max    cntrlvar 203             cntrlvar 204\n')
% fprintf(fid,'*\n')
% fprintf(fid,'20502100 TotPow  sum 1.0 996000000. 1\n')
% fprintf(fid,'20502101 0.0 1.0 cntrlvar 205 1.0 rkfipow 0\n')
% fprintf(fid,'*\n')
% fprintf(fid,'*\n')
%%%
fprintf(fid,'*================================================================
============\n');
fprintf(fid,'* Reactor Kinetics - To be inserted once steady state is reached
-\n');
fprintf(fid,'*================================================================
============\n');
fprintf(fid,'*\n');
fprintf(fid,'30000000 point separabl\n');
fprintf(fid,'*\n');
fprintf(fid,'*        fp-decay  power    rinit     beta/lambda   fp-y   u239-
y  G-factor\n');
fprintf(fid,'30000001 gamma      1000.e6  -1.0e-60  9305.556       1.0    1.0e-
60 0\n');
fprintf(fid,'*\n');
fprintf(fid,'*        Mod.-Dens Reactivity ($) - Density effects included in
vol. temp. feed\n');
fprintf(fid,'30000501 0000.00   0.000000\n');
fprintf(fid,'30000502 1000.00   0.000000\n');
fprintf(fid,'*\n');
```

```
%%%%%%%%%%%%%%%%%%%%%%%%%%%%%%%%%%%%%%%%%%%%%%%%%%%%%%%%%%%%%%%%%%%%%%%%%%%%%%
%%%%%%%%%%
%%%%%%%%%%  Expansion Feedbacks
%%%%%%%%%%%%%%%%%%%%%%%%%%%%%%%%%%%%%%%%%%%%%%%%%%%%%%%%%%%%%%%%%%%%%%%%%%%%%%
%%%%%%%%%%
fprintf(fid,'30000011 18200 *radial expansion $ $ $This was input by MJM on
11-04-08$ $ $\n');
fprintf(fid,'30000012 18201 *CRDL expansion feedback $alpha = 1.9e-5/C, Lo =
10m, reac = .49$/cm\n');
fprintf(fid,'30000013 18202 *Structural expansion $This is positive feedback
for vessel expansion\n');
fprintf(fid,'30000014 18203 *axial expansion $ this is for expansion of clad
and assembly walls\n');
fprintf(fid,'30000015   990 *This is the control rod ejection reactivity
insertion (input by MJM on 2/2/09)\n');
% fprintf(fid,'30000016   991 *SCRAM\n');
% fprintf(fid,'30000017   992 *SCRAM\n');
% fprintf(fid,'30000018   993 *SCRAM\n');
fprintf(fid,'*\n');
%%%%%%%%%%%%%%%%%%%%%%%%%%%%%%%%%%%%%%%%%%%%%%%%%%%%%%%%%%%%%%%%%%%%%%%%%%%%%%
%%%%%%%%%
%%%%%%%%%% Fuel Feedbacks
%%%%%%%%%%%%%%%%%%%%%%%%%%%%%%%%%%%%%%%%%%%%%%%%%%%%%%%%%%%%%%%%%%%%%%%%%%%%%%
%%%%%%%%%
fprintf(fid,'* Doppler Reactivity  + Fuel Expansion/Density Feedback (-0.006
$/C)\n');
fprintf(fid,'*          Fuel-Temp Reactivity($) (F.C. = -0.0013 $/C +- 30
percent)\n');
fprintf(fid,'*  Doppler T (K) vs alpha, sigma (c/C)  EOC Numbers\n');
fprintf(fid,'*  450          -0.3205   +-20percent  * sigma taken from ANL-IFR-
80\n');
fprintf(fid,'*  750          -0.1587   +-20percent\n');
fprintf(fid,'*  1050         -0.0912   +-20percent\n');
fprintf(fid,'*  1200         -0.085    +-30percent  ******NOTE, this is a
conservative made up number...MCNP Data does not go beyond 1050oC.\n');
fprintf(fid,'*                                     Higher uncertainties are thus
used\n');
fprintf(fid,'*\n');
fprintf(fid,'30000601  %f %f \n',temp(1),rho(1));
fprintf(fid,'30000602  %f %f \n',temp(2),rho(2));
fprintf(fid,'30000603  %f %f \n',temp(3),rho(3));
fprintf(fid,'30000604  %f %f \n',temp(4),rho(4));
fprintf(fid,'30000605  %f %f \n',temp(5),rho(5));
fprintf(fid,'30000606  %f %f \n',temp(6),rho(6));
fprintf(fid,'\n');
fprintf(fid,'*\n');
%%%%%%%%%%%%%%%%%%%%%%%%%%%%%%%%%%%%%%%%%%%%%%%%%%%%%%%%%%%%%%%%%%%%%%%%%%%%%%
%%%%%
%%%%%  Sodium Density
%%%%%%%%%%%%%%%%%%%%%%%%%%%%%%%%%%%%%%%%%%%%%%%%%%%%%%%%%%%%%%%%%%%%%%%%%%%%%%
%%%%%
fprintf(fid,'* Sodium Temperature/Density Feedback (+0.0011 $/C)\n');
fprintf(fid,'*\n');
fprintf(fid,'* Inner Driver\n');
fprintf(fid,'*          hydro-vol# inc  weight     temp-coeff\n');
fprintf(fid,'30000701   111050000   0   1.0   %d\n',sod111(1));
fprintf(fid,'30000702   111060000   0   1.0   %d\n',sod111(2));
```

```
fprintf(fid,'30000703   111070000   0   1.0   %d\n',sod111(3));
fprintf(fid,'30000704   111080000   0   1.0   %d\n',sod111(4));
fprintf(fid,'30000705   111090000   0   1.0   %d\n',sod111(5));
fprintf(fid,'*\n');
fprintf(fid,'* Outer Driver\n');
fprintf(fid,'*              hydro-vol# inc   weight      temp-coeff\n');
fprintf(fid,'30000706   123050000   0   1.0   %d\n',sod123(1));
fprintf(fid,'30000707   123060000   0   1.0   %d\n',sod123(2));
fprintf(fid,'30000708   123070000   0   1.0   %d\n',sod123(3));
fprintf(fid,'30000709   123080000   0   1.0   %d\n',sod123(4));
fprintf(fid,'30000710   123090000   0   1.0   %d\n',sod123(5));
fprintf(fid,'*\n');
fprintf(fid,'* Hot Driver\n');
fprintf(fid,'*              hydro-vol# inc   weight      temp-coeff\n');
fprintf(fid,'30000711   150050000   0   1.0   %d\n',sod150(1));
fprintf(fid,'30000712   150060000   0   1.0   %d\n',sod150(2));
fprintf(fid,'30000713   150070000   0   1.0   %d\n',sod150(3));
fprintf(fid,'30000714   150080000   0   1.0   %d\n',sod150(4));
fprintf(fid,'30000715   150090000   0   1.0   %d\n',sod150(5));
fprintf(fid,'*\n');
fprintf(fid,'* Fuel Density/Temperature Feedback & Doppler Weights\n');
fprintf(fid,'*\n');
fprintf(fid,'* Hot Channel\n');
fprintf(fid,'*              ht-str#  inc  weight      fuel-temp-coeff\n');
fprintf(fid,'30000801   1502001   0   0.001148   -0.00\n');
fprintf(fid,'30000802   1502002   0   0.001547   -0.00\n');
fprintf(fid,'30000803   1502003   0   0.001686   -0.00\n');
fprintf(fid,'30000804   1502004   0   0.001547   -0.00\n');
fprintf(fid,'30000805   1502005   0   0.001148   -0.00\n');
fprintf(fid,'*\n');
fprintf(fid,'* Inner Driver\n');
fprintf(fid,'*              ht-str#  inc weight      fuel-temp-coeff\n');
fprintf(fid,'30000816   1112001   0   0.077075   -0.00\n');
fprintf(fid,'30000817   1112002   0   0.103739   -0.00\n');
fprintf(fid,'30000818   1112003   0   0.113137   -0.00\n');
fprintf(fid,'30000819   1112004   0   0.103739   -0.00\n');
fprintf(fid,'30000820   1112005   0   0.077075   -0.00\n');
fprintf(fid,'*\n');
fprintf(fid,'* Outer Driver\n');
fprintf(fid,'*              ht-str#  inc  weight      fuel-temp-coeff\n');
fprintf(fid,'30000831   1232001   0   0.084119   -0.00\n');
fprintf(fid,'30000832   1232002   0   0.113221   -0.00\n');
fprintf(fid,'30000833   1232003   0   0.123478   -0.00\n');
fprintf(fid,'30000834   1232004   0   0.113221   -0.00\n');
fprintf(fid,'30000835   1232005   0   0.084119   -0.00\n');
fprintf(fid,'*\n');
fprintf(fid,'. *end of file\n');
fclose('all');
```

X.2 RELAP Automation

The RELAP Automation module consists of *.bat files which automate the running of multiple RELAP simulations.

X.2.A Multi_RELAP.bat

```
set relapdir= C:\r5\r3d236ie\relap
set mydir= %CD%
set rundir=C:\Users\Matt\Documents\Runs\runtape
set inputdir=C:\Users\Matt\Documents\RELAP\InputGen\importance\In1

del %inputdir%\*.

copy %inputdir%\*.i %inputdir%\*.

for /F %%a IN ('dir /b %inputdir%\*.') do CALL run %%a

pause
```

X.2.B Run.bat

```
set inputfile=%1

del %inputfile%.o
del %inputfile%.r

copy %rundir%\ABR1000ssM.r %inputfile%.r


cd %relapdir%
relap5 -i %inputdir%\%inputfile%.i -o %mydir%\%inputfile%.o -r %mydir%\%inputfile%.r -m
%rundir%\tpfna2> %mydir%\%inputfile%.out
cd %mydir%
```

X.3 RELAP Output Extraction

The RELAP Output extraction module removes the minor edits from the hundreds of RELAP simulation and creates MATLAB arrays which can be used in post-processing.

X.3.A Multi.bat

```
REM This is the main file
SET INDEX_FILE=list.l
del %INDEX_FILE%

REM del folder_out.l

REM dir /B /AD * > folder_out.l
```

```
SET FOLDER_FILE=folder_out.l
SET HOME_DIR=%CD%



FOR /F %%A IN (%FOLDER_FILE%) DO CALL make_list %%A

Pause
```

X.3.B Folder.bat

```
cd %1
set OUTPUTS=all_outs.l

copy output.o output.l

del output.o

del %OUTPUTS%

dir /B *.o > %OUTPUTS%


FOR /F %%A IN (%OUTPUTS%) DO ECHO %CD%\%%A >> %HOME_DIR%/list.l

REM FOR /F %%A IN (%OUTPUTS%) DO  ECHO %CD%\%%A >> %HOME_DIR%/list.l


cd ..
```

X.3.C Output_Process.m

```
numfiles=1;

cd C:\Users\Matt\Documents\RELAP\OutputSort

runcoutner=0;
for i=1:numfiles
    left=numfiles-i;
%     list=sprintf('list%d.l',i);
    list=sprintf('list.l');
    ARRAY=sortdata(list,left);
    [nn] = size(ARRAY,2);
    start=runcoutner+1;
    runcoutner=runcoutner+nn;
    reactbin3(start:runcoutner)=ARRAY;
end
```

```
ARRAY=reactbin3;

save METALTOPLOHS3 ARRAY
clear all
load METALTOPLOHS3

pause
cd C:\Users\Matt\Documents\RELAP\Damage

Object_builder
```

X.3.D Sortdata.m

```
function [ARRAY]=sortdata(list,nn)

close all

fid = fopen(list, 'r');  %opens file with list of output files to read
i=0;
while feof(fid) == 0
    i=i+1;
    tline = fgetl(fid);   %reads line
    if i==1
        files=tline;
    else
        files=strvcat(files,tline);  % adds extra files to list
    end
end
fclose(fid);

clear i

[m,n]=size(files);

% Print Verification of output list to Screen
fprintf(1,'\n');
fprintf(1,'Output Files In List\n');
fprintf(1,'\n');
for i=1:m
    fprintf(1,'%s\n',files(i,:));  % Prints ith file name
end
fprintf(1,'\n');
fprintf(1,'End of Output Files In List\n');
fprintf(1,'\n');

clear i time
time=0;
for i=1:m
    tic;
    ARRAY(i).VALUE=reader(files(i,:));
    time=time+toc;
    ave_time=time/i;
```

```
    left=(m-i)*(nn+1);
    time_remaining=(left)*ave_time;
    fprintf(1,'%d files remain: Finished %s with ~ %6.2f min
remaining\n',left,files(i,:),time_remaining/60);
end

%%%%%%%%%%%%%%%%%%%%%%%%%%%%%%%%%%%%%%
%  nn = number of time steps
%%%%%%%%%%%%%%%%%%%%%%%%%%%%%%%%%%%%%

save Output_Data ARRAY

plotter
```

X.3.E Reader.m

```
function apend = reader(filename)
% Search for number of string matches per line.
% For RELAP Files, literal should be MINOR EDIT in capital Letters
% This file is for 15 outputs.  If outputs are between 10 and 18, then vary
% Outputs accordingly.  If 9 or below, comment out 4 lines which indicate so
% And change the 10 in first to #M.E. +1

outputs=15;

literal='MINOR EDIT';

fid = fopen(filename, 'rt');
y = 0;
while feof(fid) == 0
   tline = fgetl(fid);                %Moves to the next line and copies it
in tline
   matches = findstr(tline, literal); %Is tline what you were looking for?
   num = length(matches);             %How many times did what you were
looking for
                                      %appear in the line?
   if num > 0                         %Did you get a hit?
      y = y + num;                    %How many hits do we have?

      for i=1:4
          skip=fgets(fid);            %Skip 4 lines after target word
      end

      first=fscanf(fid,'%e',[10,50]); %reads in first 10 RELAP MINOR EDIT
parameters
                                      %, prints out 50 points at a time



      if size(first,2)==50
          n=5;
          if first(1,50)==1
```

```
            first(:,50)=[];
            n=4;
          end
      else
          n=4;
          first(:,size(first,2))=[];
      end



      for i=1:n
          skip=fgetl(fid);           %Skips an extra 4 lines
      end


      %reads in second 7 RELAP MINOR EDIT parameters
      %, prints out 50 points at a time
      second=fscanf(fid,'%e',[outputs+2-10,50]);

      if y==1
          apend1=first;              %Starts Matrix1
          apend2=second;             %Starts Matrix2  (Comment out if less
than 10 M.E.)
      else
          apend1=cat(2,apend1,first);  %Builds off Matrix 1
          apend2=cat(2,apend2,second); %Builds off Matrix 2 (Comment out if
less than 10 M.E.)
      end

   end
end

apend2(1,:)=[];                      % Removes second time column (Comment
out if less than 10 M.E.)
apend=cat(1,apend1,apend2);          % Combines Matrix 1 and 2    (Comment
out if less than 10 M.E.)
% apend=apend1;                      %(Comment in if less than 10 M.E.)

fclose(fid);
```

X.3.F Plotter.m

```
%%%%%%%%%%%%%%%%%%%%%%%%%%%%%%%%%%%%%%
%  ll = number of files....should equal m
%  mm = 1 + number of outputs
%  nn = number of time steps
%%%%%%%%%%%%%%%%%%%%%%%%%%%%%%%%%%%%%

ll = size(ARRAY,2);

% % %% Pull Time
```

```
%%  Pull Peak Clad Temperature
figure(1)
for j=1:ll
    time=ARRAY(j).VALUE(1,:);
    pctemp=ARRAY(j).VALUE(10,:)-273.15;
    plot(time,pctemp)
    if j ~= ll
        hold on
    else
        hold off
    end
end

title('Peak Clad Temperature vs Time')
xlabel('Time (s)')
ylabel('Peak Clad Temperature ( ^o C)')

%%  Pull Core Outlet Temperature

figure(2)
for j=1:ll
    time=ARRAY(j).VALUE(1,:);
    potemp=ARRAY(j).VALUE(6,:)-273.15;
    plot(time,potemp)
    if j ~= ll
        hold on
    else
        hold off
    end
end

title('Core Outlet Temperature vs Time')
xlabel('Time (s)')
ylabel('Core Outlet Temperature ( ^o C)')

%%  Pull Peak Fuel Temperature

figure(3)
for j=1:ll
    time=ARRAY(j).VALUE(1,:);
    pftemp=ARRAY(j).VALUE(11,:)-273.15;
    plot(time,pftemp)
    if j ~= ll
        hold on
    else
        hold off
    end
end

title('Peak Fuel Temperature vs Time')
xlabel('Time (s)')
ylabel('Peak Fuel Temperature ( ^o C)')
```

```
%%  Power
figure(4)
for j=1:11
    time=ARRAY(j).VALUE(1,:);
    pow=ARRAY(j).VALUE(8,:)/1e7;
    plot(time,pow)
    if j ~= 11
        hold on
    else
        hold off
    end
end

title('% Full Power vs Time')
xlabel('Time (s)')
ylabel('Thermal Power (%)')%%  Power


%%  Reactivity
figure(5)
for j=1:11
    time=ARRAY(j).VALUE(1,:);
    react=ARRAY(j).VALUE(16,:);
    plot(time,react)
    if j ~= 11
        hold on
    else
        hold off
    end
end

title('Reactivity vs Time')
xlabel('Time (s)')
ylabel('Reactivity ($)')
```

X.4 Cladding Failure Calculation

The Cladding Failure Calculation Module takes the arrays from the Output Extraction module and calculates Fractional Cladding Damage for each simulation, and determines the total weight of failed simulations, where failure is defined as creep rupture of the cladding, local boiling in the hot channel, or bulk sodium boiling.

X.4.A Object_Builder.m

```
mrd=1;
n=size(ARRAY,2);
fprintf(1,'%d to go \n',n)
```

```
for k=1:mrd
    for i=1:n
        [r,h,f,ftime,f2]=dimension(ARRAY(i).VALUE(1,:),...
            (ARRAY(i).VALUE(10,:)));
        [l,m]=size(ARRAY(i).VALUE(1,:));
        if k==1
            ARRAY(i).DEFORM=zeros(mrd,m);
            ARRAY(i).DAMAGE=zeros(m,mrd);
            ARRAY(i).DEFORM(1,:)=r;
            ARRAY(i).DEFORM(2,:)=h;
        end
        ARRAY(i).DEFORM(1,:)=r;
        ARRAY(i).DEFORM(2,:)=h;
        ARRAY(i).DAMAGE(:,k)=f';
        ARRAY(i).FRAC_DAMAGE(k)=f2;
        ARRAY(i).FTIME(k)=ftime;
        if mod(i,10)==0
            fprintf(1,'%d ',i)
        end

    end
    fprintf(1,'\nDONE\n')
end
save 1_9_11_TOP ARRAY
jjj=567;
ll=n;
damageplotter
```

X.4.B Creep_Failure.m

```
function [r,h,f,ftime,f2]=creep_failure_metal_fuel(time,pctemp)    %  Main
Function

%% Initial Parameters

% pctemp is the peak clad temperature. creep is typically calculated at the
% clad midwall, but pctemp is used for ease and conservatism.

% If the initial EOL plenum pressure is assumed to be 10MPa, then 14.3MPa
% will provide a conservative rupture time prediction for all clad
% temperatures. Effective plenum pressure may be produced by additional
% fission gas release for fuel swelling. After 900oC, this code produces
% extremely conservative results. See Creep Verification.xlsx for
% comparative plot.
P=14.3;                   %Internal Pressure in MPa
E=HT9_E(510+273.15);            %Elasticity
v=.7;                   %Poisson Ratio

% Steady burnup correction form ANL-FRA-1996-3. Is used to reduce the
% predicted rupture time to account for radiation damage of the clad.
BU=15;                %atom percent
SS_D=(1+BU)^-0.544669;
```

```
% Initial dimensions
hi=.056;                  % clad thickness
ri=.755/2-hi/2;           % clad radius

et=P*ri/(2*E*hi)*(2-v);   % Theta Strain due to Fission Gas Pressure
ez=P*ri/(2*E*hi)*(1-2*v); % Axial Strain due to Fission Gas Pressure

dr=ri*et;                          % Change in SS r due to strain
r(1,:)=ri+dr;                      % New SS Radius
dh=-hi*(1-1/((1+et)*(1+ez)));      % Change in SS h due to strain
h(1,:)=hi+dh;                      % New SS thickness

[m,n] = size(time);
[mm,nn] = size(pctemp);

testm=mm-m;
testn=nn-n;

if (testm+testn)~=0
    fprintf(1,'The dimensions of time and temp do not match')
end

% pctemp=pctemp+273.15;

f=ones(nn,1)*0.0006;  % Superprism EOL Highbreeding Metal cumulative damage
fraction
dhe=0;
dre=0;
mrd=0;
for i=1:(nn-1)
    dt=time(i+1)-time(i);
    dtemp=pctemp(i+1)-pctemp(i);

%      if dt==0
%          sprintf('wtf')
%      end

    %% DEFORM5 Module
    if dt~=0
        if i<nn

                det=D5_creep(dt,pctemp(i),r(i,1),h(i,1),P);    %Calculates
the change in et due to creep
                %%% Creep
                et=et+det;
                dh=-hi*(1-1/((1+et)*(1+ez)));
                if pctemp(i)>923
                    %%% Eutectic                 (Eutectic starts @ 650oC)
                    hdot=1e-4*exp(22.847-27624/pctemp(i));  %  Eutectic
wastage of cladding wall
                    dhe=dhe-hdot*dt;
                    dre=dre+hdot*dt/2;
                end
```

```
                r(i+1,1)=ri*(1+et)+dre;     %Adjust radius   {ri*(1+et) is
creep and dre is eutectic}
                h(i+1,1)=hi+dh+dhe;         %Adjust thickness
{h(i+1,1)=hi+dh+dhe;}

                %%% MTTF for state

tf(1)=D5_failure_time(dt,dtemp,pctemp(i),r(i+1,1),h(i+1,1),P);

                %%% Failure Fraction for State
                f(i+1,1)=f(i,1)+dt/(tf(1)*SS_D);          % Last portion is a
burnup correction factor
        end
    else
            f(i+1,1)=f(i,1);
            r(i+1,1)=r(i,1);
            h(i+1,1)=h(i,1);
    end


    if ((f(i+1)>1.0) && (mrd<0.5))
        mrd=1;
        ftime=time(i+1);
    end


end
 f2(1)=f(nn,1);
 if f2<1.0
    ftime=0;
 end

end




function E=HT9_E(T)  %Elasticity of HT9 as a function of Temperature

E=2.12e11*(1.144-4.856e-4*T); %(Pa) ANL-FPA-1996-3 V-3 Eq. 11.3-42

end

function [sige,sigt]=stress(r,h,P)

sigt=P*r/h;                % Average Stress in the theta direction
                           % Average Stress in the radial direction (=P~0, thin
shell)
sige=(1.5/2)^.5*sigt;      % Equivalent Stress

end

function tf=D5_failure_time(dt,dtemp,temp,r,h,P)
```

```
[sige,sigt]=stress(r,h,P);

C=-(0.5*(1+tanh((sige-200)/50)))*(0.75*(1+tanh((dtemp/dt-58)/17)));
B=12/(1.5+.5*tanh(((sige-200)/50)));
A=-34.8+tanh((sige-200)/50)+C;

theata=exp(A+B*log(log(730/sige)));          %Dorn Parameter...strain
hardening

tf=theata*exp(36739/temp);

if isnan(tf(1))==1
    sprintf('bad trouble in D5 Failure Time')
end

end

function det=D5_creep(dt,pctemp,r,h,P)

[sige,sigt]=stress(r,h,P);

edot_oos=5.1966e10;             %s
sigso=3.9593e-3*HT9_E(pctemp);    %Pa
QoverR=36739;                   %K

creeprate=edot_oos*(sige/(sigso*1e-6))^2.263*exp(-QoverR/pctemp);

det=dt*creeprate/sige*3/4*sigt;

end
```

X.4.C Damage Plotter.m

```
 n=size(ARRAY,2);

clear f
figure(jjj)
for j=1:n
    time=ARRAY(j).VALUE(1,:);
    f=ARRAY(j).DAMAGE;
%     loglog(time,f(:,1),time,f(:,2)); grid on
    for k=1:mrd
        subplot(1,mrd,k)
        loglog(time,f(:,k)); grid on
        loglog(time,ones(size(time)),'r','LineWidth',1);
        if j ~= 11
            hold on
        else
            hold off
        end
    end
end
```

```
% axis([1,max(ARRAY(1).VALUE(1,:)),1e-4,10])
% title('Failure Fractions')
% xlabel('Time (s)')
% ylabel('Cumulative Clad Damage Fraction')
for k=1:mrd
    subplot(1,mrd,k)
%     tite=sprintf('Clad Damage Fraction for %d^oC \n Core Outlet
Temperature',COT(k)+510);
    tite=sprintf('%d^oC Core\nOutlet Tempeature',COT(k)+510);
    axis([1,max(ARRAY(1).VALUE(1,:)),1e-4,10])
    title(tite)
    xlabel('Time (s)')
    ylabel('Cumulative Damage Fraction')
end
%% Do I fail?
clear fail s wieght
fail=zeros(n,3*mrd+1);

for k=1:mrd
    for i=1:n
        if max(ARRAY(i).DAMAGE(:,k))>=1.0
            fail(i,k)=1;
        else
            fail(i,k)=0;
        end
    end
end

%% Do I Boil?
for k=1:mrd
    for i=1:n
        if min(ARRAY(i).VALUE(17,:)-(ARRAY(i).VALUE(7,:)-273+COT(k)))<=0
            fail(i,k+mrd)=1;
        else
            fail(i,k+mrd)=0;
        end
    end
end

%% Do I Boil?
for k=1:mrd
    for i=1:n
        if min(ARRAY(i).VALUE(17,:)+273-(ARRAY(i).VALUE(6,:)+COT(k)))<=0
            fail(i,k+2*mrd)=1;
        else
            fail(i,k+2*mrd)=0;
        end
    end
end

%% Arrange failure weights
load UTOPLOF_PAR
[x,y]=size(Par.wgt);

for i=1:x
    for j=1:y
       fail(j+(i-1)*y,3*mrd+1)=Par.wgt(i,j);   % load weights
```

```
%        fail(j+(i-1)*y,3*mrd+2)=i;                    % folder number
    end
end

[m,n]=size(fail);

wieght=zeros(m,n-1);
s=zeros(1,n-1);
max=sum(fail(:,n));
for i=1:(n-1)
    wieght(:,i)=fail(:,i).*fail(:,n);
%     s(i)=sum(wieght(:,i));
    s(i)=sum(wieght(:,i))*m/max;
end
```

X.4.D Failure Prob.m

```
clear all
n=1e4;
a(1)=26.2;
a(2)=1;
b=350;
c=1;

x=logspace(-8,0,n);
y1=betapdf(x,a(1),b-a(1));


figure(201)
loglog(x,y1)
xlabel('Probability of Clad Rupture')
ylabel('Probability Density Function of Clad Rupture,  \pi''(p)dp')
legend('590\circC Core Outlet Temperature')
axis([1e-8 1 1e-3 1e8])

% z1=y1;
% z1(1)=exp(log(z1(1))*log(x(2)-x(1)));
%
% z2=y2;
% z2(1)=exp(log(z2(1))*log(x(2)-x(1)));
%
% for i=2:n
%     z1(i)=z1(i-1)+exp(log(y1(i))*log(x(i)-x(i-1)));
%     z2(i)=z2(i-1)+exp(log(y2(i))*log(x(i)-x(i-1)));
% end


z1=betainc(x,a(1),b);


figure(202)
semilogx(x,z1)
xlabel('Probability of Clad Rupture')
ylabel('Cumulative  Probability of Clad Rupture, \int\pi''(p)dp')
```

```
legend('590\circC Core Outlet Temperature')
axis([1e-8 1 .9 1])
grid on

x1ave=a(1)/b*c
x195=betainv(.95,a(1),b-a(1))*c




% n=1e4;
% a(1)=.05;
% a(2)=0.65;
% b=363;
% c=0.007;
%
% x=logspace(-15,0,n);
% y1=betapdf(x,a(1),b);
% y2=betapdf(x,a(2),b);
%
%
% figure(203)
% loglog(x,y1,x,y2,'--')
% xlabel('Probability of Clad Rupture')
% ylabel('Probability Density Function of Clad Ruputre, \pi''(p)dp')
% legend('510\circC Core Outlet Temperature','550\circC Core Outlet
Temperature')
% axis([1e-8 1 1e-3 1e8])
%
% % z1=y1;
% % z1(1)=exp(log(z1(1))*log(x(2)-x(1)));
% %
% % z2=y2;
% % z2(1)=exp(log(z2(1))*log(x(2)-x(1)));
% %
% % for i=2:n
% %      z1(i)=z1(i-1)+exp(log(y1(i))*log(x(i)-x(i-1)));
% %      z2(i)=z2(i-1)+exp(log(y2(i))*log(x(i)-x(i-1)));
% % end
%
%
% z1=betainc(x,a(1),b);
% z2=betainc(x,a(2),b);
%
%
% figure(204)
% semilogx(x,z1,x,z2,'--')
% xlabel('Probability of Clad Rupture')
% ylabel('Cumulative  Probability of Clad Rupture, \int\pi''(p)dp')
% legend('510\circC Core Outlet Temperature','550\circC Core Outlet
Temperature')
% axis([1e-8 1 0 1])
%
% x1ave=a(1)/b*c
% x195=betainv(.95,.05,363)*c
% x2ave=a(2)/b*c
% x295=betainv(.95,.65,363)*
```

XI APPENDIX D – EUTECTIC MODEL UNCERTAINTY CODES (MUTT)

MUTT is a model uncertainty code developed to create uncertainty distributions around the predictive rate eutectic formation correlations.

XI.1 Main.m

```
% This script is the main code for the model uncertainty methodology as
% applied to metal fuel/clad eutectic. 4 support files are needed:
% sample_evidence, double_integral, validate, and compile.

close all
clear all

names(1).file='bauer';
names(2).file='ANL';
names(3).file='1storder';
names(4).file='2ndorderU';

tic;
for iii=1:4
    filedata=strcat(names(iii).file,'data');   % attempts to separate basic
data from processed data

    load(names(iii).file)    %loads processed data

    sample_evidence  % run script to generate joint pdf

    save(filedata,'X','Y','Z','dx','dy','Chain','Marg_b','Marg_s',...
        'data','filedata')

    load(filedata)

    double_integral  % run script to perform double integration

    save(filedata,'X','Y','Z','dx','dy','Chain','Marg_b','Marg_s','data',...
        'ratio','r_pdf','r_cdf','r_mesh','dr','r_per')

    r_per            % prints 5th, 50th, mean, 95th

    validate         % prints comparison of calculated cdf to data cdf

end

time=(toc)/60;       % converts elapsed time from sec to min
fprintf(1,'\n The elapsed time is %.1f  min \n',time)

compile              % compares all
```

XI.2 Sample Evidence.m

```
%%% This script is called from main.m and creates the joint distribution of
%%% bm and sm based off the evidence loaded before the script is called.
%% set up MC
Niter=2e5;    % # of samples analyzed
Npar=3;       % bm, sm, pi

[N,m]=size(data);  % how many datapoints available
bmin=-4;           % min bias value considered
bmax=2;
smax=2.5;
%% Begin MC

b0=rand*(bmax-bmin)+bmin;    % prior of b is a uniform dist between bmin and
max
s0=rand*smax;                % prior of s is a uniform dist beween 0 and smax
pi0=1;                       % likelihood of evidence is 1.0 before evidence
for j=1:N
    pi0=pi0*lognpdf(data(j),b0,s0);   % likelihood of evidence given b0 and
s0 after evidence
end

Chain=zeros(Niter,Npar);   %3 parameters: bias, sd of bias, and likelihood
Chain(1,:)=[b0,s0,pi0];    %3 parameters: bias, sd of bias, and likelihood

for i=2:Niter  %begin Monte Carlo looop <------------------------------!
    pi0=1;  %prior likelihood (value does not matter)                  !
    b0=rand*(bmax-bmin)+bmin; % randomly select b0                     !
    s0=rand*smax;             % randomly select s0                     !
    for j=1:N % begin loop over evidence <--------------------------  !
        pi0=pi0*lognpdf(data(j),b0,s0);   %Evaluate evidence        !  !
    end % loop over all eviedence --------------------------------->!  !
    Chain(i,:)=[b0,s0,pi0];  %group posterior evidence                 !
end  % end Monte Carlo Loop ------------------------------------------>!

Chain(:,3)=Chain(:,3)./sum(Chain(:,3));  %Normalize MC points

x=Chain(:,1);
y=Chain(:,2);
z=Chain(:,3);
%% Create normalized mesh marginal distributions
density=500;   % how close are the mesh points in the x and y direction

xlin = linspace(bmin,bmax,density);   % linearly interpolate x over a evenly
spaced mesh
ylin = linspace(1e-6,smax,density);   % linearly interpolate y over a evenly
spaced mesh

[X,Y] = meshgrid(xlin,ylin);          % creates a mesh over x and y points
defined above

Z = griddata(x,y,z,X,Y,'cubic');      % interpolates z points
```

```
dx=abs(xlin(2)-xlin(1));              % x spacing (dbm)
dy=abs(ylin(2)-ylin(1));              % y spacing (dsm)
xxx=0;                                % initialize normalization constant

for i=1:density  % begin loop over bm <-------------------------------------
    for j=1:density  % begin loop over sm<-------------------------------- !
        if isnan(Z(i,j))==1           % if likelihood below computer     ! !
                                      %     limit (NaN)                  ! !
            Z(i,j)=1e-300;            % set likelihood to 1e-300         ! !
            xxx=xxx+Z(i,j)*dx*dy;     % sum                              ! !
        elseif Z(i,j)<=0              % if interpolation extrapolates     ! !
                                      %     likelihood to negative values! !
            Z(i,j)=1e-300;            % set likelihood to 1e-300         ! !
            xxx=xxx+Z(i,j)*dx*dy;     % sum                              ! !
        else                          %                                  ! !
            xxx=xxx+Z(i,j)*dx*dy;     % else, num integrate              ! !
        end                           % end if statement                 ! !
    end  % end loop over sm -------------------------------------------->! !
end  % end loop over bm -------------------------------------------------->!
Z=Z/xxx;     % normalize posterior joint pdf
%%  Calculate Marginal Distributions
[density,n]=size(X);

Marg_b=zeros(density,1);
Marg_s=zeros(density,1);

for i=1:density %<--------------------------
    for j=1:density %--------------------- !
        Marg_b(i)=Marg_b(i)+Z(j,i)*dy; % ! !
    end %integrate over sm --------------! !
end % loop over all bm --------------------!

for i=1:density %<--------------------------
    for j=1:density %<-------------------- !
        Marg_s(i)=Marg_s(i)+Z(i,j)*dx; % ! !
    end %integrate over bm --------------! !
end % loop over all sm --------------------!

%% plot MC results, normalized mesh posterior, and marginal distributions
figure(1)
mesh(X,Y,Z); %interpolated
axis tight; hold on
xlabel('Bias Factor, (bm)')
ylabel('Standard Error of b, (sm)')
zlabel('Posterior PDF \pi(bm,sm)dbm dsm')
grid on

figure(15)
plot3(x,y,z,'.','MarkerSize',10) %nonuniform
xlabel('Bias Factor, (bm)')
ylabel('Standard Error of b, (sm)')
zlabel('Posterior PDF \pi(bm,sm)dbm dsm')

figure(3)
subplot(2,1,1)
```

```
plot(X(1,:),Marg_b)
xlabel('Bias Factor, (bm)')
ylabel('PDF of bm,\pi(bm)dbm')
subplot(2,1,2)
plot(Y(:,1),Marg_s)
xlabel('Standard Error of b, (sm)')
ylabel('PDF of sm,\pi(sm)dsm')
```

XI.3 Double Integral.m

```
% The following script calculates the double integral of the lognormal
% likelihood and the meshed MC generated posterior distribution around bm
% and sm

% Initialize Variables
r_mesh=[1000,500];  % # of fine mesh points, # of course mesh [points
rtrans=4;          % transition from course to fine mesh
rmax=35;           % max ratio value (must not be set to low or mean and
                   % effected
ratio=cat(2,linspace(1e-6,rtrans,r_mesh(1)),...        %combine fine mesh
    linspace(rtrans+(rmax-rtrans)/(r_mesh(2)),rmax,r_mesh(2)));%with course
dr(1)=ratio(2)-ratio(1);                               %fine mesh spacing
dr(2)=ratio(sum(r_mesh))-ratio(sum(r_mesh)-1);         %course mesh spacing
r_pdf=zeros(sum(r_mesh),1)';                             %initialize pdf
[density,n]=size(X);            % Determine # of x and y points

pdf=zeros(sum(r_mesh),density)';
c_pdf=zeros(sum(r_mesh),density)';

%% Perform integration over likelihood function
tic % start time
for i=1:(density) % begin loop through bm <--------------------------------
    for j=1:(density) % begin loop through sm <---------------------------!
        r_pdf=r_pdf+lognpdf(ratio,X(1,i),Y(j,1))*Z(j,i);              % !!
                 % existing likelihood of R + )likelihood at new b and   !!
                 % s) times prob of b and s being together               !!
    end  % end loop over all sm -----------------------------------------!!
    if mod(i,25)==0                  % every 10 outer loops               !
        fprintf(1,'%.0f%% ',i/density*100)   % print counter              !
    end                              %                                    !
    if (mod(i,200)==0 )% every 100 outer loops                            !
        fprintf(1,'\n ')             % reset line                         !
    end                              %                                    !
end   % end loop through bm ---------------------------------------------->
%% Normalize posterior PDF
tot=0; %initialize integral
for i=1:2 %begin mesh transition <----------------------------------
    if i==1   % is mesh fine?                                      !
        for k=1:r_mesh(i)  % begin integration over fine mesh <--  !
            tot=tot+r_pdf(k)*dr(i); %                            ! !
        end   % end integration over fine mesh ----------------->! !
    else      % mesh mush be course                                !
        for k=(r_mesh(i-1)+1):sum(r_mesh) % begin integration <-   !
            tot=tot+r_pdf(k)*dr(i); %       over course mesh     ! !
        end   % end integration over course mesh --------------->! !
```

```
    end                                                       %  !
end % end mesh transition -------------------------------------->!
r_pdf=r_pdf/tot; %normalize pdf
%% Calculate CDF
r_cdf=zeros(sum(r_mesh),1);  %initialize cdf variable
for i=1:2 %begin mesh transition <--------------------------------
    if i==1 % is mesh fine?                                      !
        for k=2:r_mesh(i) % begin integration over fine mesh <-- !
            r_cdf(k)=r_cdf(k-1)+r_pdf(k)*dr(i); %              ! !
        end  % end integration over fine mesh ---------------->! !
    else      % mesh mush be course                              !
        for k=(r_mesh(i-1)+1):sum(r_mesh) % begin integration <- !
                                          % over course mesh   ! !
            r_cdf(k)=r_cdf(k-1)+r_pdf(k)*dr(i); %              ! !
        end  % end integration over course mesh -------------->! !
    end                                                       %  !
end % end mesh transition -------------------------------------->!


%% Validation Ratios of Interest
r_per(1)=interp1(r_cdf,ratio,0.05);  %Interpolate 5th percentile
r_per(2)=interp1(r_cdf,ratio,0.5);   %Interpolate 50th percentile
r_per(3)=sum(r_pdf(1:r_mesh(1)).*ratio(1:r_mesh(1))*dr(1))+...

sum(r_pdf((r_mesh(1)+1):sum(r_mesh)).*ratio((r_mesh(1)+1):sum(r_mesh))*dr(2))
;  %Calculate mean
r_per(4)=interp1(r_cdf,ratio,0.95);  %Interpolate 95th percentile

%% Plots


figure(5)
subplot(3,1,1)
plot(X(1,:),Marg_b)
xlabel('Bias Factor, (bm)')
ylabel('PDF of bm,\pi(bm)dbm')
subplot(3,1,2)
plot(Y(:,1),Marg_s)
xlabel('Standard Error of b, (sm)')
ylabel('PDF of sm,\pi(sm)dsm')
subplot(3,1,3)
%%% duel y axis
hl1 = line(ratio,r_pdf,'Color','r');
ax1 = gca;
set(ax1,'XColor','r','YColor','r')
xlabel('Validation Ratio, R')
ylabel('PDF of R, \pi (R)dR')
ax2 = axes('Position',get(ax1,'Position'),...
           'XAxisLocation','top',...
           'YAxisLocation','right',...
           'Color','none',...
           'XColor','k','YColor','k');
axis([0,max(ratio),0,1])
hl2 = line(ratio,r_cdf,'Color','k','Parent',ax2);
ylabel('CDF of R,\int \pi (R)dR')
```

XI.4 Validate.m

```
% This script compares the calculated cumulative distribution to the
% empirical cumulative distribution
[N,m]=size(data);  % how much data?
cumdata=zeros(2*N,1); % Initialize the empirical cumulative distribution
xx=zeros(2*N,1); % Twice as many x,y point e
cumdata(1)=0;
xx(1)=0;
cumdata(2)=0;
xx(2)=data(1);
for i=3:(2*N+1)
    if mod(i,2) == 0
        cumdata(i)=cumdata(i-1);
        xx(i)=data((i)/2);
    else
        cumdata(i)=cumdata(i-1)+data((i-1)/2);
        xx(i)=data((i-1)/2);
    end
end
cumdata=cumdata/max(cumdata);

xx=sort(xx);

figure(6)
plot(xx,cumdata,ratio,r_cdf)
xlabel('Validation Ratio, R')
ylabel('CDF of R, \int \pi(R)dR')
```

XII APPENDIX E - CALCULATION OF PEAK CLADDING TEMPERATURES USING THE HORIZONTAL METHOD

Appendix D overviews the calculations of the mid-wall and peak cladding temperatures using the horizontal semi-statistical approach for hot channel factors. The calculations will first be performed for oxide fuel, and then for metal fuel.

XII.1 Oxide Cladding Temperatures (16)

First, the total direct hot channel factor is determined for the coolant, film, and cladding, as shown in Table 40.

Table 40 – Oxide Fuel Direct Hot Channel Factors

	HCF for Coolant Temperature Rise	HCF for Film Temperature Rise	HCF for Cladding Temperature Rise
Power Level	1.0	1.0	1.0
Inlet Flow	1.02	1.006	1.0
Flow Dist. Calc.	1.03	1.0	1.0
Clad. Circ. T Var.	1.0	2.1	0.84
Pellet-Clad Ecc.	1.0	1.14	1.14
Physics	1.02	1.1	1.1
Control Rod	1.02	1.02	1.02
ZPPR	1.0	1.0	1.0
Product	1.093	2.702	1.074

Then, using temperature rises determined from the direct hot channel factors, the statistical hot channel factors are determined by adding each row in Table 41 and then combining each row in a root-mean-square method to determine the total statistical temperature rise.

Table 41- Oxide Fuel 3σ Statistical Hot Channel Factors

Statistical (3σ)	Inlet T (°F)	Coolant ΔT (°F)	Film ΔT (°F)	Cladding MW ΔT (°F)	Total $3\sigma_{MW}$ (°F)
Reactor ΔT and inlet temperature variation		27.5			27.5
Inlet flow maldistribution		27.1	0.5		27.6
Loop temperature imbalance	7.4				7.4
Wire wrap orientation		4.6			4.6
Subchannel flow area		8.7			8.7
Film heat transfer coefficient			3.9		3.9
Pellet-cladding eccentricity			5.6	2.6	8.2
Cladding thickness and conductivity				0.0	0
Coolant properties		7.8			7.8
Flow distribution calculational uncertainty (calibration)		26.6	0.2		26.8
Nuclear Data		32.1	2.3	1.1	35.5
Criticality		4.6	0.3	0.2	5.1
Fissile fuel management		23.9	1.7	0.8	26.4
Overall 3σ=					67.2

This yields the following temperature rises, shown in Table 42, for the nominal, direct, and 2σ cases, assuming the inlet temperature is 356°C, which corresponds to an averaged core outlet temperature of 510°C.

Table 42 – Oxide Fuel Hot Channel Factor Temperature Rises

	Inlet T (°C)	Coolant ΔT (°C)	Film ΔT (°C)	Cladding MW ΔT (°C)	Cladding MW T (°C)
Nominal	356	179	2	4.7	541.7
Direct	356	195.7	5.4	5.0	562.1
2σ	-	-	-	-	606.9

XII.2 Metal Cladding Temperatures (15)

First, the total direct hot channel factor is determined for the coolant, film, and cladding, as shown in Table 43.

Table 43 – Metal Fuel Direct Hot Channel Factors

	HCF for Coolant Temperature Rise	HCF for Film Temperature Rise	HCF for Cladding Temperature Rise
Power Level	1.0	1.0	1.0
Inlet Flow	1.02	1.006	1.0
Flow Dist. Calc.	1.03	1.0	1.0
Clad. Circ. T Var.	1.0	2.1	0.84
Pellet-Clad Ecc.	1.0	1.0	1
Physics	1.02	1.1	1.1
Control Rod	1.02	1.02	1.02
ZPPR	1.0	1.0	1.0
Product	1.093	2.370	0.942

Then, using temperature rises determined from the direct hot channel factors, the statistical hot channel factors are determined by adding each row in Table 44 and then combining each row in a root-mean-square method to determine the total statistical temperature rise.

Table 44- Metal Fuel 3σ Statistical Hot Channel Factors

Statistical (3σ)	Inlet T (°F)	Coolant ΔT (°F)	Film ΔT (°F)	Cladding MW ΔT (°F)	Total $3\sigma_{MW}$ (°F)
Reactor ΔT and inlet temperature variation		27.5			27.5
Inlet flow maldistribution		27.1	0.5		27.6
Loop temperature imbalance	7.4				7.4
Wire wrap orientation		4.6			4.6
Subchannel flow area		8.7			8.7
Film heat transfer coefficient			3.9		3.9
Pellet-cladding eccentricity			0.0	0.0	0.0
Cladding thickness and conductivity				0.0	0.0
Coolant properties		7.8			7.8
Flow distribution calculational uncertainty (calibration)		26.6	0.2		26.8
Nuclear Data		32.1	2.3	1.1	35.5
Criticality		4.6	0.3	0.2	5.1
Fissile fuel management		23.9	1.7	0.8	26.4
Overall 3σ=		27.5			27.5

This yields the following temperature rises, shown in Table 45, for the nominal, direct, and 3σ cases, assuming the inlet temperature is 356°C, which corresponds to an averaged core outlet temperature of 510°C.

Table 45– Metal Fuel Hot Channel Factor Temperature Rises

	Inlet T (°C)	Coolant ΔT (°C)	Film ΔT (°C)	Cladding MW ΔT (°C)	Cladding MW T (°C)
Nominal	356	179	2	4.7	541.7
Direct	356	195.7	4.7	4.4	560.8
2σ	-	-	-	-	605.6